

Static aeroelastic optimization of composite wind turbine blades using variable stiffness laminates

Exploring twist coupled composite blades in stall control

Ferede, Etana

DOI

[10.4233/uuid:b4fe0ca4-b8c7-4e23-a2f1-247ac3b61aeb](https://doi.org/10.4233/uuid:b4fe0ca4-b8c7-4e23-a2f1-247ac3b61aeb)

Publication date

2016

Document Version

Final published version

Citation (APA)

Ferede, E. (2016). *Static aeroelastic optimization of composite wind turbine blades using variable stiffness laminates: Exploring twist coupled composite blades in stall control*. [Dissertation (TU Delft), Delft University of Technology]. <https://doi.org/10.4233/uuid:b4fe0ca4-b8c7-4e23-a2f1-247ac3b61aeb>

Important note

To cite this publication, please use the final published version (if applicable).
Please check the document version above.

Copyright

Other than for strictly personal use, it is not permitted to download, forward or distribute the text or part of it, without the consent of the author(s) and/or copyright holder(s), unless the work is under an open content license such as Creative Commons.

Takedown policy

Please contact us and provide details if you believe this document breaches copyrights.
We will remove access to the work immediately and investigate your claim.

STATIC AEROELASTIC OPTIMIZATION OF COMPOSITE WIND TURBINE BLADES USING VARIABLE STIFFNESS LAMINATES

EXPLORING TWIST COUPLED COMPOSITE BLADES IN
STALL CONTROL

STATIC AEROELASTIC OPTIMIZATION OF COMPOSITE WIND TURBINE BLADES USING VARIABLE STIFFNESS LAMINATES

**EXPLORING TWIST COUPLED COMPOSITE BLADES IN
STALL CONTROL**

Proefschrift

ter verkrijging van de graad van doctor
aan de Technische Universiteit Delft,
op gezag van de Rector Magnificus prof. ir. K. C. A. M. Luyben,
voorzitter van het College voor Promoties,
in het openbaar te verdedigen op 14 November 2016 om 12:30 uur

door

Etana FEREDÉ

Aerospace Engineer, Delft University of Technology
geboren op 23 Mei 1986 te Bishoftu, Ethiopie.

This dissertation has been approved by the
promotor: Prof. dr. G. J. W. van Bussel
copromotor: Dr. M. M. Abdalla

Composition of the doctoral committee:

Rector Magnificus,	chairman
Prof. dr. G. J. W. van Bussel	Technische Universiteit Delft, promotor
Dr. M. M. Abdalla	Technische Universiteit Delft, copromotor

Independent members:

Prof. dr. R. Benedictus	Technische Universiteit Delft
Prof. dr. C. L. Bottasso	University of Munchen, Germany
Prof. dr. F. Gandhi	Rensselaer Polytechnic University, USA
Prof. dr. P. -W. Cheng	University of Stuttgart, Germany
Prof. dr. ir. G. A. M. van Kuik	Technische Universiteit Delft, reservelid



Keywords: Isogeometric analysis, Stall Control, Adaptive blades, Composite Optimization, Blade Element Momentum theory

Printed by: Ridderprint drukkerij

Email: etana.ferede@gmail.com

Copyright © 2016 by E. Ferede
ISBN 978-94-6299-421-8

An electronic version of this dissertation is available at
<http://repository.tudelft.nl/>.

Dedicated to my Parents

PREFACE

At the end of a long journey, I look back and reflect on those that helped me to get where I am today, stirring in me a deep sense of gratitude.

First and foremost I would like to thank the Lord God Almighty that has been a source of love, wisdom, strength and refuge from the day I was born.

I would like to thank the FLOW project that financed my Ph.D. research. I would like to thank my promoter Prof. dr. G.J.W. van Bussel for giving me the opportunity to pursue my doctoral research in wind energy and also for his supervision. I would like to thank my co-promoter Dr. Mostafa Abdalla for his supervision during my Ph.D. research. His patience and guidance were instrumental for me to successfully finish my doctoral thesis. Not only was he a source of technical knowledge, I also enjoyed our conversation ranging from a philosophical discussion on life in general to the current spectacle that is called US presidential election. I would also like to thank Dr. Johannes Dillinger for his valuable help during the last phase of my research.

I would like to thank my colleagues in the wind energy group: Ricardo, Lars, Marten, Ye, Cyril, Gael, Daniel, Carlos, Lorenzo, Giuseppe, and others, that made my time as a Ph.D. student a pleasant experience. As I write this, my thought goes to my former colleague Cyril who passed away suddenly in 2014. I remember that he gave me the French comic book 'Asterix Le Gaulois' to help me learn the French language. *may you rest in peace*. Furthermore, I would like to thank my colleague and friend Ricardo. I immensely enjoyed our collaboration during our Ph.D. research. I also enjoyed our discussion on different topics, ranging from politics to books one needs to read in his or her lifetime. I also thank you for introducing me to delicious Portuguese cuisine. Not only are you a good researcher but also a pleasant person to work with and I wish you a brilliant future. I would like to thank Prof. dr.ir. G.A.M. van Kuik for his help in connecting me with other researchers with a similar research topic. I also would like to thank Sylvia for her help. She has been a great help for me with administrative matters, especially towards the end of my thesis.

I would like to thank my brother Mosissa for being an awesome big brother. I would like to thank my friends: Valmir, Deborah, Eliakim, Dorine, Joseph, Thomas, Eliza, Idse, Jesse, and others, for being a pleasant addition to my life. I would like to thank Eliakim for helping me with the correction of the Dutch summary and propositions. I would also like to thank Rosa for being part of my life. Although you came late into my life, your presence has been a welcome addition.

I would like to thank my Pastor Jacques litu for his guidance in my spiritual life. The example he showed to put God first then others and as last oneself resonates deeply in my heart to follow the same example.

I would like to thank Saba for the kindness and love she showed me and my brother. At last, I would like to convey my deepest gratitude to my parents who have been a pillar of support in my life. I would not have come so far if it was not for the sacrifices they have made for me and my brother to have a better life and opportunity than they had. The discipline of my father and the steadfastness of my mother are a source of inspiration and a character trait I endeavour to cultivate in my life.

Finally, I would like to shed light on the struggles of my Brothers and Sisters in Ethiopia, who are crying for freedom and equal opportunity which I was lucky enough to have in the Netherlands. I form the symbol of non-violent protest (X), in solidarity with them.

Etana Ferede
Delft, June 2016

SUMMARY

The number of wind turbines in offshore wind farms is increasing rapidly over the past decades. However, there are still many challenges ahead for making the costs of generating energy from wind competitive with other energy sources. One method for making the cost of energy from wind market competitive, especially for offshore wind farms, is to reduce the operational and maintenance costs of wind turbines. The operational and maintenance costs of wind turbines may be reduced by eliminating the rotating components, which are prone to wear and tear, as much as possible. The control mechanism for regulating power is among the rotating components and it would be cost effective if it is replaced with stall control scheme. Furthermore, with recent advances in composite technology for tailoring the structural response of composite structures, it may be possible to apply the composite tailoring to the conventional passive stall control scheme to improve its performance. Particularly, the use of twist coupling for power regulation shows a promise to design adaptive blades for stall regulated wind turbines.

The objective of this research is to develop a variable stiffness composite optimization method for wind turbines and investigate the benefits of using composite materials to design twist coupled blades for large scale stall regulated wind turbines. The optimization strategy consists of separating the optimization problem in three consecutive parts, allowing the use of a suitable optimization tool at each stage. For the first step, stiffness-based optimization is carried out on the composite structure of wind turbine rotor blades using continuous laminate design variables while satisfying structural and aeroelastic constraints. For the second step, a stacking sequence optimization is carried out using the optimized stiffness solution from the previous step as the objective, while satisfying constraints related to stacking sequence. For the third step, a fiber path optimization is performed while satisfying constraints related to manufacturability, that depends on the selected type of manufacturing technique, e.g. fiber placement. The second and third steps do not depend significantly on the underlying physical problem and are not considered in the current work.

The composite optimization strategy consists first of an NURBS-based framework that unifies the parametrization of a wind turbine rotor blade and wind turbine aeroelastic analysis, in an isogeometric fashion. The blade geometry, including its finite element model, is generated based on the isogeometric principle. Afterwards, a static wind turbine aeroelastic analysis is performed using isogeometric based module comprised of Blade Element Momentum theory for the aerodynamic loads and non-linear Timoshenko beam model for the structural deformation. Furthermore, a detailed structural anal-

ysis is carried out using the finite element solver NASTRAN by applying the aeroelastic loads onto a (shell) finite element model of the rotor blade. The optimization framework uses a response approximation formulation that is based on a linear and reciprocal approximation of the responses in terms of the design variables, i.e. elements of the membrane and bending stiffness matrix of a laminate together with the laminate thickness. Accordingly in the second step, an approximation model is formulated using both the responses and their sensitivities, while satisfying the essential properties of convexity, separability, and conservativeness. The response approximations are then passed to the optimizer which iterates on the approximated model until the minimum that satisfies the constraints is found.

Both structural and aeroelastic constraints are considered in the present optimization study. The structural constraints are strength and buckling. A failure criterion, based on lamination parameter space, is adopted for the strength constraints. The aeroelastic constraints are maximum tip deflection, maximum power, and the cost of energy. The cost of energy is based on the NREL cost model for pitch regulated wind turbines, which is modified to calculate the cost of energy of stall regulated wind turbines with similar rated power.

The performance of the proposed optimization framework is demonstrated by investigating the benefit of variable stiffness design of composite blades to tailor the twist coupling of rotor blades for improved performance of stall regulated wind turbines. The advantage of unbalanced laminates over balanced laminates to design twist coupled blades is investigated using the cost of energy as the objective function while complying with structural and aeroelastic constraints. A complete stiffness variation along the blade span is considered during the optimization. Furthermore, two operation configurations of the wind turbine are considered, i.e. up-wind and down-wind configuration, where for the down-wind configuration, the constraint on the maximum tip displacement is relaxed. Finally, the capability of twist coupled blades to limit the aerodynamic power of stall regulated wind turbine is investigated by adding an additional constraint on the maximum power during the optimization.

SAMENVATTING

Het aantal windturbines in windmolenparken op zee neemt snel toe in de afgelopen decennia. Echter, er zijn nog veel uitdagingen om de kosten van het opwekken van energie uit wind goedkoper te maken. Een methode om de kosten van windenergie, in het bijzonder bij offshore-wind parken, concurrerend te maken op de energiemarkt, is de onderhoudskosten van windturbines te reduceren. De onderhoudskosten kunnen verminderd worden door zoveel mogelijk bewegende onderdelen die gevoelig zijn aan slijtage te reduceren. Het mechanisme om het vermogen te reguleren is een van de onderdelen die gevoelig zijn aan slijtage en het vervangen van dit systeem zal de onderhoudskosten van windturbines verminderen. Dit is mogelijk door op overtrekmethode over te gaan om het vermogen en de belasting op de rotorbladen te regelen. Bovendien, door recente vooruitgang op het gebied van composieten, is het nu mogelijk om vezel sturing methode van een composiet laminaat te gebruiken bij een conventionele overtrekmethode voor betere prestaties. Met name het gebruik van twist koppeling in rotorbladen, in combinatie met overtrekmethode, toont betere prestatie om het vermogen van windturbines te reguleren.

Het doel van dit onderzoek is het ontwikkelen van een raamwerk voor variabele stijfheid composiet optimalisatie voor windturbine-bladen en het voordeel nagaan van composiet laminaten in twist-gekoppelde bladen bij overtrekgeregelde windturbines op grote schaal. De optimalisatie-strategie bestaat uit het opdelen van het optimalisatie probleem in drie delen, zodat een geschikte methode gebruikt kan worden in elke fase van optimaliseren van de composiet structuren. Voor het eerste deel wordt stijfheid gebaseerde optimalisatie uitgevoerd op de windturbine-rotorbladen door gebruik te maken van doorlopende laminaat variabelen, terwijl de structurele en aeroelastische beperkingen zijn inbegrepen tijdens de optimalisatie. Voor het tweede deel wordt een optimalisatie in stapelvolgorde van de composiet laminaat uitgevoerd door gebruik te maken van de optimale stijfheid ontwerp uit de voorgaande deel, terwijl beperkingen met betrekking tot stapelvolgorde van de compositie laminaat zijn gehandhaafd tijdens het optimalisatie proces. Voor de derde deel wordt het optimale pad van een composiet vezel bepaald, terwijl beperkingen met betrekking tot productie, die afhankelijk zijn van het gekozen type van de productietechniek (bijvoorbeeld fiber placement) zijn inbegrepen tijdens de optimalisatie. Het tweede en derde deel van het composiet optimalisatie proces zijn niet afhankelijk van de onderliggende fysieke probleem en zijn niet beschouwd in het huidige werk.

De samengestelde optimalisatie strategie bestaat in de eerste plaats uit een NURBS-gebaseerd raamwerk dat de parametrisatie van een windturbine

rotor-blad en windturbine aeroelastische analyse integreert in een isogeometrische wijze. De geometrie van het rotor-blad, inclusief zijn eindige element-model, wordt gegenereerd door gebruik te maken van het isogeometrische principe. Daarna wordt aeroelastische analyse van de windturbine uitgevoerd door gebruik te maken van een isogeometrische module bestaande uit Blad Element Impuls theorie (voor de aerodynamische belastingen) en niet-lineaire Timoshenko beam model (voor de structurele vervormingen). Verder wordt een gedetailleerde structurele analyse uitgevoerd met behulp van de eindige elementen software NASTRAN waarbij de aeroelastische belasting op de eindige elementen model van het rotorblad worden toegepast. Het optimalisatie raamwerk gebruikt lokale benadering van de functie, gebaseerd op een lineaire en inverse benadering van de functie ten opzichte van de ontwerp variables, d.w.z. elementen van axiale en buigstijfheid matrixen van het laminaat plus de laminaat dikte. In de tweede stap wordt een benaderingsmodel opgesteld met zowel de functies en hun gevoeligheden, terwijl de essentiële eigenschappen van convexiteit, scheidbaarheid en conservatisme worden voldaan. De functie benaderingen worden vervolgens doorgegeven aan de optimizer die op de functie-benadering itereert totdat het minimum dat aan de beperkingen voldoet wordt gevonden.

Zowel structurele als aeroelastische beperkingen worden beschouwd in de huidige optimalisatie studie. De structurele beperkingen zijn sterkte en knik. Een bezwijkingscriterium, gebaseerd op laminaat parameter ruimte, is gebruikt voor de sterkte beperkingen. De aeroelastische beperkingen zijn maximale tip doorbuiging, maximaal vermogen, en de kosten van energie. De kosten van energie zijn gebaseerd op het NREL kostenmodel voor pitch-geregelde windturbines, die aangepast is om de kosten van de energie voor overtrek-geregelde windturbines met vergelijkbaar nominaal vermogen te berekenen.

De prestatie van het voorgestelde optimalisatie raamwerk wordt gedemonstreerd door het onderzoeken van het voordeel van variabele stijfheid ontwerp van composieten rotorbladen om de twist koppeling van de rotorbladen te optimaliseren voor verbeterde prestaties van overtrek-geregelde windturbines. Het voordeel van ongebalanceerde laminaten boven gebalanceerde laminaten om twist gekoppelde bladen te ontwerpen wordt onderzocht door het minimaliseren van de kosten van energie en door inachtneming van de structurele en aeroelastische beperkingen tijdens de optimalisatie. Een volledige stijfheid variatie over de blad lengte wordt geacht tijdens de optimalisatie. Bovendien, twee configuraties van de windturbine worden beschouwd, up-wind en down-wind configuratie, waarbij voor de down-wind configuratie, de beperking van de maximale tip verplaatsing is verwijderd uit het optimalisatie-proces. Tot slot wordt de capaciteit van twist gekoppelde bladen om de aerodynamische kracht van overtrek geregeld windturbine te beperken onderzocht door het toevoegen een beperking op het maximale vermogen van de windturbine.

CONTENTS

Preface	i
Summary	iii
Samenvatting	v
Nomenclature	xi
1 Introduction	1
1.1 Wind turbine control strategy	2
1.2 Twist coupling in wind turbine blades for power and load regulation	4
1.3 Aeroelastic optimization of composite structures	6
1.4 Research goals	7
1.5 Thesis layout	8
2 Overview on different disciplines used in the dissertation	11
2.1 Wind Turbine Aerodynamics	12
2.1.1 Blade Element Momentum theory	12
2.1.2 Tip and Root Corrections to BEM theory	16
2.2 Isogeometric Analysis	16
2.2.1 Fundamentals of Non-Uniform Rational B-Splines	17
2.2.2 Geometric Algorithm: Knot refinement	19
2.3 Composite Laminates	20
2.3.1 Stacking sequence	21
2.3.2 Lamination parameters	24
2.3.3 Membrane stiffness visualization	25
3 Multi fidelity optimization framework for wind turbine application	27
3.1 Optimization Framework	28
3.2 Design variables	32
3.3 Response definition	32
3.4 Summary	33
4 Parametric Wind Turbine Blade Generation	35
4.1 Geometry Model	36
4.1.1 Beam axis	37
4.1.2 Cross-section	38
4.2 Finite Element Model	40
4.2.1 Interface Model	40

4.3	Optimization Model	41
4.3.1	Design variable definition in IGA.	41
4.3.2	Design variable definition in FEM	42
4.4	Summary	44
5	Stiffness constants of thin Walled composite Cross-Sections	45
5.1	Introduction	46
5.2	Kinematics	46
5.3	Sectional Stiffness Constants	50
5.3.1	Euler Model	50
5.3.2	Timoshenko Model	52
5.4	Validation of Sectional Stiffness Constants	55
5.4.1	Closed cross-section	55
5.4.2	Open cross-section	58
5.4.3	Comparison with experimental result	60
5.5	Summary	63
6	Geometrically exact Beam Model	65
6.1	Introduction	66
6.2	Geometrically exact 3D beam model	67
6.3	Isogeometric formulation.	69
6.3.1	Approximation of the displacement and rotation variables	69
6.3.2	Load vector and tangent stiffness matrix.	71
6.4	Structural Validation	74
6.4.1	A cantilever beam subject to a free-end moment.	74
6.4.2	The MacNeal and Harder test problems	74
6.4.3	A cantilever beam subject to two transversal loads.	76
6.4.4	Curved cantilever beam under transversal tip load.	77
6.4.5	Composite I beam	77
6.4.6	Composite box beam	78
6.5	Centrifugal & Gravitational Load	80
6.6	Summary	84
7	Aeroelastic model	85
7.1	Aerodynamics.	86
7.2	Aero-Structural coupling	89
7.3	Aeroelastic Verification	90
7.4	Summary	92
8	Finite Element Analysis	93
8.1	Apply design dependent loads	94
8.2	Response definition.	95
8.2.1	Stress	95
8.2.2	Buckling	96

8.3	Output definition	96
8.3.1	Responses & Sensitivities	97
8.3.2	Additional alters	97
8.4	Summary	97
9	Response approximation	99
9.1	Methods in Design Optimization	100
9.1.1	Approximation Method for Composite Optimization	101
9.1.2	Sensitivity processing	102
9.2	Response	103
9.2.1	Aeroelastic responses	103
9.2.2	Structural responses	105
9.2.3	Mass & Cost Of Energy	106
9.3	Sensitivity analysis	109
9.3.1	Aeroelastic	109
9.3.2	Finite element	109
9.4	Response approximation	110
9.4.1	Aeroelastic responses	111
9.4.2	Structural responses	111
9.4.3	Objective functions	114
9.5	Summary	115
10	Aeroelastic Optimization of wind turbine blade	117
10.1	Model description	118
10.2	Material properties	120
10.3	Finite element model	121
10.4	Optimization model	122
10.5	Initial design	124
10.6	Baseline design: Mass minimization	125
10.7	Design studies of twist coupled turbine blade: COE minimiza- tion	129
10.7.1	Up-Wind turbine configuration:Balanced laminates	130
10.7.2	Up-Wind turbine configuration: Unbalanced laminates	135
10.7.3	Down-Wind turbine configuration:Unbalanced lami- nates	139
10.7.4	COE minimization with constrained power	144
10.8	Summary	147
11	Conclusions and Recommendations	151
11.1	Conclusions.	152
11.1.1	Stiffness Optimization methodology for wind turbine blades	152
11.1.2	Twist coupled rotor blade design for stall regulated wind turbines	153
11.2	Recommendations	156

A Finite Element Analysis Alters	159
A.1 Responses and Sensitivities	159
A.2 Alter: Correct error in DSCM2.	159
A.3 Alter: Import Sensitivities	160
Bibliography	161
Curriculum Vitae	173
List of Publications	175

NOMENCLATURE

Acronyms

BEM	Blade Element Momentum
CAD	Computer Aided Design
CFD	Computational Fluid Dynamics
CP	Control Point
FE	Finite Element
FEA	Finite Element Analysis
FEM	Finite Element Model
HAWT	Horizontal Axis Wind Turbine
IEC	International Electrotechnical Commission
IGA	Isogeometric analysis
MBD	Maximum Blade Deflection
NURBS	Non-Uniform Rational B-Splines

Coordinate frames

$\Lambda_a(\xi)$	Body attached aerodynamic frame
$\Lambda_s(\xi)$	Body attached structural frame
\mathbf{a}_i	Base vector of the global frame
\mathbf{e}_i	Base vector of the rotating frame

Greek Symbols

α	Local angle of attack
λ	Tip speed ratio
λ_r	Local tip speed ratio
Ω	Rotation of the rotor disc

ω	Local rotational speed
ϕ	Azimuthal position of the blade in the rotor plane
θ	Local twist
$\theta_s(\xi)$	Radial twist variation
φ	Local inflow angle
Ξ	Knot vector
ξ	Coordinate of the parametric space

Latin Symbols

Γ_i	material invariant matrix
\mathcal{L}	Knot refinement matrix between non-homogeneous control points
\mathcal{L}_w	Knot refinement matrix between homogeneous control points
A	Membrane stiffness matrix of a Laminate
B	Coupling stiffness matrix of a Laminate
D	Bending stiffness matrix of a Laminate
K	Structural stiffness matrix
K_{cs}	Centrifugal stiffness matrix
Q	Reduced stiffness matrix of a single lamina
R	Matrix representation of rotation
T	Transformation matrix
f_s	Generalized structural load vector
f_a	Generalized aerodynamic load vector
f_{cs}	Generalized centrifugal load vector
f_g	Generalized gravitational load vector
N	Average membrane stress resultant
P_i^w	Homogeneous control point
P_i	Non-homogeneous control point
q	Quaternion representation of rotation
R_θ	Residual load vector

a	Axial induction factor
a'	Tangential induction factor
B	Number of blades
$c_s(\xi)$	Radial chord variation
C_t	Thrust coefficient
dF_D	Differential drag
dF_L	Differential lift
dF_N	Differential normal force
$J(\xi)$	Jacobian that maps the ξ -parametric space and s -geometric space (beam axis)
$N_{i,p}(\xi)$	B-spline basis function of degree p
P_θ	Generalized coordinate
$R_{i,p}(\xi)$	NURBS basis function of degree p
w_i	Positive weight factor of B-spline function
dQ	Differential torque
dT	Differential thrust
n	Number of univariate spline basis functions
p	Polynomial degree of a B-spline

1

INTRODUCTION

THERE is a growth in the energy consumption of the world, leading to rapid depletion of natural resources, such as fossil fuels. Added to that, the environmental impact of fossil fuels (e.g. global warming) makes a renewable source of energy a better alternative for power generation. Among renewable energy sources, generating energy from wind is becoming more popular.

Wind turbines are designed with increasing efficiency, making the cost of generating energy from wind, market competitive. So far, the vast majority of wind turbines has been built on land, but recently the number offshore wind farms has also increased over the past decade and is projected to increase further in the future; at the same time a steady increase in the size of Horizontal Axis Wind Turbines (HAWTs) is observed [129]. Offshore wind farms are becoming more popular since the wind conditions in offshore sites are stronger and more stable than onshore sites. Moreover, the amount of available onshore area for wind farms, especially in US and Europe, is decreasing due to population growth. The move towards fewer and larger wind turbines in offshore wind farms is motivated by the fact that: (I) larger wind turbines are able to capture more of the energy from wind; (II) most of the cost components of a wind turbine, e.g. infrastructure and operation and maintenance cost, decrease for wind farms with fewer and larger turbines compared to wind farms with smaller and more turbines, having the same capacity.

Although the number of, installed, wind turbines in offshore wind farms is increasing rapidly, there are still many challenges ahead for making the cost of generating energy from offshore wind competitive with other energy sources. One method for making the cost of energy from wind competitive is to reduce the operational and maintenance cost of wind turbines, which is more substantial for offshore wind farms compared to their onshore counterparts [67]. The operational and maintenance cost of wind turbines may be reduced by eliminating, as much as possible, rotating components of the turbine which are prone to wear and tear. Among the rotating components of a wind tur-

bine, the blade pitch system, the control mechanism for regulating power and load is of interest in this thesis.

1.1. WIND TURBINE CONTROL STRATEGY

WIND conditions on any sites are not constant but vary stochastically. Consequently, wind turbines must be able to extract the kinetic energy from wind efficiently for low wind speeds, while ensuring no structural failure for high wind speeds. This is accomplished by means of wind turbine control methods, which are categorized into two groups: passive and active control methods; see figure 1.1 for a representative of active and passive control strategies for power regulation.

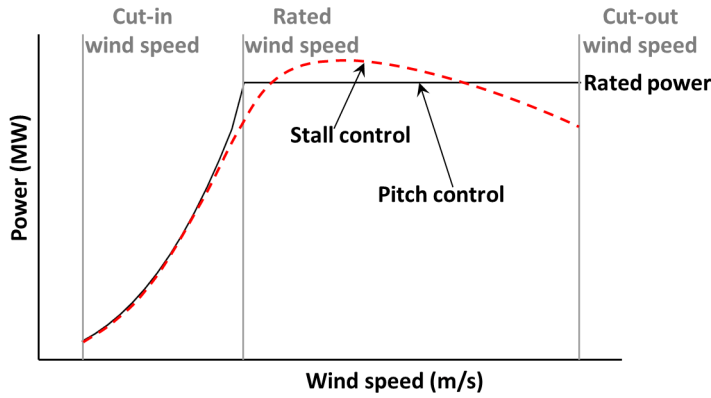


Figure 1.1: Representative power curves for pitch and stall controlled wind turbines

PASSIVE CONTROL

For a passive control method, the aerodynamic characteristics of the wind turbine blades are designed to control the aerodynamic loads on wind turbine blades, without using active mechanism for changing the configuration of the wind turbine. It is the first control method for regulating the extracted power, where much of early wind turbines use passive stall control method for power regulation [94].

These early wind turbines, employing stall control, operate with a fixed pitch angle and at constant rotational speed [56]. Power control is realized by passively increasing the angle of attack for increasing wind speed. As the angle of attack increases, the outer board of the wind turbine blade goes into stall, reducing the lift and increasing the drag. This will level of the trust on the wind turbine rotor while decreasing the torque, hence regulating aerodynamic load and power.

ACTIVE CONTROL

For an active control scheme, the pitch mechanism is used to actively change the blade pitch and hence the angle of attack throughout the blade length, in order to regulate lift and drag distribution along the blade span. This enables to actively keep the thrust, torque, and power within the design envelope. The pitch mechanism can be used to increase the angle of attack, referred to as *active stall regulation* or decrease the angle of attack, referred to as *pitch regulation*.

As the size and capacity of wind turbines increase, slender blades are designed in order to save weight. Consequently, the blades on large scale stall control wind turbines experience larger thrust, leading to increase blade loads and larger tip deflection of the blades. Therefore, stall regulation is no longer economically viable solution for load and power regulation on large scale wind turbines. Alternatively, most modern wind turbines employ pitch regulation, where the pitch mechanism is used to manage the angle of attack along the length of the turbine blade and hence the blade load. For low wind speeds, the pitch mechanism rotates the blade for maximum power extraction, while for higher wind speeds the blade is rotated towards feather, reducing the angle of attack, to keep the aerodynamic loading within the design envelop.

MOVE TOWARDS PASSIVE CONTROL FOR LARGE WIND TURBINES

In order to reduce the cost of generating power from wind, different cost components of modern, pitch regulated, wind turbines are examined. Among the cost components, the pitch mechanism has a noticeable share of the initial capital cost and of the operation and maintenance cost of wind turbines. Quite often the pitch system is not able to provide an operational life time of 20 years, and needs to be replaced once or twice over the lifetime of the wind turbine. These cost components can reduce if the task of the pitch mechanism, to regulate power, is replaced by passive stall control scheme for large-scale wind turbines because passive control methods are less complex, robust and more reliable than active control method.

Earlier concepts for adjusting, passively, the angle of attack in order for the blade to adapt to the incoming wind include: regulation of the extracted power using centrifugally loaded mass on elastic arm [34], load balancing by cyclically adjusting the blade pitch [19], passively adjusting the blade pitch, both for power and load control [41], and mitigation of yaw loads using cyclic adjustments of blade pitch [62]. All these methods are using some sort of mechanism to adjust the angle of attack in response to the aerodynamic or inertial loads.

With recent advances in composite technology for tailoring the structural response of composite structures, it may be possible to apply the composite tailoring to the conventional passive stall control scheme. Particularly, the use of twist coupling for regulating, passively the angle of attack, thus also the torque and power of the wind turbine, shows a promise to design adaptive blades for stall regulated wind turbines, with improved performance in terms

of power and load control, as well as in terms of cost reduction.

1.2. TWIST COUPLING IN WIND TURBINE BLADES FOR POWER AND LOAD REGULATION

CHANGE in twist distribution along the blade span, has a direct influence on the angle of attack, thereby altering the aerodynamic loading on the blade as well as the extracted power. The following deformation coupling is possible for a twist coupled blade; (I) the blade undergoes twist deformation due to bending load, or (II) due to an extension load such as centrifugal force on the wind turbine blade. The angle of attack is altered by the *induced* twist, causing a different aerodynamic load distribution along the blade span. The change in aerodynamic load has again an effect on the 'induced' twist and the aero-structural interaction continues until an equilibrium is achieved. Here, the term *induced* refers to the change in the blade twist by the structural deformation of the wind turbine blade. This enables twist coupled blades to have an increased capability in regulating the aerodynamic load on wind turbine blades and an increased efficiency to extract energy from wind. Twist coupled blades can be tailored to reduce the angle of attack for higher wind speeds (pitch to feather) or increase the angle of attack (pitch to stall).

Twist coupled blades are designed by means of aeroelastic tailoring. Two approaches are investigated that cause twist coupling in wind turbine blades: (I) material twist coupling, where biased fiber angles (with respect to the blade axis) are used to cause bend-twist and/or extension-twist coupling, (II) geometric twist coupling, where swept blades (in the plane of rotation) induce twist coupling. See figure 1.2a and 1.2b for schematic representation of the two methods for creating twist coupling in wind turbine blades.

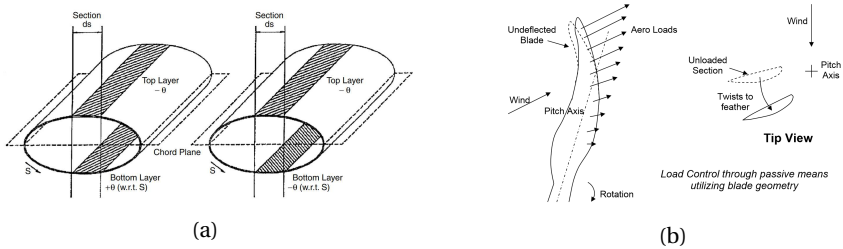


Figure 1.2: The two methods for causing twist coupling: (1.2a) material twist coupling, (left) bend-twist coupling due to symmetric lay-up, (right) extension-twist coupling due to asymmetric lay-up (from [73]), (1.2b) geometric twist coupling using swept blade design (from [81])

Earlier investigations towards incorporating twist coupling in wind turbine blades, where mainly focused on the, theoretically, maximum twist coupling that can be achieved using biased (fibers that are angled with respect to the blade axis) lay-ups. A review on twist coupled blades for enhancing

the performance of HAWTs is provided in [87], which includes all the research conducted in this field, prior to 2001.

Among others, the seminal work of Karaolis et al. [73] investigates the potential gain of twist coupling to control the aerodynamic loading on wind turbines. Different coupling schemes were investigated that include bend-twist and extension-twist coupling. Furthermore, the amount of twist coupling gained by pressurizing the interior of the wind turbine blade is also investigated. However, the aerodynamic performance of the blade models was not assessed using wind turbine aeroelastic simulations, which makes the conclusions from this work on the possible twist coupling that can be achieved in wind turbine blades purely theoretical.

Similarly, several research papers [78, 101, 43] are dedicated to finding the optimal fiber angle that maximizes the amount of twist coupling in composite blades. The research papers come to the same conclusion that fibers at 20%, with respect to the blade axis, result in maximum twist coupling. These research papers, however, do not assess, simultaneously, the effect of twist coupled blades on the aerodynamic performance of the wind turbine blades.

A few research papers are published that evaluate the aerodynamic performance of twist coupled blades by prescribing the amount of twist coupling during the aerodynamic simulation. For example, the work of Lobitz et al. [88, 87] shows the potential of bend-twist coupled blades in enhancing energy extraction and reducing fatigue loads, while assuming a prescribed bend-twist coupling during the analysis.

Recent investigations towards twist coupled blades looks into the benefit of twist coupling using more reliable methods for calculating the aeroelastic response of the blades. Maheri et al. [92] uses analytical/FEA coupled aeroelastic simulation to design adaptive blades, with improved energy capture capability of a stall regulated wind turbine having adaptive blades. However, the method lacks in a detailed parameterization of the design variables and also uses limited constraints during the optimization process. Especially, structural constraints such as stress distribution across the blade skin, buckling, and maximum tip deflection are not considered.

Alternatively, Maheri et al. [93] proposed another method to design adaptive blades, where the structural and aerodynamic designs are carried out separately. The method incorporates the *induced* twist during the aerodynamic design, as part of the design parameters, while during the structural design, the material, and structural parameters are optimized that meet the *induced* twist requirement from the aerodynamic design. However, this method suffers from simplifications that are assumed for decoupling the structural and aerodynamic design. Furthermore, detailed structural constraints (stress buckling, tip deflection) were not considered during the optimization.

The works of Capuzzi et al. [23, 24, 25], follow a similar approach as in [93], where the aerodynamic and structural design of adaptive blades is performed separately. First, the 'target' twist curves for optimum power production is determined during the aerodynamic design [23]. The 'target' twist curves are

parametrized in terms of the radial position and wind speed. Subsequently, a structural design is carried out that achieves the 'target' twist curves [24]. Furthermore, starting from the structural design of the adaptive blade in [24], a detailed structural design, including strength and buckling constraints, is performed in [25].

Bottasso et al. [18] present a parametric design of bend-twist coupled blades for passive and a combination of passive-active method for load alleviation. To evaluate the level of bend-twist coupling, different blade designs are studied consisting of a single biased fiber angle (with respect to the blade axis), placed partially or fully along the blade span. A multidisciplinary optimization (MDO) procedure is then used to design the different blades, subjected to multilevel constraints.

A parametric study for load mitigation, using aeroelastic tailoring for maximum bend-twist coupling, is carried out in [58]. However, the method does not include any structural constraints (stress, buckling and tip deflection) during the parametric study.

Another method for inducing twist coupling in wind turbine blades is through geometric design. By designing a swept blade planform, the additional moment caused by the blade sweep twists the blade to stall or to feather depending on the direction of the blade sweep [142]. A swept blade design by Sandia [6] demonstrates the benefit of swept blades for enhancing power capture, without increasing the trust load.

Most of the research conducted so far is to investigate the benefit of twist coupled blades for power and/or load regulation; either based on a parametric study using few design variables or using simplified models for analyzing the aeroelastic response of adaptive blades. The next step would be to perform a detailed optimization study using variable stiffness laminates, to evaluate the potential of twist coupled blades to enhance the aerodynamic performance of stall controlled wind turbines. Furthermore, detailed structural and aerodynamic constraints need to be included in the optimization study, while using an analysis tool with sufficient complexity to accurately capture the aeroelastic response of twist coupled blades.

1.3. AEROELASTIC OPTIMIZATION OF COMPOSITE STRUCTURES

WITH the potential benefit of fiber reinforced plastics for controlling their properties in any direction, a significant amount of research has been carried out for formulating optimization methods that capitalize the additional benefit of composite materials. Gürdal et al. [54] and Haftka et al. [55] provide a detailed description on composite optimization. Variable stiffness design has the advantage of finding the minimum of the required objective (e.g. mass or cost of energy) while fulfilling all required constraints (e.g. strength, buckling, tip deflection, etc..). For variable stiffness designs, the laminate thickness and the direction of the fibers vary across the structural

component. Two methods can be identified for stiffness parametrization in optimization study using variable stiffness: (I) based on stacking sequence, (II) based on laminate parameters.

For parametrization based on stacking sequence, the laminate stiffness is defined based on ply/layer angles and thickness (see section 2.3.1). This suggests that for a laminate composed of m layers, there are a maximum of $2m$ design variables to be considered during optimization. Most of the optimization methods used for tailoring the twist coupling of wind turbine blades are based on some variation of stacking sequence parametrization.

For parametrization based on lamination parameters, the laminate stiffness is parametrized with a maximum of 12 laminate variables, while a set of constraints imposed on the variables guarantee that the stiffness design, based on lamination parameters, can be converted into feasible stacking sequence (see section 2.3.2). This gives optimization based on lamination parameters a clear advantage over stacking sequence scheme, for complex optimization cases with variable stiffness across the structure and composite laminates with multiple layers. Additionally, there is a linear and continuous relationship between lamination parameters and laminate stiffness matrices; while parametrization based on stacking sequence introduces non-linearity and discontinuity to achieve feasible designs. The facts that smaller set of design variables are used in lamination parameters, together with the advantage of having linear and continuous relationship between the laminate parameters and stiffness matrices, makes lamination parameters a preferable choice for detailed composite optimization.

However, lamination parameters have a drawback in that an additional step is required for converting the lamination parameters into feasible designs. To this end, many research papers have been published, among others: [66, 15, 132, 86].

1.4. RESEARCH GOALS

THE objective of the thesis is to develop a variable stiffness composite optimization method for wind turbine rotor blades and investigate the benefit of using composite materials to design twist coupled blades for large scale, stall regulated, wind turbines. To achieve the objective, the task is divided into the following stages. For the first stage:

Develop a general framework capable of efficiently parametrizing a wind turbine rotor blade in terms of its geometry and material; afterwards, perform a static aeroelastic analysis on the wind turbine rotor blade, together with the analysis of response sensitivities, for use in a gradient based composite optimizer.

The framework should be capable of efficiently parametrizing a wind turbine rotor blade in terms of the blade planform, beam axis (e.g. curved blades), laminate thickness together with the fiber angles of a composite material. The framework should be capable of analysing the wind turbine performance us-

ing a multi-fidelity approach; where a low-fidelity model is used for static aeroelastic analysis and a high-fidelity model is used for detailed structural analysis, applying the aeroelastic loads (from the low-fidelity model) as static loads on a detailed finite element model of the wind turbine blade.

For the second stage of the thesis, an optimization model based on lamination parameters, formulated by IJsselmuiden [66], should be used to investigate the potential of twist coupled blades to regulate the power on stall regulated wind turbines, while taking into account both structural (e.g. strength, buckling, maximum blade deflection) and aerodynamic constraints. The second stage of the thesis is comprised of:

Perform an optimization study, based on minimization of the cost of energy (COE), to evaluate the additional benefit of adaptive blades on the performance of large stall regulated wind turbines.

A cost function for calculating the cost of energy of 5MW stall regulated machines needs to be formulated, and used to evaluate the performance of the new blade designs. The cost of energy will follow a similar approach to the cost model of [49], used to estimate the COE of pitch controlled machines of different size. Since the preferred optimization model of IJsselmuiden [66] uses response approximates during optimization, a general approximation method of the aeroelastic responses and the objective functions needs to be formulated, based on a linear and reciprocal approximation of the responses in terms of the design variables (elements of the membrane and bending stiffness matrix of a laminate).

1.5. THESIS LAYOUT

THE organization of the thesis is as follows. Chapter 2 introduces the different disciplines implemented in this thesis, including a brief description of the aerodynamic model, specifically on the blade element theory; the theory of isogeometric formulation, implemented in the proposed framework; an account of different methods to parametrize the stiffness matrices of composite laminates.

In chapter 3, an overview of the major steps in the framework for wind turbine blade optimization is presented; including a brief overview of the isogeometric framework for evaluating the aeroelastic responses; a method for passing design dependent loads onto a finite element model of the wind turbine blade, for detailed structural analysis; formulation of response approximations, suitable for the considered optimization tool. The framework is intended for stiffness-based optimization of composite structures of wind turbine blades.

Chapter 4 describes a method, based on the isogeometric framework, for parametrizing a wind turbine rotor blade. The generation of the geometric model, using NURBS functions, is explained in detail; containing a description of the finite element model, used in a detailed structural analysis. Furthermore, an interface model is developed for passing design dependent

loads from the low-fidelity model unto the high-fidelity structural model. This chapter also elucidates on the approach for parametrizing the composite laminates and the definition of the design variables, together with a way to link the design variables to the material properties of the blade model (both low-fidelity and high-fidelity models).

Chapter 5 contains a formulation for calculating the sectional properties of thin-walled, multi-cell, and prismatic beams with anisotropic material properties and arbitrary cross-sectional shape. The sectional stiffness properties are part of a beam model, used for calculating the deformation of a wind turbine blade, which is part of the low-fidelity aeroelastic model. The formulation, for analyzing the sectional stiffness properties, is based on the classical laminate theory, making it suitable for use in composite optimization.

The (low-fidelity) aeroelastic module is composed of an IGA based structural and aerodynamic models. Chapter 6 contains the description of the structural model for calculating the large deflection of the wind turbine blade. The model is based on an isogeometric formulation of geometrically exact 3D beam theory. Chapter 7 presents the aerodynamic model that is based on BEM theory, for calculating the aerodynamic loads on a turbine blade. Furthermore, the aerodynamic model contains a method for modifying the aerodynamic loads to account for a change in the blade shape due to the blade deformation. This allows, among others, to include the *induced* twist in the aerodynamic model.

Chapter 8 elucidates on the responses of the high-fidelity model, obtained from structural analysis using, the finite element solver, *NASTRAN*. Moreover, a description of modifications (*Alters*) on the default run of *NASTRAN* is provided. These modifications serve to extract the relevant responses (streamlined for optimization), and correct the sensitivity results from the *NASTRAN* analysis.

Chapter 9 provides a description of the final piece of optimization framework, introduced in chapter 3. In this chapter, the derivation of the response approximations in terms of the laminate design variables is presented. The different responses that are part of the optimization are described in this chapter; starting with the introduction of a general form of the response approximations that is tailored for composite optimization, followed by a description of the two methods of sensitivity analysis, employed in the current optimization framework, then a description of the response approximation for the various aeroelastic and structural responses.

Chapter 10 contains the optimization study into performance enhancement of twist coupled wind turbine blades for stall regulated wind turbines. First a baseline design for stall regulated 5MW wind turbine is adapted from the blade design of the NREL5MW pitch regulated wind turbine, followed by successive optimization studies to evaluate the potential gain of twist coupling and the resulting aerodynamic performance of the new blades, optimized under structural and aeroelastic constraints, using the COE as an objective during the optimization.

1

Finally, conclusions and recommendation for further research are given in chapter 11.

2

OVERVIEW ON DIFFERENT DISCIPLINES USED IN THE DISSERTATION

This chapter is dedicated to briefly introduce the different disciplines used in this dissertation. Section 2.1 presents a brief description of the aerodynamic model used for calculating the aerodynamic loads, followed by section 2.2 that addresses the implementation of isogeometric analysis in the framework presented in chapter 3. Finally, section 2.3 provides an insight into the different methods to parametrize the stiffness properties of composite laminates.

2.1. WIND TURBINE AERODYNAMICS

There are various methods to calculate the aerodynamic loads on horizontal axis wind turbine blade [57], with varying accuracy, computational time and complexity. Computational Fluid Dynamic (CFD) is the most accurate method, but it is also computationally expensive. Other methods that are computationally less expensive than CFD are vortex line and panel methods. The most common methods used in industry to calculate the aeroelastic loads of HAWT'S are based on Blade Element Momentum (BEM) theory. BEM is popular, especially in aeroelastic simulation of HAWT'S, because of its relatively simple and fast implementation in aeroelastic codes with generally good performance, provided that accurate 2D airfoil characteristics are available at the appropriate Reynolds number. There is extensive literature on BEM theory [94]. Therefore, this section introduces the subject briefly.

2.1.1. BLADE ELEMENT MOMENTUM THEORY

Blade Element Momentum theory is a combining two distinct methods. The momentum balance of an annular stream tube passing through a plane of a turbine is equated with blade element theory that calculates the sectional aerodynamic properties of a turbine blade. This will give a set of equations that need to be solved iteratively. The advantage of this method is the fact that the 3D characteristic of the airflow is decomposed into 1D momentum balance and 2D sectional aerodynamics.

MOMENTUM THEORY

The forces and flow conditions on wind turbine blades may be derived from conservation of momentum, since forces are the rate of change of momentum. Consider a stream tube around an actuator disc normal to the plane of rotation, as shown in figure 2.1. The four stations are: '1' upstream the disc, '2' right before the disc, '3' right after the disc and '4' downstream of the actuator disc. The thrust on the rotor disc is calculated by considering conservation of linear momentum to an annular control volume at radius r and thickness dr , see figure 2.1. The differential thrust, dT , on the rotor disc, at radius r and thickness dr , is given as,

$$dT = \rho U^2 4a(1-a)\pi r dr, \quad (2.1)$$

where ρ is the air density, U is the undisturbed wind speed and a is axial induction factor, which is a function of the radius r . The differential torque, dQ , on the rotor disc is calculated by applying the conservation of angular momentum to an annular control volume at radius r and thickness dr , resulting in the expression for dQ as,

$$dQ = 4a'(1-a)\rho U \pi r^3 \Omega dr, \quad (2.2)$$

where Ω is the rotation of the rotor disc, and a' is the angular induction factor, which is also a function of the radius. Hence, the momentum theory provides

expressions for the thrust and torque on the rotor disc as a function of the axial and angular induction factors which represent the flow condition.

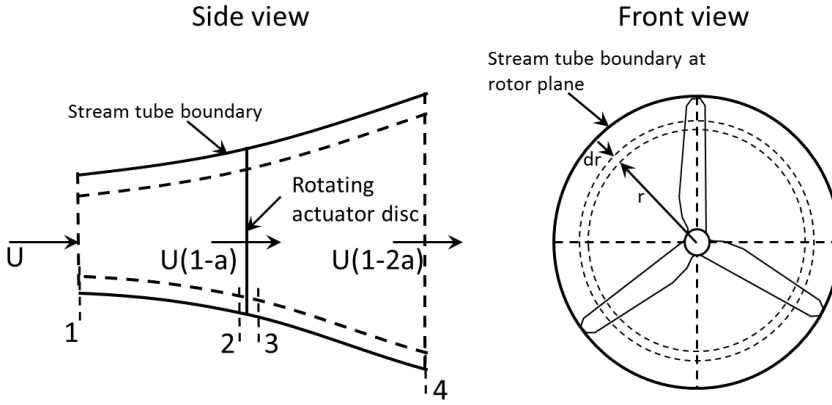


Figure 2.1: The geometry of the rotor, for the definition of variables that are used in BEM theory (adapted from [94]).

BLADE ELEMENT THEORY

The forces on the blades may be determined solely from the airfoil characteristics and the angle of attack. The airfoil characteristics refers to the lift and drag of the airfoil for varying angle of attack. The aerodynamic loads are calculated by dividing the blade in N sections, which are also referred to as elements. The following assumptions are employed for the blade element theory:

- There is no aerodynamic interaction between different blade segments.
- The forces on the blades are determined exclusively from the 2D aerodynamic characteristics of the local airfoil shapes.

Figure 2.2 shows a schematic representation of the airfoil section, seen from the blade tip. The lift and drag, denoted respectively by dF_L and dF_D , are perpendicular and parallel, respectively, to the local relative wind velocity U_{rel} . The relative wind velocity U_{rel} is a vector sum of the wind velocity at the blade, $U(1-a)$, and the local angular velocity, $\Omega r(1+a')$. The angle of attack is denoted by α , while φ represents the local inflow angle. The local pitch, θ , is composed of global pitch of the blade and local twist angle. The local thrust and torque are denoted respectively by dF_N , and rdF_T , where r is the radial distance of the airfoil section, from the center. Based on the geometric relations shown in figure 2.2, two expressions for the inflow angle φ are obtained,

$$\varphi = \theta + \alpha, \quad \text{and} \quad \tan(\varphi) = \frac{1-a}{\lambda_r(1+a')}, \quad (2.3)$$

where θ and α are respectively, the local twist and angle of attack; the local tip speed ratio is defined as,

$$\lambda_r = \frac{\Omega r}{U}. \quad (2.4)$$

The local lift and drag forces are expressed as,

$$dF_L = \frac{1}{2} \rho U_{rel}^2 C_l c dr, \quad \text{and} \quad dF_D = \frac{1}{2} \rho U_{rel}^2 C_d c dr, \quad (2.5)$$

where C_l and C_d are respectively, the lift and drag coefficients of the local air-foil section. Assuming the rotor has B number of blades, the normal force on the section, at a distance of r from the center, is calculated as,

$$dF_N = B \frac{1}{2} \rho U_{rel}^2 (C_l \cos \varphi + C_d \sin \varphi) c dr. \quad (2.6)$$

Similarly, the torque due to the tangential force, at a distance of r from the center, is calculated as,

$$dQ = B \frac{1}{2} \rho U_{rel}^2 (C_l \sin \varphi - C_d \cos \varphi) c r dr. \quad (2.7)$$

Increasing the drag tends to increase the thrust of the blade while decreasing the torque. By equating the thrust and torque expressions from the two theo-

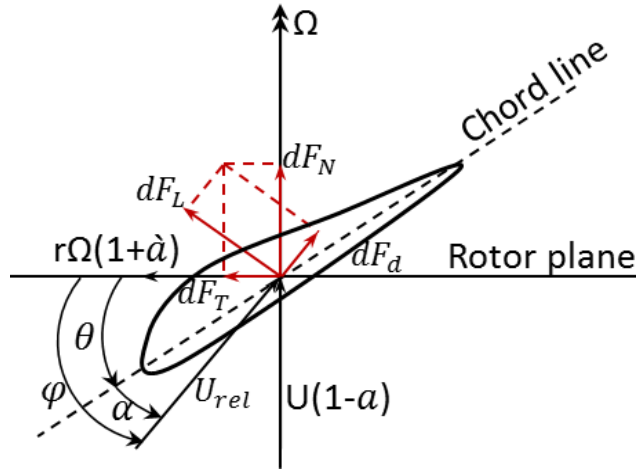


Figure 2.2: Schematic representation of airfoil geometry and the definition of various variables, used in Blade Element theory.

ries, a residual equation is derived as,

$$R_{res} = Ct - 4a(1 - a) = 0, \quad (2.8)$$

where,

$$Ct = \frac{1}{2\pi} \frac{c}{r} \sqrt{f} (C_d(1-a) + C_l \lambda_r (1+a')), \text{ for} \quad (2.9)$$

$$a' = \lambda_r^{-1} a(1-a) \text{ and } f = (1-a)^2 + \lambda_r^2 (1+a')^2.$$

From equation 2.8, Ct is the trust coefficient calculated from the blade element theory, while the remaining term is the trust coefficient from the momentum theory. Since the angular induction factor is determined from the axial induction factor (see equation 2.9), the residual equation, R_{res} , is only a function of the axial induction factor and the airfoil characteristics. Therefore, equation 2.8 is solved iteratively for the axial induction factor a . After solving for the axial induction factor, the forces on the turbine blade are calculated based on the converged solution for a , at each radial position r . The measured performance of wind turbine blades matches closely with BEM results at low axial induction factors. However, for large values of axial induction factor ($a > 0.5$), the momentum theory is no longer valid and empirical data between the thrust coefficient and the axial induction factor is used to predict the wind turbine performance. Figure 2.3, shows, from the momentum theory, the relationship between the thrust coefficient and axial induction factor. For low axial induction factor ($a \leq 0.4$), the standard $Ct - a$ relationship derived from the momentum theory is used, while for higher values of a , modified Glauert correction from [98] is applied. Based on figure 2.3, the residual of equation 2.8 is modified as,

$$R_{res} = Ct - \begin{cases} 4a(1-a), & \text{if } a \leq 0.4 \\ c_0 + c_1 a + c_2 a^2, & \text{otherwise} \end{cases} \quad (2.10)$$

where $c_0 = 8/9$, $c_1 = -4/9$, and $c_2 = 14/9$.

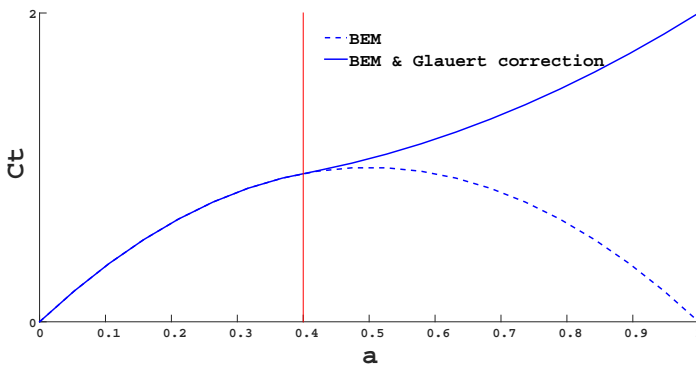


Figure 2.3: Relationship between thrust coefficient and axial induction factor with Glauert correction.

2.1.2. TIP AND ROOT CORRECTIONS TO BEM THEORY

Due to the finite blade length, the pressure difference, between the upper and lower surface of the blade, induces a vortex at the blade tip. This tip vortex results in the reduction of the lift towards the blade tip, which needs to be taken into account during BEM calculation of the aerodynamic forces on the blade. The tip loss correction factor of Shen et al. [121] is used to correct the thrust coefficient, derived from the blade element theory, i.e.,

$$Ct = F_{tip} \frac{1}{2\pi} \frac{c}{r} \sqrt{f} (C_d(1-a) + C_l \lambda_r (1+a')), \quad (2.11)$$

where the tip loss correction factor, F_{tip} , is given by,

$$F_{tip} = \frac{2}{\pi} \cos^{-1} \left\{ \exp \left(-\frac{R-r}{2R} \frac{gB}{\sin \varphi_{tip}} \right) \right\}, \quad \text{where} \quad g = \exp \left(\frac{1}{8} (21 - B\lambda) + \frac{1}{10} \right), \quad (2.12)$$

and R is the rotor radius, while φ_{tip} and λ refer respectively, the inflow angle at the blade tip and the tip speed ratio. Furthermore, the lift and drag forces of equation 2.5 are scaled by the tip loss correction factor F_{tip} .

In addition, the flow on a rotating blade experiences pressure difference in radial direction, resulting in radial velocity component. This induces a Coriolis force in the direction of the trailing edge, acting as a positive pressure gradient in chord direction that delays flow separation. This Coriolis force has the same effect as blowing air in chord wise direction of an airfoil, which is used to prevent flow separation. Therefore, a root correction is included to account for rotational stall delay [21], applied directly to the 2D airfoil characteristics. The lift and drag coefficients of the airfoils are corrected for rotational stall delay using the Selig and Eggars method [72].

2.2. ISOGEOMETRIC ANALYSIS

Isogeometric analysis (IGA) is a numerical method proposed in [64, 36], that bridges the gap between Computer Aided Design (CAD) and Finite Element Analysis (FEA). The main idea behind IGA is to use the basis functions (B-splines or NURBS) both to represent the geometry in CAD and for approximation of the field variables, in a isoparametric fashion. This reduces the computation time, associated with mesh generation and refinement process in FE analysis, which was the main motivation behind IGA. Furthermore, due to the high-regularity properties of its basis functions, IGA shows, for a number of problems, better accuracy per degree of freedom and increased robustness. Among others, IGA has been successfully implemented in fluid mechanics [10, 3, 11, 22], Solids and structures [38, 37, 8, 85, 27, 65], including plate and shell elements [76, 130, 46, 100].

The use of IGA in the current framework allows to easily vary the different parameters of the turbine blade, such as the blade planform, beam axis and material distribution, while easily analysing the effect of these parameters on

the wind turbine blade performance in an isoparametric fashion. The implementation of NURBS in isogeometric formulation is popular, since NURBS is a well-developed concept in CAD technology with widespread use.

This section presents a brief description on NURBS and its relevant properties for the current framework. Furthermore, the parametrization of curves using one dimensional NURBS is discussed, together with an elucidation on the geometric algorithm that facilitates the formulation of multilevel discretization scheme, presented in chapter 4. A detailed explanation on NURBS and its implementation within the isogeometric precept can be found in [36].

2.2.1. FUNDAMENTALS OF NON-UNIFORM RATIONAL B-SPLINES B-SPLINE

Starting with the description on B-splines, one-dimensional B-splines are defined over an interval on the real axis described by a *knot vector* Ξ ,

$$\Xi = \{\xi_1 = \dots = \xi_{p+1} = 0, \xi_{p+2}, \dots, \xi_n, \xi_{n+1} = \dots = \xi_{n+p+1} = 1\}, \xi_1 \leq \xi_2 \leq \dots \leq \xi_{n+1}, \quad (2.13)$$

consisting of non-decreasing entries referred to as knots ξ_i , for $i = 1 \dots n+p+1$, where p , and n represent respectively, the polynomial degree, and the number of univariate spline basis functions defined on the knot vector. The present framework employs open knot vectors, ensuring the end point interpolation of the defined curve, which is a desired property in CAD. Based on Ξ , the B-splines are defined recursively as,

$$N_{i,0}(\xi) = \begin{cases} 1 & \text{if } \xi_i \leq \xi < \xi_{i+1} \text{ and,} \\ 0 & \text{otherwise} \end{cases} \quad (2.14)$$

$$N_{i,p}(\xi) = \frac{\xi - \xi_i}{\xi_{i+p} - \xi_i} N_{i,p-1}(\xi) + \frac{\xi_{i+p+1} - \xi}{\xi_{i+p+1} - \xi_{i+1}} N_{i+1,p-1}(\xi).$$

Detailed description on B-spline functions can be found in [108].

NURBS

The p^{th} degree Non-Uniform Rational B-Spline(NURBS) is a piecewise rational function defined by the projective transformation,

$$R_{i,p}(\xi) = \frac{N_{i,p}(\xi) w_i}{w(\xi)}, \quad (2.15)$$

where w_i is a positive weight factor of the B-spline function $N_{i,p}(\xi)$. The denominator of equation 2.15 is referred to as weighting function, i.e.

$$w(\xi) = \sum_{j=1}^n N_{j,p}(\xi) w_j. \quad (2.16)$$

The continuity properties of the B-spline functions carry over to NURBS functions. B-spline may be recovered from NURBS by assigning uniform

weights to all basis functions. The additional freedom in choice of weights make NURBS representations more versatile than B-splines. Moreover, common geometric shapes such as conic sections are exactly representable using NURBS. Some of the characteristic features of B-splines and NURBS is illustrated in figure 2.4, where the basis functions of B-splines and NURBS are plotted for $p = 3$ and $n = 7$.

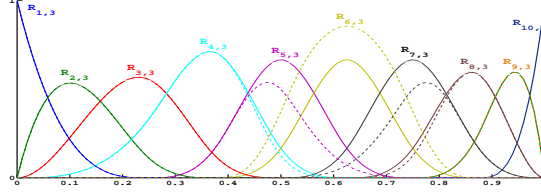


Figure 2.4: Cubic basis functions of B-splines and NURBS. The solid lines represent the B-spline basis $N_{i,3}$, with $i = 1, \dots, n$, whereas modifying a single weight ($w_7 = 2$) results in $p + 1$ rational basis functions $R_{i,3}$ with $i = 4, \dots, 7$, represented by dashed lines. All other basis functions are unaffected by the modified weight w_7 .

A d -dimensional NURBS curve is obtained by projecting a $d + 1$ dimensional homogeneous B-spline curve[108]. A homogeneous B-spline curve is a linear combination of B-spline functions and homogeneous control points, $\mathbf{P}_i^w \in \mathbb{R}^{d+1}$. The position vector of a point on the homogeneous curve is given by,

$$\mathbf{r}^w(\xi) = \sum_{i=1}^n N_{i,p}(\xi) \mathbf{P}_i^w, \quad (2.17)$$

where the homogeneous control point, written as,

$$\mathbf{P}_i^w = \begin{pmatrix} \mathbf{P}_i w_i \\ w_i \end{pmatrix}, \quad (2.18)$$

form the so-called control polygon, with the non-homogeneous control points denoted by $\mathbf{P}_i \in \mathbb{R}^d$. The $d + 1$ component of \mathbf{P}_i^w is the control point weight. A d -dimensional NURBS curve, $\mathbf{r}(\xi)$, is the projected image of $\mathbf{r}^w(\xi)$, i.e.

$$\mathbf{r}(\xi) = \frac{\mathbf{r}_l^w(\xi)}{w}, \quad (2.19)$$

where $l = 1, \dots, d$ and w refer respectively, the component of a vector and the weighting function defined in equation 2.16. Alternatively, the same NURBS curve may be written directly in terms of NURBS function and non-homogeneous control points as,

$$\mathbf{r}(\xi) = \sum_{i=1}^n R_{i,p}(\xi) \mathbf{P}_i. \quad (2.20)$$

A NURBS curve generated by an open knot vector is tangent to the control polygon at either end. Because the NURBS shape functions have local support, change of a control point \mathbf{P}_i or its weight w_i results only in local change

of the NURBS curve. Because the NURBS shape functions have local support, change of a control point P_i or its weight w_i results only in local change of the NURBS curve, as illustrated in figure 2.5.

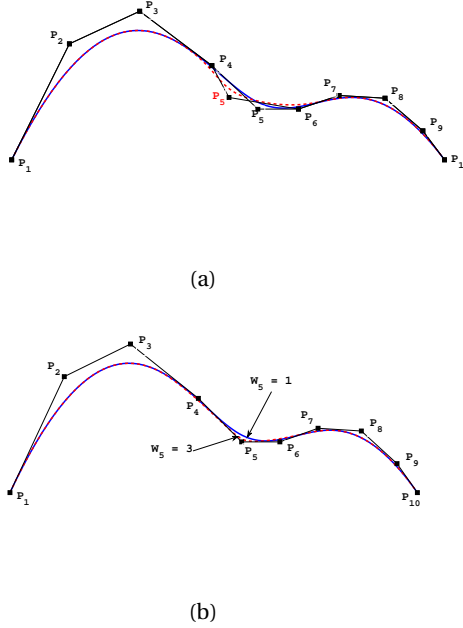


Figure 2.5: Local change of NURBS curve resulting from local change of a single control point co-ordinate(a) or the associated weight(b)

2.2.2.2. GEOMETRIC ALGORITHM: KNOT REFINEMENT

Knot refinement gives flexibility for the proposed framework to have different level of parametrization while preserving the geometry. The coarse knot vector for instance is used to define the geometric properties of the structure and, the refined knot vector is used for analysis.

Knot refinement is the application of multiple *knot insertion* simultaneously, while for *knot insertion*, a single knot $\xi \in [\xi_k, \xi_{k+1})$ is added to the knot vector Ξ , resulting in the extended knot vector $\Xi \subset \hat{\Xi}$ [108].

Assuming that the old knot vector Ξ is extended with r new knots, the *knot refinement* may be expressed in matrix form as

$$\tilde{\mathbf{P}}^w = \mathcal{L} \mathbf{P}^w, \quad (2.21)$$

where \mathbf{P}^w and $\tilde{\mathbf{P}}^w$ are matrix representation of the coarse and refined homogeneous control points, respectively. The columns of \mathbf{P}^w and $\tilde{\mathbf{P}}^w$ are the components of a single control point. The symbol \mathcal{L} is a banded matrix of size $(n+r \times n)$ containing information on the knot refinement. An efficient method

of performing knot refinement is discussed extensively in [51]. An example of a knot refinement is given in figure 2.6, where the control polygon, which is a linear approximation of the curve (black line), moves closer to the interpolated curve (red line), for increasing number of *knot spans*.

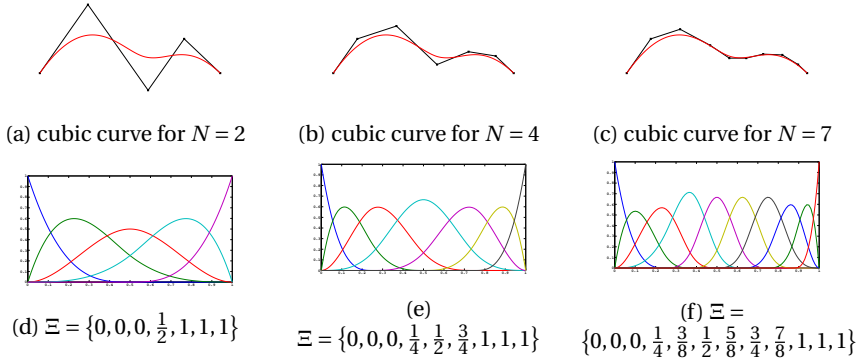


Figure 2.6: Multi level discretization for increasing number of knot-spans(N): (2.6a) original curve, and (2.6d) corresponding basis function, while (2.6b)-(2.6c) represent increasing number of knot-spans together with corresponding basis function shown in (2.6e)-(2.6f).

The refined non-homogeneous control points $\tilde{\mathbf{P}}_j$ are related to the coarse non-homogeneous control points \mathbf{P}_i as,

$$\tilde{\mathbf{P}} = \mathcal{L}_w \mathbf{P}, \quad (2.22)$$

where

$$\mathcal{L}_w = \tilde{\mathbf{W}}^{-1} \mathcal{L} \mathbf{W}, \quad (2.23)$$

and \mathbf{P} and $\tilde{\mathbf{P}}$ are matrix representation of the coarse and refined non-homogeneous control points, respectively. The diagonal matrix \mathbf{W} contains the weights w_i , with $i = 1, \dots, n$, for control points \mathbf{P} , whereas $\tilde{\mathbf{W}}$ contains the weights w_j , with $j = 1, \dots, n + r$, for control points $\tilde{\mathbf{P}}$.

2.3. COMPOSITE LAMINATES

Fiber reinforced composite laminate consists of two components: the fiber providing the strength and stiffness of the laminates, while the matrix holds the fibers in the desired location and maintains their shape. This section describes two analytical methods for parametrizing the stiffness properties of fiber reinforced composite laminates, which are based on classical lamination theory. The first method is based on stacking sequence, where the layer/ply angle and thickness are used for parametrization of the laminate stiffness (section 2.3.1). The second method is based on lamination parameters (section 2.3.2). Finally, a method for visualizing the in-plane stiffness distribution of the composite laminate is presented in section 2.3.3.

2.3.1. STACKING SEQUENCE

Consider figure 2.7, where a schematic representation of a single composite layer, also referred to as a ply, is given. The fibers, for each ply, are all aligned in the same direction. The axis x_1 is aligned with the fibers, while the axis x_2 is perpendicular to the fibers. The X and Y axis form the global coordinate system of the laminate, spanning the plane of a laminate. Starting from the general 3D stress-strain relationship, and assuming plain stress assumption ($\sigma_3 = \tau_{13} = \tau_{23} = 0$), the stress-strain relationship in the principal (x_1, x_2) direction of a single ply is reduced to,

$$\begin{Bmatrix} \sigma_1 \\ \sigma_2 \\ \tau_{12} \end{Bmatrix} = \begin{bmatrix} Q_{11} & Q_{12} & 0 \\ Q_{12} & Q_{22} & 0 \\ 0 & 0 & Q_{66} \end{bmatrix} \begin{Bmatrix} \epsilon_1 \\ \epsilon_2 \\ \gamma_{12} \end{Bmatrix} \rightarrow \boldsymbol{\sigma} = \mathbf{Q}\boldsymbol{\epsilon}, \quad (2.24)$$

where the non-zero elements of the \mathbf{Q} matrix, referred to as reduced stiffness, are written as,

$$Q_{11} = \frac{E_1}{1 - \nu_{12}\nu_{21}}, \quad Q_{11} = \frac{E_2}{1 - \nu_{12}\nu_{21}}, \quad (2.25)$$

$$Q_{12} = \frac{\nu_{21}E_1}{1 - \nu_{12}\nu_{21}} = \frac{\nu_{12}E_2}{1 - \nu_{12}\nu_{21}}, \quad Q_{66} = G_{12}. \quad (2.26)$$

The stresses and strains of equation 2.24 are transformed from the

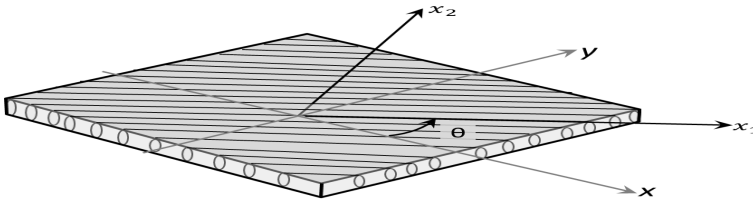


Figure 2.7: Coordinate system on ply level.

x_1, x_2 -coordinate system to the x, y - coordinate system using the transformation matrix that is a function of the ply angle θ , shown in figure 2.7. The transformation matrix is given by,

$$\mathbf{T} = \begin{bmatrix} \cos^2\theta & \sin^2\theta & 2\cos\theta\sin\theta \\ \sin^2\theta & \cos^2\theta & -2\cos\theta\sin\theta \\ -\cos\theta\sin\theta & \cos\theta\sin\theta & \cos^2\theta - \sin^2\theta \end{bmatrix}. \quad (2.27)$$

Using the transformation matrix, given in equation 2.27, the stress-strain relationship in x, y - coordinate system is defined as,

$$\begin{Bmatrix} \sigma_x \\ \sigma_y \\ \tau_{xy} \end{Bmatrix} = \tilde{\mathbf{Q}} \begin{Bmatrix} \epsilon_x \\ \epsilon_y \\ \gamma_{xy} \end{Bmatrix}, \quad (2.28)$$

where

$$\tilde{\mathbf{Q}} = \mathbf{T}^{-1} \mathbf{Q} \mathbf{R} \mathbf{T} \mathbf{R}^{-1}, \quad (2.29)$$

and

$$\mathbf{R} = \begin{bmatrix} 1 & 0 & 0 \\ 0 & 1 & 0 \\ 0 & 0 & 2 \end{bmatrix} \quad (2.30)$$

is a matrix that accounts for the difference between the engineering shear strain γ_{12} and the tensorial shear strain ϵ_{12} . The matrix \mathbf{R} is added in equation 2.29 to take into account the fact that the transformation matrix \mathbf{T} is applied between the tensorial strains, defined in different coordinate systems. The derivation of the stiffness of a laminate is based on the assumption of classical lamination theory, stating:

- Each layer is assumed to bond perfectly with adjacent layers, having infinitely thin adhesive layers between them.
- The layers are assumed to undergo similar shear deformation, for in-plane loads, and for bending loads, linearly varying shear deformation in thickness direction.

Furthermore, no assumption is made on the symmetric nature of the layers about the mid-plane, see figure 2.8. The variation of strains across the laminate thickness (z direction) is linearised in-terms of the mid-plane strains and curvatures, i.e.,

$$\begin{Bmatrix} \epsilon_x \\ \epsilon_y \\ \gamma_{xy} \end{Bmatrix} = \begin{Bmatrix} \epsilon_x^0 \\ \epsilon_y^0 \\ \gamma_{xy}^0 \end{Bmatrix} + z \begin{Bmatrix} \kappa_x \\ \kappa_y \\ \kappa_{xy} \end{Bmatrix}, \quad (2.31)$$

where the superscript 0 denotes mid-plane strains and κ is the change in mid-plane curvature. Substituting equation 2.31 into the stress-strain relationship

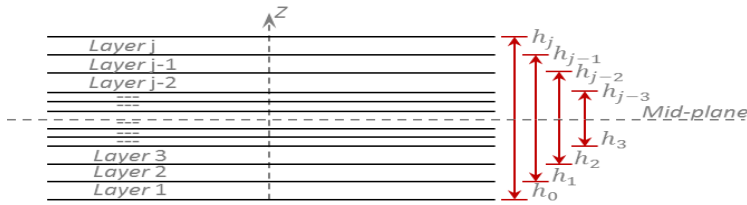


Figure 2.8: Laminate cross-section made up of multiple plies or layers.

of equation 2.28, results a strain-stress relationship of ply j , in-terms of the mid-plane strains, as follows,

$$\begin{Bmatrix} \sigma_x \\ \sigma_y \\ \tau_{xy} \end{Bmatrix}_j = \tilde{\mathbf{Q}}_j \begin{Bmatrix} \epsilon_x^0 \\ \epsilon_y^0 \\ \gamma_{xy}^0 \end{Bmatrix} + z \tilde{\mathbf{Q}}_j \begin{Bmatrix} \kappa_x \\ \kappa_y \\ \kappa_{xy} \end{Bmatrix}, \quad (2.32)$$

where $\tilde{\mathbf{Q}}_j$ is the transformed reduced stiffness matrix of the j^{th} ply/layer. The stress resultants, across the laminate thickness, are obtained by integrating equation 2.32 in thickness direction, i.e.,

$$\begin{aligned} \begin{Bmatrix} N_x \\ N_y \\ N_{xy} \end{Bmatrix} &= \sum_{j=1}^n \int_{h_{j-1}}^{h_j} \left(\tilde{\mathbf{Q}}_j \begin{Bmatrix} \epsilon_x^0 \\ \epsilon_y^0 \\ \gamma_{xy}^0 \end{Bmatrix} + z \tilde{\mathbf{Q}}_j \begin{Bmatrix} \kappa_x \\ \kappa_y \\ \kappa_{xy} \end{Bmatrix} \right) dz \\ \begin{Bmatrix} M_x \\ M_y \\ M_{xy} \end{Bmatrix} &= \sum_{j=1}^n \int_{h_{j-1}}^{h_j} \left(z \tilde{\mathbf{Q}}_j \begin{Bmatrix} \epsilon_x^0 \\ \epsilon_y^0 \\ \gamma_{xy}^0 \end{Bmatrix} + z^2 \tilde{\mathbf{Q}}_j \begin{Bmatrix} \kappa_x \\ \kappa_y \\ \kappa_{xy} \end{Bmatrix} \right) dz, \end{aligned} \quad (2.33)$$

where n is the number of layers of the laminate. It is observed from equation 2.33 that the stresses across a single layer are integrated, and subsequently summer over the laminate. The stress resultant-strain relationship may be written in compact form as,

$$\begin{aligned} \begin{Bmatrix} N_x \\ N_y \\ N_{xy} \end{Bmatrix} &= \mathbf{A} \begin{Bmatrix} \epsilon_x^0 \\ \epsilon_y^0 \\ \gamma_{xy}^0 \end{Bmatrix} + \mathbf{B} \begin{Bmatrix} \kappa_x \\ \kappa_y \\ \kappa_{xy} \end{Bmatrix}, \\ \begin{Bmatrix} M_x \\ M_y \\ M_{xy} \end{Bmatrix} &= \mathbf{B} \begin{Bmatrix} \epsilon_x^0 \\ \epsilon_y^0 \\ \gamma_{xy}^0 \end{Bmatrix} + \mathbf{D} \begin{Bmatrix} \kappa_x \\ \kappa_y \\ \kappa_{xy} \end{Bmatrix}, \end{aligned} \quad (2.34)$$

where

$$\begin{aligned} \mathbf{A} &= \sum_{j=1}^n \tilde{\mathbf{Q}}_j (h_j - h_{j-1}), \\ \mathbf{B} &= \frac{1}{2} \sum_{j=1}^n \tilde{\mathbf{Q}}_j (h_j^2 - h_{j-1}^2), \\ \mathbf{D} &= \frac{1}{3} \sum_{j=1}^n \tilde{\mathbf{Q}}_j (h_j^3 - h_{j-1}^3), \end{aligned} \quad (2.35)$$

represent the laminate membrane, coupling, and bending stiffness matrix, all of which are symmetric matrices. The coupling matrix \mathbf{B} denotes the mutual influence of in-plane and out-of-plane loadings and deformations, which reduces to zero for symmetric layup of a laminate with respect to mid-plane (see figure 2.8). Furthermore, the A_{13} , and A_{23} elements of the membrane stiffness matrix \mathbf{A} are coupling terms between the two in-plane strains (ϵ_x, ϵ_y) and the shear strain (γ_{xy}). For non zero values of these coupling coefficients, the laminate experiences shear strains when it is loaded in tension, which is a desired property in aeroelastic tailoring. This tension-shear strain coupling coefficients are zero for balanced laminates. Balanced laminates refer to laminates that have for each ply with positive ply angle (θ) a ply with negative angle ($-\theta$). This makes unbalanced laminates better suited for aeroelastic tailoring.

In addition, the elements D_{13} , and D_{23} of the bending stiffness matrix \mathbf{D} refer to the (laminate) bend-twist coupling. These elements of the bending matrix cause the laminate to twist under pure bending load. These coefficients are zero for weaved ply, meaning a single ply has two fiber angles with the same magnificent but opposite direction.

2.3.2. LAMINATION PARAMETERS

Besides the use of a staking sequence for parametrizing the laminate stiffness matrices $(\mathbf{A}, \mathbf{B}, \mathbf{D})$, lamination parameters may also be used to parametrize the stiffness properties of a laminate. Lamination parameters, initially introduced in [131], express the layer angles in an integrated form across the laminate thickness, expressed mathematically as,

$$\begin{aligned} (V_{1A}, V_{2A}, V_{3A}, V_{4A}) &= \frac{1}{h} \int_{-h/2}^{h/2} (\cos 2\theta, \sin 2\theta, \cos 4\theta, \sin 4\theta) dz, \\ (V_{1B}, V_{2B}, V_{3B}, V_{4B}) &= \frac{4}{h^2} \int_{-h/2}^{h/2} z (\cos 2\theta, \sin 2\theta, \cos 4\theta, \sin 4\theta) dz, \\ (V_{1D}, V_{2D}, V_{3D}, V_{4D}) &= \frac{12}{h^3} \int_{-h/2}^{h/2} z^2 (\cos 2\theta, \sin 2\theta, \cos 4\theta, \sin 4\theta) dz, \end{aligned} \quad (2.36)$$

The laminate stiffness matrices are defined using the lamination parameters, together with the material invariant matrices $\mathbf{\Gamma}_i$, as shown in equation 2.37:

$$\begin{aligned} \mathbf{A} &= h (\mathbf{\Gamma}_0 + \mathbf{\Gamma}_1 V_{1A} + \mathbf{\Gamma}_2 V_{2A} + \mathbf{\Gamma}_3 V_{3A} + \mathbf{\Gamma}_4 V_{4A}), \\ \mathbf{B} &= \frac{h^2}{4} (\mathbf{\Gamma}_1 V_{1B} + \mathbf{\Gamma}_2 V_{2B} + \mathbf{\Gamma}_3 V_{3B} + \mathbf{\Gamma}_4 V_{4B}), \\ \mathbf{D} &= \frac{h^3}{12} (\mathbf{\Gamma}_1 V_{1D} + \mathbf{\Gamma}_2 V_{2D} + \mathbf{\Gamma}_3 V_{3D} + \mathbf{\Gamma}_4 V_{4D}), \end{aligned} \quad (2.37)$$

where h is the laminate thickness. Furthermore, the laminate stiffness matrices may be defined as the product of thickness normalized stiffness components and the laminate thickness, i.e.,

$$\hat{\mathbf{A}} = \frac{1}{h} \mathbf{A}, \quad \hat{\mathbf{B}} = \frac{4}{h^2} \mathbf{B}, \quad \hat{\mathbf{D}} = \frac{12}{h^3} \mathbf{D}, \quad (2.38)$$

where the parameters in hat, $\hat{}$, represent thickness normalized stiffness matrices. The material invariant matrices $\mathbf{\Gamma}_i$ are derived from the material invariants U_i , which depend only on material properties. The material invariant matrices U_i may be obtained from elements of the reduced stiffness matrix \mathbf{Q} ,

as follows,

$$\begin{aligned}
 U_1 &= \frac{1}{8} (3Q_{11} + 3Q_{22} + 2Q_{12} + 4Q_{66}), \\
 U_2 &= \frac{1}{2} (Q_{11} - Q_{22}), \\
 U_3 &= \frac{1}{8} (Q_{11} + Q_{22} - 2Q_{12} - 4Q_{66}), \\
 U_4 &= \frac{1}{8} (Q_{11} + Q_{22} + 6Q_{12} - 4Q_{66}), \\
 U_5 &= \frac{1}{8} (Q_{11} + Q_{22} - 2Q_{12} + 4Q_{66}).
 \end{aligned} \tag{2.39}$$

Finally, the material invariant matrices Γ_i , which do not depend on the fibre direction, are expressed in-terms of the material invariants U_i as,

$$\begin{aligned}
 \Gamma_0 &= \begin{bmatrix} U_1 & U_2 & 0 \\ U_4 & U_1 & 0 \\ 0 & 0 & U_5 \end{bmatrix}, \Gamma_1 = \begin{bmatrix} U_2 & 0 & 0 \\ 0 & -U_2 & 0 \\ 0 & 0 & 0 \end{bmatrix}, \\
 \Gamma_2 &= \begin{bmatrix} 0 & 0 & U_2/2 \\ 0 & 0 & U_2/2 \\ U_2/2 & U_2/2 & 0 \end{bmatrix}, \Gamma_3 = \begin{bmatrix} U_3 & -U_3 & 0 \\ -U_3 & U_3 & 0 \\ 0 & 0 & -U_3 \end{bmatrix}, \Gamma_4 = \begin{bmatrix} 0 & 0 & U_3 \\ 0 & 0 & -U_3 \\ U_3 & -U_3 & 0 \end{bmatrix}.
 \end{aligned} \tag{2.40}$$

Equation 2.37 and 2.40 provide an insight on the effect of the lamination parameters and the stiffness matrices. An arbitrary stacking sequence can be successfully parametrized with the full set of the lamination parameters. For symmetric layup, $\mathbf{B} = \mathbf{0}$, the lamination parameters, \mathbf{V}_{iB} , are set to zero; the remaining eight parameters define a symmetric and unbalanced laminate. For balanced laminates, the lamination parameters multiplied with Γ_2 and Γ_4 are equal to zeros, leaving only four lamination parameters to define symmetric and balanced laminates.

2.3.3. MEMBRANE STIFFNESS VISUALIZATION

In order to visualize the distribution of the in plane stiffness matrix, \mathbf{A} , the thickness-normalized engineering modulus of elasticity, $\hat{E}_{11}(\theta)$, for $\theta = 0$ to 360 deg, may be calculated using,

$$\hat{E}_{11}(\theta) = \frac{1}{\hat{\mathbf{A}}_{11}^{-1}(\theta)}, \tag{2.41}$$

where

$$\hat{\mathbf{A}}^{-1}(\theta) = \mathbf{T}^T \hat{\mathbf{A}}^{-1} \mathbf{T}. \tag{2.42}$$

The matrix, \mathbf{T} , is similar to the transformation matrix of equation 2.27, used in the strain-stress relationship. Figure 2.9, contains the polar plot of characteristic laminate sequence, where the normalized engineering modulus of

elasticity is calculated using equation 2.41. In figure 2.9, the x axis refers to the 0° fiber angle, while the y axis refers to the 90° fiber angle. The laminate stiffness matrix of the different laminates is generated using the ply properties of table 2.1. The engineering modulus of elasticity, \hat{E}_{11} , of all laminates is

Table 2.1: Material properties of a single ply

E_{11}	E_{22}	G_{12}	ν	ρ
$35.0e^9$	$8.33e^9$	$4.12e^9$	0.33	1920

normalized with the largest value of the modulus of elasticity of a single ply (E_{11}).

Figure 2.9a shows \hat{E}_{11} of laminate where the fibers are all aligned in x direction, while figure 2.9c shows the engineering modulus of elasticity of a laminate with all the fibers aligned along the y axis. Figure 2.9b shows that all the fibers of the laminate are all aligned 60° with respect to the x axis. The membrane stiffness distribution of a quasi-isotropic laminate is depicted in figure 2.9e, where the membrane stiffness is equally distributed in all direction. Finally, figure 2.9d and 2.9f show a polar plot of \hat{E}_{11} for $\pm 45^\circ$ layup and a semi quasi-isotropic layup, having the majority of the fibers aligned along the x axis.

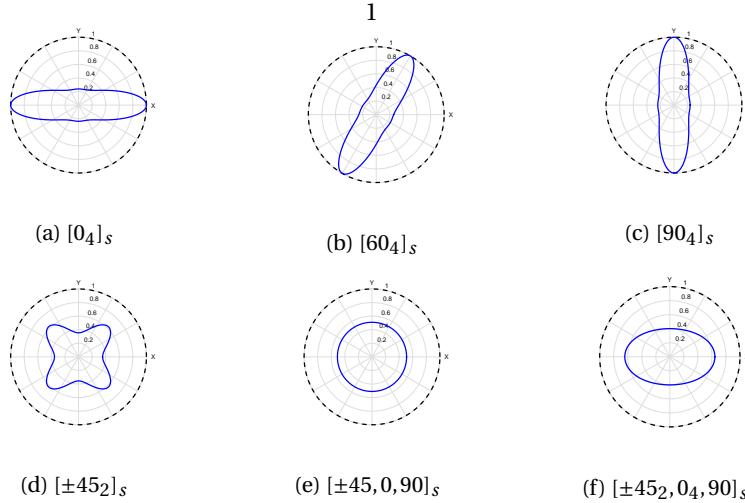


Figure 2.9: $\hat{E}_{11}(\theta)$ stiffness distribution for various stacking sequence.

3

MULTI FIDELITY OPTIMIZATION FRAMEWORK FOR WIND TURBINE APPLICATION

Composite optimization of large structures such as wind turbine blades is quite complex and thus a challenging task to perform . This stems from the existence of contradictory constraints ranging from material failure and buckling constraints to aeroelastic constraints. In addition, manufacturing constraints that include constraints relating to the laminate layup technique make the optimization process even more difficult. It would therefore be advantageous to simplify the optimization process by decomposition into several steps. The decomposition of the optimization process allows the use of suitable optimization method for each step.

The optimization strategy employed in this work is such that the composite optimization of a wind turbine blade is decomposed into three steps. For the first step, stiffness-based optimization is carried-out on the composite structure of wind turbine blades. In the first step, continuous laminate design variables are used in gradient based optimization while satisfying material, buckling and aeroelastic constraints. For the second step, a stacking sequence optimization is carried out using the optimized stiffness solution from step one as the objective, while satisfying constraints related to stacking sequence. For the third step, a fibre path optimization is performed while satisfying constraints related to manufacturability, that depend on the selected type of manufacturing technique, e.g. fibre placement. General overview of the three optimization steps is given in [66]. An optimization framework is presented in [44] that is based on the first step of the current optimization strategy, to optimize

the stiffness distribution of composite aircraft wings. This thesis follows the same strategy as in [44], where a framework for stiffness-based optimization of composite wind turbine blades is presented.

This chapter presents an overview of the developed framework for stiffness-based optimization of composite wind turbine blades. Detailed description of the modules that constitute the framework is given in the following chapters. An overview of the optimization process and a brief description of the major components of the framework is presented in section 3.1. Afterwards, a short account of the design variables is given in section 3.2, followed by section 3.3 where a concise description of the various responses implemented in the current optimization framework is given.

3.1. OPTIMIZATION FRAMEWORK

The optimization framework presented in this thesis is intended for optimizing the stiffness of composite laminates used in the design of the structural components of wind turbine blades. A framework, in the context of this thesis, is the interaction of different software modules created to perform a desired task, where in this case the task is the stiffness-based optimization of composite structures of wind turbine blades. The optimization process employed in this thesis corresponds to a successive optimization of convex local approximations of the responses, using a gradient based optimizer. A schematic overview of the optimization framework is given in figure 3.1, where each component is described briefly in this section, while detailed elaboration of the components is presented in subsequent chapters. Examining figure 3.1,

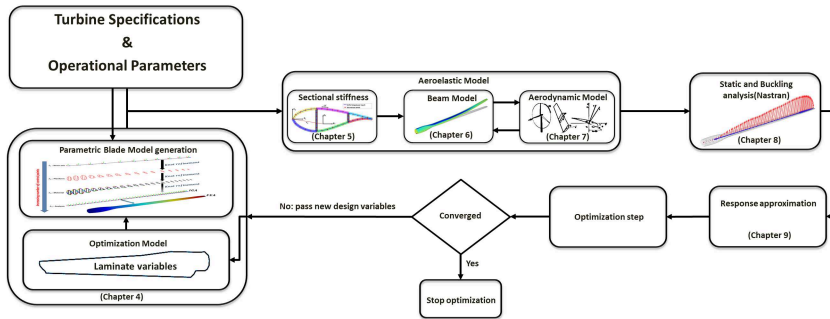


Figure 3.1: Schematic overview of the optimization methodology

the optimization process follows two basic steps. For the first step, starting from the initial design point and user supplied turbine specifications (Rotor diameter, blade planform, etc..), the sequence of generating the required responses and their sensitivities is divided in three tasks. First, the blade geometry, including its *FE* model, is generated based on the *IGA* principle. Second, based on the user supplied operational parameters (range of operational wind speeds, turbines rotational speed, etc..), the aeroelastic loads are cal-

culated using a *low-fidelity* model, generating the aeroelastic responses and their sensitivities with respect to the design variables. The (*low-fidelity*) aeroelastic module is a one dimensional model, based on the *IGA* precept, to predict both the aerodynamic loads and the structural deformations. Third, the aeroelastic loads are applied, together with their sensitivity with respect to the design variables, as design dependent loads in an *FE* model. This is followed by detailed structural analysis, together with the sensitivity of the structural responses, using the *FE* solver *NASTRAN*, referred in this thesis as *high-fidelity* model.

In the second step, after generating the responses and their sensitivities, an approximation model, suitable for the chosen optimization tool, is formulated using both the responses and their sensitivities, while satisfying the essential properties of convexity, separability, and conservativeness. The response approximations are then passed to the optimizer which iterates on the approximated model till the minimum that satisfies the constraints is found, resulting in new design variables. The new design variables are then passed to the analysis module and the whole process is repeated till the difference between successive optimum values of the objective function is below a given tolerance.

In the remaining part of this section, a brief elucidation is given on the different modules of the optimization framework.

TURBINE SPECIFICATIONS & OPERATIONAL PARAMETERS

This framework gets as input general turbine specifications, which are then used to model the geometry of the blade and define the turbine's configuration. The user supplied turbine specifications are: rotor radius, blade radius, hub radius, hub height, number of blades and blade planform data. The blade planform data consists of the chord and twist distribution along the blade radius. The hub height together with the wind speed at hub height is employed to calculate the wind shear profile, using the power law relationship. The wind shear profile is then used as input to analyse the average aerodynamic load on the blade, per blade rotation.

In addition to the turbine specifications, operational parameters such as: cut-in, rated and cut-out wind speeds, together with the rated rotational speed and optimum tip speed ratio are used to determine the aeroelastic loads on the wind turbine blade. Since the framework takes into account the effect of wind shear, discrete sampling points of the azimuth angle are initially supplied to calculate the average aerodynamic loads on the rotor disc, see section 4.1. Furthermore, the Weibull's probability density function for hub height wind speeds is supplied by the user to evaluate the annual energy production, see section 9.2.3.

OPTIMIZATION MODEL

The optimization model defines the type of design variables passed to the optimizer. The design variables considered in this thesis are elements of the

membrane A and bending D stiffness matrix together with the laminate thickness h . See section 2.3.2 for further details on parametrization of composite laminates. The method of parametrizing the material distribution along the blade span and along the chord, together with the linking of the design variables to the blade model, is given in section 4.3.

MODEL GENERATION

A parametric approach used to model wind turbine blades, with generic shapes and materials, forms the starting point of the current optimization process. The present method makes use of the 1D NURBS functions to parametrize the blade shape and material properties.

The geometry of a wind turbine blade is defined as a series of oriented cross-sections connected by a beam axis. The beam axis is described as a 3D NURBS curve with the corresponding control points locations. The cross-section variation, along the blade span, is parametrized by associating an airfoil geometry with each control point and interpolating using NURBS functions. The airfoil geometry associated with each control point is generated by a linear combination of pre-defined airfoil shapes. The orientation of each airfoil is defined by the local twist which is also represented by a NURBS function.

For the *FE* model of the blade, the outer shape of the blade and the spars are modelled by shell elements. The properties of the shell elements are defined using laminate membrane and bending stiffness matrix and thickness.

The geometry of the model and its Finite Element discretization remains unchanged during the optimization, except the material properties, which are altered by the optimizer. For detailed description on parametric modelling of wind turbine blades, the reader is directed to chapter 4.

AEROELASTIC MODULE

The aeroelastic module is used to calculate the loads on a wind turbine blade. This module consists of three components. The first module calculates the sectional stiffness constants of thin-walled blade sections with an arbitrary composite layup. In the second module, the blade deformations are modelled using isogeometric formulation of geometrically exact 3D beam theory, where the sectional stiffness constants, calculated in the first module, are used as input. Additionally, the second module also calculates the gravitational and centrifugal loads on a rotating blade. The aerodynamic loads are calculated in the third module using Blade Element Momentum theory, while accounting for the effect of large blade deformations on the aerodynamic loads. The aeroelastic equilibrium is evaluated by iterating, for all given wind speeds, between the aerodynamic and structural modules until equilibrium condition is reached.

In chapter 5, the method to calculate the sectional stiffness constants is explained in detail, whereas chapter 6 describes the module for calculating the deformations of the wind turbine blade. The module that calculates the

aerodynamic loads and the method for finding the aeroelastic equilibrium, is discussed in chapter 7.

FINITE ELEMENT MODULE

The aeroelastic loads are passed to a structural solver in order to perform detailed structural analysis. The finite element solver *NASTRAN* is used to calculate the stress and buckling responses using the *FE* model of the blade. The aeroelastic loads, including the centrifugal and gravitational loads from the aeroelastic module, are applied as design dependent loads to the *FE* model. The stress and buckling responses are then extracted from the *NASTRAN* analysis, together with their sensitivities with respect to the design variables. Details on passing aeroelastic loads to *NASTRAN* and extracting relevant responses is given in chapter 8

3

RESPONSE APPROXIMATION

This model defines a procedure to approximate the responses before passing the response approximations to the optimizer. First, the type of responses, passed to the optimizer are defined. Different kind of responses may be requested, for example the tip deflection from the aeroelastic module or the buckling load factor from the Finite Element module, depending on the type of objective to be minimized and the corresponding constraints that need to be met.

Second, the sensitivities of the requested responses with respect to the design variables are calculated to formulate the response approximations, which are then passed to the optimizer. The sensitivities are calculated both in the aeroelastic module and in the finite element module. The sensitivities of the aeroelastic loads are calculated using the adjoint method, while the sensitivities of the *NASTRAN* responses are solved using the direct method. Furthermore, a method is developed to pass the sensitivities of the aeroelastic loads, calculated outside *NASTRAN*, into the *NASTRAN* analysis. This results in correct application of design dependent loads into the *FE* model, resulting in correct sensitivity results from the *NASTRAN* analysis.

Once the response vector and the sensitivity matrix are generated, the response approximation can be formulated. The required responses are approximated based on their sensitivities with respect to the design variables. The sensitivities are extracted from *NASTRAN* or the aeroelastic analysis, depending of the type of response considered. The response approximation need to comply with three characteristics: convex, separable, and conservative. Therefore, a physical insight of each type of response is necessary for choosing the appropriate approximation strategy that satisfies the above requirements. Details on defining the responses, their sensitivity and approximation strategy is given in chapter 9.

3.2. DESIGN VARIABLES

The material properties of a wind turbine rotor blade are made from Composite laminates. The number of design variables and the number of responses in stiffness-based optimization of detailed structural entities can be in the range of thousands. The size of a sensitivity matrix is a product of the number of responses and the number of design variables, leading to a sensitivities matrix with tens of thousands entries. It is therefore necessary to develop a method where limited design variables are used while providing detailed description of the material destitution along the wind turbine blade, leading to a reduction of the computational time during the optimization process.

Symmetric laminates are used in the current optimization studies; therefore, components of the laminate stiffness matrix describing the coupling between membrane and bending \mathbf{B} is zero for all considered laminates. The laminate properties are comprised of the laminate thickness h , membrane stiffness matrix \mathbf{A} , and bending stiffness matrix \mathbf{D} . Thirteen design variables per laminate are used: one variable for the laminate thickness, six variables for the membrane stiffness matrix and six variables for the bending stiffness matrix, exploiting the symmetric nature of the matrices. See section 2.3 for further details on optimization of composite structures.

DESIGN VARIABLE DEFINITION IN IGA

Based on the precepts of *IGA*, the design variables for the beam model are defined at the control points of the L_3 level, from the multilevel parametrization scheme of a wind turbine blade, shown in figure 4.2. before assigning laminate properties over the blade section, a generic discretization of the cross-section is carried out. This determines, among others, the region of a cross-section that the properties of each laminate, per cross-section, is applied to. The method of defining the design variables within the context of isogeometric analysis, to calculate the sectional stiffness constants (chapter 5), is given in section 4.3.1.

DESIGN VARIABLE DEFINITION IN FEM

The material properties of the blade model are defined in the finite element solver *NASTRAN* using a combination of the *PHSELL* and *MAT2* property cards. The shell thickness are defined using the *PHSELL* card, while the *MAT2* card is used to define the thickness normalized membrane $\hat{\mathbf{A}}$ and bending $\hat{\mathbf{D}}$ stiffness matrix. The method of passing material design variables and converting the sensitivities from the finite element analysis to the *IGA* framework is given in section 4.3.2.

3.3. RESPONSE DEFINITION

This thesis focuses on static aeroelastic optimization of wind turbine blades. Particularly, the use of twist coupling to enhance the performance of stall regulated wind turbines is investigated. With this in mind, the current optimiza-

tion work contains two types of responses; responses derived from the aeroelastic analysis and responses from the finite element analysis. The definition of the responses and their response approximations is outlined in chapter 9.

AEROELASTIC RESPONSES

The responses for the aeroelastic analysis are used in two folds. First, the aeroelastic loads calculated using the aeroelastic model are passed as design dependent loads for detailed finite element analysis using *NASTRAN*. Second, several responses from the aeroelastic module are used to calculate the cost of energy and are also used directly as design constraints in the optimization process (for example the maximum blade deflection is constrained). A detailed description of the aeroelastic responses is given in section 9.2.1.

STRUCTURAL RESPONSES

The responses from the detailed finite element analysis are essential in the current optimization framework to size the wind turbine blade. The structural responses consist of stresses of all shell elements, from the finite element model, and the buckling load factors. Based on the stress responses together with their sensitivities with respect to the design variables, the strain failure constraints are calculated using the method proposed in [66]. Additionally, the buckling load factors are used to construct the buckling failure constraints. A detailed description of the structural responses is given in section 9.2.2.

BLADE MASS & COST OF ENERGY

Both the blade mass and the cost of energy are used as objectives in the current optimization work. A baseline for stall regulated 5MW wind turbine blade is designed using the blade mass as the objective to be minimized. The cost of energy is used as an objective to investigate the benefit of using composite materials to enhance the performance of large stall regulated wind turbine machines. The reader is directed to section 9.2.3 for detailed description on the cost model.

3.4. SUMMARY

An overview of the major steps of the optimization process is presented, which includes a brief overview of the Isogeometric framework for calculating the aeroelastic responses, a method of passing design dependent loads for detailed structural analysis, and setting up response approximations suitable for the considered optimization process. The reader will find, in the subsequent chapters, detailed information of the topics mentioned in this chapter.

4

PARAMETRIC WIND TURBINE BLADE GENERATION

This chapter presents a method for parametrically describing the geometry and material properties of a wind turbine blade. The blade geometry is parametrized in-terms of its chord, twist and the position vector of the beam axis. The cross-section variation along the blade axis is parametrized in-terms of pre-defined airfoil geometries. The material properties for all the structural entities of the blade are defined from a set of laminates. The parametric modelling, proposed in this chapter, allows to efficiently investigate the effect of changing different parameters of the rotor blade on the wind turbine rotor performance.

NURBS representations are commonly used to construct Computer Aided Design descriptions of engineering products. More recently NURBS representations are applied to model physical response quantities both in structural analysis [36], where they are used to describe the variation of displacements and/or stresses, and in aerodynamic analysis where they are used to describe the variation of flow velocities and pressures [63]. The use of the same description for both geometry and physics is termed isogeometric analysis. In this chapter, an *IGA* based framework is created to model both the geometric and material properties of a wind turbine blade.

Section 4.1 describes the parametrization of a wind turbine blade geometry. Followed by a description on generating finite element model for detailed structural analysis, in section 4.2. Finally, the optimization model used in the current thesis is described in section 4.3.

This chapter is based on a paper titled *Isogeometric based framework for aeroelastic wind turbine blade analysis* by E.A. Ferde, M.M. Abdalla, and G.J.W. van Bussel, Wind Energy, 2016. Note: symbols may have been changed to ensure consistency throughout the thesis.

4.1. GEOMETRY MODEL

A parametric approach is set-up to model wind turbine blades with generic shapes including general planform shapes, sweep or curvature of the centre-line. The parametrization is intended to be used for performing parametric design studies and preliminary optimisation of the blade planform, blade axis, and material properties.

The blade geometry is modelled in the rotating, XYZ frame, as shown in figure 4.1. The base vector e_3 is orthogonal to the rotor plane, while e_1 , e_2 span the rotor plane. Moreover, a fixed frame is formed by the orthonormal triad a_1 , a_2 , and a_3 , with the origin at the bottom of the tower. The position of the blade in global coordinates is specified by the azimuth position ϕ , which is important in the calculation of the gravity load and wind shear effects. The present method makes use of the NURBS functions, described in

4

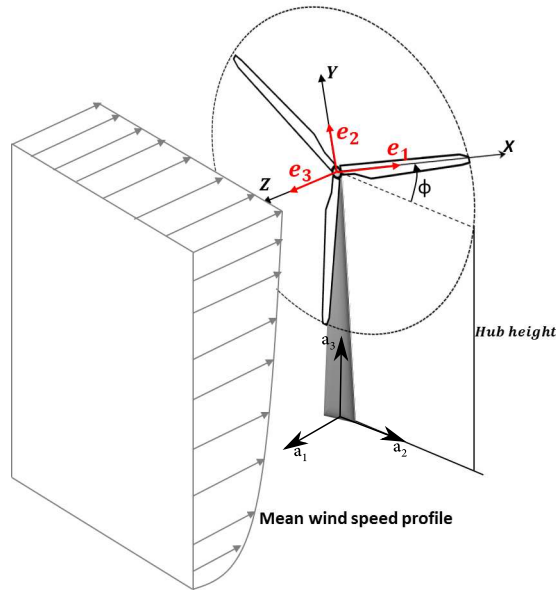


Figure 4.1: Definition of moving reference frame and wind shear for wind turbine aeroelastic analysis

section 2.2, to parametrise the blade shape and material properties. A multi-level discretization scheme is used to parametrize the beam axis geometry, blade planform shape, material distribution, and response using successively finer control point nets as shown in figure 4.2. The mapping between different levels of refinement is performed according to the *Knot refinement* method described in section 2.2.2.

The geometry of a wind turbine blade may be defined as a series of oriented cross-sections connected by a beam axis. The beam axis is described as a 3D NURBS curve with the corresponding control points locations P_i^r , $i =$

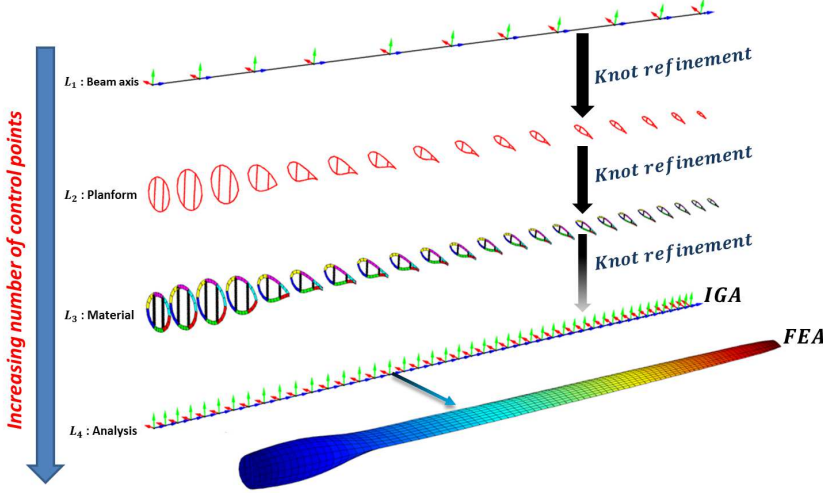


Figure 4.2: Multi level parametrization of a wind turbine blade

$1, \dots, n^r$. The cross-section variation is parametrized by associating an airfoil geometry with each control point and interpolating using NURBS functions. The airfoil geometry associated with each control point is generated by a linear combination of pre-defined airfoil shapes. The orientation of each airfoil is defined by the local twist which is also represented by a NURBS function.

4.1.1. BEAM AXIS

The position of an arbitrary point on the beam axis is interpolated as,

$$\mathbf{r}_b(\xi) = \sum_{i=1}^{n^r} R_{i,p}(\xi) \mathbf{P}_i^r, \quad (4.1)$$

where \mathbf{P}_i^r are control point locations.

The arc-length, measured from the root of the blade, is given by,

$$s(\xi) = \int_0^\xi J(\xi) d\xi, \quad (4.2)$$

where $J(\xi)$ is the Jacobian,

$$J(\xi) = \left\| \frac{d\mathbf{r}_b}{d\xi} \right\|. \quad (4.3)$$

The cross-sections are orthogonal to the beam axis. Consequently, the body attached base vector normal to the cross-section is tangent to the beam axis,

$$\mathbf{g}_1 = \frac{1}{J} \frac{d\mathbf{r}_b}{d\xi}. \quad (4.4)$$

The reference chord direction, i.e. for untwisted blade, is defined as the projection of \mathbf{e}_2 onto the plane of the cross section, viz.,

$$\tilde{\mathbf{g}}_2(\xi) = \frac{\mathbf{e}_3 \times \mathbf{g}_1(\xi)}{\|\mathbf{e}_3 \times \mathbf{g}_1(\xi)\|}, \quad (4.5)$$

The vector $\tilde{\mathbf{g}}_3$ is calculated to complete the orthogonal triad as,

$$\tilde{\mathbf{g}}_3(\xi) = \tilde{\mathbf{g}}_1(\xi) \times \tilde{\mathbf{g}}_2(\xi), \quad (4.6)$$

In the case of a twisted blade, the base vectors \mathbf{g}_2 and \mathbf{g}_3 are rotated by the structural twist,

$$\mathbf{g}_2(\xi) = \cos(\theta)\tilde{\mathbf{g}}_2 - \sin(\theta)\tilde{\mathbf{g}}_3 \quad \text{and} \quad \mathbf{g}_3(\xi) = \sin(\theta)\tilde{\mathbf{g}}_2 + \cos(\theta)\tilde{\mathbf{g}}_3, \quad (4.7)$$

where $\theta(\xi)$ is the structural twist calculated using the control point value \mathbf{P}_i^θ and the NURBS function as,

$$\theta(\xi) = \sum_{i=1}^{n^c} R_{i,p}(\xi) \mathbf{P}_i^\theta. \quad (4.8)$$

Note that the twist angle is defined at the second discretization level together with airfoil shapes.

The base vectors spanning a cross-section at ξ define an orientation matrix, $\Lambda_0(\xi) = [\mathbf{g}_1, \mathbf{g}_2, \mathbf{g}_3]$.

4.1.2. CROSS-SECTION

The cross-sectional shape of a turbine blade at a parametric point ξ is modelled using a set of user supplied airfoil shapes, also referred as base airfoils. The user supplies the desired number of elements in chord direction (N_c) and the chord-wise position of the spars (\mathbf{V}_{sp}), which is then used to discretize the base airfoils (with unit chord) with the same number of elements while preserving the connectivity between the nodes of the base airfoils. The discretized position vectors of the base airfoils, denoted by \mathbf{P}^{baf} , together with the parameter \mathbf{C} , are used to calculate the position vectors of an airfoil shape at a control point. The parameter \mathbf{C} is an $n^c \times m$ matrix, where m refers to the number of base airfoils and n^c refers to the number of control points at the L_2 discretization level (see figure 4.2). The column wise summation of \mathbf{C} results in the chord length per control point, while row wise elements of \mathbf{C} refer to chord coefficients of the base airfoils for a particular control point. This method of parametrizing the cross-section enables to smoothly vary the cross-sectional shape along the span, for example by continuously morphing one airfoil shape from the root to another airfoil shape at the tip. The position vector of an airfoil shape at a control point i is calculated as,

$$\mathbf{P}_i^{af} = \sum_{j=1}^m C_{i,j} \mathbf{P}_j^{baf}. \quad (4.9)$$

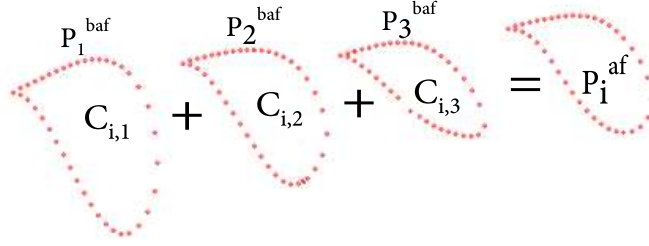


Figure 4.3: A linear combination of three base airfoils P_j^{baf} with their respective chord coefficients $C_{i,j}$

4

An example of equation 4.9 is shown in figure 4.3, where three base airfoils, with their respective chord coefficients, are summed together to get an airfoil shape at a single control point. The shape of a cross-section, in a plane spanned by \mathbf{g}_2 and \mathbf{g}_3 , is given as,

$$\mathbf{R}_{2D}(\xi) = \mathbf{r}_{2D}^0 + \sum_{i=1}^{n^c} R_{i,p}(\xi) \mathbf{P}_i^{af}, \quad (4.10)$$

where,

$$\mathbf{r}_{2D}^0 = \sum_{i=1}^{n^c} \sum_{j=1}^m C_{i,j} \mathbf{P}_i^{2D}, \quad (4.11)$$

and \mathbf{P}_i^{2D} is a non-dimensional vector, at control point i , defining the intersection of the beam axis with the cross-sectional plane (see figure 4.4). The position vector of a cross-section, with respect to the moving frame, at ξ is given by,

$$\mathbf{R}(\xi) = \mathbf{r}_b(\xi) + \Lambda_0(\xi) \mathbf{R}_{2D}(\xi), \quad (4.12)$$

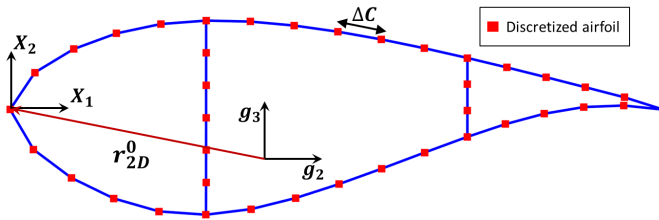


Figure 4.4: Example of airfoil discretization, where the local airfoil coordinates are denoted by X_1 and X_2 , while \mathbf{g}_2 and \mathbf{g}_3 are the base vectors of the beam axis that span the cross-section.

4.2. FINITE ELEMENT MODEL

Based on the geometry of the wind turbine blade described in section 4.1, the finite element model is generated. The blade geometry is discretized using quadrilateral elements. The nodal position of these elements are generated using the discretized cross-sections discussed in section 4.1.2. The parametric point ξ , at which the intermediate cross-sections are calculated, is determined by the, user supplied, aspect ratio(ar) between the element size in chord direction and span wise direction, as can be seen in figure 4.5.

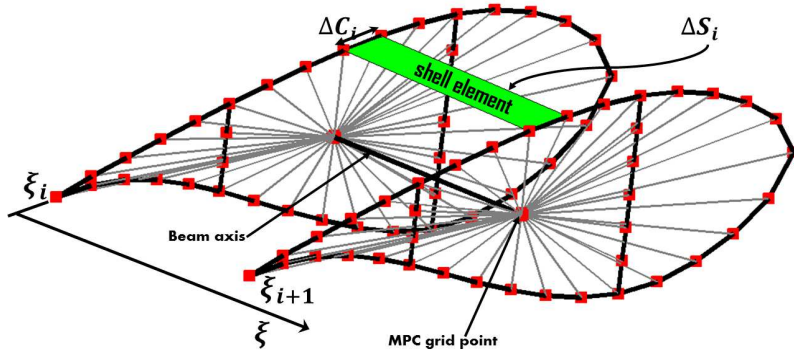


Figure 4.5: Discretization of the geometry in span wise direction and representation of RBE3 connection

The finite element solver *NASTRAN* is used to calculate the structural response of a wind turbine rotor. The elements used to discretize the outer skin of the wind turbine blade, including the spars, are the *NASTRAN CQUAD4* elements. The laminate properties may be defined in *NASTRAN* using a combination of *PSHELL* and *MAT2* input options, which are referred in *NASTRAN* as card. The *PSHELL* card is used to assign the laminate thickness, while the *MAT2* card is used to assign the, thickness normalized, membrane \hat{A} and bending \hat{D} stiffness properties. The laminate properties, for elements between the cross-sections at ξ_i and ξ_{i+1} , are calculated using equation 4.13, for $\xi = \frac{1}{2}(\xi_i + \xi_{i+1})$. The method to define the material properties of the *NASTRAN* model is covered in section 4.3.2.

4.2.1. INTERFACE MODEL

The interface model is used to apply the aeroelastic loads, calculated outside *NASTRAN*, unto the finite element model for detailed structural analysis. To this end, additional grid points are created where the aeroelastic loads are applied. The grid points, where the aeroelastic loads are applied, are connected to the existing grid points of the finite element model using multi point weighted connection. This type of connection averages the displacement of the new grid point, where the loads are applied, from the displacement of the existing grid points of the finite element model. This leads to a smooth intro-

duction of the external loads to the finite element model. The corresponding *NASTRAN* element is called *RBE3*. An example of the multipoint connections, per cross-section, using the *RBE3* cards is shown in figure 4.5.

4.3. OPTIMIZATION MODEL

The material properties of the wind turbine blades, proposed in this thesis, are composed of Composite materials. The number of design variables and the number of responses, in stiffness-based optimization of detailed structural entities, can be in the range of thousands. The size of a sensitivity matrix is a product of the number of responses and the number of design variables, leading to a sensitivity matrix with tens of thousands entries. It is therefore necessary to develop a method where limited design variables are used while providing detailed description of the material destitution along the wind turbine blade, leading to a reduction of the computational time during the optimization process.

Symmetric laminates are used in the current optimization studies. Therefore, the laminate properties are comprised of the laminate thickness h , membrane stiffness matrix \mathbf{A} , and bending stiffness matrix \mathbf{D} . There are thirteen design variables per laminate: one variable for the laminate thickness, six variables for the membrane stiffness matrix, and six variables for the bending stiffness matrix, exploiting the symmetric nature of the matrices. See section 2.3 for further details on optimization of composite structures. First the method of defining the design variables within the context of isogeometric analysis is presented in section 4.3.1. Followed by section 4.3.2, where the definition of the design variables employed in detailed structural analysis using the finite element solver *NASTRAN* is described.

4.3.1. DESIGN VARIABLE DEFINITION IN IGA

Following the precepts of *IGA*, the laminate properties are defined at the control points. First, the number of laminates per control point are determined by dividing the cross-section in N_{pr} sections, where the contour of the cross-section is defined by $N_{pr} - 1$ laminates, while the shear webs with a single laminate (see figure 4.6). The, user supplied, vector \mathbf{V}_{pr} determines the discretization of the (non-dimensional)chord for material assignment. This vector is used to determine the elements, per cross-section, having the same material properties, linking the property of the laminates per cross-section with the property of the elements. The laminate properties at a parametric point ξ (along the blade span) are calculated using the laminate properties at the

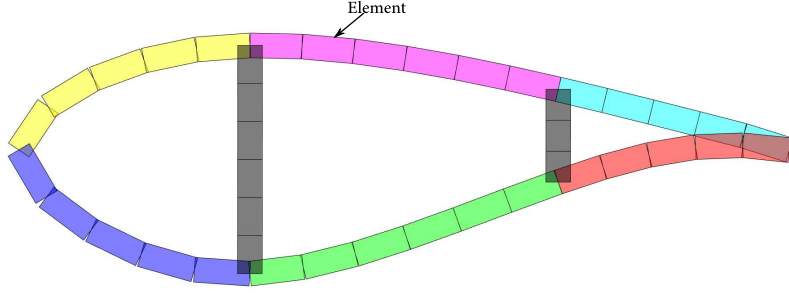


Figure 4.6: Example of property assignment on cross-section level, where each colour represents a single laminate.

control points and the NURBS function as:

$$\begin{aligned}
 h^k(\xi) &= \sum_{i=1}^m R_{i,p}(\xi) \mathbf{P}_{h,i}^k, \\
 \mathbf{A}^k(\xi) &= \sum_{i=1}^m R_{i,p}(\xi) \mathbf{P}_{A,i}^k, \\
 \mathbf{D}^k(\xi) &= \sum_{i=1}^m R_{i,p}(\xi) \mathbf{P}_{D,i}^k,
 \end{aligned} \tag{4.13}$$

where $k = 1, \dots, N_{pr}$, is an index running over the laminates per control point and m is the number of control points to parametrize the material properties, defined at the L_2 parametrization level shown in figure 4.2. The control point laminate properties are denoted by \mathbf{P}_h^k , \mathbf{P}_A^k , and \mathbf{P}_D^k . Hence, the design variables \mathbf{x} are comprised of the laminate variables defined at the control points, where the size of \mathbf{x} is $13N_{pr}m$.

4.3.2. DESIGN VARIABLE DEFINITION IN FEM

The material characteristics of a blade model are defined in the finite element solver *NASTRAN* using the property cards. Material properties of shell elements are defined using the *PSHELL* cards. This card is used to define the shell thickness and identification numbers of the cards that contain the material properties of the shell elements. The material properties, for orthotropic laminates, are defined using the *MAT2* card, which contains, for symmetric laminates, the thickness normalized membrane $\hat{\mathbf{A}}$ and bending $\hat{\mathbf{D}}$ stiffness matrix.

Design variables are defined in *NASTRAN* using a combination of three cards. The *DESVAR* card contains the labels and the initial values of the design variables. The *DVPREL1* or *DVMREL1* cards are used respectively, to link the

design variables, defined in the *DESVAR* card, to the *PSHELL* or *MAT2* cards. A schematic representation of the links described above is shown in figure 4.7.

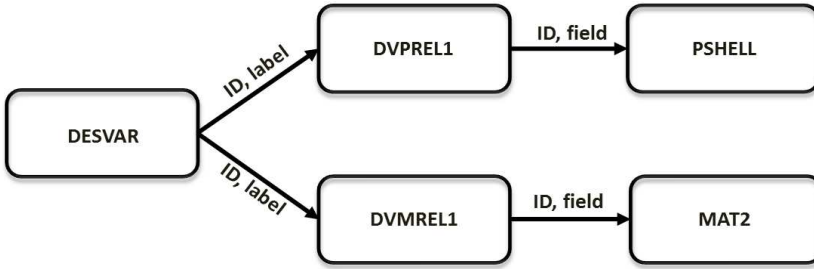


Figure 4.7: Schematic representation of design variable definition in Nastran

4

Increasing the number of design variables has the disadvantage of increasing the computational time for solving the design optimum of the approximated model. In addition, larger design variables constitute in an increased local minima of the real non-convex design space. Furthermore, the manufacturing process also poses a constraint on the maximum number of design variables used for optimization. To this end, based on the precepts of IGA, the laminate properties passed to the finite element model are calculated using the laminate properties at the control points, see equation 4.13. A schematic example of interpolating the laminate properties from control points to the fem model is given in figure 4.8, for the top skin. According to this example, twelve laminates are defined at the control points while three laminates are associated to each control point. The laminates at the control points serve as design variables. The material properties of the shell elements, constituting the top skin, are obtained by interpolating the laminate properties at the control points and the *NURBS* shape functions, according to equation 4.13.

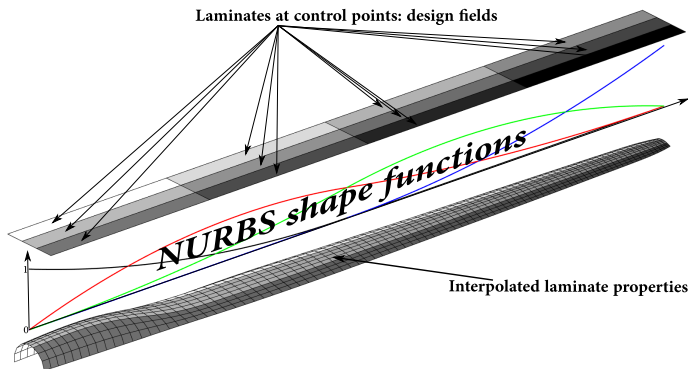


Figure 4.8: Design fields for the top skin

The laminates passed to *NASTRAN* as design variables are the interpolated laminates (see figure 4.8). This means that the sensitivities of the responses from *NASTRAN* are with respect to the interpolated laminate properties. The sensitivity of the *NASTRAN* response f with respect to the control point laminate variables $(h_{cp}, \mathbf{A}_{cp}, \mathbf{D}_{cp})$ are calculated from the sensitivities of the *NASTRAN* responses as:

$$\begin{aligned} \frac{\partial f}{\partial h_{cp}} &= \frac{\partial f}{\partial \hat{h}_i} \frac{\partial \hat{h}_i}{\partial h_i} \frac{\partial h_i}{\partial h_{cp}} + \frac{\partial f}{\partial \hat{\mathbf{A}}_i} \frac{\partial \hat{\mathbf{A}}_i}{\partial h_i} \frac{\partial h_i}{\partial h_{cp}} + \frac{\partial f}{\partial \hat{\mathbf{D}}_i} \frac{\partial \hat{\mathbf{D}}_i}{\partial h_i} \frac{\partial h_i}{\partial h_{cp}}, \\ \frac{\partial f}{\partial \mathbf{A}_{cp}} &= \frac{\partial f}{\partial \hat{\mathbf{A}}_i} \frac{\partial \hat{\mathbf{A}}_i}{\partial \mathbf{A}_i} \frac{\partial \mathbf{A}_i}{\partial \mathbf{A}_{cp}}, \\ \frac{\partial f}{\partial \mathbf{D}_{cp}} &= \frac{\partial f}{\partial \hat{\mathbf{D}}_i} \frac{\partial \hat{\mathbf{D}}_i}{\partial \mathbf{D}_i} \frac{\partial \mathbf{D}_i}{\partial \mathbf{D}_{cp}}, \end{aligned} \quad (4.14)$$

where the coefficients with the subscripts i are summed over the number of interpolated laminates. The subscripts cp and i indicate the laminate variables at the control points and the interpolated laminate variables respectively. The relation between normalized laminate variables and the full laminate variables: $(\hat{h}, \hat{\mathbf{A}}, \hat{\mathbf{D}}) \mapsto (h, \mathbf{A}, \mathbf{D})$, is given in section 2.3.2. Finally, the derivatives of the interpolated laminate variables with respect to the laminates at control points: $\frac{\partial h_i}{\partial h_{cp}}$, $\frac{\partial \mathbf{A}_i}{\partial \mathbf{A}_{cp}}$, and $\frac{\partial \mathbf{D}_i}{\partial \mathbf{D}_{cp}}$, are derived from equation 4.13.

4.4. SUMMARY

An isogeometric framework is presented for parametrizing a wind turbine rotor blade, where the geometric model generation, using NURBS function, is described in detail. The generation of the finite element model is described afterwards, together with a description on the interface model to connect the aeroelastic loads, calculated using *low-fidelity* model, with the *high-fidelity* structural model using *NASTRAN*. Finally, detailed description on the optimization model for defining the material design variables is given. The first component of the *low-fidelity* model is the analysis of the sectional stiffness constants, used to determine the blade deformation. A detailed description on the method to calculate the sectional stiffness properties of thin-walled composite beams with generic cross-sectional shape is given in the following chapter.

5

STIFFNESS CONSTANTS OF THIN WALLED COMPOSITE CROSS-SECTIONS

This chapter presents a computationally efficient finite element method to calculate the sectional properties of thin-walled composite beams with arbitrary open and closed cross-sections. The formulation is based on the classical laminate theory, making it suitable for use in composite optimisation. Finite element method is then employed to evaluate the sectional stiffness constants of composite blades, which are then implemented in a beam model that is based on an isogeometric formulation of a geometrically exact 3D beam theory.

First, the motivation for proposing a novel method to calculate the sectional constants is presented in section 5.1, followed by a formulation of the generalized shell strains in terms of the beam strain resultants (Euler-Bernoulli for extension and bending while Saint-Venant for torsion) and the unknown cross-sectional warping in section 5.2. A finite element procedure is presented in sections 5.3.1 (Euler model) and 5.3.2 (Timoshenko model), where the warping displacements are solved using the principle of minimum strain energy and recast back into the strain energy expression, from which the sectional stiffness constants are determined. In section 5.4, the sectional stiffness constants, calculated using the present method, are compared with literature results for a family of closed and open cross-sections.

This chapter is based on a paper titled *Cross-sectional modelling of thin-walled composite beams* by E.A. Ferde and M.M. Abdalla, submitted to journal of thin-walled structures. Note: symbols may have been changed to ensure consistency throughout the thesis.

5.1. INTRODUCTION

The 3D non-linear elastic problem of slender structures can be decoupled into 2D linear sectional analysis to calculate the elastic constants and 1D non-linear analysis to calculate the global deformation. A review on modelling composite beam cross-sections is given in [33], where the methods in calculating the sectional stiffness constants can be classified in analytical or finite element method. Analytical solutions for the elastic constants of composite beams are available [102, 103, 114, 14, 69, 89, 125, 126, 112, 135, 77, 2], but are limited to special cases, making them unsuitable for optimization.

In contrast, numerous finite element methods are developed to calculate the sectional properties of composite beams, which may be subdivided into three categories. (1) a semi discretization method, where finite element representation of a bi-dimensional problem is solved using spectral decomposition of the eigenvalue problem of the equilibrium equations. The central solutions, corresponding to null eigenvalues, are asymptotic to the Saint-Venant solutions for extension, bending, torsion, and flexure [50]. A finite element code NABSA is developed based on this formulation. (2) Finite element methods are available for constructing the Saint-Venant solutions for extension, bending, torsion, and flexure, either using the semi inverse method [79] or the Iesan's rational scheme [118, 80, 83]. (3) The variational asymptotic beam sectional analysis (VABS) [60, 139, 138, 137, 109, 111, 110, 61, 29, 30, 31, 32] is a finite element code, based on the variational asymptotic method (VAM) [12], to calculate the sectional stiffness properties of composite beams. Although all the finite element methods mentioned here are in general generic and thus capable of accounting complexity in terms of material and geometry, detailed discretization of the cross-section is necessary, requiring detailed information of the ply properties across the thickness (thin-walled beams). However, detailed information on composite ply properties is in general unknown at the preliminary design stage and more importantly one wants to reduce the number of design variables during the optimization process.

5.2. KINEMATICS

This paper considers only thin-walled beams where the structure is modelled as a thin shell and the beam length is much larger than the cross-sectional dimensions. The shell is also assumed to be cylindrical, representing a straight and prismatic beam (see figure 5.1). Figure 5.1 shows the cartesian coordinates denoted by: x , y , and z . The x axis of the cartesian coordinate system is parallel to the curvilinear coordinate which is also denoted by x . The curvilinear coordinate s is the arc-length along the contour of the cross-section. n is the curvilinear coordinate normal to the shell mid plane. Components of the beam displacement in x , y , and z axis are denoted by u_{x0} , u_{y0} , and u_{z0} , respectively. Components of the beam rotations in x , y , and z axis are denoted by θ_{x0} , θ_{y0} , and θ_0 , respectively. The displacement components along x , and s are denoted by u , and v . The displacement component normal to the shell

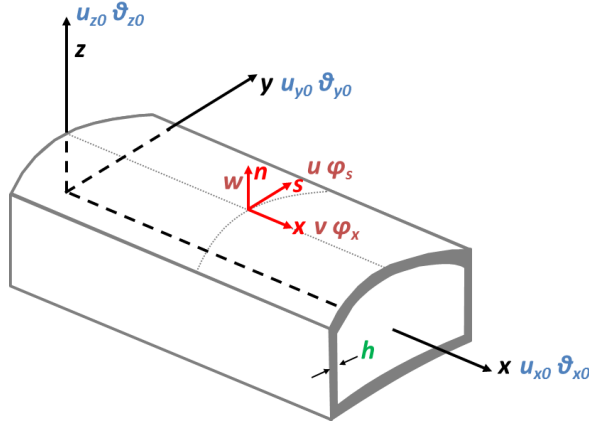


Figure 5.1: Shell kinematics

mid plane is denoted by w . Changes in shell normal are denoted by ϕ_s , and ϕ_x . The skin thickness, which is not constant along the cross-section, is denoted by h .

Starting from the work of [122] and assuming small displacements and rotations, the mid-plane strains and change in curvature, are expressed in terms of the mid-plane displacements of the shell and change in shell normal, i.e.

$$\varepsilon_{\alpha,\beta} = \frac{1}{2}(u_{\alpha,\beta} + u_{\beta,\alpha}) + \kappa_{\alpha\beta} w \quad \text{and} \quad \rho_{\alpha,\beta} = \frac{1}{2}(\phi_{\alpha,\beta} + \phi_{\beta,\alpha}), \quad (5.1)$$

where ε is the (mid-plane)shell strain, and ρ is the change in curvature. The Greek indices α, β run from 1 to 2 over shell surface coordinates, and $\kappa_{\alpha\beta}$ is the initial curvature of the shell. u_α are the components of in-plane displacement in the curvilinear coordinate system (in this case u , and v), and w is the displacement normal to the mid-plane.

The change in shell normal has components ϕ_α , which are ϕ_s , and ϕ_x . For thin shells the Kirchhoff assumption is valid and $\phi_\alpha = -w_{,\alpha}$. A comma subscript indicates derivatives with respect to a surface coordinate.

For the cylindrical shell under consideration, the surface is parametrized in terms of two coordinates x , and s (see figure 5.1). A prime and a dot are used to indicate derivatives with respect to x and s respectively. The displacements in curvilinear coordinate are grouped in the vector $\mathbf{u} = \{u \ v \ w \ \phi_s \ \phi_x\}^T$, while mid-plane strains and change in shell curvature are grouped in a generalised strain vector $\mathbf{\Gamma}$. The strain-displacement relationship may now be cast in the form,

$$\mathbf{\Gamma} = \mathbf{B}_0 \mathbf{u} + \mathbf{B}_1 \mathbf{u}', \quad (5.2)$$

where

$$\mathbf{B}_0 = \begin{bmatrix} 0 & 0 & 0 & 0 & 0 \\ 0 & \frac{\partial}{\partial s} & \frac{1}{R} & 0 & 0 \\ \frac{\partial}{\partial s} & 0 & 0 & 0 & 0 \\ 0 & 0 & 0 & 0 & 0 \\ 0 & 0 & 0 & \frac{\partial}{\partial s} & 0 \\ 0 & 0 & 0 & 0 & \frac{\partial}{\partial s} \end{bmatrix} \quad \text{and} \quad \mathbf{B}_1 = \begin{bmatrix} 1 & 0 & 0 & 0 & 0 \\ 0 & 0 & 0 & 0 & 0 \\ 0 & 1 & 0 & 0 & 0 \\ 0 & 0 & 0 & 0 & 1 \\ 0 & 0 & 0 & 0 & 0 \\ 0 & 0 & \frac{1}{R} & 1 & 0 \end{bmatrix}. \quad (5.3)$$

The shell displacements are decomposed into *beam* displacements, where the cross-section translate and rotate rigidly, and warping displacements, i.e.

$$\mathbf{u} = \mathbf{R}\mathbf{u}_0 + \mathbf{w}, \quad (5.4)$$

where \mathbf{w} is the warping displacement. The beam displacements and rotations, in Cartesian coordinate system, are grouped in a vector $\mathbf{u}_0 = \{u_{x0} \ u_{y0} \ u_{z0} \ \theta_{x0} \ \theta_{y0} \ \theta_{z0}\}^t$. The rigid translations and rotations of the cross-section, in curvilinear coordinate system, are represented by the matrix \mathbf{R} , written as

$$\mathbf{R} = \mathbf{R}_0(s)(\mathbf{I} + x\tilde{\mathbf{E}}), \quad (5.5)$$

where

$$\mathbf{R}_0 = [\mathbf{r}_1 \ \mathbf{r}_2 \ \mathbf{r}_3 \ \mathbf{r}_4 \ \mathbf{r}_5 \ \mathbf{r}_6] \quad \text{and} \quad \tilde{\mathbf{E}} = [0 \ 0 \ 0 \ 0 \ -\mathbf{e}_3 \ \mathbf{e}_2]. \quad (5.6)$$

The columns of \mathbf{R}_0 , and $\tilde{\mathbf{E}}$ are expressed in curvilinear coordinate system as,

$$\begin{aligned} \mathbf{r}_1 &= \{1 \ 0 \ 0 \ 0 \ 0\}^t \\ \mathbf{r}_2 &= \{0 \ \dot{y} \ -\dot{z} \ 0 \ 0\}^t \\ \mathbf{r}_3 &= \{0 \ \dot{z} \ \dot{y} \ 0 \ 0\}^t \\ \mathbf{r}_4 &= \{0 \ y\dot{z} - z\dot{y} \ z\dot{z} + y\dot{y} \ -1 \ 0\}^t \\ \mathbf{r}_5 &= \{z \ 0 \ 0 \ 0 \ \dot{y}\}^t \\ \mathbf{r}_6 &= \{-y \ 0 \ 0 \ 0 \ \dot{z}\}^t \\ \mathbf{e}_2 &= \{0 \ 1 \ 0 \ 0 \ 0\}^t \\ \mathbf{e}_3 &= \{0 \ 0 \ 1 \ 0 \ 0\}^t \end{aligned} \quad (5.7)$$

\mathbf{r}_1 to \mathbf{r}_3 are rigid translations of the cross-section in x , y , and z directions respectively, whereas \mathbf{r}_4 to \mathbf{r}_6 are rotations in x , y , and z directions respectively. \mathbf{I} is a six by six identity matrix.

There is no strain due to rigid body displacements or rotations. Therefore, setting the warping displacement (\mathbf{w}) to zero and substituting $\mathbf{u} = \mathbf{R}$ into equation 5.2 while using equation 5.5 yields relationships between \mathbf{B}_0 and \mathbf{B}_1 at each cross-section, defined as

$$\mathbf{B}_0\mathbf{R}_0 + \mathbf{B}_1\mathbf{R}_0\tilde{\mathbf{E}} = \mathbf{0}. \quad (5.8)$$

Analysing equation 5.8, it is found that $\mathbf{B}_0 \mathbf{r}_i = \mathbf{0}$, for $i = 1 \dots 4$, which shows that \mathbf{B}_0 is rigid-body invariant. In addition, a relationship between the two bending modes with the two transverse shear modes is obtained, such that

$$\mathbf{B}_0 \mathbf{r}_5 = \mathbf{B}_1 \mathbf{r}_3 \quad \text{and} \quad \mathbf{B}_0 \mathbf{r}_6 = -\mathbf{B}_1 \mathbf{r}_2. \quad (5.9)$$

The Euler-Bernoulli assumption stipulates that

$$\theta_{y0} = -u'_{z0} \quad \text{and} \quad \theta_{z0} = u'_{y0}. \quad (5.10)$$

Substituting equation 5.4 into 5.2, and using the relations between \mathbf{B}_0 , and \mathbf{B}_1 (given in equation 5.8) together with the relations given in equation 5.10, the strain-displacement relationship is defined explicitly in-terms the beam displacements and the unknown warping functions, i.e.

$$\boldsymbol{\Gamma} = \mathbf{G}\boldsymbol{\epsilon} + \mathbf{B}_0 \mathbf{w} + \mathbf{B}_1 \mathbf{w}', \quad (5.11)$$

where $\boldsymbol{\epsilon}$ is the Euler beam strain, defined as

$$\boldsymbol{\epsilon} = \left\{ u'_{x0}, \theta'_{x0}, \theta'_{y0}, \theta'_{z0} \right\}^t, \quad (5.12)$$

and the matrix \mathbf{G} is given by

$$\mathbf{G} = \mathbf{B}_1 \mathbf{R}_e \quad (5.13)$$

with

$$\mathbf{R}_e = \begin{bmatrix} \mathbf{r}_1 & \mathbf{r}_4 & \mathbf{r}_5 & \mathbf{r}_6 \end{bmatrix} \quad (5.14)$$

containing the four Euler rigid body modes: extension, torsion and bending in two directions.

From classical lamination theory [70], the stress resultants \mathbf{N} are related to the generalized shell strains through the laminate stiffness matrix, i.e.

$$\mathbf{N} = \mathbf{C}\boldsymbol{\Gamma} \quad (5.15)$$

where \mathbf{C} is the stiffness matrix of a laminate. The total strain energy of a beam is defined as

$$U = \frac{1}{2} \int_L \left(\int_s \mathbf{N}^t \boldsymbol{\Gamma} ds \right) dL = \int_L \hat{U} dL, \quad (5.16)$$

where

$$\hat{U} = \frac{1}{2} \int_s \boldsymbol{\Gamma}^t \mathbf{C} \boldsymbol{\Gamma} ds \quad (5.17)$$

is the strain energy per unit length. The beam model is the outer solution of the 3D non-linear elasticity problem of a slender structure. The beam model

is valid away from boundaries and points of load introduction. The outer solutions are known as St. Venant solutions and can be decomposed into two hierarichal sets: Euler-Bernoulli and Timoshenko. The strain energy per unit length (\hat{U}) may be expressed using the Euler-Bernoulli model or the Timoshenko model as

$$\hat{U} = \frac{1}{2} \boldsymbol{\epsilon}^t \mathbf{S}_e \boldsymbol{\epsilon} \quad \text{or} \quad \hat{U} = \frac{1}{2} \mathbf{f}^t \mathbf{S}^{-1} \mathbf{f}, \quad (5.18)$$

where \mathbf{f} is the sectional force resultant, \mathbf{S}_e is the Euler stiffness matrix, and \mathbf{S} is the Timoshenko stiffness matrix.

5.3. SECTIONAL STIFFNESS CONSTANTS

This section describes the Euler and Timoshenko stiffness matrices, derived for a thin walled beam with generic cross-sectional shape and anisotropic material. First the strain energy per unit length (\hat{U}) is minimized with respect to the approximation of the warping displacement \mathbf{w} , which is then used to re-write \hat{U} in terms of the beam strains (Euler model) or sectional force resultant (Timoshenko model), together with the sectional stiffness matrix (Euler or Timoshenko).

5.3.1. EULER MODEL

For the Euler-Bernoulli model, the stresses and strains are independent of x . If warping is independent of x , the first approximation of the generalized shell strain, given in equation 5.11, reduces to

$$\boldsymbol{\Gamma}_0 = \mathbf{G}\boldsymbol{\epsilon}_0 + \mathbf{B}_0\mathbf{w}_0. \quad (5.19)$$

The first approximation of \hat{U} is then written in terms of the first approximation of the Euler beam strains and warping displacements as,

$$\begin{aligned} \hat{U}_0 &= \frac{1}{2} \int_s (\mathbf{G}\boldsymbol{\epsilon}_0 + \mathbf{B}_0\mathbf{w}_0)^t \mathbf{C} (\mathbf{G}\boldsymbol{\epsilon}_0 + \mathbf{B}_0\mathbf{w}_0) ds \\ &= \frac{1}{2} \int_s (\boldsymbol{\epsilon}_0^t \mathbf{G}^t \mathbf{C} \mathbf{G} \boldsymbol{\epsilon}_0 + \mathbf{w}_0^t \mathbf{B}_0^t \mathbf{C} \mathbf{B}_0 \mathbf{w}_0 + \mathbf{w}_0^t \mathbf{B}_0^t \mathbf{C} \mathbf{G} \boldsymbol{\epsilon}_0 + \boldsymbol{\epsilon}_0^t \mathbf{G}^t \mathbf{C} \mathbf{B}_0 \mathbf{w}_0) ds. \end{aligned} \quad (5.20)$$

The cross-section is discretized using finite element method. Linear shape function are used to describe the shell's in-plane displacements (u and v), whereas quadratic shape functions are used to describe the displacement normal to shell's mid-plane and change in normals. Detailed description on the finite element implementation is given in the appendix.

The integral coefficients of equation 5.20, for a single element, are

$$\mathbf{F}_e = l_e \int_0^1 \mathbf{G}^t \mathbf{C} \mathbf{G} d\zeta \quad \mathbf{H}_{0e} = l_e \int_0^1 \mathbf{B}_0^t \mathbf{C} \mathbf{G} d\zeta \quad \mathbf{K}_{00e} = l_e \int_0^1 \mathbf{B}_0^t \mathbf{C} \mathbf{B}_0 d\zeta, \quad (5.21)$$

where l_e is the length of a single element. The strain energy of the discretized model is expressed as

$$\hat{U}_0 = \frac{1}{2} (\epsilon_0^t F \epsilon_0 + w_0^t K_{00} w_0 + w_0^t H_0 \epsilon_0 + \epsilon_0^t H_0^t w_0), \quad (5.22)$$

where F , K_{00} , and H_0 are assembled using their element properties given in equation 5.21. The unknown warping displacement (w_0) is solved by minimizing the strain energy, with respect to w_0 , using the Euler-Lagrange equation. Applying the Euler-Lagrange on the strain energy expression given in equation 5.22 gives a relationship between the Euler strains and the warping displacements, expressed as

$$K_{00} w_0 = -H_0 \epsilon_0. \quad (5.23)$$

Note that $K_{00} r_i = 0$, for $i = 1 \dots 4$, which suggest that the solution matrix K_{00} is four times singular. Because of this property, the way the cross-section is constrained, to make K_{00} non-singular, does not affect the strain energy, thus also the sectional stiffness coefficients.

The warping displacement is the sum of the solution from equation 5.23 and linear combination of r_i , $i = 1 \dots 4$, i.e.

$$w_0 = (V_0 + R_n Q) \epsilon_0, \quad (5.24)$$

where

$$R_n = [r_1 \quad r_2 \quad r_3 \quad r_4], \quad (5.25)$$

and Q is an arbitrary four by four matrix. Substituting equation 5.24 into 5.23 gives the first approximation of the warping displacements, defined as

$$K_{00} V_0 = -H_0. \quad (5.26)$$

Substituting equation 5.24 into equation 5.19, and noting that $B_0 R_n = 0$, gives an expression for the first approximation of the generalized shell strains in terms of only the Euler strains (see equation 5.27).

$$\Gamma_0 = (G + B_0 V_0) \epsilon_0. \quad (5.27)$$

Substituting the first order warping solution from equation 5.24 into the strain energy expression given in equation 5.22, and after collecting terms, the strain energy per unit length is expressed as

$$\hat{U}_0 = \frac{1}{2} \epsilon_0^t S_e \epsilon_0, \quad (5.28)$$

where the Euler stiffness matrix is given as

$$S_e = F + H_0^t V_0. \quad (5.29)$$

In order to verify the expression for the Euler stiffness matrix given in equation 5.29, the Euler forces (extension, bending in two directions and torsion) calculated using 5.29 as

$$\mathbf{F}_e = \mathbf{S}_e \boldsymbol{\epsilon}_0, \quad (5.30)$$

are compared with integral of the stress resultants over the cross-section, given by

$$\mathbf{F}_e = \int_s \mathbf{R}_e^t \mathbf{B}_1^t \mathbf{C} (\mathbf{G} + \mathbf{B}_0 \mathbf{V}_0) \boldsymbol{\epsilon}_0 ds = \mathbf{R}_e^t (\mathbf{H}_1 + \mathbf{K}_{10} \mathbf{V}_0) \boldsymbol{\epsilon}_0, \quad (5.31)$$

where $\mathbf{R}_e^t \mathbf{B}_1^t$ selects components of the stress resultant (normal and in plane of the cross-section), and \mathbf{H}_1 , and \mathbf{K}_{10} are assembled from their element properties, defined as

$$\mathbf{H}_{1e} = L \int_0^1 \mathbf{B}_1^t \mathbf{C} \mathbf{G} d\zeta \quad \mathbf{K}_{10e} = L \int_0^1 \mathbf{B}_1^t \mathbf{C} \mathbf{B}_0 d\zeta. \quad (5.32)$$

Noting that $\mathbf{G} = \mathbf{B}_1 \mathbf{R}_e$, and the expressions given in equation 5.32, equation 5.31 reduces to

$$\mathbf{F}_e = (\mathbf{F} + \mathbf{H}_0^t \mathbf{V}_0) \boldsymbol{\epsilon}_0 = \mathbf{S}_e \boldsymbol{\epsilon}_0 \quad (5.33)$$

verifying that the Euler stiffness given in equation 5.29 is derived correctly.
Put text here.

5.3.2. TIMOSHENKO MODEL

The Timoshenko model is an extension to the Euler-Bernoulli model by taking the transverse shear into account. For the Timoshenko model, higher order approximations of the generalized strain expression is added to the first approximation $\boldsymbol{\Gamma}_0$.

$$\boldsymbol{\Gamma}_1 = \boldsymbol{\Gamma}_0 + \mathbf{G} \boldsymbol{\epsilon}_1 + \mathbf{B}_0 \mathbf{w}_1 + \mathbf{B}_1 \mathbf{w}'_1, \quad (5.34)$$

where $\boldsymbol{\epsilon}_1$ and \mathbf{w}_1 are the second approximation of the beam strains and warping displacements, respectively. The second approximation of the strain energy is then given by

$$\begin{aligned} \hat{U}_1 = \frac{1}{2} \int_s & (\mathbf{G} \boldsymbol{\epsilon}_0 + \mathbf{B}_0 \mathbf{w}_0 + \mathbf{G} \boldsymbol{\epsilon}_1 + \mathbf{B}_0 \mathbf{w}_1 + \mathbf{B}_1 \mathbf{w}'_1)^t \mathbf{C} \\ & (\mathbf{G} \boldsymbol{\epsilon}_0 + \mathbf{B}_0 \mathbf{w}_0 + \mathbf{G} \boldsymbol{\epsilon}_1 + \mathbf{B}_0 \mathbf{w}_1 + \mathbf{B}_1 \mathbf{w}'_1) ds. \end{aligned} \quad (5.35)$$

After substituting the solution for \mathbf{w}_0 from equation 5.24 into equation 5.35, the second approximation of \hat{U} is given in terms of the second approximation of warping displacements (\mathbf{w}_1), as shown here

$$\begin{aligned} 2\hat{U}_1 = 2\hat{U}_0 + \boldsymbol{\epsilon}_0^t & \left(\mathbf{S}_e \boldsymbol{\epsilon}_1 + (\mathbf{H}_1 + \mathbf{K}_{10} \mathbf{V}_0)^t \mathbf{w}'_1 \right) + \left(\boldsymbol{\epsilon}_1^t \mathbf{S}_e + (\mathbf{w}'_1)^t (\mathbf{H}_1 + \mathbf{K}_{10} \mathbf{V}_0) \right) \boldsymbol{\epsilon}_0^t \\ & + \boldsymbol{\epsilon}_1^t \mathbf{F} \boldsymbol{\epsilon}_1 + \mathbf{w}_1^t \mathbf{K}_{00} \mathbf{w}_1 + \underline{(\mathbf{w}'_1)^t \mathbf{K}_{11} \mathbf{w}'_1} + \boldsymbol{\epsilon}_1^t \mathbf{H}_0^t \mathbf{w}_1 + \mathbf{w}_1^t \mathbf{H}_0 \boldsymbol{\epsilon}_1 + \underline{\boldsymbol{\epsilon}_1^t \mathbf{H}_1^t \mathbf{w}'_1} \\ & + \underline{(\mathbf{w}'_1)^t \mathbf{H}_1 \boldsymbol{\epsilon}_1} + \underline{\mathbf{w}_1^t \mathbf{K}_{10}^t \mathbf{w}'_1} + \underline{(\mathbf{w}'_1)^t \mathbf{K}_{10} \mathbf{w}_1}. \end{aligned} \quad (5.36)$$

The strain energy given in equation 5.36 is minimized with respect to \mathbf{w}_1 using the Euler-Lagrange equation. After applying the Euler-Lagrange equation on the strain energy expression, terms coming from the underlined and double underlined terms of equation 5.36 are neglected due to St. Venant assumption (underlined), and the fact that ϵ' is neglected to this level of approximation (double underlined). This results in the following relation between \mathbf{w}_1 , ϵ_0 , and ϵ_1

$$\mathbf{K}_{00}\mathbf{w}_1 = (\mathbf{H}_1 + \mathbf{K}_{10}\mathbf{V}_0)\epsilon'_0 - \mathbf{H}_0\epsilon_1, \quad (5.37)$$

so that the solution for the second approximation of the warping displacement is given by

$$\mathbf{w}_1 = \mathbf{V}_1\epsilon'_0 + \mathbf{V}_0\epsilon_1, \quad (5.38)$$

where

$$\mathbf{K}_{00}\mathbf{V}_1 = (\mathbf{H}_1 + \mathbf{K}_{10}\mathbf{V}_0). \quad (5.39)$$

In order to prove that the second approximation of the strain expression gives the correct shear forces, components of the second approximation of the stress resultants that contribute to the shear forces are integrated over the cross-section (see equation 5.40).

$$\mathbf{v} = \int_s \mathbf{R}_v^t \mathbf{B}_1^t \mathbf{C} (\mathbf{G}\epsilon_1 + \mathbf{B}_0\mathbf{w}_1) ds = [\mathbf{r}_2, \mathbf{r}_3]^t (\mathbf{H}_1\epsilon_1 + \mathbf{K}_{10}\mathbf{w}_1), \quad (5.40)$$

where \mathbf{v} is a vector containing the two shear forces, and \mathbf{R}_n contains the two transverse rigid body modes. Using the relation between \mathbf{B}_0 and \mathbf{B}_1 given in equation 5.8, the shear force resultants are expressed in terms of the two bending modes, as shown here

$$\mathbf{v} = [-\mathbf{r}_6, \mathbf{r}_5]^t (\mathbf{H}_0\epsilon_1 + \mathbf{K}_{00}\mathbf{w}_1). \quad (5.41)$$

Substituting the expression for $\mathbf{K}_{00}\mathbf{w}_1$ from equation 5.37 into 5.41 and using the fact that $[-\mathbf{r}_6, \mathbf{r}_5]^t = \mathbf{E}^t \mathbf{R}_e^t$, the shear forces are given as a function of ϵ'_0 only, i.e.

$$\mathbf{v} = \mathbf{E}^t \mathbf{R}_e^t (\mathbf{H}_1 + \mathbf{K}_{10}\mathbf{V}_0) \epsilon'_0, \quad (5.42)$$

where

$$\mathbf{E}^t = \begin{bmatrix} 0 & 0 & -1 & 0 \\ 0 & 1 & 0 & 0 \end{bmatrix}. \quad (5.43)$$

Multiplying the Euler forces given in equation 5.31 with \mathbf{E}^t and taking the derivative with respect to x yields the same expression for the shear forces as in equation 5.42, proving that the second approximation of the warping function does indeed give the correct expression for the shear forces.

Now that it is proven that the second approximation of the warping function indeed gives the correct shear forces, a relation between ϵ_1 and ϵ'_0 is obtained using the fact that Euler forces calculated from the second approximation of the generalized shell strains ($\Gamma_1 - \Gamma_0$) are zero.

$$F_e^1 = \int_s R_e^t B_1^t C (G\epsilon_1 + B_0 w_1) ds = R_e^t (H_1 + K_{10} V_0) \epsilon_1 + R_e^t K_{10} V_1 \epsilon'_0 = 0. \quad (5.44)$$

By comparing the expression for the Euler stiffness matrix (S_e) in equation 5.29 to the expression for the Euler force resultant (F_e) in equation 5.31, it can be shown that

$$S_e = R_e^t (H_1 + K_{10} V_0) \quad \text{and} \quad H_0^t = R_e^t K_{10}. \quad (5.45)$$

Substituting the relations given in 5.45 into equation 5.44 gives the following relation between ϵ_1 and ϵ'_0

$$S_e \epsilon_1 + H_0^t V_1 \epsilon'_0 = 0. \quad (5.46)$$

The strain energy is formulated in terms of the force resultants rather than the strains. Therefore, the following three compatibility equations are needed that relate the cross-sectional force vector: $f = \{f_1 \ f_2 \ f_3 \ m_1 \ m_2 \ m_3\}^t$ to ϵ_0 and ϵ'_0

$$S_e \epsilon_0 = f_e \quad S_e \epsilon'_0 = E^t v \quad S_e \epsilon_1 + P \epsilon'_0 = 0, \quad (5.47)$$

where

$$f_e = \{f_1 \ m_1 \ m_2 \ m_3\}^t \quad v = \{f_2 \ f_3\}^t \quad P = H_0^t V_1. \quad (5.48)$$

Substituting equation 5.47 together with the warping solutions (w_0, w_1) into the expression for the total shell strain of equation 5.34, yields the following expression for the shell strains in terms of the force resultants

$$\Gamma_1 = \left((G + B_0 V_0) S_e^{-1} I_e + (B_0 V_1 - (G + B_0 V_0) S_e^{-1} P) S_e^{-1} E^t I_s \right) f. \quad (5.49)$$

The definitions of I_e and I_s are shown in figure 5.2. Finally, substituting equation 5.49 into equation 5.36, the strain energy per unit length is written in terms of the cross-sectional force vector f and the Timoshenko compliance matrix. Subsequently, taking the inverse of the compliance yields an expression for the Timoshenko stiffness matrix as shown in equation 5.50.

$$S = \left(I_e^t S_e^{-1} I_e + I_s^t S_s^{-1} I_s - I_e^t S_{es}^{-t} I_s - I_s^t S_{es}^{-1} I_e \right)^{-1}, \quad (5.50)$$

where

$$S_e^{-1} = \left(F + H_0^t V_0 \right)^{-1},$$

$$S_s^{-1} = E S_e^{-1} \left(V_1^t K_{00} V + P^t S_e^{-1} P \right) S_e^{-1} E^t,$$

$$\text{and } S_{es}^{-1} = S_e^{-1} P S_e^{-1} E^t \quad (5.51)$$

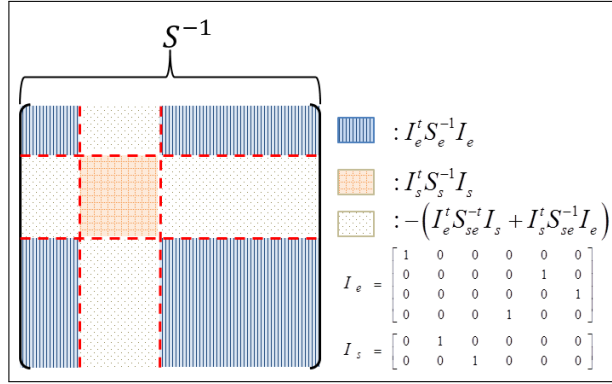


Figure 5.2: Components of the compliance matrix

5.4. VALIDATION OF SECTIONAL STIFFNESS CONSTANTS

This section presents a comparison of numerical results between the present method and available literature. First the stiffness properties, for a family of closed cross-sections, is compared with the results from [110]. Followed by comparison of the stiffness properties of open cross-sections, with results from [80]. Finally a comparison with experimental data [47] is performed for a set of box beams.

5.4.1. CLOSED CROSS-SECTION

A convergence test is first performed to determine the minimum number of elements required to obtain converged solution for the present method. The convergence error (ϵ) is calculated using the Richardson extrapolation method described in [28] as,

$$\epsilon = \frac{S_{ij} - S_{ij_{extrap}}}{S_{ij_{extrap}}}, \quad (5.52)$$

where S_{ij} is a component of the Timoshenko stiffness matrix calculated using the present method. The error estimation is performed on the Timoshenko stiffness matrix of a rectangular cross-section (figure 5.3b), with stacking sequence of layup 1 and corresponding ply properties given in table 5.1. Figure 5.3a shows the relative error (ϵ) against $\frac{t}{h}$, where t and h are respectively, the minimum skin thickness of the cross-section and element size. The figure contains the relative error for a number of components of the Timoshenko stiffness matrix. From figure 5.3a, it can be concluded that converged solution is achieved ($\epsilon < 1e^{-2}\%$) for $\frac{t}{h} = 0.8$. This amounts roughly to 80 elements for the rectangular cross-section shown in figure 5.3b, and skin thickness of $0.03mm$. Therefore, for all comparison studies performed in this paper, $\frac{t}{h} = 0.8$, is used to determine the amount of elements needed for con-

verged results.

Table 5.1: Dimension and material properties of a box beam

Dimension				
	a	0.53	in	
	b	0.953	in	
	t	0.03	in	
Ply properties				
	E ₁₁	20.59×10 ⁶	psi	
	E ₂₂	1.42×10 ⁶	psi	
	G ₁₂	0.87×10 ⁶	psi	
	ν ₁₂ ⁺	0.3/0.42	[-]	
Layups				
Layup	Upper wall	Lower wall	Left wall	Right wall
1	[15] ₆	[15] ₆	[15] ₆	[15] ₆
2	[(30,0)] ₃	[(30,0)] ₃	[(30,0)] ₃	[(30,0)] ₃
3	[15] ₆	[-15] ₆	[±15] ₆	[±15] ₆

⁺Poisson's ratio is 0.3 for layup 1 and 0.42 for layup 2 and 3 in accordance with [32]

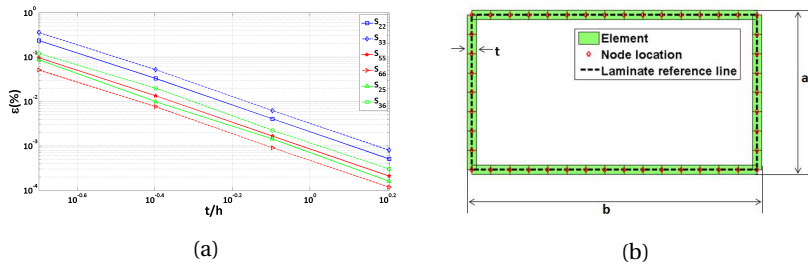


Figure 5.3: 5.3a Plot of the Convergence error against t/h , for a rectangular cross section with stacking sequence of layup 1; 5.3b Geometry of rectangular cross-section.

The Timoshenko stiffness matrix from the present method is compared with the results of VABS [32] and NABSA [50]. The results from NABSA are used as a benchmark in the present study. A rectangular box with dimensions and material properties given in figure 5.3b and table 5.1 respectively, is used for comparison. The present method uses 80 beam elements to generate converged results compared to NABSA which uses 216 planar quadrilaterals (8 nodes per element) and VABS 289 planar quadrilaterals (6 or 8 nodes per elements). In addition to the results of the Timoshenko stiffness constants, components of the Euler stiffness constants are calculated for the results from the literature using static condensation on the two transverse shear rows and columns, which is equivalent to the Euler stiffness constants given in equation 5.29.

The relative difference of the energy norm is a measure of how well the strain energy is captured by the two methods (Present and VABS) compared to NABSA, and is given by,

$$\delta_e = |\lambda - 1|_{max}, \quad (5.53)$$

where λ is the generalized Eigen-value solution of the difference in the energy norm with respect to NABSA, defined as,

$$(\mathbf{S} - \lambda \mathbf{S}_{NABSA})\epsilon = \mathbf{0}, \quad (5.54)$$

where \mathbf{S} is the stiffness matrix calculated using the present method or VABS, and \mathbf{S}_{NABSA} is the stiffness matrix calculated using NABSA.

The relative difference for the Timoshenko stiffness matrix and its reduced equivalent is given in table 5.2. From this table it is evident that the present method captures the strain energy comparable to VABS in case the transverse shears are taken into account (Timoshenko stiffness matrix). However, for the reduced stiffness matrix (Euler stiffness), VABS performs better in general.

Table 5.2: Relative error(%) of the Timoshenko stiffness matrix and its reduced equivalent

Layup	$S_{6 \times 6}$ Present	$S_{4 \times 4}$ Present	$S_{6 \times 6}$ VABS	$S_{4 \times 4}$ VABS
1	5.03	2.44	45.80	5.30
2	5.04	3.98	12.03	0.20
3	8.24	4.00	80.40	1.80

Next, the stiffness constants of the Timoshenko stiffness matrix and its reduced equivalent are shown in tables 5.3, 5.4, and 5.5, for the three layups given in table 5.1. The 3rd and 6th columns of each table contain the stiffness coefficients calculated using VABS, whereas the 4th and 7th columns contain the stiffness coefficients calculated using the present method. The stiffness components of the reduced stiffness matrix are denoted as $NABSA_R$, $VABS_R$, and $Present_R$. The values in brackets are the relative errors of VABS and the present method with respect to NABSA.

Table 5.3: Comparison of stiffness coefficients for layup 1

Stiffness Coefficients	NABSA	VABS(%)	Present(%)	$NABSA_R$	$VABS_R$ (%)	$Present_R$ (%)
$S11 \times 10^7$	0.1438	0.1432(-0.42)	0.1437(-0.04)	0.1438	0.1432(0.4)	0.1437(-0.04)
$S14 \times 10^6$	0.1075	0.1060(-1.40)	0.1073(-0.16)	0.1075	0.1060(1.4)	0.1073(-0.16)
$S22 \times 10^5$	0.9018	0.5113(-43.10)	0.9293(3.04)	-	-	-
$S25 \times 10^5$	-0.5204	-0.2951(43.29)	-0.5438(-4.50)	-	-	-
$S33 \times 10^5$	0.3932	0.2132(-45.8)	0.3838(-2.38)	-	-	-
$S36 \times 10^5$	-0.5637	-0.2989(47.0)	-0.5662(-0.45)	-	-	-
$S44 \times 10^5$	0.1678	0.1689(0.60)	0.1656(-1.34)	0.1678	0.1689(-0.7)	0.1656(-1.34)
$S55 \times 10^5$	0.6622	0.5513(-16.7)	0.6735(1.71)	0.3619	0.3810(-5.3)	0.3552(-1.84)
$S66 \times 10^6$	0.1726	0.1365(-20.9)	0.1731(0.28)	0.09179	0.09460(-3.1)	0.08960(-2.44)

In table 5.3, the stiffness constants for layup 1 are shown. In the case of the Timoshenko stiffness matrix, the present method overestimates the bending coefficients by 1.71% and 0.28% respectively, compared to the results from NABSA. For the transverse shear coefficients and coupling between transverse shear and bending, the difference between the present method and NABSA are between -4.5% and 3%. For the reduced stiffness constants, the relative error for the present method is less than three percent.

The stiffness constants for the second layup are given in table 5.4. For this layup, results from VABS are almost identical to NABSA for the diagonal

Table 5.4: Comparison of stiffness coefficients for layup 2

Stiffness Coefficients	NABSA	VABS(%)	Present(%)	NABSA _R	VABS _R (%)	Present _R (%)
S11×10 ⁷	0.125	0.125(0.0)	0.124(-1.13)	0.125	0.125(0.0)	0.124(-1.13)
S14×10 ⁵	0.521	0.521(0.0)	0.514(-1.40)	0.521	0.521(0.0)	0.514(-1.40)
S22×10 ⁵	0.981	0.871(-11.2)	0.979(-0.24)	-	-	-
S25×10 ⁵	-0.264	-0.234(11.4)	-0.263(0.28)	-	-	-
S33×10 ⁵	0.424	0.373(-12.0)	0.405(-4.44)	-	-	-
S36×10 ⁵	-0.278	-0.244(12.2)	-0.276(0.84)	-	-	-
S44×10 ⁵	0.177	0.177(0.0)	0.171(-3.70)	0.177	0.177(0.0)	0.171(-3.70)
S55×10 ⁵	0.614	0.606(-1.30)	0.593(-3.37)	0.543	0.543(0.0)	0.523(-3.77)
S66×10 ⁶	0.152	0.150(-1.32)	0.150(-1.48)	0.134	0.134(0.0)	0.131(-2.08)

Table 5.5: Comparison of stiffness coefficients for layup 3

Stiffness Coefficients	NABSA	VABS(%)	Present(%)	NABSA _R	VABS _R (%)	Present _R (%)
S11×10 ⁷	0.137	0.137(0.0)	0.138(0.84)	0.099	0.099(0.0)	0.098(-0.42)
S12×10 ⁶	-0.184	-0.184(0.0)	-0.190(-3.17)	-	-	-
S13×10 ³	0.144	1.730(1122.2)	0.009(-93.49)	-	-	-
S22×10 ⁵	0.884	0.883(-0.1)	0.904(2.26)	-	-	-
S23×10 ²	-0.821	-8.420(-925.6)	-0.045(94.56)	-	-	-
S33×10 ⁵	0.395	0.775(80.4)	0.428(8.24)	-	-	-
S44×10 ⁵	0.173	0.174(0.6)	0.167(-3.38)	0.173	0.173(0.0)	0.167(-3.38)
S45×10 ⁵	0.180	0.180(0.0)	0.175(-2.59)	0.180	0.180(0.0)	0.175(-2.59)
S46×10 ³	0.358	-0.362(-201.12)	0.000(-100)	0.358	-0.362(201.1)	0(-100)
S55×10 ⁵	0.608	0.608(0.0)	0.591(-2.88)	0.608	0.608(0.0)	0.591(-2.88)
S56×10 ³	0.377	-0.372(-198.67)	0.000(-100)	0.377	-0.372(198.7)	0(-100)
S66×10 ⁶	0.143	0.143(0.0)	0.141(-1.43)	0.143	0.143(0.0)	0.141(-1.43)

components of the Euler stiffness matrix (extension, bending, and torsion). Although the stiffness constants from the present method are not identical with NABSA, for the aforementioned stiffness constants, the error is still less than four percent. The transverse shear coefficients and the coupling terms between transverse shear and bending are less than 4.5% for the present method. The fact that rotation of the shell normal is taken into account for the present method, it influenced the results for transverse shear coefficients beneficially. This is reflected back in the relative error of the energy norm shown in table 5.2. The same trend is also observed for the third layup (see table 5.5).

From the results shown in tables 5.3 to 5.5, it can be concluded that the present method performs well in calculating the stiffness constants (Euler or Timoshenko). The relative error of the diagonal stiffness constants is less than ten percent, which is sufficient for a tool intended for preliminary design phase. In addition, the various coupling terms are also calculated with reasonable accuracy. However, the present method does not have the same level of detail in retrieving the stress distribution across the cross section, as compared to VABS and NABSA.

5.4.2. OPEN CROSS-SECTION

For open cross-sections, the work of [80] is used to assess the performance of the present method. The method considers Saint-Venant's solutions for prismatic beams; which uses semi-analytical finite element analysis of a 3D structure to determine the stiffness constants of anisotropic, and heterogeneous beams, making it suitable for use as a benchmark. Two open cross-sections

are considered: L-shaped, and C-shaped sections. The L-shaped section has a width of 1 and a height of 1.5. The C-shaped section has a height of 1, and a width of 0.75 at the top, and 1.5 at the bottom. Figures 5.4a and 5.4b show the dimensions and the way the sections are modelled for the present analysis. Both sections have a skin thickness of 0.1. The origin is taken at the bottom

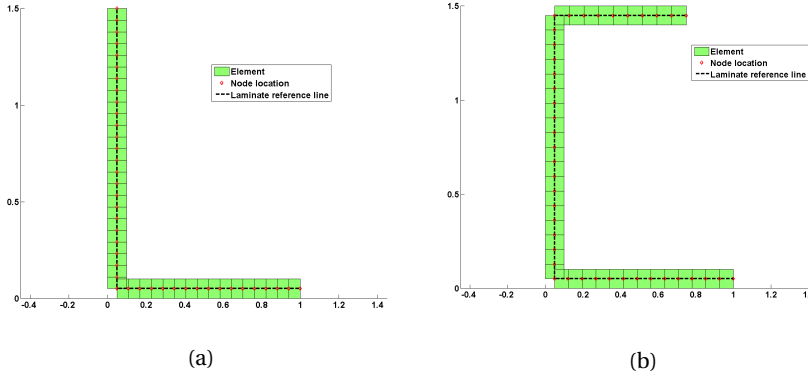


Figure 5.4: 5.4a L-shaped geometry; 5.4b C-shaped geometry.

left corner for both cases. Both sections are composed of two ply sheets with $\pm 30^\circ$ ply angles, and 0.05 ply thickness. The material properties used for comparison are variation of graphite epoxy composite, i.e.

$$\frac{E_{22}}{E_{11}} = 10; \quad \frac{G_{12}}{E_{11}} = 0.4; \quad \nu_{12} = 0.3 \quad .$$

Based on the results from the convergence study, both cross-sections are discretized using 40 beam elements. The comparison of results is limited to Euler stiffness constants, because [80] contains only Euler stiffness results for both cases. The stiffness constants for the L-shaped section are given in table 5.6. The columns contain the results of Kosmatka and the present method respectively. The last column contains the relative difference between the present method and Kosmatka. The diagonal terms are predicted fairly close to the results from [80]. The off diagonal terms have a maximum difference less than 15 percent which is not that bad for a tool intended for initial design/optimization of slender structures. Table 5.7 contains the stiffness constants of the C-shaped section. The results for this cross-section are not as good as the previous one; especially, the stiffness constants for the two bending moments are over predicted by 30% to 36%, and the coupling terms have relative error between 7% to 78%. On the other hand, the stiffness constant for torsion (K_{22}) has a relative difference of only 6.6% (which is consistent for both sections). One explanation for the decrease in performance for the channel section (C-section) is that the cross-section is not completely thin-walled. The thickness to width ratio for the top wall is more than 13%. This means that thin walled assumption is not totally accurate in this case. This might explain

the difference in results, since the present method is based on shell theory. Another explanation might be that the results from [80] are not converged results for the C-section; because the stiffness matrix shown in [80] for the C-section is not symmetric. Furthermore, there is no mention of convergence test in [80].

Table 5.6: Comparison of stiffness coefficients for L shaped cross-section

Stiffness Coefficients $\times \frac{E_{11}}{10^3}$	Kosmatka	Present	Difference(%)
S11	871.14	889.52	2.11
S22	399.34	422.35	5.76
S33	116.37	126.49	8.70
S44	1.20	1.28	6.67
S12	421.98	438.49	3.91
S13	202.58	213.87	5.57
S14	-19.17	-20.43	-6.57
S23	29.07	30.37	4.47
S24	-9.12	-9.97	-9.32
S34	-4.30	-4.86	-13.02

Table 5.7: Comparison of stiffness coefficients for C shaped cross-section

Stiffness Coefficients $\times \frac{E_{11}}{10^3}$	Kosmatka	Present	Difference(%)
S11	1014,44	1141,9	12,56
S22	686,17	932,8	35,94
S33	137,55	179,2	30,28
S44	1,52	1,62	6,58
S12	624,75	790,9	26,59
S13	253,92	317,8	25,16
S14	-28,25	-26	7,96
S23	101,33	181	78,62
S24	-22,41	-18	19,68
S34	-7,75	-7,2	7,10

5.4.3. COMPARISON WITH EXPERIMENTAL RESULT

A comparison of the sectional stiffness constants is performed between the present method and experimental data, for a family of boxed beams [47]. A composite beam of length $0.77m$ with an open rectangular cross-section is clamped at the root and loaded at the tip with pure bending of $0.4KNm$ or pure torsion of $0.2KNm$. The cross-section is composed of two flanges of uni-directional (UD) ply with $3.5mm$ thickness and two shear webs with C-profile made of biaxial ($\pm 45^\circ$) ply. The flanges and shear webs are bonded together with epoxy of $1.5mm$ thickness (see figure 5.5a). The cross-sectional dimensions are given in table 5.8, whereas the (nominal) material properties are given in table 5.9. For the present analysis, the cross-section is discretized using 90 elements for converged results based on the convergence analysis of section 5.4.1. Three laminates are used to define the material properties of the cross section (see figure 5.5b), namely: a laminate for the shear webs, and two laminates for the outer and mid section of the flanges. The laminate for

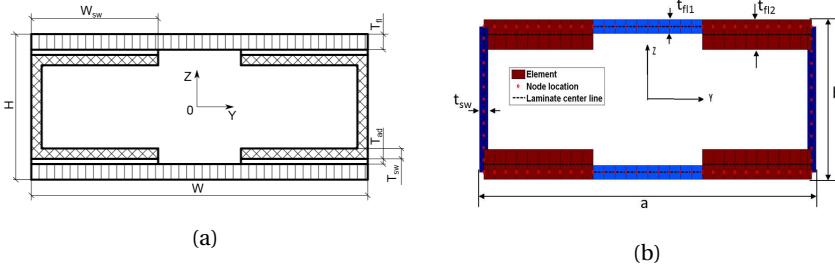


Figure 5.5: 5.5a Dimension of a rectangular cross-section used in [47]; 5.5b Discretization of the rectangular cross-section used in the present analysis(each colour represents a laminate).

Table 5.8: Dimension of the box beam from figure 5.5a.

Dimension		
W	100	mm
H	40	mm
W_{sw}	30	mm
T_{fl}	3.5	mm
T_{sw}	2.5	mm
T_{ad}	1.5	mm
Dimension of Discretized cross-section		
a	97.5	mm
b	36.3	mm
t_{fl1}	3.5	mm
t_{fl2}	7.5	mm
t_{sw}	2.5	mm

Table 5.9: Material properties the box beam

Ply properties UD ply		
E_{11}	42.68	GPa
E_{22}	8	GPa
G_{12}	4.96	GPa
ν_{12}	0.26	[-]
Ply properties of the Biaxial ply		
E_{11}	9.22	GPa
E_{22}	9.22	GPa
G_{12}	10.55	GPa
ν_{12}	0.26	[-]
Material properties of the adhesive		
E_{11}	4.56	GPa
E_{22}	-	GPa
G_{12}	-	GPa
ν_{12}	0.3	[-]

the shear webs is composed of the biaxial ply, whereas the laminate for the outer parts of the flanges is composed of the UD ply, adhesive, and the biaxial ply. The laminate for the mid section of the flanges is composed solely of

the UD ply. Three beam configuration where manufactured by biasing the UD ply of both flanges with respect to the beam axis with 0° , 15° and 25° . Two specimens where manufactured for each configuration. In addition to the experimental results, [47] contains finite element analysis (FEA) of a cantilever box beam loaded at the tip with pure bending or torsion, for all configurations used in the experiment. The finite element model is discretized using continuum-shell elements.

Since the present method solves the outer solution of the 3D elasticity problem, the stiffness properties calculated from the experiments and FEA are sampled at mid section of the beam, far away from the applied load and boundary. Figure 5.6a and 5.6b show respectively, a bar chart of the stiffness constants EI and GJ for the experimental results of the two specimens (EXP1 & EXP2), FEA and the present method. Figure 5.6c shows a bar chart of the bend-twist coupling coefficient (β).

The bending stiffness, calculated with the present method, matches well with the experimental results and the FEA analysis, with a maximum difference less than 10%. The bend-twist coupling coefficient (β) matches quite well with the reference values, having an average difference less than 5%. For the torsional stiffness, the difference between the present method and experimental results is roughly 17% for the 0° angle. This difference may be caused because, for the 0° configuration the shear stiffness of the two flanges is matrix dominated. As the box beam is loaded in torsion, the shear stiffness of the matrix decreases due to non-linearity in the material properties of the matrix. This results in the reduced shear stiffness calculated from the experiments, whereas the numerical analysis uses the nominal material properties given in table 5.9. The difference tends to decrease for increased bias of the UD laminates with respect to the beam axis, as seen in figure 5.6b, which is expected since the shear stiffness of the two flanges starts to be dominated by the property of the fibre.

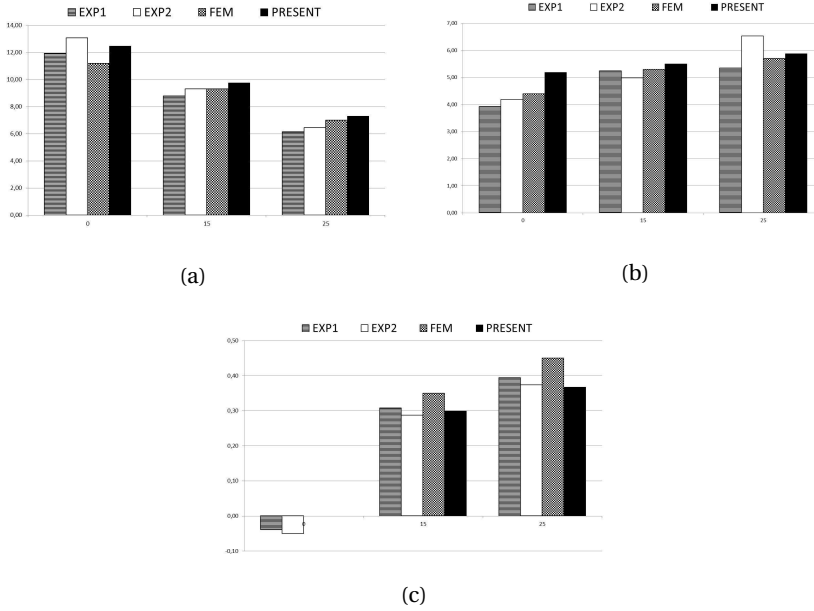


Figure 5.6: Comparison of: 5.6a EI, 5.6b GJ, and 5.6c bend-twist coupling coefficient(β) between experiments(EXP1 and EXP2), FEA and present method, for three fibre angles of 0,15 and 25 degrees.

5.5. SUMMARY

A formulation for computationally efficient method of modelling the cross-sectional properties is presented for thin-walled, multi cell, and prismatic beams with anisotropic material properties. The formulation is based on classical laminate theory which makes it suitable for use in composite optimisation. The finite element method is then employed to discretize the cross-section using one-dimensional hermitian beam elements.

The proposed method requires significantly less elements (in the order of a hundred) compared to solid models such as NABSA and VABS. The results from the present method are compared with literature results for a family of closed and open cross-section. Using NABSA stiffness results for closed cross-sections as a benchmark, the energy norm error in the Euler-Bernoulli model is less than 5% and for the Timoshenko model it is less than 10%. The method does not perform as well for the relatively thick open cross-sections considered in [80]. Comparison with experimental data for a bending-torsion coupled beam shows average relative errors less than 10% compared to both the experimental measurements and detailed three-dimensional finite element calculations. It may be concluded that the present method is suitable for use during the preliminary design/optimization of slender structures with thin-walled cross-sections and anisotropic material properties.

6

GEOMETRICALLY EXACT BEAM MODEL

This chapter presents a structural model to evaluate the non-linear deformation of large wind turbine blades. The structural model is composed of a beam model that is based on the isogeometric formulation of a geometrically exact 3D beam theory. The beam model uses quaternions to parametrize the rotation variable together with the isoparametric interpolation of the rotation parameters, defined at control points.

Section 6.1 presents a literature review on geometrically exact beam theory and IGA formulation to calculate the non-linear deformation of composite beams. A summary of Simo-Reissner non-linear 3D beam theory is elucidated in section 6.2. In section 6.3, the isogeometric implementation of the Simo-Reissner non-linear 3D beam theory is presented, followed by several numerical examples, presented in section 6.4.

6.1. INTRODUCTION

Among the earlier application of IGA in structural problems, [38] demonstrates the use of Isogeometric analysis for solving structural vibrations. Several examples are presented to demonstrate the performance of IGA in structural problems by using multiple models consisting of rods, beams, membranes, plates, and three-dimensional solids. An approach based on IGA for assessing the vibration of Timoshenko beam is presented in [82], while [136] presented a vibration analysis of non-linear Euler-Bernoulli beam using isogeometric formulation. Furthermore, [20] proposes a shear-locking free isogeometric formulation of curved and planar Timoshenko beams.

Recently IGA collocation method is used in the formulation of initially straight and planar Timoshenko beams [42], curved spatial rods [7], single-parameter formulation of planar shear deformable beams [75], and plate models [113] that describe thin-walled structures. Isogeometric collocation approach, proposed in [8], consists of the discretization of the governing partial differential equations in the strong form using the isoparametric paradigm and the higher-continuity properties of the IGA shape functions.

All the beam models mentioned here are either limited to a planar case or are based on the kinematic assumption of small displacements and rotations. To the author's best knowledge, there is no isogeometric beam formulation for solving the geometrically exact 3D beam theory.

A three dimensional non-linear rod theory is first proposed by Simo [123] together with its finite element implementation in [124]. The kinematic variable of a non-linear beam theory consists of the displacements and rotations at every point in the model, where the rotation variables belong to a non-linear manifold. since the rotation variables are part of a non-linear manifold, they require special attention when solving the geometrically exact 3D beam theory. Consequently, several publications [4, 13, 17] are dedicated on this subject. Several parametrization methods for the rotation manifold have been proposed, where a review on the parametrization of rotations is given in [4]. One of the obstacles in a finite element or isogeometric analysis of geometrically non-linear beams is that the standard interpolation of rotations results in the loss of orthogonality of the rotation variables at the integration points, which is a fundamental property of the non-linear 3D beam theory. An assessment of the most common interpolation schemes for rotations and their implementation in finite element models of geometrically exact 3D beams can be found in [117].

This chapter presents a Galerkin-based isogeometric implementation of geometrically exact 3D beam theory. Furthermore, quaternions are employed to parametrize the rotation manifold together with the isoparametric interpolation of the rotation parameters defined at the control points. The interpolated quaternions are orthogonalized to represent rotations.

6.2. GEOMETRICALLY EXACT 3D BEAM MODEL

This section gives a brief overview of geometrically exact 3D beam theory. The reader is advised to see [68, 39] for a detailed description on the subject.

GEOMETRY DESCRIPTION

A 3D beam may be defined as a series of cross-sections connected by a beam axis. Two beam configurations (initial and deformed) with arbitrary cross-sections are shown in figure 6.1. The inertial reference frame denoted by (X, Y, Z) is spanned by the right-handed orthonormal base vectors:

$$\mathbf{e}_1 = \{1 \ 0 \ 0\}^t, \quad \mathbf{e}_2 = \{0 \ 1 \ 0\}^t, \quad \text{and} \quad \mathbf{e}_3 = \{0 \ 0 \ 1\}^t. \quad (6.1)$$

The initial configuration of the beam axis is defined as $\mathbf{r}_0(x); x \in [0, L] \subset \mathbb{R}$,

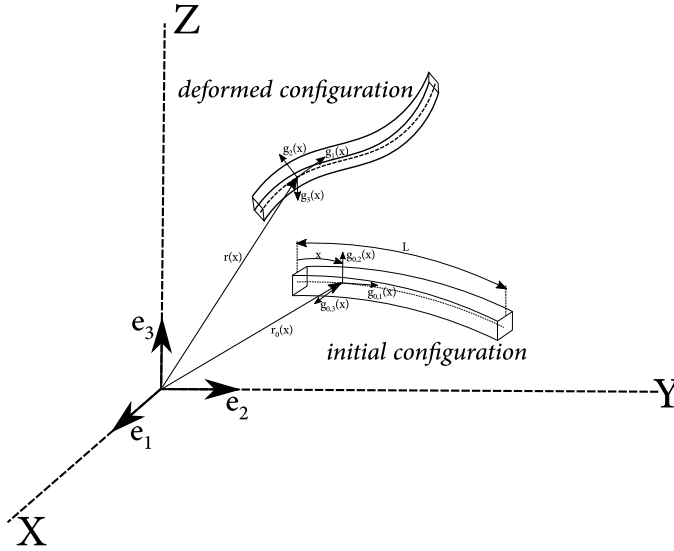


Figure 6.1: Kinematics of initial and deformed configuration of a curved beam

\mathbb{R} , where x is the arc-length of the beam axis in the initial configuration, and L is the beam length in the initial configuration. The cross-sections in the initial configuration are assumed to be orthogonal to the beam axis. Consequently, the body attached base vector normal to the cross-section ($\mathbf{g}_{0,1}$) is tangent to the beam axis, and the remaining two base vectors ($\mathbf{g}_{0,2}, \mathbf{g}_{0,3}$) are orthogonal to the beam axis, i.e.:

$$\mathbf{g}_{0,1} = \frac{\mathbf{r}'_0}{\|\mathbf{r}'_0\|}, \quad \mathbf{g}_{0,1} \cdot \mathbf{g}_{0,2} = 0, \quad \text{and} \quad \mathbf{g}_{0,3} = \mathbf{g}_{0,1} \times \mathbf{g}_{0,2}, \quad (6.2)$$

where the prime $()'$ denotes derivative with respect to the arc-length x . Furthermore, the orthonormal base vectors $\mathbf{g}_{0,i}$, for $i = 1 \dots 3$, are related to the

inertial base vectors \mathbf{e}_i through the linear transformation $\Lambda_0(s) \in \mathbf{SO}(3)$ as $\mathbf{g}_{0,i} = \Lambda_0 \mathbf{e}_i$, $i = 1 \dots 3$. $\mathbf{SO}(3)$ is a Lie group of proper orthogonal transformations having the properties: $\det \Lambda = 1$ and $\Lambda \Lambda^t = \mathbf{I} \forall x \in [0, L]$, where \mathbf{I} is a 3 by 3 identity matrix. The initial configuration of the beam axis, for all values of x , is completely determined by the initial position vector of the beam axis and the orthonormal frame attached to the cross-section, i.e. $x \mapsto C_0 = (\mathbf{r}_0, \Lambda_0) \in \mathbb{R}^3 \times \mathbf{SO}(3)$.

The beam axis in the deformed configuration is defined by a curve $x \mapsto \mathbf{r}(x) \in \mathbb{R}^3$. The cross-sections of the beam in the deformed configuration are defined by the right-handed orthonormal base vectors \mathbf{g}_i , $i = 1 \dots 3$, where \mathbf{g}_1 is not necessary tangent to the beam axis of the deformed configuration. The orthonormal base vectors \mathbf{g}_i are related to the inertial base vectors \mathbf{e}_i through the linear transformation $\Lambda(s) \in \mathbf{SO}(3)$ as $\mathbf{g}_i = \Lambda \mathbf{e}_i$, for $i = 1 \dots 3$. The deformed configuration of the beam axis, for all values of x , is completely determined by the position vector of the beam axis $\mathbf{r}(s)$ and the orthogonal frame attached to the cross-section, i.e. $x \mapsto C = (\mathbf{r}, \Lambda) \in \mathbb{R}^3 \times \mathbf{SO}(3)$.

KINEMATIC EQUATIONS

The strain measures, defined with respect to the body-attached frame, at a given cross-section are related to the beam configuration C_0 through the following relations [39]:

$$\boldsymbol{\gamma} = \Lambda^t \mathbf{r}' - \mathbf{e}_1 \quad \text{and} \quad \hat{\boldsymbol{\kappa}} = \Lambda^t \Lambda' - \Lambda_0^t \Lambda_0', \quad (6.3)$$

where $\boldsymbol{\gamma}$ is the translational strain measure and $\hat{\boldsymbol{\kappa}}$ is the skew symmetric matrix of the rotational strain measure $\boldsymbol{\kappa}$. The position vector of the beam axis in the deformed configuration is expressed as: $\mathbf{r}(s) = \mathbf{r}_0(s) + \mathbf{u}(s)$, where $\mathbf{u}(s)$ is the displacement vector of the beam axis. Similarly, $\Lambda(s)$ is expressed as: $\Lambda(s) = \mathbf{R}(s)\Lambda_0(s)$, where $\mathbf{R}(s)$ is a rotation matrix that maps the orthonormal base vectors in the initial configuration ($\mathbf{g}_{0,i}$) unto the orthonormal base vectors in the deformed configuration (\mathbf{g}_i). Substituting the expressions for \mathbf{r} and Λ , in terms of \mathbf{u} and \mathbf{R} , into the expression for the strain measure of equation 6.3 yields:

$$\boldsymbol{\gamma} = \Lambda_0^t (\mathbf{R}^t \mathbf{u}' + (\mathbf{R}^t - \mathbf{I}) \mathbf{r}_0') \quad \text{and} \quad \hat{\boldsymbol{\kappa}} = \Lambda_0^t \mathbf{R}^t \mathbf{R}' \Lambda_0. \quad (6.4)$$

CONSTITUTIVE EQUATIONS

The strain measures (translation and rotation) are related to the stress and stress-couple resultants \mathbf{N} and \mathbf{M} respectively, through the sectional stiffness constants as:

$$\begin{Bmatrix} \mathbf{N} \\ \mathbf{M} \end{Bmatrix} = \mathbf{S} \begin{Bmatrix} \boldsymbol{\gamma} \\ \boldsymbol{\kappa} \end{Bmatrix}, \quad (6.5)$$

where \mathbf{S} is a six by six matrix containing the sectional stiffness constants.

EQUILIBRIUM EQUATIONS

Assuming an external distributed load comprised of forces (\mathbf{f}) and torques (\mathbf{t}), the strong form of the equilibrium equations, expressed in the material form, are given as [39]:

$$(\mathbf{\Lambda N})' + \mathbf{f} = \mathbf{0} \quad \text{and} \quad (\mathbf{\Lambda M})' + \mathbf{r}' \times \mathbf{\Lambda N} + \mathbf{t} = \mathbf{0}. \quad (6.6)$$

The weak form of the equilibrium equations is derived from the variation of the potential energy. The potential energy is the sum of the strain energy and the work done by the external loads, expressed mathematically as:

$$\Pi = \mathcal{U} + \mathcal{V}, \quad (6.7)$$

where \mathcal{V} is the work done by external loads and \mathcal{U} is the strain energy given by:

$$\mathcal{U} = \frac{1}{2} \int_0^L (\mathbf{N}^t \boldsymbol{\gamma} + \mathbf{M}^t \boldsymbol{\kappa}) dx, \quad (6.8)$$

and L is the beam length in initial configuration. The first and second variation of the strain energy is given in terms of the variation of the strain measures as:

$$\delta \mathcal{U} = \int_0^L (\mathbf{N}^t \delta \boldsymbol{\gamma} + \mathbf{M}^t \delta \boldsymbol{\kappa}) dx, \quad \text{and} \quad \delta^2 \mathcal{U} = \int_0^L (\delta \mathbf{N}^t \delta \boldsymbol{\gamma} + \delta \mathbf{M}^t \delta \boldsymbol{\kappa} + \mathbf{N}^t \delta^2 \boldsymbol{\gamma} + \mathbf{M}^t \delta^2 \boldsymbol{\kappa}) dx, \quad (6.9)$$

where $\delta \boldsymbol{\gamma}$ and $\delta \boldsymbol{\kappa}$ are the first variation of the strain measures.

6.3. ISOGEOMETRIC FORMULATION

The weak form of the equilibrium equations are solved using the Galerkin-based isogeometric analysis. Within the isogeometric formulation, the control points represent the degrees of freedom and the knots spans are considered as elements. For the present method, NURBS are used as basis functions. Numerical integration is performed using the Gauss quadrature at the element level. Further details on isogeometric analysis can be found in [36].

6.3.1. APPROXIMATION OF THE DISPLACEMENT AND ROTATION VARIABLES

Before defining the expressions for the generalized load vector \mathbf{f} and tangent stiffness matrix \mathbf{K} , the displacement vector \mathbf{u} and the rotation matrix \mathbf{R} need

to be parametrized. The displacement vector $\mathbf{u}(\xi)$ is approximated by the function $\mathbf{u}^h(\xi)$ as:

$$\mathbf{u}^h(\xi) = \sum_{i=1}^{N_{cp}} N_{i,p}(\xi) \bar{\mathbf{u}}_i, \quad (6.10)$$

where N_{cp} are the number of control points, $N_{i,p}(\xi)$ is the basis function (B-splines or NURBS), of polynomial order p , belonging to the i^{th} control point, and $\bar{\mathbf{u}}_i$ is the control point value of the approximated function $\mathbf{u}^h(\xi)$.

The rotation group is one of the configuration variables of the geometrically exact 3D beam theory and its numerical implementation requires special attention. A set of rotations in \mathbb{R}^3 , denoted as $\mathbf{SO}(3)$, is the set of the second order orthogonal tensors with positive determinant, defined mathematically as:

$$\mathbf{SO}(3) = \{ \mathbf{\Lambda} : \mathbf{\Lambda} \mathbf{\Lambda}^t = \mathbf{I}, \det \mathbf{\Lambda} = 1 \}. \quad (6.11)$$

The $\mathbf{SO}(3)$ has a non-commutative Lie group structure under the matrix multiplication operation and its Lie algebra, denoted by $\mathbf{so}(3)$, is a linear space of second order skew symmetric tensors. Every skew symmetric tensor $\hat{\boldsymbol{\theta}}$ is associated with a unique vector $\boldsymbol{\theta}$ in \mathbb{R}^3 , such that for all \mathbf{t} in \mathbb{R}^3 , $\hat{\boldsymbol{\theta}} \mathbf{t} = \boldsymbol{\theta} \times \mathbf{t}$, where \times is the cross-product in \mathbb{R}^3 . The exponential map is a function that maps elements of $\mathbf{so}(3)$ unto rotations in $\mathbf{SO}(3)$, with a closed form expression given in [5].

Several methods are available to parametrize rotations in $\mathbf{SO}(3)$, see for example [107] for a review of most of them. For the present method, quaternions are used to parametrize rotations. Quaternions are elements in the four dimensional space \mathbb{R}^4 and each quaternion \mathbf{q} is composed of a scalar part q_0 and a vector part \mathbf{q}_v in \mathbb{R}^3 , written as:

$$\mathbf{q} = q_0 + \mathbf{q}_v. \quad (6.12)$$

The addition of two quaternions is defined as: $\mathbf{q} + \mathbf{p} = q_i + p_i$, for $i = 0, \dots, 4$. Given two quaternions \mathbf{q} and \mathbf{p} , their (non-commutative) product results in a quaternion \mathbf{r} of the form:

$$\mathbf{r} = \mathbf{q} \circ \mathbf{p} = (q_0 p_0 - \mathbf{q}_v^t \mathbf{p}_v^t) + (q_0 \mathbf{p}_v + p_0 \mathbf{q}_v + \mathbf{q}_v \times \mathbf{p}_v), \quad (6.13)$$

where the first bracket contains the scalar component of \mathbf{r} and the second bracket contains the vector component of \mathbf{r} . Another important property of a quaternion \mathbf{q} is its conjugate \mathbf{q}^* , defined as:

$$\mathbf{q}^* = q_0 - \mathbf{q}_v. \quad (6.14)$$

The norm of a quaternion $\mathbf{q} \in \mathbb{R}^4$, denoted as $\|\mathbf{q}\|$, is calculated as:

$$\|\mathbf{q}\| = \{q_0^2 + \mathbf{q}_v^t \mathbf{q}_v\}^{\frac{1}{2}}. \quad (6.15)$$

A sub-set of the quaternions, $S^3 \subset \mathbb{R}^4$, is a set of unit quaternions that are isomorphic to the rotation group $\mathbf{SO}(3)$, provided that two quaternions of the form \mathbf{q} and $-\mathbf{q}$ are identified. Furthermore, every quaternion that is part of S^3 can be expressed as:

$$\mathbf{q} = \cos\left(\frac{\theta}{2}\right) + \sin\left(\frac{\theta}{2}\right) \mathbf{v}, \quad \text{with} \quad \|\mathbf{v}\| = 1. \quad (6.16)$$

The previous expression for a unit quaternion corresponds to a rotation with a magnitude θ about the axis $\mathbf{v} \in \mathbb{R}^3$. Quaternion representation of rotation has the advantage, among others, in reducing the computational and storage cost because the rotation is stored using four parameters instead of using the matrix form. A vector $\mathbf{a} \in \mathbb{R}^3$ is rotated into another vector $\mathbf{b} \in \mathbb{R}^3$, by a rotation quaternion, \mathbf{q} , or equivalently by rotational matrix, \mathbf{R} , as:

$$\mathbf{b} = \mathbf{q}^* \mathbf{a} \mathbf{q} \quad \text{or} \quad \mathbf{b} = \mathbf{R} \mathbf{a}, \quad (6.17)$$

where the rotation matrix, \mathbf{R} , may be expressed in terms of the quaternion \mathbf{q} as:

$$\mathbf{R} = \mathbf{q}_v \mathbf{q}_v^t + (q_0 \mathbf{I} + \hat{\mathbf{q}}_v)(q_0 \mathbf{I} + \hat{\mathbf{q}}_v), \quad (6.18)$$

where \mathbf{I} is a 3 by 3 identity matrix. The variables q_0 and $\hat{\mathbf{q}}_v$ are respectively, the scalar part of \mathbf{q} and a skew symmetric matrix of the vector part of \mathbf{q} . Moreover, for every non zero quaternion and not necessarily of a unit norm, a unique rotation is obtained if the quaternion represents as before a rotation of an angle θ about a unit vector \mathbf{v} . For non unitary quaternions that represent rotation, the rotation matrix is given in terms of a rotation quaternion as:

$$\mathbf{R} = \frac{1}{\|\mathbf{q}\|^2} (\mathbf{q}_v \mathbf{q}_v^t + (q_0 \mathbf{I} + \hat{\mathbf{q}}_v)(q_0 \mathbf{I} + \hat{\mathbf{q}}_v)). \quad (6.19)$$

The approximated quaternion at the integration point is calculated from its control point quantities using a standard isoparametric interpolation, as:

$$\mathbf{q}^h(\zeta) = \sum_{i=1}^{N_{cp}} N_i(\zeta) \bar{\mathbf{q}}_i, \quad (6.20)$$

where $\bar{\mathbf{q}}$ are the control point values of $\mathbf{q}^h(\zeta)$, while N_{cp} and $N_i(\zeta)$ denote respectively, the number of control points and the basis function used for interpolating control point quantities. Since the quaternion of equation 6.20 is not unitary, the rotation matrix $\mathbf{R}(\zeta)$ is calculated using equation 6.19. This method of interpolating rotations can be understood as isoparametric interpolation followed by a normalization.

6.3.2. LOAD VECTOR AND TANGENT STIFFNESS MATRIX

The load vector and tangent stiffness matrix are derived from the first and second variation of the strain energy given in equation 6.9. First, the first variation

of the strain measures is written as:

$$\delta\boldsymbol{\gamma} = \boldsymbol{\Lambda}_0^t \mathbf{R}^t \{ \mathbf{R} \delta \mathbf{R}^t (\mathbf{r}'_0 + \mathbf{u}') + \delta \mathbf{u}' \} \quad \text{and} \quad \delta \boldsymbol{\kappa} = \boldsymbol{\Lambda}_0^t (\delta \mathbf{R}^t \mathbf{R}' + \mathbf{R}^t \delta \mathbf{R}')_{\nu}, \quad (6.21)$$

where $(\cdot)_{\nu}$ denotes the axial vector of a skew symmetric matrix. The variation of the displacement, $\delta \mathbf{u}'$, is parametrized using the NURBS function and the control point quantities of the virtual displacement, $\delta \mathbf{u}_i$, as:

$$\delta \mathbf{u}' = N'_i \delta \mathbf{u}_i, \quad (6.22)$$

where N_i is the NURBS function and $(\cdot)' = \frac{1}{J} \frac{d(\cdot)}{d\xi}$, with J denoting the Jacobian. The Einstein summation is employed here to sum over the subscript $i = 1 \dots N_{cp}$. The admissible variation of the rotation tensor, $\delta \mathbf{R}$, is given in terms of the variation of the rotation quaternion, $\delta \mathbf{q}^h$, as:

$$\delta \mathbf{R} = \frac{\partial \mathbf{R}}{\partial \mathbf{q}^h} : \delta \mathbf{q}^h, \quad (6.23)$$

where $\frac{\partial \mathbf{R}}{\partial \mathbf{q}^h} : \delta \mathbf{q}^h$ is the operation of the vector $\delta \mathbf{q}^h$ on the third order tensor $\frac{\partial \mathbf{R}}{\partial \mathbf{q}^h}$ such that $\frac{\partial \mathbf{R}}{\partial \mathbf{q}^h} : \delta \mathbf{q}^h = \frac{\partial \mathbf{R}}{\partial q_k^h} \delta q_k^h$, summing over the subscript $k = 1 \dots 4$. In order to determine the first variation of rotation quaternion, $\delta \mathbf{q}^h$, the control point quaternion, $\bar{\mathbf{q}}$, is linearised around the origin, $\bar{\mathbf{q}}_0$, in terms of the infinitesimal rotation, $\delta \boldsymbol{\theta}$, using the exponential map, i.e.:

$$\bar{\mathbf{q}} = \exp(\delta \boldsymbol{\theta}) \bar{\mathbf{q}}_0, \quad (6.24)$$

where the vector $\delta \boldsymbol{\theta}$ is an element of the tangent space of the rotation group $SO(3)$ around the origin $\bar{\mathbf{q}}_0$ such that $\delta \boldsymbol{\theta} \in so(3)$, where $so(3)$ is the Lie algebra of the rotation group. The vector $\delta \boldsymbol{\theta}$, representing the magnitude and the axis of a rotation, is mapped to the quaternion subspace S^3 following the formulation of the exponential map used in [52]. The derivative of the linearised quaternion, given in equation 6.24, is evaluated at the origin, i.e. $\delta \boldsymbol{\theta} = \mathbf{0}$. Therefore the exponential map is expanded up-to second order term in $\delta \boldsymbol{\theta}$, using the Tylor series as:

$$\exp(\delta \boldsymbol{\theta})_{Tylor} = \left\{ \left(1 - \frac{1}{8} \|\delta \boldsymbol{\theta}\|^2 \right) \right\}. \quad (6.25)$$

Substituting equation 6.25 into equation 6.24, the admissible variation $\delta \mathbf{q}^h$ is expressed as the first derivative of $\bar{\mathbf{q}}$, with respect to $\delta \boldsymbol{\theta}$, and the NURBS function, as:

$$\delta \mathbf{q}^h = N_i \left. \frac{\partial \exp(\delta \boldsymbol{\theta})}{\partial \delta \boldsymbol{\theta}} \right|_{\delta \boldsymbol{\theta} = \mathbf{0}} \delta \boldsymbol{\theta}_i \bar{\mathbf{q}}_i = \frac{1}{2} N_i \mathbf{Q}_i \delta \boldsymbol{\theta}_i, \quad (6.26)$$

where

$$\mathbf{Q}_i = \begin{bmatrix} -\bar{q}_{v,i}^t \\ \bar{q}_{0,i} \mathbf{I} - \bar{\hat{q}}_{v,i} \end{bmatrix}, \quad (6.27)$$

and \mathbf{I} is a 3 by 3 identity matrix while $\hat{\bar{q}}_{v,i}$ is a skew symmetric matrix of $\bar{q}_{v,i}$, for the i^{th} control point.

The second variation of the strain energy, defined in equation 6.9, is a function of the second variation of the strain measures. The second variation of the strain measures is defined as:

$$\begin{aligned} \delta^2 \gamma &= \Lambda_0^t \{ \delta^2 \mathbf{R}^t (\mathbf{r}'_0 + \mathbf{u}') + 2 \delta \mathbf{R}^t \delta \mathbf{u}' \} \\ &\quad \text{and} \\ \delta^2 \kappa &= \Lambda_0^t (\delta^2 \mathbf{R}^t \mathbf{R}' + \mathbf{R}^t \delta^2 \mathbf{R}' + 2 \delta \mathbf{R}^t \delta \mathbf{R}')_{\nu}. \end{aligned} \quad (6.28)$$

The second variation of the rotation tensor, $\delta^2 \mathbf{R}$, is defined in-terms of the variation of the rotation quaternion, \mathbf{q}^h , such that:

$$\delta^2 \mathbf{R} = \delta \mathbf{q}^h : \frac{\partial^2 \mathbf{R}}{\partial^2 \mathbf{q}^h} : \delta \mathbf{q}^h + \frac{\partial \mathbf{R}}{\partial \mathbf{q}^h} : \delta^2 \mathbf{q}^h, \quad (6.29)$$

where:

$$\delta \mathbf{q}^h : \frac{\partial^2 \mathbf{R}}{\partial^2 \mathbf{q}} : \delta \mathbf{q}^h = \sum_{j=1}^4 \sum_{i=1}^4 \frac{\partial^2 \mathbf{R}}{\partial q_j^h \partial q_i^h} \delta q_i^h \delta q_j^h. \quad (6.30)$$

Substituting equation 6.25 into equation 6.24, the second variation of the quaternion, $\delta^2 \mathbf{q}^h$, is expressed as the second derivative of $\bar{\mathbf{q}}$, with respect to $\delta \boldsymbol{\theta}$, and the NURBS function, i.e.:

$$\delta^2 \mathbf{q}^h = N_i \left. \frac{\partial^2 \exp(\delta \boldsymbol{\theta})}{\partial^2 \delta \boldsymbol{\theta}} \right|_{\delta \boldsymbol{\theta}=\mathbf{0}} : \delta^2 \boldsymbol{\theta} \bar{\mathbf{q}} = -\frac{1}{4} N_i \bar{\mathbf{q}}_i \delta \boldsymbol{\theta}_i^t \delta \boldsymbol{\theta}_i \quad (6.31)$$

The admissible variations for the displacement-based formulation consist of the displacement ($\delta \mathbf{u}$), and rotation ($\delta \boldsymbol{\theta}$) variables defined at the control points. The displacements and rotations are collected in a single vector: $\delta \mathbf{p} = \left\{ \{ \delta \mathbf{u}, \delta \boldsymbol{\theta} \}_1, \dots, \{ \delta \mathbf{u}, \delta \boldsymbol{\theta} \}_i, \dots, \{ \delta \mathbf{u}, \delta \boldsymbol{\theta} \}_{N_{cp}} \right\}^t$, where i refers to the i^{th} control point.

Based on the principle of minimum potential energy, the load vector is defined as the first derivative of the first variation of the strain energy, defined in equation 6.9, with respect to the generalized coordinate $\delta \mathbf{p}$ as:

$$\mathbf{f} = \int_0^1 \left(\mathbf{N}^t \frac{\partial \delta \gamma}{\partial \delta \mathbf{p}} + \mathbf{M}^t \frac{\partial \delta \kappa}{\partial \delta \mathbf{p}} \right) J(\xi) d\xi, \quad (6.32)$$

where $J(\xi) = \left| \frac{\partial \mathbf{r}_0(\xi)}{\partial \xi} \right|$ is the Jacobian, representing the mapping between the ξ -parameter space and the physical space. Similarly, the tangent stiffness matrix is the second derivative of the second variation of the strain energy, defined in equation 6.9, with respect to the generalized coordinate $\delta \mathbf{p}$, i.e.:

$$\mathbf{K} = \int_0^1 \left\{ \left(\frac{\partial \delta \mathbf{N}}{\partial \delta \mathbf{p}} \right)^t \frac{\partial \delta \gamma}{\partial \delta \mathbf{p}} + \left(\frac{\partial \delta \mathbf{M}}{\partial \delta \mathbf{p}} \right)^t \frac{\partial \delta \kappa}{\partial \delta \mathbf{p}} + \mathbf{N}^t \frac{\partial^2 \delta \gamma}{\partial \delta \mathbf{p} \partial \delta \mathbf{p}} + \mathbf{M}^t \frac{\partial^2 \delta \kappa}{\partial \delta \mathbf{p} \partial \delta \mathbf{p}} \right\} J(\xi) d\xi. \quad (6.33)$$

The non-linear equilibrium equations are solved using the Newton-Raphson iteration scheme for finding the root of the residual between the generalized external load \mathbf{f}_{ext} and the generalized internal load vector \mathbf{f} :

$$\mathbf{R} = \mathbf{f} - \lambda \mathbf{f}_{ext} = \mathbf{0}, \quad (6.34)$$

where λ is the load stepping parameter. The solution to 6.34 requires the linearisation of the residual around a solution $\delta \mathbf{p}_0$, such that:

$$\mathbf{R}(\delta \mathbf{p}_0) + \mathbf{K} \Delta \delta \mathbf{p} - \mathbf{f}_{ext} \Delta \lambda = \mathbf{0}, \quad (6.35)$$

where $\Delta \lambda$ is the load increment. The increment in the generalized coordinate $\Delta \delta \mathbf{P}$ is calculated in two steps. For the first step, when advancing between two load steps, $\Delta \delta \mathbf{p}$ is calculated solely from the change in load, i.e. $\mathbf{f}_{ext} \Delta \lambda$. In the second step, when the load is kept constant, $\Delta \delta \mathbf{p}$ is calculated using the standard Newton-Raphson scheme. Equilibrium is achieved when the norm of $\Delta \delta \mathbf{p}$ or \mathbf{R} converges to zero.

6.4. STRUCTURAL VALIDATION

In order to demonstrate the performance of the present method, results from several numerical examples are compared with available literature. The numerical implementation of the model is carried out in *Matlab* computing environment. NURBS shape functions with a different polynomial degree and inter-element continuity are used as basis functions. Isogeometric mesh with a multiple number of knot spans, henceforth named elements(N), are used for discretization.

6.4.1. A CANTILEVER BEAM SUBJECT TO A FREE-END MOMENT

A straight cantilever beam with the material and geometric properties:

$E = 2.1e4$	$G = 1.05e4$	$L = 100$
$A_1 = 20$	$A_1 = A_2 = 16$	
$J = 6.4566$	$I_1 = 1.6667$	$I_2 = 666.66$

is subjected to a bending moment $M_Y = 1000$ (see figure 6.2a). This results in large displacement and rotation in the X-Z plane. The in-plane rotation of the beam is compared with the analytical solution given in [127]. The structural deformation under the bending moment is calculated for increasing number of elements and for two polynomial orders (p). Figure 6.2b shows the in-plane rotation versus the number of control points. In addition, figure 6.2b also contains the analytical solution given in [127]. From figure 6.2b, it can be observed that a converged result is achieved for 100 control points, which amounts to 97 elements for a polynomial order $p = 3$.

6.4.2. THE MACNEAL AND HARDER TEST PROBLEMS

A standard set of problems is presented in [91] to test the finite element accuracy of beam, shell, and solid elements. The problem sets used in this paper

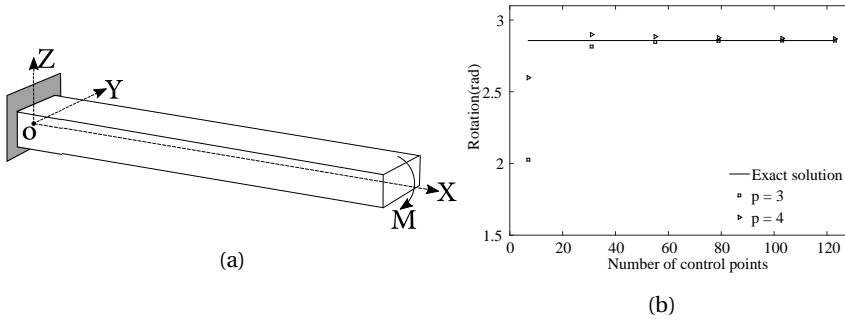


Figure 6.2: 6.2a Cantilever beam under bending moment; 6.2b In-plane rotation for increasing number of elements.

are a straight and curved cantilever beams, as shown in figures 6.3a and 6.3b respectively. The geometric and material data of the straight beam are:

$$\begin{aligned}
 E &= 1e7 & G &= 3.84615e6 & L &= 6 \\
 A_1 &= 0.02 & A_1 &= A_2 = 0.016 \\
 J &= 4.8630e-5 & I_1 &= 6.6667e-5 & I_2 &= 1.66667e-5,
 \end{aligned}$$

where L is the beam length. Four load cases are considered: three unit forces in the three coordinate directions, and a unit twist moment. For the curved beam with a shape of a quarter circle with a radius $R = 4.22$, only $G = 4e6$ and $J = 4.4050e-5$ are different from the material properties of the straight beam. Only two load cases are considered in this case: two unit loads in X and Y direction. The results for both the straight and curved beams are shown in table

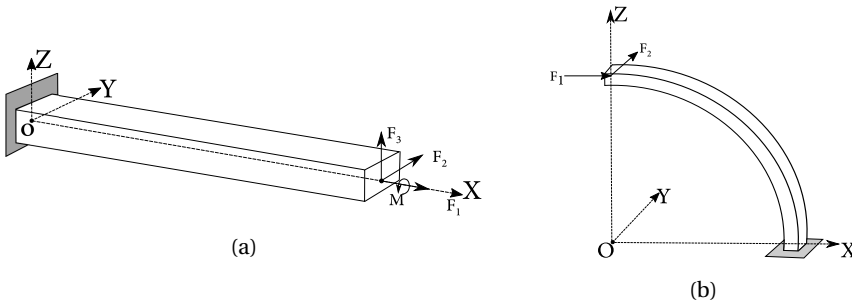


Figure 6.3: 6.3a Cantilever beam under various tip loads; 6.3b Curved beam under different loading.

6.1. The results of the present method are obtained using C^2 continuous cubic polynomial ($p = 3$) and a different number of elements. In table 6.1, the displacement results are in the direction of the applied load. In addition, results from [91], and the analytical result of the linearised Reissner beam theory [141] are also included for comparison. For the straight beam, the results from the

Table 6.1: Comparison of results for the MacNeal and Harder test problems

Initial beam type	Type of solution	Displacement in the direction of the applied load			
		Extension (F_1)	Deflection in Z (F_2)	Deflection in Y (F_3)	Twist (M_1)
Straight	N = 10	3.0e-5	0.1049	0.4012	0.0323
	N = 50	3.0e-5	0.1082	0.4294	0.0321
	N = 100	3.0e-5	0.1082	0.4301	0.0321
	Theoretical[91]	3.0e-5	0.1081	0.4321	0.0321
	Analytical[141]	3.0e-5	0.1081	0.4321	0.0321
Curved	N = 10	-	0.0838	0.4849	-
	N = 50	-	0.0871	0.5027	-
	N = 100	-	0.0871	0.5030	-
	Theoretical[91]	-	0.0873	0.5022	-
	Analytical[141]	-	0.0886	0.5062	-

present method (using 100 elements) match with literature up-to three significant digits for an extension (deflection in Z direction) and twist. For the deflection in Y direction, the results match up-to two significant digits. For the curved beam, a difference in results between the theoretical and analytical formulation is observed, which may be caused due to the different theoretical assumption of the two beam theories. The result from the present method, for $N = 100$, matches with the theoretical results up-to two significant digits.

6

6.4.3. A CANTILEVER BEAM SUBJECT TO TWO TRANSVERSAL LOADS

A cantilever beam loaded by two transversal loads, one at the tip and the other close to the mid-span (see figure 6.4) is used for comparison. The beam has a cross-sectional area $A = 0.2$, bending stiffness $EI = 5e6$ and shear modulus $G = 1.153846e7$. Several authors [26, 40] have considered this problem and analytical solution for this problem is also available [45]. The results of the present method are obtained using C^2 continuous cubic polynomials ($p = 3$) and for a different number of elements. Moreover, the load is applied in 10 equally spaced increments, with an average of 5 iterations per increment. Ta-

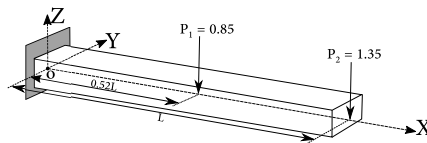


Figure 6.4: Cantilever beam under two vertical loads.

ble 6.2 contains the tip displacement and rotation obtained from different formulations and for different mesh density. The results obtained by the present method are compared with [26, 40] and the analytical results from [45].

Table 6.2: Comparison of results for cantilever beam with two transversal load

Formulation	Number of elements	Displacement		
		Longitudinal	Transversal	Rotation
Present	10	-19.24	-51.20	-0.87
	50	-29.22	-65.04	-1.02
	100	-30.33	-66.40	-1.04
Cardona [26]	2	-28.99	-65.85	-1.1
	4	-30.26	-66.63	-1.06
	8	-30.62	-66.87	-1.05
Crivelli [40]	2	-28.99	-65.86	-1.10
	4	-30.26	-66.63	-1.06
	8	-30.62	-66.87	-1.05
Analytical	-	-30.75	-66.96	-

6.4.4. CURVED CANTILEVER BEAM UNDER TRANSVERSAL TIP LOAD

The curved cantilever beam under transversal tip load is one of the classical finite element tests because it includes all natural mode of deformation of a beam: extension, bending, torsion, and shear. A curved beam, located in the $X - Y$ plane, with a radius $R = 100$, is shown in figure 6.5. The beam has a unit cross-sectional area A , elastic and shear moduli of $E = 1e7$, and $G = 0.5e7$, respectively. The beam is loaded with a concentrated vertical tip load $P = 600$. The present method employs 100 elements to discretize the beam. The basis functions consists of NURBS of C^2 continuous cubic polynomials. In table

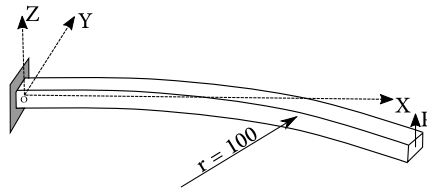


Figure 6.5: In-plane curved beam under tip loading.

6.3, the position vector of the tip of the curved beam, in the deformed configuration, is tabulated for different intermediate load levels and for different formulations. The results from [9] are taken as a reference since they are obtained with more refined elements compared to the other formulations.

6.4.5. COMPOSITE I BEAM

A cantilever beam, made of composite material of length $L = 2.5m$, is loaded with a concentrated vertical tip load of $P = 250N$. The cross-section of the beam is in the shape of I , with equal width and height of $50mm$ (see figure 6.6). The walls of the beam consist of symmetric laminates with the lay-up $[\pm\theta]_{4s}$, where θ is varied between 0 and 90 degree. Each layer is $0.13mm$ thick with the following material properties: $E_1 = 53.78GPa$, $E_2 = 17.93GPa$, $G_{12} = 8.96GPa$, and $\nu_{12} = 0.25$. The present method employs 100 elements to discretize the beam. The basis functions consists of NURBS of C^2 continuous cubic polyno-

Table 6.3: Comparison of results for the 45-degree cantilever beam with transversal tip load

Formulation	Component	Load level		
		300	450	600
Present	rx	22.11	18.37	15.56
	ry	58.53	51.97	46.89
	rz	40.49	48.71	53.61
Bathe [9]	rx	22.33	18.62	15.79
	ry	58.84	53.32	47.23
	rz	40.08	48.39	53.37
Simo [124]	rx	22.50	-	15.90
	ry	59.20	-	47.23
	rz	39.50	-	53.37
Cardona [26]	rx	22.14	18.38	15.55
	ry	58.64	52.11	47.04
	rz	40.35	48.59	53.50
Crivelli [40]	rx	22.31	18.59	15.75
	ry	58.85	53.34	47.25
	rz	40.08	48.39	53.37

mials. The sectional stiffness constants of the beam are calculated using an in-house tool [48], which calculates the sectional stiffness constants of a prismatic and thin-walled composite beam with arbitrary cross-sectional shape (open or closed). The axial (X-direction) and vertical (Z-direction) displace-

6

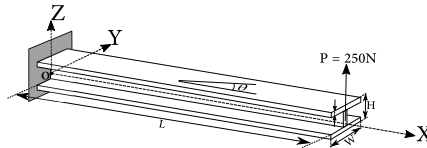


Figure 6.6: Composite I beam

ments at the tip of the beam are considered for comparison. Table 6.6, contains a comparison of the tip displacement of a cantilever I-beam under a vertical tip load $P = 250$ and for different Lay-ups. For comparison purpose, the results from Lee et al. [134], and Abaqus is included in table 6.6. The Abaqus results are obtained from a non-linear analysis of a cantilever beam using 600 nine-noded shell elements (S9R5). The results from the present method agree quite well with the results obtained by the other formulations, for all considered Lay-ups.

6.4.6. COMPOSITE BOX BEAM

For a final example, a composite box beam with the dimensions: length $L = 100in$, width $W = 4in$, height $H = 2in$, and wall thickness $t = 0.1008in$, is loaded by a concentrated vertical tip load $P = 400lb$ (see figure 6.7). The walls are made of eight ply laminates with the layup: top flange $[0/\theta_2/90]_s$, bottom flange $[0/-\theta_2/90]_s$, and both shear webs $[(0/90)_2]_s$. The parameter θ is the off-axis angle of a single ply (see figure 6.7). A T300/5208 graphite/epoxy with

Table 6.4: Comparison of results for the composite I beam of different lay-ups and under a vertical tip load of $P = 250N$.

Lay-ups	Formulation	Displacement	
		Axial(cm)	Vertical(cm)
$[0]_s$	Abaqus	-0.6124	15.9760
	Lee	-0.6075	15.9113
	Present	-0.6123	15.9810
$[15/-15]_s$	Abaqus	-0.7474	17.6434
	Lee	-0.7432	17.6002
	Present	-0.7476	17.6520
$[30/-30]_s$	Abaqus	-1.3416	23.6133
	Lee	-1.3404	23.6384
	Present	-1.3430	23.6364
$[45/-45]_s$	Abaqus	-2.7501	33.7463
	Lee	-2.7600	33.9294
	Present	-2.7537	33.7867
$[60/-60]_s$	Abaqus	-4.3164	42.2037
	Lee	-4.3443	42.5798
	Present	-4.3177	42.2301
$[75/-75]_s$	Abaqus	-5.0482	45.6077
	Lee	-5.0838	46.0678
	Present	-5.0460	45.6168
$[90/-90]_s$	Abaqus	-5.1983	46.2755
	Lee	-5.2341	46.0678
	Present	-5.1960	46.2841
$[0/90]_s$	Abaqus	-1.3488	23.6829
	Lee	-1.3569	23.7830
	Present	-1.3481	23.6855

the properties:

$$\begin{aligned}
 E_1 &= 21.3e^6 \text{ psi} & E_2 &= 1.6e^6 \text{ psi} \\
 G_{12} &= 0.9e^6 \text{ psi} & \nu &= 0.28,
 \end{aligned}$$

is used as ply properties. The beam is analysed for θ ranging between 0 and 90 degrees. The results from the present method are obtained using 100 elements, and basis functions comprised of C^2 continuous cubic NURBS. The sectional stiffness constants of the beam are calculated using an in-house tool [48], which calculates the sectional stiffness constants of a prismatic and thin-walled composite beam with arbitrary cross-sectional shape (open or closed). The tip displacements (u, v, w) and twist angle of the box beam under a verti-

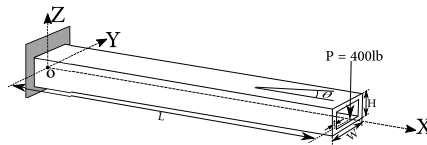


Figure 6.7: Composite box beam

cal load of $P = 400lb$ and for different off-axis ply angle θ are shown in figures 6.8a and 6.8d. Furthermore, the results from [128] are also included for comparison. From figure 6.8c, it is observed that the tip deflection doubles when

θ is varied from 0 to 90, which is expected since most of the beam stiffness in the direction of the beam axis is reduced for $\theta = 90$. The same is also observed from the displacement in the axial direction (see figure 6.8a). The effect of bend-twist coupling is observed from figure 6.8d, where the twist angle is plotted against θ . There is zero twist for $\theta = 0$ and 90, which correspond to zero bend-twist coupling coefficient. Figure 6.8b shows the tip displacement in the chord direction, caused by the coupling between the vertical load and the horizontal displacement. From figures 6.8a to 6.8d it is evident that the present method agrees well with the results from [128]. The present method is, therefore, capable of capturing the geometric non-linear response of a composite beam.

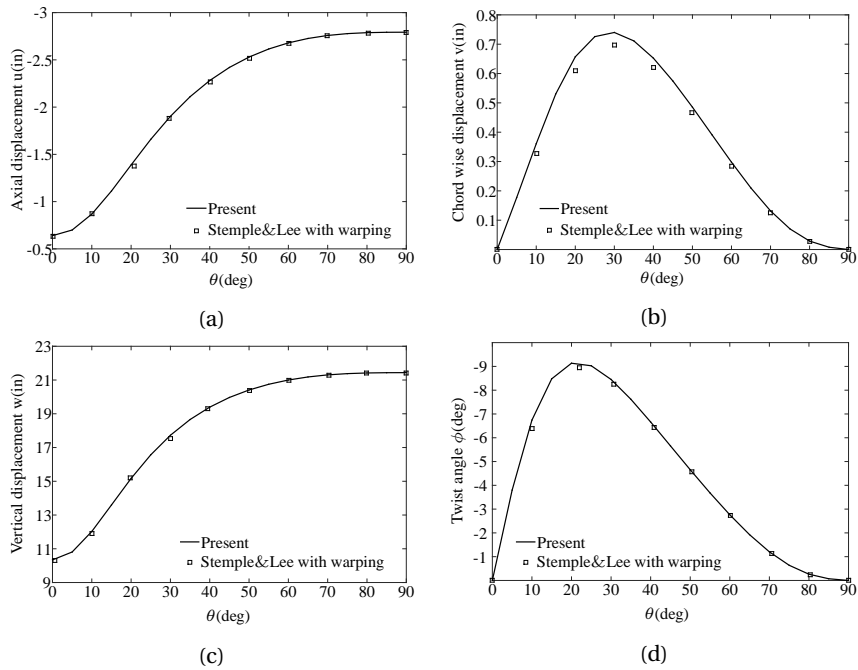


Figure 6.8: Tip displacement components of a box beam loaded by vertical tip load and for different off axis ply angles.

Since only static aeroelastic analysis is performed in this work, only the centrifugal load is considered in this thesis.

6.5. CENTRIFUGAL & GRAVITATIONAL LOAD

CENTRIFUGAL LOAD

Rotating bodies experience centrifugal effects. These forces are non-existent in an inertial frame of reference, however, in a rotating frame, the centrifugal effects are seen as an inertial force. This inertial force can be decomposed into

centrifugal force and Coriolis force. The centrifugal force is solely dependent on the displacement whereas the Coriolis force is also dependent on the velocity. Only centrifugal load is considered in this thesis. The centrifugal load is derived from the kinetic energy of a rotating body as:

$$T = \frac{1}{2} \int_M |\mathbf{v}_l|^2 dm \quad (6.36)$$

where \mathbf{v}_l is the velocity of the differential mass dm with respect to the rotating frame. Assuming only static blade deformations, $\mathbf{v}_l = \omega \hat{\mathbf{e}}_\omega \mathbf{r}_l$, where ω and $\hat{\mathbf{e}}_\omega$ are respectively, the magnitude and direction (in skew symmetric notation) of the angular velocity of the rotor blade. Since $dm = \rho dA ds$, where dA and ds are the differential area and arc-length respectively, the kinetic energy is expressed as double integral along the cross-section and the arch-length as:

$$T = \frac{1}{2} \int_0^L \int_A |\mathbf{v}_l|^2 \rho dA ds, \quad (6.37)$$

where ρ is the material density. Assuming thin-walled structures (see figure 6.9), the position vector \mathbf{r}_l is discretized in terms of the position vector of the beam axis and rigid-body rotation of the cross-section as:

$$\mathbf{r}_l(s, \eta) = \mathbf{r}(s) + \mathbf{\Lambda}(s) \mathbf{r}_\eta(\eta), \quad (6.38)$$

where η is a parameter running over the cross-section, and \mathbf{r}_η is local position vector of a material point (see figure 6.9). Substituting equation 6.38 into the

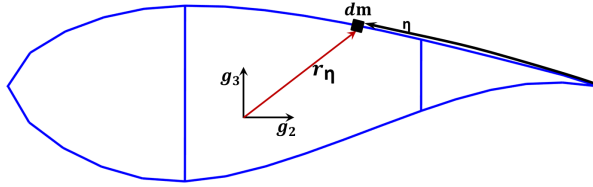


Figure 6.9: Schematic representation of a differential mass on the cross-section of a wind turbine blade

relation for \mathbf{v}_l , the kinetic energy is re-written as:

$$T = -\frac{1}{2} \omega^2 \int_0^L \oint_\eta \left(\mathbf{r}^t \hat{\mathbf{e}}_\omega \mathbf{r} + \mathbf{e}_\omega^t \mathbf{\Lambda} \hat{\mathbf{r}}_\eta^2 \mathbf{\Lambda}^t \mathbf{e}_\omega - 2 \mathbf{r}^t \hat{\mathbf{e}}_\omega \mathbf{\Lambda} \hat{\mathbf{r}}_\eta \mathbf{\Lambda}^t \mathbf{e}_\omega \right) h(\eta) \rho(\eta) d\eta ds, \quad (6.39)$$

where $h(\eta)$ is the wall thickness of the cross-section. The position vector of the beam axis \mathbf{r} and the rigid body rotation tensor of the cross-section $\mathbf{\Lambda}$, in the deformed configuration, are approximated linearly in-terms of the displacement $\mathbf{u}(s)$ and rotation $\boldsymbol{\theta}(s)$ of the beam axis as:

$$\mathbf{r}(s) = \mathbf{r}_0(s) + \mathbf{u}(s) \quad \text{and} \quad \mathbf{\Lambda}(s) = \left(\mathbf{I} + \hat{\boldsymbol{\theta}}(s) \right) \mathbf{\Lambda}_0(s). \quad (6.40)$$

Substituting equation 6.40 into equation 6.39, the generalized centrifugal load vector is defined as the first derivative of the kinetic energy with respect to the generalized coordinates \mathbf{p} , i.e.:

$$\begin{aligned} \mathbf{f}_{ct} = & -\omega^2 \int_0^1 \left\{ \frac{\partial \mathbf{u}}{\partial \mathbf{p}} \right\}^t (\hat{\mathbf{e}}_\omega^2 \mathbf{r}_0 m_0 - \hat{\mathbf{e}}_\omega \Lambda_0 \mathbf{m}_1 \Lambda_0^t \mathbf{e}_\omega) J d\xi \\ & + \omega^2 \int_0^1 \left\{ \frac{\partial \boldsymbol{\theta}}{\partial \mathbf{p}} \right\}^t (\{\hat{\mathbf{e}}_\omega \mathbf{r}_0\}_{sk} \Lambda_0 \mathbf{m}_1 \Lambda_0^t \mathbf{e}_\omega + \hat{\mathbf{e}}_\omega \Lambda_0 \mathbf{m}_1 \Lambda_0^t \hat{\mathbf{r}}_0 \mathbf{e}_\omega + \hat{\mathbf{e}}_\omega \Lambda_0 \mathbf{m}_2 \Lambda_0^t \mathbf{e}_\omega) J d\xi, \end{aligned} \quad (6.41)$$

where:

$$m_0 = \oint_\eta h \rho d\eta, \quad \mathbf{m}_1 = \oint_\eta \hat{\mathbf{r}}_\eta h \rho d\eta, \quad \mathbf{m}_2 = \oint_\eta \hat{\mathbf{r}}_\eta^2 h \rho d\eta, \quad (6.42)$$

and $\{\hat{\mathbf{e}}_\omega \mathbf{r}_0\}_{sk}$ is a skew symmetric matrix of $\hat{\mathbf{e}}_\omega \mathbf{r}_0$. The Jacobian J relates the parametric space to the geometric space. Similarly, the centrifugal stiffness matrix is defined as the second derivative of the kinetic energy with respect to the generalized coordinates \mathbf{p} as:

$$\begin{aligned} \mathbf{K}_{ct} = & -\omega^2 \int_0^1 \left(\left\{ \frac{\partial \mathbf{u}}{\partial \mathbf{p}} \right\}^t \hat{\mathbf{e}}_\omega^2 m_0 \frac{\partial \mathbf{u}}{\partial \mathbf{p}} \right) J d\xi \\ & + \omega^2 \int_0^1 \left(\left\{ \frac{\partial \boldsymbol{\theta}}{\partial \mathbf{p}} \right\}^t (\hat{\mathbf{e}}_\omega \Lambda_0 \mathbf{m}_2 \Lambda_0^t \hat{\mathbf{e}}_\omega + 2 \{\hat{\mathbf{e}}_\omega \mathbf{r}_0\}_{sk} \Lambda_0 \mathbf{m}_1 \Lambda_0^t \hat{\mathbf{e}}_\omega) \frac{\partial \boldsymbol{\theta}}{\partial \mathbf{p}} \right) J d\xi \\ & - \omega^2 \int_0^1 \left\{ \frac{\partial \mathbf{u}}{\partial \mathbf{p}} \right\}^t (\hat{\mathbf{e}}_\omega \{\Lambda_0 \mathbf{m}_1 \Lambda_0^t \mathbf{e}_\omega\}_{sk} - \hat{\mathbf{e}}_\omega \Lambda_0 \mathbf{m}_1 \Lambda_0^t \hat{\mathbf{e}}_\omega) \frac{\partial \boldsymbol{\theta}}{\partial \mathbf{p}} J d\xi, \end{aligned} \quad (6.43)$$

where $\{\Lambda_0 \mathbf{m}_1 \Lambda_0^t \mathbf{e}_\omega\}_{sk}$ is the skew symmetric matrix of $\Lambda_0 \mathbf{m}_1 \Lambda_0^t \mathbf{e}_\omega$.

The derivation for the centrifugal load is validated using *NASTRAN* by evaluating the stress response of rotating blade shown in figure 6.10. The blade consist of two spars at 30% and 50% of chord location having a cross-section in the shape of 40% thick DU airfoil. The blade is 61m long with a constant chord of 4m. For material property, a carbon fiber quasi-isotropic laminate is used, with a thickness and material density of 2cm and 1220Kg/m³ respectively. The finite element solver *NASTRAN* is used twice to calculate the stress distribution caused by centrifugal load. First, static analysis is performed using *NASTRAN* for a rotational speed of $\omega = 12.1rpm$, while including the effect of rotation using the *RFORCE* card[90]. Second, static analysis is performed using *NASTRAN* by applying the centrifugal load, calculated using the present method for $\omega = 12.1rpm$, unto the *NASTRAN* model as a

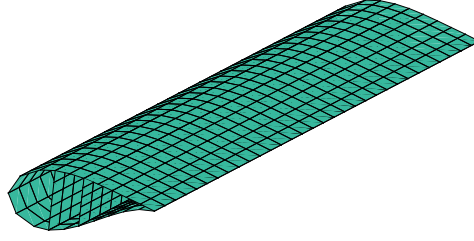


Figure 6.10: FEM of a blade having a cross-section in the shape of 40% thick DU airfoil

static load. The centrifugal load is applied unto the *NASTRAN* model using the method described in chapter 8. In both cases, the average membrane stress resultant $\mathbf{N} = \{N_x, N_y, N_{xy}\}^t$ per element i is calculated as:

$$\mathbf{N}_i = \frac{1}{2} \hat{h}_i (\boldsymbol{\sigma}_i^u + \boldsymbol{\sigma}_i^l), \quad (6.44)$$

where \hat{h}_i is the shell thickness of element i , while $\boldsymbol{\sigma}_i^u$ and $\boldsymbol{\sigma}_i^l$ are the stress responses at the upper and lower side of element i . The stress responses due to centrifugal load, for all the elements of the model shown in figure 6.10, are presented in figure 6.11, both for *NASTRAN* results and the results using the present method. Detailed description on how to extract the stress responses from *NASTRAN* can be found in chapter 8.

Figure 6.11 shows that the two methods match quite well in general. There is a small difference in the results of the stress component N_{xy} towards the blade tip. However, the order of magnitude of N_{xy} is much smaller than N_x . Therefore, the results for the stress component N_x are used for comparison and the results from the two methods are practically on top of each other for N_x .

GRAVITATIONAL LOAD

Wind turbine blades also experience a large variation of the gravitational load during operation and is also included in the current framework. The generalized gravitational load vector is determined from the first variation of the work done by gravity on a single blade as:

$$\mathbf{f}_g = g \int_0^L \left\{ \left(\frac{\partial \mathbf{u}}{\partial \mathbf{p}} \right)^t \mathbf{e}_g m_0 + \left(\frac{\partial \boldsymbol{\theta}}{\partial \mathbf{p}} \right)^t \boldsymbol{\Lambda}_0 \mathbf{m}_1 \boldsymbol{\Lambda}_0^t \mathbf{e}_g \right\} ds, \quad (6.45)$$

where g is the gravitational acceleration and $\mathbf{e}_g = -\{\sin \phi, \cos \phi, 0\}^t$, with ϕ the azimuth position of the blade (see figure 4.1). Finally, \mathbf{u} and $\boldsymbol{\theta}$ are respectively, the virtual displacement of the beam axis and rotation of the body attached coordinates.

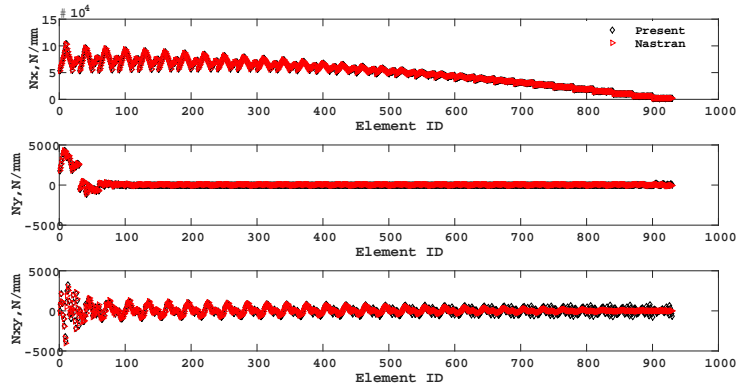


Figure 6.11: Element stress resultant due to centrifugal effect

6.6. SUMMARY

An isogeometric formulation of geometrically exact 3D beam theory is presented. Quaternions are employed to parametrize the rotation variable together with the isoparametric interpolation of the rotation parameters defined at the control points. Using NURBS with appropriate inter-element continuity for discretization, an isogeometric Galerkin approach is established based on the weak form of the equilibrium equations. Several numerical examples are provided to demonstrate the accuracy, stability, and robustness of the present formulation. The present method requires large number of elements to get converged results, which may be caused by shear locking. However, within the aeroelastic analysis of the present framework, the number of control points used to discretize the beam are determined by the level of detail needed to resolve the aerodynamic loads on the rotor blade (see chapter 7 where the aeroelastic model is discussed). Furthermore, as part of the optimization model, detailed structural analysis is carried out using a finite element model of the rotor blade consisting of shell elements. Therefore the cost of the aeroelastic beam model is a fraction of the total computation cost of the analysis. The numerical results show that the present method agrees well with other formulations mentioned in this chapter.

7

AEROELASTIC MODEL

This chapter describes the method for calculating the aerodynamic loads and for finding the aero-structural equilibrium point. Several aeroelastic codes for wind turbine analysis have been developed. Most approaches [120, 133, 104, 1, 84] use Blade Element Momentum theory for calculating the aerodynamic loads, while the structural models are based either on FEM, modal approach or Multi-body dynamics. A detailed review on wind turbine aeroelasticity can be found in [140].

The trend in wind energy shows that the size of the rotor blades increases in order to capture more energy from wind. Furthermore, novel designs of the rotor blade shapes are investigated that result in enhanced performance, such as the design of curved rotor blades that induce bend-twist coupling for increased power extraction or load mitigation. Therefore, when calculating the aerodynamic loads using BEM theory, corrections need to be applied to account for the effect of blade flexibility and/or unconventional blade geometry (e.g. curved blade axis). To this end, this chapter presents a first order correction method to BEM theory, together with a method for the aeroelastic analysis.

This chapter is organised as follows. In section 7.1, corrections to the Blade Element Momentum theory is described, that include the effects of blade flexibility and/or non conventional blade shape on the aerodynamic blade loads. Subsequently, the method to calculate the aeroelastic loads is given in section 7.2. Finally, the validation and verification of the aeroelastic module is given in section 7.3.

This chapter is based on a paper titled *Isogeometric based framework for aeroelastic wind turbine blade analysis* by E.A. Ferde, M.M. Abdalla, and G.J.W. van Bussel, Wind Energy, 2016. Note: symbols may have been changed to ensure consistency throughout the thesis.

7.1. AERODYNAMICS

The Blade Element Momentum theory with tip loss correction, described in section 2.1, is used to calculate, at the integration point ξ , the aerodynamic force and moment vector per unit length. The BEM model requires as input among others: the blade radius $r(\xi)$, chord $c_a(\xi)$, twist $\theta_a(\xi)$ and the polar data of the airfoil $\mathbf{A}_{af}(\xi)$. Starting from the expression for the deformed beam axis:

$$\mathbf{r}(\xi) = \sum_{i=1}^n R_{i,p}(\xi)(\mathbf{P}_{ri} + \mathbf{u}_i), \quad (7.1)$$

the radius along the blade span is calculated as:

$$r(\xi) = r_h + \|\mathbf{r}(\xi) \times \mathbf{e}_3\|, \quad (7.2)$$

where \mathbf{P}_{ri} and \mathbf{u}_i are respectively control point values of the initial position vector of the beam axis and its displacement. The parameter r_h is the hub radius and \mathbf{e}_3 is a component of the rotating frame shown in figure 4.1.

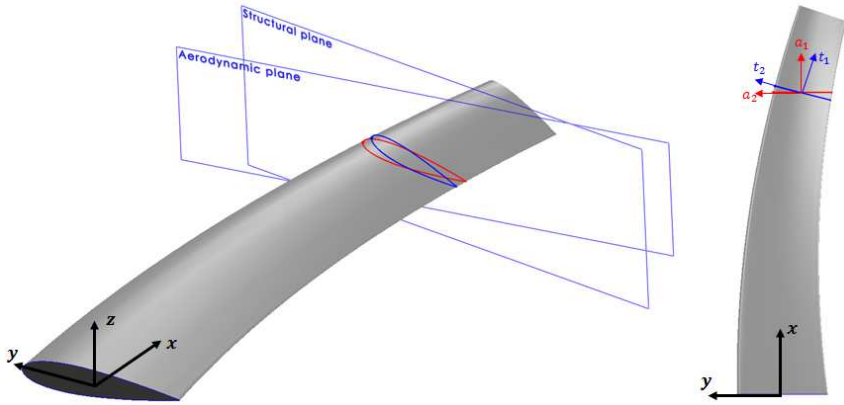


Figure 7.1: 3D and top view of a curved and twisted blade where \mathbf{a}_i are base vectors of the aerodynamic frame and \mathbf{t}_i are base vectors of the structural frame

For flexible blades or blades with initially curved beam axis, the undisturbed airflow sees a different airfoil shape than the structural airfoil shape (see figure 7.1), where the aerodynamic plane is tangent to the stream tube (used in BEM theory for calculating the local aerodynamic load on the blade) at the intersection point with the beam axis, while the structural plane is normal to the beam axis. This requires airfoil analysis within the aeroelastic analysis, increasing the computational time, which is not suitable for fast analysis or optimization. Furthermore, since this framework is intended for use in gradient based design optimization, it is not possible to determine the gradient of the polar data of the projected airfoil shapes. Alternatively, the present method uses correction only on the chord and twist by projecting the airfoil

shape defined in the structural frame unto the aerodynamic frame and calculating the chord and twist of the projected airfoil shape, as shown in figure 7.2. To apply this correction, it is assumed that the chord and twist vary slowly along the blade span. The chord c_s and twist θ_s at the parametric point ξ are

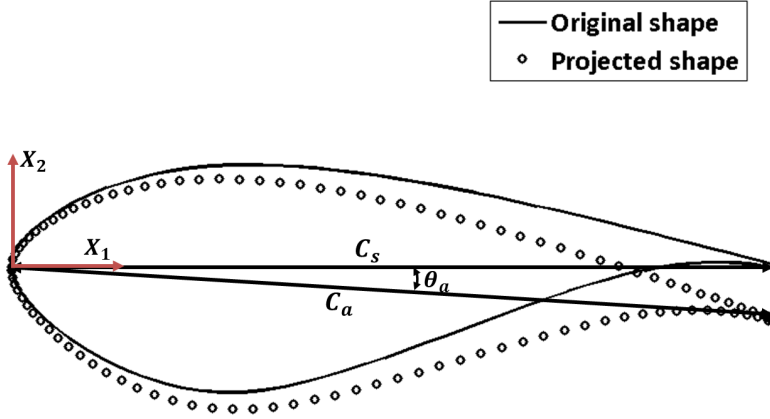


Figure 7.2: Projection of a cross-section from the structural plane unto the aerodynamic plane along \mathbf{a}_1

define as:

$$c_s(\xi) = \sum_{j=1}^m \sum_{i=1}^n R_{i,p}(\xi) C_{i,j} \quad \text{and} \quad \theta_s(\xi) = \sum_{i=1}^n R_{i,p}(\xi) P_{\theta,i}. \quad (7.3)$$

As mentioned earlier, the chord and twist, given in equation 7.3, are corrected for the flexibility of the rotor blade, first by projecting the airfoil shape defined in the structural plane to the aerodynamic plane (see figure 7.2). The cross-sectional shape of a blade at ξ may be expressed with respect to the body-attached structural frame $\Lambda_s(\xi)$ or the aerodynamic frame $\Lambda_a(\xi)$ as:

$$\Lambda_s(\xi) \mathbf{r}_s = \Lambda_a(\xi) \mathbf{r}_a, \quad (7.4)$$

where $\mathbf{t}_i = \mathbf{R} \mathbf{g}_i$, for $i = 1, \dots, 3$, are the base vectors of the structural frame. The vectors \mathbf{a}_i , for $i = 1, \dots, 3$, are the base vectors of the aerodynamic frame Λ_a , defined as:

$$\mathbf{a}_1 = \frac{1}{\|\mathbf{r}(\xi) \times \mathbf{e}_3\|} \mathbf{I}_1^t \mathbf{r}(\xi), \quad \mathbf{a}_2 = \frac{1}{\|\mathbf{r}(\xi) \times \mathbf{e}_3\|} \mathbf{I}_2^t \mathbf{r}(\xi), \quad \text{and} \quad \mathbf{a}_3 = \mathbf{e}_3, \quad (7.5)$$

where $\mathbf{I}_1 = [\mathbf{e}_1, \mathbf{e}_2, \mathbf{0}]$ and $\mathbf{I}_2 = [\mathbf{e}_2, \mathbf{e}_1, \mathbf{0}]$. The vectors \mathbf{r}_s and \mathbf{r}_a are the position vectors of the cross-section with respect to the structural and aerodynamic frame, respectively. Since $\mathbf{e}_1^t \mathbf{r}_s = 0$, $\mathbf{r}_{a,1}$ is expressed as:

$$\mathbf{r}_{a,1} = -\frac{\mathbf{t}_1^t \mathbf{a}_2}{\mathbf{t}_1^t \mathbf{a}_1} \mathbf{r}_{a,2} - \frac{\mathbf{t}_1^t \mathbf{a}_3}{\mathbf{t}_1^t \mathbf{a}_1} \mathbf{r}_{a,3}, \quad (7.6)$$

where $\mathbf{r}_{a,i}$, for $i = 1, \dots, 3$, is the i^{th} component of \mathbf{r}_a . The cross-section, defined in the structural plane, is projected unto the aerodynamic plane along \mathbf{a}_1 , such that:

$$\bar{\mathbf{r}}_a = \mathbf{P} \bar{\mathbf{r}}_s, \quad (7.7)$$

where:

$$\mathbf{P} = \bar{\mathbf{I}}^t \Lambda_s^t \bar{\Lambda}_a, \quad (7.8)$$

and $\bar{\mathbf{I}} = [\mathbf{e}_2, \mathbf{e}_3]$. $\bar{\mathbf{r}}_s$ is the position vector of the airfoil shape in the structural plane, whereas $\bar{\mathbf{r}}_a$ is the position vector of the projected airfoil shape in the aerodynamic plane. Components of $\bar{\Lambda}_a = [\bar{\mathbf{a}}_2, \bar{\mathbf{a}}_3]$ are determined by substituting equation 7.6 into $\Lambda_a(\xi) \mathbf{r}_a$ and collecting terms with respect to $\mathbf{r}_{a,2}$ and $\mathbf{r}_{a,3}$, such that:

$$\bar{\mathbf{a}}_2 = \mathbf{a}_2 - \frac{t_1^t \mathbf{a}_2}{t_1^t \mathbf{a}_1} \mathbf{a}_1 \quad \text{and} \quad \bar{\mathbf{a}}_3 = \mathbf{a}_3 - \frac{t_1^t \mathbf{a}_3}{t_1^t \mathbf{a}_1} \mathbf{a}_1. \quad (7.9)$$

The chord, corrected for blade flexibility and/or initially curved beam axis, is calculated using the projection matrix \mathbf{P} as:

$$c_a = c_s \sqrt{\bar{\mathbf{e}}_1^t \mathbf{P}^t \mathbf{P} \bar{\mathbf{e}}_1}, \quad (7.10)$$

where $\bar{\mathbf{e}}_1 = \{1, 0\}^t$ and c_s is the structural chord. The corrected twist θ_a is calculated as:

$$\theta_a = \sin^{-1} \left(\frac{c_s}{c_a} \bar{\mathbf{e}}_2^t \mathbf{P} \bar{\mathbf{e}}_1 \right) \frac{180}{\pi}, \quad (7.11)$$

where $\bar{\mathbf{e}}_2 = \{0, 1\}^t$.

The polar data of the airfoil shapes along the blade span are interpolated from the polar data of the base airfoils. This is sufficiently accurate, assuming that the interpolation is performed only for airfoils of the same family. The polar data of the airfoil shape at the parametric point ξ is calculated from the polar data of the base airfoils as:

$$\mathbf{A}^{af}(\xi) = \frac{1}{c_s(\xi)} \sum_{j=1}^m \sum_{i=1}^{n^c} R_{i,p}(\xi) \mathbf{C}_{i,j} \mathbf{A}_j^{baf}, \quad (7.12)$$

where $\mathbf{A}_j^{baf}(\xi)$ is a matrix containing the polar data of the j^{th} base airfoil, where the columns contain the values of C_l , C_d , and C_m , for a range of angle of attack (α). The coefficient $\mathbf{C}_{i,j}$ ensures that the interpolation of the polar data is performed only between family airfoils.

Wind shear is taken into account when calculating the aerodynamic loads on a single blade (see figure 4.1). The wind speed, of all blades, at $r(\xi)$ is sampled for a range of, user supplied, azimuth angle and hub height wind speed U , using the power law defined in the IEC guidelines. The average aerodynamic force and moment at ξ are given by:

$$\bar{\mathbf{f}}(\xi) = \sum_{i=1}^{N_w} w_i \mathbf{f}_i(\xi), \quad \text{and} \quad \bar{\mathbf{m}}(\xi) = \sum_{i=1}^{N_w} w_i \mathbf{m}_i(\xi), \quad (7.13)$$

where N_w are the number of azimuth positions, w_i is the weight of the aerodynamic load calculated at the azimuth position ϕ_i , such that $\sum_{i=1}^{N_w} w_i = 1$.

7.2. AERO-STRUCTURAL COUPLING

In most cases of structural design or optimization of wind turbine blades, the aerodynamic loads are applied as fixed loads, meaning the aerodynamic loads are not dependent on the structural deformation. This assumption is only valid for stiff structures. For flexible structures, the aerodynamic loads are dependent on the structural deformation and vice-versa. The aeroelastic solution is obtained by equating the internal loads with external loads, expressed mathematically as,

$$\mathbf{R} = \mathbf{f}_{int}(\mathbf{q}, \mathbf{u}) - \mathbf{f}_{ext}(\mathbf{q}, \mathbf{u}) = \mathbf{0}, \quad (7.14)$$

where \mathbf{R} is the residual vector, \mathbf{p} is the generalized displacement and rotation vector, and u is the mean wind speed. The generalized internal and external load vectors (\mathbf{f}_{int} , and \mathbf{f}_{ext}) are defined as,

$$\mathbf{f}_{int} = \mathbf{f}_s - \omega^2 \mathbf{K}_{cs} \mathbf{p}, \quad \text{and} \quad \mathbf{f}_{ext} = \mathbf{f}_a + \mathbf{f}_g + \omega^2 \mathbf{f}_{cs}, \quad (7.15)$$

where ω is the rotational speed, and \mathbf{f}_s and \mathbf{f}_{cs} are the generalized structural and centrifugal load vectors. The generalized load vector for the aerodynamic loads (\mathbf{f}_a) is calculated using the principle of virtual work,

$$\mathbf{f}_a = \int_0^1 \left(\frac{\partial \mathbf{u}^t}{\partial \mathbf{p}} \Lambda_a \bar{\mathbf{f}} + \frac{\partial \theta^t}{\partial \mathbf{p}} \Lambda_a \bar{\mathbf{m}} \right) J d\xi, \quad (7.16)$$

where J is the Jacobian, given in equation 4.3, that relates the ξ -parameter space to the S -parameter geometrical space.

Aeroelastic equilibrium is achieved when the residual converges to zero. To simulate the operation of pitch regulated wind turbine rotors, an additional equilibrium equation is added, namely the power after the rated wind speed is equal to the rated power. An additional variable, the pitch angle, is added to the generalized displacement and rotation vector \mathbf{p} as, $\mathbf{p}_\theta = \{\mathbf{p}^t, \theta\}^t$. Therefore, the augmented equilibrium equations are,

$$\mathbf{R}_\theta = \left\{ \begin{array}{l} \mathbf{f}_{int}(\mathbf{p}_\theta, u) - \mathbf{f}_{ext}(\mathbf{p}_\theta, u) \\ P(\mathbf{p}_\theta, u) - P_{rated} \end{array} \right\} = \mathbf{0}, \quad (7.17)$$

where P_{rated} and P are the rated power and the power calculated at wind speed u .

The non-linear aeroelastic equilibrium is calculated by dividing the wind speed u into a given number of steps, controlled by the parameter λ , running from 0 to 1. At a given wind speed λu , a prediction of the equilibrium point for the next wind speed is made by linearising the equilibrium equation 7.17 around the current equilibrium point. Followed by a correction phase, keeping λ constant and varying the generalized coordinates \mathbf{p}_θ until the equilibrium equations in 7.17 are satisfied.

7.3. AEROELASTIC VERIFICATION

AERODYNAMIC VERIFICATION

The aerodynamic module of the present method is validated using the experimental results of the EU-sponsored project *MEXICO*. For this project, a three bladed wind turbine rotor with a diameter of 4.5m is tested in a wind tunnel with dimensions: $9.5 \times 9.5\text{m}^2$. The rotor blade consists of the following airfoils: circular from 0 to 20% span, *DU91-W2-250* from 20 to 45% span, *RISO-A1-21* from 55 to 65% span, *NACA 64418* from 70 to 100% span. Detailed description of the experimental campaign and the dimensions of the wind turbine rotor can be found in [119]. The normal and tangential force distribution, calculated using the present method, are compared with experimental data of the *MEXICO* project, for tip speed ratio $\lambda = 6.7$, wind speed $U = 15\text{m/s}$ and rotational speed $\omega = 44.5\text{rad/s}$. The current method calculates the aerodynamic loads at 54 integration points. Figures 7.3a and 7.3b show the comparison of the normal and tangential force distribution for the pitch angles $\theta = -2.3^\circ$ and 0.7° respectively.

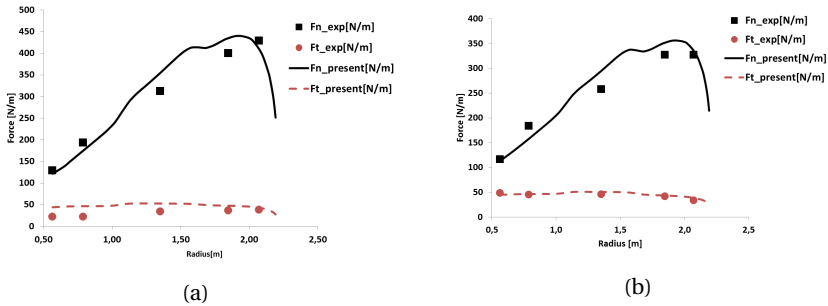


Figure 7.3: Comparison of the axial force F_n and tangential force F_t distribution with the *MEXICO* experimental results at wind speed of 15m/s and pitch angles: (7.3a) -2.3° and (7.3b) 0.7° .

From figures 7.3a and 7.3b, the present method predicts the normal and tangential forces quite well towards the root of the blade. The tip loads are predicted quite well with the current model, for both the pitch angles of -2.3° and 0.7° . There is a difference in the tangential force between the experimental data and the present method for the -2.3° pitch angle. The experimental data for the tangential force is not accurate, since pressure data is used to calculate the force distribution, which doesn't account for viscous forces. The tangential force distribution is dependent on the viscous force, thus is less accurately accounted by the experimental data. It is therefore concluded that the present model predicts the aerodynamic loads with sufficient accuracy.

AEROELASTIC VERIFICATION

The aeroelastic module is verified against *FAST*[71] and the commercially available aeroelastic code *GH Bladed* [16]. A quasi-steady analysis is per-

formed on the NREL 5MW reference turbine [72]. The blade geometry is generated using B-spline basis functions of degree 3 and knot spans of 20. The aerodynamic loads are calculated at 60 integration points. Detailed description of the turbine and blade properties can be found in [72].

The parameters used as representative of aeroelastic behaviour of the turbine are: power, thrust, (flap-wise) root bending moment, and the (flap-wise) tip deflection. The comparison of the parameters mentioned above, is shown in figures 7.4a to 7.5b for wind speeds 5 m/s till 18 m/s . The power curve, shown in figure 7.4a, agrees quite well between the three methods. The thrust calculated by the present method and GH Bladed agree (see figure 7.4b), while there is a noticeable difference between the results obtained by FAST and the present method. This is also observed for the (flap-wise) root bending moment 7.5a and tip deflection 7.5b.

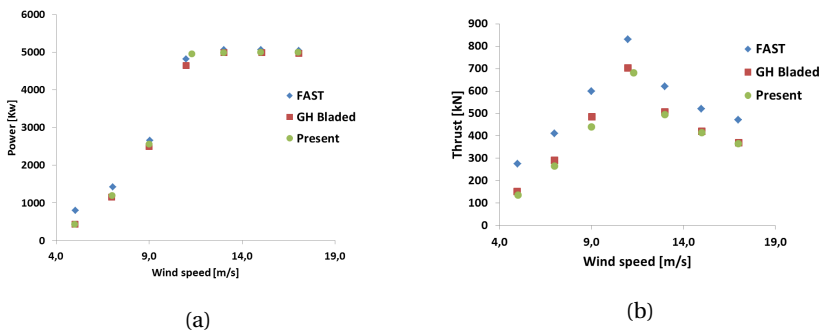


Figure 7.4: Comparison of: power(7.4a) and thrust(7.4b), between three methods, for the NREL 5MW machine.

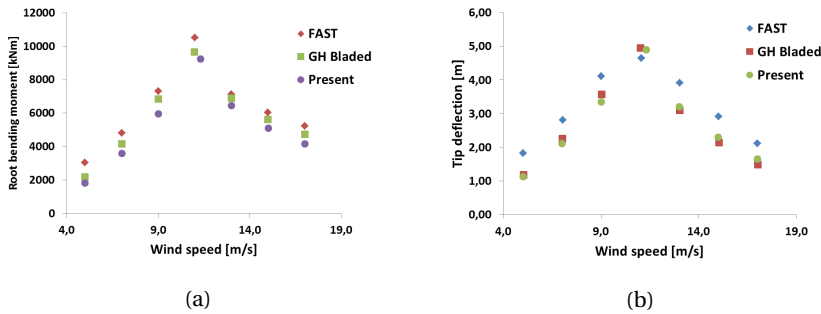


Figure 7.5: Comparison of: (flap-wise) root bending moment (7.5a) and (flap-wise) tip deflection, between three methods, for the NREL 5MW machine.

7.4. SUMMARY

An isogeometric based aero-structural model is presented for analysing the static aeroelastic loads on wind turbine rotor blade. The aerodynamic loads are calculated using a standard BEM theory. Moreover, the aerodynamic loads calculated using BEM theory are modified to account for change in the blade shape due to blade deformation. The aerodynamic module is validated against the experimental data of the EU-sponsored *MEXICO* project, showing a good match between experiment and the present method. Finally, the aeroelastic module is verified using the NREL 61.5m rotor blade as a baseline for comparison, showing a good agreement with results from GH *GH Bladed* and a small difference between the results from *FAST*. In the next chapter, the method of applying the aeroelastic loads unto the finite element model to calculate both the stress and buckling responses are elucidated, together with the description on the method of extraction the required responses from *NAS-TRAN*.

8

FINITE ELEMENT ANALYSIS

After generating the aeroelastic loads using the *low-fidelity* model, detailed structural analysis is carried out on the finite element model, described in chapter 4, using *NASTRAN*. The finite element solver *NASTRAN* is chosen for performing detailed structural analysis due to its wide acceptance in industry, particularly the aerospace branch. Furthermore, *NASTRAN* is capable of calculating the responses, together with the response sensitivities, of large structural entities with thousands of responses in computationally efficient manner [95].

This chapter is organized as follows. First the method to apply design dependent loads unto an *FE* model is described in section 8.1, followed by section 8.2, where the type of responses and how they are requested from *NASTRAN* analysis is elaborated. Finally, section 8.3 describes the method of efficiently exporting *NASTRAN* outputs.

8.1. APPLY DESIGN DEPENDENT LOADS

The finite element solver *NASTRAN* is used to perform detailed structural analysis, where the responses from *NASTRAN* are used to formulate the structural constraints that are passed to the optimizer, see chapter 9 on the type of responses used in the optimization framework. Both static and buckling analysis are carried out by applying the aeroelastic loads, calculated using the aeroelastic module, as design dependent loads in *NASTRAN*. The aeroelastic loads, consisting of: the aerodynamic, centrifugal and gravitational loads, are applied unto the *NASTRAN* model using the *RBE3* card described in section 4.2.1. The aeroelastic force and moment resultants per unit length are interpolated on the *RBE3* elements using the principle of virtual work as:

$$\mathbf{f}_{RBE3} = \int_0^1 \mathbf{N}^t(\xi) \mathbf{f}_{interp}(\xi) J(\xi) d\xi \quad \text{and} \quad \mathbf{m}_{RBE3} = \int_0^1 \mathbf{N}^t(\xi) \mathbf{m}_{interp}(\xi) J(\xi) d\xi, \quad (8.1)$$

where,

$$\mathbf{N}(\xi) = \begin{bmatrix} n_1(\xi) & 0 & 0 & n_2(\xi) & 0 & 0 \\ 0 & n_1(\xi) & 0 & 0 & n_2(\xi) & 0 \\ 0 & 0 & n_1(\xi) & 0 & 0 & n_2(\xi) \end{bmatrix}, \quad (8.2)$$

and n_1 and n_2 are linear shape functions of the two grid points connected to the *RBE3* element. The definition of the Jacobian $J(\xi)$ is given in equation 4.3. The force and moment vectors, $\mathbf{f}_{interp}(\xi)$ and $\mathbf{m}_{interp}(\xi)$ respectively, are linear interpolation of the aeroelastic loads, i.e.

$$\mathbf{f}_{interp}(\xi) = \Psi(\mathbf{f}(\xi_{ae}), \xi) \quad \text{and} \quad \mathbf{m}_{interp}(\xi) = \Psi(\mathbf{m}(\xi_{ae}), \xi), \quad (8.3)$$

where Ψ is the *Matlab interp1* function, used to interpolate the aeroelastic loads sampled at discrete parametric points ξ_{ae} . The aeroelastic force \mathbf{f} and moment \mathbf{m} resultants are the sum of the aerodynamic, centrifugal and gravitational loads at the converged aeroelastic equilibrium, defined mathematically as:

$$\mathbf{f} = \mathbf{f}_a + \mathbf{f}_g - \omega^2 \mathbf{f}_{ct} \quad \text{and} \quad \mathbf{m} = \mathbf{m}_a + \mathbf{m}_g - \omega^2 \mathbf{m}_{ct}, \quad (8.4)$$

where the subscripts a , g and ct indicate the aerodynamic, gravitational and centrifugal loads respectively. Figure 8.1 shows a representation of applying the aeroelastic loads onto the finite element model for detailed structural analysis, where the red and blue arrows indicate the distributed force and moment resultants respectively.

After applying the aeroelastic loads unto the *FE* model, a static and buckling analysis are run using *NASTRAN*, together with the sensitivity analysis of the stress and buckling responses. The the design optimization solution sequence is evoked with the execution control statement *SOL 200*, while setting the parameter *END=SENS* of the *NASTRAN DSAPRT* card to halt *NASTRAN* analysis after generating the responses with their sensitivities.

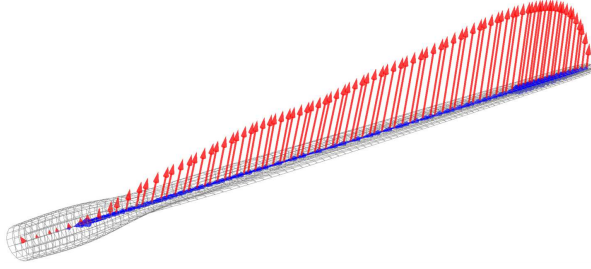


Figure 8.1: Application of aeroelastic loads unto a finite element model

8.2. RESPONSE DEFINITION

Detailed structural responses are key components in the aeroelastic optimization framework for wind turbine blades, proposed in the current thesis. The finite element solver *NASTRAN* is suitable to generate the relevant structural responses together with their sensitivities, making it useful in the current optimization framework. There are possibilities available in *NASTRAN* to specify the responses. The direct specification of the structural responses calculated by *NASTRAN* is done using the *DRESP1* card while the *DRESP2* card allows the combination of the *NASTRAN* responses into new ones. In the current framework, only the *DRESP1* is used to specify the various responses from *NASTRAN*. For further details on how to extract responses from *NASTRAN* can be found in [99].

8.2.1. STRESS

The stress responses from the finite element analysis are used to calculate the element membrane stress resultants, defined in section 9.2.2, which are then used to formulate the strain failure index, in section 9.4.2. The first type of responses requested from *NASTRAN*, using the *DRESP1* card, are the element stresses. For each element of the *FE* model, six different stress responses are requested using six *DRESP1* card, each card having the string *STRESS* as response type identifier. The type of stress responses requested in the current framework, for a single element, is shown in table 8.1. As can be seen in table

Table 8.1: Stress responses per element with *DRESP1*

Type	Distance from center	Item code
σ_x	z_1	3
σ_y	z_1	4
τ_{xy}	z_1	5
σ_x	z_2	11
σ_y	z_2	12
τ_{xy}	z_2	13

8.1, the three components of the stress σ at the top(z_1) and the three components at the bottom(z_2), in the direction of the shell thickness, are requested using the *NASTRAN* item code, required in *DRESP1*. By default *NASTRAN* outputs the stresses with respect in the element coordinate system. However, the stress outputs need to be in the material coordinate system, needed for the evaluation of the stress failure indices discussed in section 9.4.2. The stress outputs from *NASTRAN* are provided in the material coordinate system by specifying the '*PARAM OMID yes*' in the *NASTRAN* input file. Finally, each stress response has a unique ID.

8.2.2. BUCKLING

The buckling responses are used to formulate the buckling failure indices that are passed to the optimizer, defined in section 9.4.2. The buckling responses may be requested from the *NASTRAN* analysis using the *DRESP1* card. Each buckling load factor, requested from the *NASTRAN* analysis using the *EIGRL* card, is specified with the *DRESP1* card, each card having the string *LAMA* as response type identifier, the identification number of the buckling load factor, a unique *ID* and a label.

8.3. OUTPUT DEFINITION

The default method for retrieving the various responses from *NASTRAN* is the *f06* output format. The *f06* format contains the user specified vectors and matrices generated during the *NASTRAN* analysis and saves them in *ASCII* format. The the size of the *FE* model increases and the number of response also increase accordingly, the file size of the *f06* increases substantially, making it time consuming and inefficient to extract the data contained in the *f06* using another software such as *Matlab*. This of course will increase the computational time of the optimization process and an efficient method for saving data from the *NASTRAN* analysis is desired. Additionally, not all the responses calculate in *NASTRAN* can be retrieved using this method.

Fortunately, *NASTRAN* provides a possibility to change with its internal solution sequence by a means of a so-called *Alters*. The programming language of *NASTRAN*, referred to as *DMAP*, offers the possibility to write the *DMAP Alters* [116]. This language provides the possibility to insert additional commands to the various solution sequences of *NASTRAN* to get the desired result of the user. Amongst others, the *DMAP* programming language offers possibility to evoke the export of vectors, matrices and tables during the execution of a *NASTRAN* module. The user however needs to find out the proper *SUB-DMAP* module and the right position to insert the required *DMAP* commands to perform the desired action.

Handful *Alters* were written to export various vectors, matrices and tables to external files, where the content of these external files is described in the following subsection. The external files are provided in *NASTRAN*-specific output formats *op2* and *op4*, where *op2* is used to store tables and *op4* is used to

store vectors and matrices. The definition of the output format to extract vectors, matrices, and tables from any *SUBDMAP* module can be found in [116].

8.3.1. RESPONSES & SENSITIVITIES

The *FE* model used in the current optimization set-up, with m responses and n design variables, has a sensitivity matrix comprised of $n \times m$ elements. The current optimization set-up has structural responses in the order of 20000 and design fields in the order of 100, which amounts to $13 \times 100 \times 20000 = 26e^6$ elements of the sensitivity matrix. This is a large set of responses and sensitivity matrix that requires an efficient method of importing vectors and matrices from the *NASTRAN* analysis to speed up the optimization process.

This is achieved by extracting the design sensitivity matrix *DSCM2* and the response vector *RIVALRG*, requested using the *DRESP1* card. The *Alter* commands added to the *NASTRAN* file management section and the executive control section for requesting *DSCM2* and *RIVALRG* can be found in appendix A.1. The module where the code modifications are added is named *EXITOPT*.

In addition, the alter given in appendix A.1 is also capable of extracting a table called *DSCMCOL* which supplies a list, correlating each response in the *RIVALRG* vector to the columns of the sensitivity matrix *DSCM2*. This table is particularly important when different types of responses are requested from different load cases during a *NASTRAN* analysis. This table is written in binary *op2* format, where detailed description on this table can be found in [95].

8.3.2. ADDITIONAL ALTERS

As the *FE* model size increased together with the increase of different type of responses, some *NASTRAN* errors occurred, which are solved using the *Alter* command, listed in appendix A.2. This *Alter* corrects the error in the *DSCM2* sensitivity matrix sequence, such that the correlation table *DSCMCOL* refers, for each element of *RIVALRG*, the right column of the *DSCM2* matrix.

Furthermore, an additional *Alter* command, listed in appendix A.3, is provided to import the sensitivities of the aeroelastic force and moment resultants, discussed in section 8.1, into the *NASTRAN PSLGDV* module, which calculates the response sensitivities. Detailed elaboration on how the sensitivities of the *NASTRAN* responses are corrected, can be found in section 9.3.

8.4. SUMMARY

This wraps up the description of defining the *NASTRAN* responses and the various *Alters* used to export *NASTRAN* outputs and the *Alters* that correct the sensitivity results of the *NASTRAN* analysis. Now that all the responses and their sensitivities are calculated, it is time to formulate the response approximations that are suitable for the type of optimization method under consideration, as discussed in the next chapter.

9

RESPONSE APPROXIMATION

Gradient based optimizations are preferred over direct search methods for stiffness-based optimization. This is due to the fact that for responses that depend on large number of design variables, such as stiffness-based optimization, evaluating the responses using subsequent analysis is time consuming. Furthermore, replacing the analysis model with a method that approximates actual responses as a function of the design variables reduces further the computational costs significantly.

For stiffness-based optimization, the design variables consist of the thickness normalized membrane and bending stiffness matrices, $\hat{\mathbf{A}}$ and $\hat{\mathbf{D}}$, together with the laminate thickness h . After explaining the different analysis models of the optimization framework, introduced in chapter 3, the method of approximating the structural and aeroelastic responses needs to be defined. A general description of the approximation method employed in this thesis and the method of processing the sensitivities is given in section 9.2. Next, the description of the sensitivity analysis used in the current optimization framework is given in section 9.3. Finally, detailed description of the response approximations for the aeroelastic and structural responses is given in section 9.4.

9.1. METHODS IN DESIGN OPTIMIZATION

After deciding on the blade design and establishing the methodology for analysing the structural and aeroelastic responses, the design needs to be modified such that the predefined design criteria is met. This is accomplished by selecting an objective function, which is then used to evaluate the optimality of the design while satisfying the constraints that ensure the feasibility of the design. The optimization of the aeroelastic problem can be defined as the search for the global minimization of the objective function, subjected to various constraints, expressed mathematically as:

$$\begin{aligned} & \underset{\mathbf{x}}{\text{minimize}} && f_0(\mathbf{x}) \\ & \text{subject to} && f_i(\mathbf{x}) \leq 0; \quad i = 1, \dots, n, \\ & \text{and} && x_j^l \leq x_j \leq x_j^u; \quad j = 1, \dots, m, \end{aligned} \tag{9.1}$$

where n and m represents respectively, the number of constraints and design variables. The objective function is represented by f_0 while f_i represent the constraints, indicating the feasible domain of the design space, constrained by the lower x_j^l and upper x_j^u bound of the design variable \mathbf{x} . There is in general no explicit expression connecting the design variables to the responses. Therefore, numerical techniques are used to solve the minimization problem of equation 9.1.

There are different optimization strategies available, which can be classified in two categories: the direct search methods and gradient based methods. The direct search methods are only dependent on the function values and as such a large functional analysis is needed to find the optimum solution. The composite optimization under consideration is composed of large number of design variables. As a consequence, the number of function evaluations needed for direct search methods is very large, rendering this type of optimization scheme unsuited for practical applications. The second type of optimization strategies make use of the derivatives of the objective function and constraints, with respect to the design variables, in-order to find the descend direction. In this case, the number of constraints and the number of design variables influence substantially the computational time. However, the computational expense is compensated by the fast convergence rates achieved by this type of methods. In-order to mitigate the computational expense of gradient based methods, due to large number of design variables and constraints, approximation methods are used to replace the objective and constraints shown in equation 9.1. Two types of approximation methods exist; global approximation methods, such as response surface methods, and local approximation methods. The local approximation method refers to approximating the objective and constraints in the vicinity of current design point, making the response approximation valid only near the current design point.

The optimization method employed in this thesis is part of the local approximation methods. Using the local approximation method, the minimization problem of equation 9.1 is replaced by a local minimization of a subprob-

lem, of the form:

$$\begin{aligned} & \underset{\mathbf{x}}{\text{minimize}} && \bar{f}_0(\mathbf{x}) \\ & \text{subject to} && \bar{f}_i(\mathbf{x}) \leq 0; \quad i = 1, \dots, n, \\ & \text{and} && x_j^l \leq x_j \leq x_j^u; \quad j = 1, \dots, m, \end{aligned} \quad (9.2)$$

where \bar{f}_0 and \bar{f}_i are the approximate functions of the objective function and the constraints, around the local design point \mathbf{x} . The design values are updated based on equation 9.2, and the whole process is iterated until the convergence criteria, given in equation 9.3, is met.

$$\left| \frac{f_0|_{k+1} - f_0|_k}{f_0|_k} \right| \leq \delta_{conv}, \quad (9.3)$$

where k and δ_{conv} are respectively, the iteration number and the stopping criteria for the optimization formulation of equation 9.2. Detailed information on gradient based optimization using local approximation of the objective function and the constraints can be found in [55].

9.1.1. APPROXIMATION METHOD FOR COMPOSITE OPTIMIZATION

Considering the optimization scheme proposed in the previous section, linear approximation of the objective function and the constraints is formulated using *Taylor* series expansion of the responses in terms of the laminate membrane \mathbf{A} and bending \mathbf{D} stiffness matrix, together with the laminate thickness h . In addition, the responses are also approximated in terms of the reciprocals of the membrane and bending stiffness matrix. A general approximation form for a response f is written as:

$$\tilde{f} = \sum_{i=1}^n \left(\hat{\Psi}_i^m|_0 : \hat{\mathbf{A}}_i + \hat{\Psi}_i^b|_0 : \hat{\mathbf{D}}_i + \Phi_i^m|_0 : \mathbf{A}_i^{-1} + \Phi_i^b|_0 : \mathbf{D}_i^{-1} + \alpha_i|_0 h_i \right) + C_0, \quad (9.4)$$

where n represents the number of laminates used for response approximation while the superscripts m and b denote respectively, sensitivities with respect to the membrane and bending stiffness matrix. The approximation constant C_0 is calculated based on the response values at current design point. The operation $\Psi : \mathbf{D} = \text{trace}(\Psi \mathbf{D})$, is known as matrix contraction, which is composed of matrix multiplication followed by the summation of the diagonal elements. Although the response approximation in equation 9.5 is expressed in terms of the thickness normalized membrane and bending stiffness matrices, the sensitivity matrices (Ψ, Φ) are given to the optimizer. The linear and reciprocal sensitivities of a function f with respect to: membrane and bending stiffness matrix and laminate thickness, are defined as:

$$\Psi^m = \frac{\partial f}{\partial \mathbf{A}}, \quad \Psi^b = \frac{\partial f}{\partial \mathbf{D}}, \quad \Phi^m = \frac{\partial f}{\partial \mathbf{A}^{-1}}, \quad \Phi^b = \frac{\partial f}{\partial \mathbf{D}^{-1}}, \quad \alpha = \frac{\partial f}{\partial h}. \quad (9.5)$$

The accuracy of the response approximation is increased by expressing the approximation a combination of the linear and reciprocal terms. This however is not possible for all responses, since not all approximations will have the contributions of the linear and reciprocal terms at once, only the terms that provide the most accurate representation of the original response will be considered. Therefore, physical insight is necessary for all type of responses before formulating their approximate functions. The three important characteristics of the response approximation of equation 9.5 are: Convexity, Separability and Conservativeness.

CONVEXITY

Convexity of the approximated functions must be enforced to guarantee the existence of a global optimum in the approximated model. The linear terms in the approximated function are convex by default. However, the reciprocal terms are not necessary convex. One way of ensuring the convexity of the approximation is by simply omitting the reciprocal part from equation 9.5 if the response under consideration is not dependent on the reciprocal terms of the laminate stiffness. Another method would be to convexify the reciprocal part using the method described in [44].

SEPARABILITY

The separability of the design variables is inherent for the approximated function, since the function of equation 9.5 is composed as linear combination of laminate design variables. This feature facilitates separate consideration per laminate i in equation 9.5, allowing for efficient and parallel optimization process.

CONSERVATIVENESS

The conservativeness of the approximated response is enforced, which guarantees that the approximated response is always larger than the original response at the new design optimum of the approximation model. The optimization algorithm takes care of the conservativeness of the approximated model by adding damping coefficients to increase the conservativeness of the approximated function. The more damping is added to the response approximate, the closer the approximation minimum shifts towards the design point where the response is approximated, increasing the optimization iteration steps needed to reach the design optimum. The optimizer implemented in this work is able to vary, for each iteration, the conservativeness of the response approximation by changing, for each response, the level damping, see [66] for further details.

In the next section, description on sensitivity preprocessing steps is provided, which are then used to set-up the response approximation.

9.1.2. SENSITIVITY PROCESSING

The response sensitivities in equation 9.5 are provided in matrix form. Therefore the first step in formulating response approximation is grouping, for each

response, the sensitivities with respect to the laminate stiffness matrices into a matrix form as:

$$\frac{\partial f}{\partial \mathbf{A}} = \begin{bmatrix} \frac{\partial f}{\partial A_{11}} & \frac{\partial f}{\partial A_{12}} & \frac{\partial f}{\partial A_{13}} \\ \frac{\partial f}{\partial A_{12}} & \frac{\partial f}{\partial A_{22}} & \frac{\partial f}{\partial A_{23}} \\ \frac{\partial f}{\partial A_{13}} & \frac{\partial f}{\partial A_{23}} & \frac{\partial f}{\partial A_{33}} \end{bmatrix}, \quad \frac{\partial f}{\partial \mathbf{D}} = \begin{bmatrix} \frac{\partial f}{\partial D_{11}} & \frac{\partial f}{\partial D_{12}} & \frac{\partial f}{\partial D_{13}} \\ \frac{\partial f}{\partial D_{12}} & \frac{\partial f}{\partial D_{22}} & \frac{\partial f}{\partial D_{23}} \\ \frac{\partial f}{\partial D_{13}} & \frac{\partial f}{\partial D_{23}} & \frac{\partial f}{\partial D_{33}} \end{bmatrix}. \quad (9.6)$$

The linear components of the approximation function shown in equation 9.4 are in terms of the thickness normalized membrane $\hat{\mathbf{A}}$ and bending $\hat{\mathbf{D}}$ stiffness matrices. However, the optimizer requires the sensitivity matrices with respect to the non-normalized laminate stiffness components. Hence, the sensitivity matrices from *NASTRAN*, which are with respect to the thickness normalized laminate stiffness components, are transformed to the regular laminate stiffness components using:

$$\begin{aligned} \frac{\partial f}{\partial \mathbf{A}} &= \frac{1}{\hat{h}} \frac{\partial f}{\partial \hat{\mathbf{A}}}, \\ \frac{\partial f}{\partial \mathbf{D}} &= \frac{12}{\hat{h}^3} \frac{\partial f}{\partial \hat{\mathbf{D}}}, \\ \frac{\partial f}{\partial h} &= \frac{\partial f}{\partial \hat{h}} - \frac{1}{\hat{h}^2} \frac{\partial f}{\partial \hat{\mathbf{A}}} : \mathbf{A} - \frac{36}{\hat{h}^4} \frac{\partial f}{\partial \hat{\mathbf{D}}} : \mathbf{D}, \end{aligned} \quad (9.7)$$

where $\hat{h} = h$. Furthermore, the response sensitivities with respect to the reciprocal terms of the membrane and bending stiffness matrix are obtained from the linear sensitivity matrices (Ψ^m, Ψ^b) using the following conversion:

$$\Phi^m = -\mathbf{A}^T \Psi^m \mathbf{A}, \quad \Phi^b = -\mathbf{D}^T \Psi^b \mathbf{D}, \quad (9.8)$$

where the superscript T denotes matrix transpose.

Before proceeding to the formulation of response approximations, the responses used in current optimization campaign, either as objective or constraints, are described in the next section.

9.2. RESPONSE

The current optimization work contains two types of responses; responses derived from the aeroelastic analysis and responses from the finite element analysis. Section 9.2.1 describes the responses from aeroelastic analysis, which are used to formulate the aeroelastic constraints. In section 9.2.2, the responses from the finite element analysis that are used to formulate the structural constraints are described. Additionally, the aeroelastic responses are used to formulate the cost of energy, which is one of the responses used as objective during the optimization process, see section 9.2.3.

9.2.1. AEROELASTIC RESPONSES

This section describes the aeroelastic responses used to formulate the aeroelastic constraints and for calculating the cost of energy. The aeroelastic re-

sponses considered in current work are: torque, thrust, power and tip deflection. The first three aeroelastic responses are calculated based on the total aerodynamic force resultant (\mathbf{f}_r) and the moment resultant (\mathbf{m}_r) calculated at the blade root. The total aerodynamic force and moment resultants are calculated for a hub-height wind speed u as:

$$\mathbf{f}_r(u) = \int_0^L \mathbf{f}(u, s) ds, \quad \text{and} \quad \mathbf{m}_r(u) = \int_0^L (\mathbf{m}(u, s) + \mathbf{r}(u, s) \times \mathbf{f}(u, s)) ds, \quad (9.9)$$

where L is the blade length. The aerodynamic force and moment along the blade length are given by \mathbf{f} and \mathbf{m} respectively. Further details on the aerodynamic loads is given in chapter 7. The the position vector of the deformed beam axis with respect to the origin of the rotating frame is denoted as \mathbf{r} , see chapter 4.

Since the aeroelastic analysis is performed for finite (hub-height) wind speeds, the maximum for each aeroelastic response, given in equations 9.10 to 9.13, is calculated using the bracketing method. Figure 9.1 shows a schematic representation of the bracketing scheme to find the maximum of each response. The bracketing scheme finds the maximum of each response in two

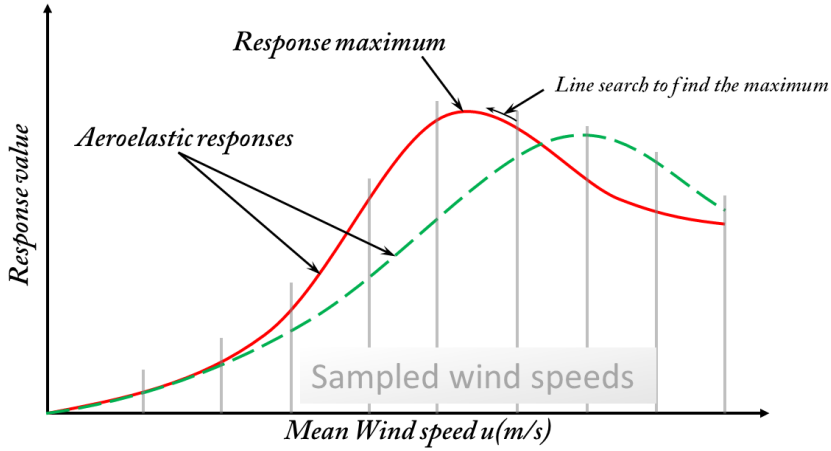


Figure 9.1: Bracketing method to find the maximum values of the aeroelastic responses

steps. First, for a given list of response values, calculated at sampled wind speeds, the wind speed range (u^l, u^u) containing the response maximum is determined. Second, assuming the response curve is convex between (u^l, u^u) , the line search method is used to find the wind speed $\tilde{u} \in [u^l, u^u]$ for which the response has reached its maximum value.

TORQUE

The aeroelastic torque response affects the initial capital cost of the wind turbine cost model, see section 9.2.3. The cost of the generator, high and low

speed shafts, and the cost of the gear box are all dependent on the torque response. The total torque on the low speed shaft is calculated as:

$$r_{to}(u) = B \mathbf{e}_3^t \mathbf{m}_r(u) \quad (9.10)$$

where B refers to the number of blades and $\mathbf{e}_3 = \{0, 0, 1\}^t$.

THRUST

Again from the wind turbine cost model, the costs of the tower and the support structure are affected primarily by the total thrust on the wind turbine rotor. The total thrust is the sum of the thrusts on all the blades, calculated as:

$$r_{th}(u) = B \mathbf{e}_3^t \mathbf{f}_r(u), \quad (9.11)$$

where \mathbf{f}_r is the total aerodynamic force on an single blade.

POWER

The aerodynamic power is used to calculate the annual energy production, which is a component of the cost of energy. Furthermore, the maximum aerodynamic power is used to calculate the cost of power electronics (see section 9.2.3). The aerodynamic power is calculates as:

$$P(u) = \omega(u) B \mathbf{e}_3^t \mathbf{m}_r(u), \quad (9.12)$$

where ω is the rotational speed.

MAXIMUM BLADE DEFLECTION

For upwind turbines, a constraint on the maximum blade deflection is imposed so that the blades do not hit the tower during operation. Since the deformation of the blade resembles the deformation of a cantilever beam, the maximum blade deflection is at the blade tip. The tip deflection of the blade is calculated as:

$$\delta_{tip}(u) = \sum_{i=1}^n R_{i,p}(\xi = 1) \mathbf{u}_i(u), \quad (9.13)$$

where $\mathbf{u}_i(u)$ is the displacement vector of the beam axis at control point i .

9.2.2. STRUCTURAL RESPONSES

The structural responses are essential in the current optimization framework to size the wind turbine blade. The structural responses consist of stresses of all shell elements (of the finite element model), and the buckling load factors.

STRESS

Using the stress responses obtained from the static analysis solution by *NASTRAN*, the membrane stress resultants $\mathbf{N} = \{N_x, N_y, N_{xy}\}^t$ of element i are given by:

$$\mathbf{N}_i = \frac{1}{2} \hat{h}_i \left(\boldsymbol{\sigma}_i^u + \boldsymbol{\sigma}_i^l \right), \quad (9.14)$$

where \hat{h}_i is the shell thickness of element i and σ_i^u and σ_i^l are the stresses at the upper and lower end of element i . The method of extracting the stress responses σ_i^u and σ_i^l is covered in chapter 8.

BUCKLING

In addition to the stress responses, *NASTRAN* is also used to calculate the buckling load factor λ_n . *NASTRAN* calculates the buckling load factor based on the equation:

$$\{\mathbf{K} + \lambda_n \mathbf{K}_d\} \boldsymbol{\phi}_n = \mathbf{0}, \quad (9.15)$$

where $\boldsymbol{\phi}_n$ is the mode shape of the buckling load λ_n , whereas \mathbf{K} , and \mathbf{K}_d are respectively, the stiffness matrix and differential stiffness of the finite element model. The differential stiffness is a function of the geometry and the displacement, where the displacement is a solution of a particular static solution used in the buckling analysis. Again, in chapter 8 the method of extracting the buckling loads together with their sensitivities is explained.

9.2.3. MASS & COST OF ENERGY

MASS

The blade mass is also part of the optimization process. It is used to calculate the cost of energy. Furthermore, the blade mass can also be used as an objective function. The blade mass depends on the laminate thickness and its density. The density of all elements is not necessarily the same, because some parts of the blade are made up of sandwich structures (to prevent buckling). The blade mass is calculated as:

$$M = \int_0^L m_0 ds, \quad (9.16)$$

where L is the blade length and m_0 is the mass per unit length, calculated in section 6.5.

COST OF ENERGY

The cost model described in this section is based on the *NREL* cost model for pitch regulated wind turbines and modified in [106] to calculate the Cost Of Energy (*COE*) of stall regulated wind turbines. The *COE* is used to evaluate the optimality of each design iteration that meets the desired criteria.

The *COE* is calculated from the expected annual energy production and the cost of each *HAWT* component as:

$$COE = \frac{FCR \times ICC}{AEP_{Net}} + AOE, \quad (9.17)$$

where *FCR* is the fixed charge rate and *ICC* is the initial capital cost. The net annual energy production AEP_{Net} is defined as:

$$AEP_{Net} = \text{availability} \times \int_{u_{ci}}^{u_{co}} P(u) f_p(u) du, \quad (9.18)$$

where u_{ci} and u_{co} are the cut-in and cut-out wind speeds respectively, $P(u)$ is the power production as a function of the mean wind speed, and $f_p(u)$ is the probability of occurrence, calculated with the Weibull distribution [59]. The shape and scale parameters for the Weibull distribution are chosen to match an off-shore wind climate[97].

The annual operation expenses, AOE , are expressed as:

$$AOE = \frac{OM + LRC}{AEP_{Net}} + LLC, \quad (9.19)$$

where OM are the levelized operation and maintenance costs, LRC is the levelized replacement and overhaul cost, and LCC is the land lease cost. It is assumed that for stall regulated machines, the pitch mechanism is not used for power regulation, while the component is still used during emergency or parked state of the turbine. Furthermore, the LLC is assumed unaffected in current optimization while the remaining components of the COE are either dependent on the design variables or on the pitch factor. The pitch factor determines the fraction of OM and LRC compared to the respective cost components of the *NREL 5MW* pitch machine, assuming that the pitch system is not used for power regulation, such that:

$$OM = \beta OM_{ref} \quad \text{and} \quad LRC = \beta LRC_{ref} \quad (9.20)$$

where OM_{ref} and LRC_{ref} are respectively, the levelized operation and maintenance costs and the levelized replacement and overhaul costs of the *NREL5MW* pitch machine, while $\beta \in [0, 1]$ is the pitch factor.

During the optimization process, the change in initial capital cost, ICC , is calculated from the load overshoots: power, torque and thrust together with the blade mass. The overshoots in power, torque, and thrust are defined as the maximum power, torque, or thrust of the new design divided by its rated equivalent of the *NREL 5MW* pitch machine, i.e.:

$$\psi_i = \frac{r_i}{r_i^{ref}}, \text{ for } i = 1 \dots 4, \quad (9.21)$$

where i refers to the type of overshoot. The aeroelastic response of the new design is denoted by r_i , while r_i^{ref} refers, for the same response, the (rated) aeroelastic response of the *NREL 5MW* pitch regulated machine. The ICC of each *HAWT* component of the *NREL 5MW* pitch regulated machine is multiplied by the appropriate ψ_i to determine the ICC of the new design. Table 9.1 contains component-wise breakdown of the ICC and the design driving load types for the relevant *HAWT* component, which is consistent with the cost model of [49]. The electrical interface cost is calculated assuming a 7 by 7 array spacing [106]. Furthermore, it is noted that the initial capital costs of the blades and hub are affected by the blade mass while the blade mass is sized by the structural load types: stress, buckling and Maximum Blade Deflection (MBD). The effect of the structural load types on the ICC components is also

Table 9.1: Design driving load types for each HAWT component and breakdown of ICC per component

Load Type	HAWT components(% of ICC)
Stress, Buckling & MBD	Blades(8), Hub(1)
Maximum Torque	Low Speed Shaft(< 1), Gearbox(7), Main Brakes(< 1), Generator(3)
Maximum Power	Power Electronics(4), Electrical Connections(2), Nacelle(< 1), Hydraulics and Cooling(< 1), Electrical Interface(13)
Maximum Thrust	Tower(7), Support Structures(16)

shown in table 9.1. The present cost model assumes a fixed rotor radius, resulting in fixed cost for the main bearings, yaw drive and bearings, nose cone, control hardware and marinization.

Figure 9.2 illustrates the sensitivity of relative ICC to the overshoots, i.e.: power, torque, thrust, and blade mass, where ICC_{ref} refers to the ICC of NREL 5MW pitch regulated machine. The ICC is most sensitive to thrust overshoot and least sensitive to the change in blade mass. Furthermore, figure 9.2 shows that large load overshoots result only in relatively small increase in ICC, which is expected since the turbine components contribute only a fraction of the total ICC.

This cost model is only a first order approximation of the COE for stall regulated machines, provided that the load overshoots for the new design are not large (≤ 1.5). For large load overshoots, the linearisation of the ICC in-terms of the load overshoots is not accurate and a different cost model need to be formulated. Therefore, the present cost model serves only to show the trend in COE reduction during stiffness optimization of stall regulated wind turbine blades.

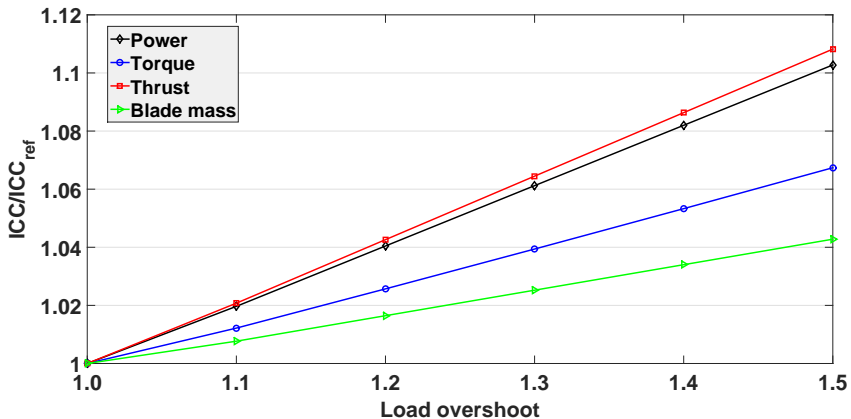


Figure 9.2: Sensitivity of ICC to different overshoots [106]

9.3. SENSITIVITY ANALYSIS

Design sensitivity analysis is the calculation of the quantitative information on how a system is affected by changing an arbitrary design variable, providing essential information to connect mathematical optimization formulations and structural/aeroelastic analysis. Isogeometric concept provides the ability for analytic sensitivity calculations, not only enhancing the accuracy of the design sensitivities but also reducing the computational time resulting in significant performance enhancement of the optimization process [35]. In accordance with IGA paradigm, the design sensitivities are also evaluated with respect to control point properties.

The responses used for optimization may be categorized in two set: responses from the aeroelastic module and responses from the *FE* module. For responses from the aeroelastic module, the adjoint method is used to evaluate the sensitivities, since there are in general more design variables than responses. For the responses from the *FE* module, *NASTRAN* uses the direct method to calculate the sensitivities of the responses. A brief description of both methods is presented in the following sub-sections.

9.3.1. AEROELASTIC

The first derivative of a single response from the aeroelastic module with respect to a single design variable x is written as:

$$\frac{dr}{dx} = \frac{\partial r}{\partial x} + \lambda^T \frac{\partial \mathbf{R}}{\partial x}, \quad (9.22)$$

where $\frac{\partial \mathbf{R}}{\partial x}$ is the first derivative of the residual with respect to x and λ represents the adjoint vector obtained by solving the linear system:

$$\mathbf{K}_{eff}^T \lambda = -\frac{\partial r}{\partial \delta \mathbf{p}}, \quad (9.23)$$

where \mathbf{K}_{eff} is the effective stiffness, which is the first derivative of the residual vector with respect to the generalized coordinates $\delta \mathbf{p}$. The residual, which is the difference between the internal and external loads, depends explicitly on the design variables.

9.3.2. FINITE ELEMENT

NASTRAN is capable of calculating the sensitivity of the structural responses with respect to the design variables. The design optimization solution sequence *SOL 200* is employed to generate the responses and their sensitivities with respect to the design variables. The analysis is set-up such that *NASTRAN* is terminated after computing the requested responses together with the sensitivity results. *NASTRAN* employs, depending on the type of responses, two methods of sensitivity analysis, i.e direct or adjoint method [95]. However, for the responses requested in the present method, *NASTRAN* employs solely the direct method. The total derivative of a response r with respect to a design

variable x is defined as:

$$\frac{\partial r}{\partial x} = \frac{\partial r}{\partial \mathbf{u}} \frac{\partial \mathbf{u}}{\partial x}, \quad (9.24)$$

where \mathbf{u} is the solution of the static equilibrium equation:

$$\mathbf{K}\mathbf{u} = \mathbf{f}, \quad (9.25)$$

where \mathbf{K} and \mathbf{f} are respectively, the structural stiffness matrix and external load vector. The partial derivative of \mathbf{u} with respect to x is given as:

$$\mathbf{K} \frac{\partial \mathbf{u}}{\partial x} = \frac{\partial \mathbf{f}}{\partial x} - \frac{\partial \mathbf{K}}{\partial x} \mathbf{u}, \quad (9.26)$$

where the right hand side of equation 9.26 is denoted as a pseudo load vector. The pseudo load vector is composed of two terms, one of which is the derivative of the applied load \mathbf{f} with respect to the design variable x . If static analysis is carried out, *NASTRAN* does not calculate the derivative of the applied load \mathbf{f} with respect to the design variable x . Therefore, the sensitivity of the applied load (design dependent load), $\frac{\partial \mathbf{f}}{\partial x}$, needs to be supplied explicitly to *NASTRAN*.

NASTRAN calculates, for a change in a single design variable Δx , the change in the displacement vector $\Delta \mathbf{u}$, using finite difference:

$$\mathbf{K} \Delta \mathbf{u} = - \left(\Delta \mathbf{K} \mathbf{u} - \frac{\partial \mathbf{f}}{\partial x} \Delta x \right), \quad (9.27)$$

where Δx is calculated inside *NASTRAN* as $\Delta x = DELB x_0$, for $DELB = 0.001$, where x_0 is the current design point. The first term on the right hand side of equation 9.27 is calculated by *NASTRAN*, whereas the second term is provided explicitly to *NASTRAN* using the *DMAP* programming language [116], see section 8.3.2 for further details. Detailed description on sensitivity analysis of *NASTRAN* responses can be found in [96].

9

9.4. RESPONSE APPROXIMATION

This section describes the approximation of the responses used in the present optimization framework. In general the response approximations are either in terms of the laminate membrane and bending stiffness matrices or their reciprocal part, together with the laminate thickness. Due to the necessity of the approximation to be convex to ensure a global minimum of the approximate function, reciprocal approximations that are not convex are convexified using the method presented in [66]. The convexification process introduces a linear term that replaces the non-definite part of the reciprocal term.

It is noted that the sensitivities in the approximation formulation are denoted as Ψ , Φ , and α , irrespective of the response type. Furthermore, the superscripts m and b on Ψ and Φ represent respectively, sensitivities with respect to laminate membrane and bending stiffness matrix.

9.4.1. AEROELASTIC RESPONSES

POWER

It may be necessary to set a limit on the power overshoot in order to guarantee the validity of the cost model presented in section 9.2.3. The failure index for the power overshoot is given by:

$$r^p = \frac{1}{\gamma^p} \frac{P}{P_{ref}}, \quad (9.28)$$

where P and P_{ref} are respectively, the maximum power and the rated power of the *NREL 5MW* machine, with the safety factor for the power overshoot denoted by γ^δ . It is not certain that the reciprocal approximation is convex. Therefore, a linear approximation is employed for this failure index, of the form:

$$\tilde{r}^p \simeq \sum_j \left(\Psi_j^m : A_j + \Psi_j^b : D_j + \alpha_j h_j \right), \quad (9.29)$$

where Ψ_j^m, Ψ_j^b and α_j are the derived from the sensitivities of the power P with respect to a laminate membrane and bending stiffness together with the laminate thickness.

TIP DEFLECTION

For upwind wind turbine configuration, the maximum blade deflection is constrained so that the blades do not hit the tower. The failure index for the maximum blade deflection is defined as:

$$r^\delta = \frac{1}{\gamma^\delta} \frac{\delta_{tip}}{\delta_{ref}}, \quad (9.30)$$

where δ_{tip} and δ_{ref} are respectively, the tip displacement and the reference value for the tip displacement. The parameter γ^δ defines the safety factor for failure index of maximum blade deflection. This ensures that failure index larger than one indicates that the blade deflection is larger than the allowed clearance. The tip deflection is dependent on the inverse of the membrane and bending stiffness, indicating that reciprocal approximation of this failure index is appropriate. However the derivative of the tip displacement with respect to the membrane and bending stiffness is in general not positive definite. A linear approximation to the reciprocal part is added by convexifying the reciprocal part. The approximate function of the failure index is then in the form of:

$$\tilde{r}^\delta \simeq \sum_j \left(\Phi_j^m : A_j^{-1} + \Psi_j^m : A_j + \Phi_j^b : D_j^{-1} + \Psi_j^b : D_j + \alpha_j h_j \right). \quad (9.31)$$

9.4.2. STRUCTURAL RESPONSES

STRENGTH

The strength is evaluated based on strain-based failure index that is calculated using the strain failure envelope. The strain failure envelope is based on

the lamination parameters[66], accounting for all possible ply angles, which ensures a conservative boundary. The failure index is a ratio between the calculated strains and the corresponding strains on the failure envelope. This means the failure strains should remain less than or equal to one, $r \leq 1$, to avoid material failure. The laminate strain is given as a function of the laminate membrane stiffness \mathbf{A} and the stress resultant \mathbf{N} as:

$$\boldsymbol{\epsilon} = \begin{Bmatrix} \epsilon_x \\ \epsilon_y \\ \gamma_{xy} \end{Bmatrix} = \mathbf{A}^{-1} \mathbf{N}. \quad (9.32)$$

The failure index is expressed in terms of the membrane stiffness and stress resultants, such that:

$$\mathbf{r}^s = \mathbf{N}^T \mathbf{A}^{-1} \mathbf{g}, \quad (9.33)$$

where $\mathbf{g} = \frac{\partial r^s}{\partial \boldsymbol{\epsilon}}$ is the gradient of the failure index with respect to the strain vector. From equation 9.33, it is evident that a reciprocal approximation of the failure index with respect to the membrane stiffness of the element under consideration is preferable. Consequently, the strain failure index of element i depends on the inverse of the local membrane strain stiffness and the stress resultant. The approximation of the strain failure index then becomes:

$$\tilde{r}_i^s \simeq \frac{\partial r_i^s}{\partial \mathbf{A}_i^{-1}} : \mathbf{A}_i^{-1} + \mathbf{s}_i^t \Delta \mathbf{N}_i, \quad (9.34)$$

where $\mathbf{s}_i = \frac{\partial r_i^s}{\partial \mathbf{N}_i}$. The term $\Phi_i^m = \frac{\partial r_i^s}{\partial \mathbf{A}_i^{-1}}$ is in general not positive definite [74]. Therefore, a local linear approximation Ψ_i^m is added to replace the non-definite part in Φ_i^m . The resulting approximation of the strain-failure index is then given as:

$$\tilde{r}_i^s \simeq \Phi_i^m : \mathbf{A}_i^{-1} + \Psi_i^m : \mathbf{A}_i + \mathbf{s}_i^t \Delta \mathbf{N}_i \quad (9.35)$$

In general, the change in load \mathbf{N}_i of element i is dependent on the stiffness changes of all other elements j . Therefore, change in the local stress resultant $\Delta \mathbf{N}_i$ is approximated linearly in terms of the membrane and bending stiffness matrices together with the laminate thickness as:

$$\Delta \mathbf{N}_i \simeq \sum_j \frac{\partial \mathbf{N}_i}{\partial \mathbf{A}_j} : \mathbf{A}_j + \frac{\partial \mathbf{N}_i}{\partial \mathbf{D}_j} : \mathbf{D}_j + \frac{\partial \mathbf{N}_i}{\partial h_j} h_j. \quad (9.36)$$

The failure index and its local sensitivities, i.e. r_i^s , Φ_i^m , Ψ_i^m , and \mathbf{s}_i , are generated based on the strain envelope, which is a function of \mathbf{A}_i and \mathbf{N}_i . The sensitivities in equation (9.36) are derived from the sensitivities of the stress responses generated by *NASTRAN*, where the sensitivities are with respect to the thickness normalized membrane $\hat{\mathbf{A}}$ and bending $\hat{\mathbf{D}}$ stiffness matrix, and

the laminate thickness \hat{h} , i.e.:

$$\begin{aligned}\frac{\partial N_i}{\partial \hat{A}_j} &= \frac{1}{2} \hat{h}_i \left(\frac{\partial \sigma_i^u}{\partial \hat{A}_j} + \frac{\partial \sigma_i^l}{\partial \hat{A}_j} \right) \\ \frac{\partial N_i}{\partial \hat{D}_j} &= \frac{1}{2} \hat{h}_i \left(\frac{\partial \sigma_i^u}{\partial \hat{D}_j} + \frac{\partial \sigma_i^l}{\partial \hat{D}_j} \right) \\ \frac{\partial N_i}{\partial \hat{h}_j} &= \frac{1}{2} \hat{h}_i \left(\frac{\partial \sigma_i^u}{\partial \hat{h}_j} + \frac{\partial \sigma_i^l}{\partial \hat{h}_j} \right) + \frac{1}{2} (\sigma_i^u + \sigma_i^l) \delta_{ij},\end{aligned}\quad (9.37)$$

where δ_{ij} is equal to one for $i = j$, and zero otherwise. Sensitivities with respect to the thickness normalized variables ($\hat{h}_j, \hat{A}_j, \hat{D}_j$) are transformed to the sensitivities with respect to (h_j, A_j, D_j) using equation 9.7. Finally, the sensitivity of the membrane stress resultant, N , with respect to the control point laminate variables is calculated using equation 4.14.

BUCKLING

Buckling analysis is performed using the *FE* model of the wind turbine blade. For each mean wind speed, the aeroelastic load distribution, along the blade span, is applied to the *FE* model, followed by static and buckling analysis. The buckling failure index is calculated as:

$$r^b = \frac{1}{\gamma^b} \frac{1}{\lambda}, \quad (9.38)$$

where, γ^b is a buckling safety factor. Equation 9.38 indicates that the buckling failure index should remain less than or equal to one to avoid failure under buckling. The derivative of the buckling failure index r_i^b with respect to an arbitrary design variable x is given by:

$$\frac{\partial r_i^b}{\partial x} = -\frac{1}{\gamma^b} \frac{1}{\lambda_i^2} \frac{\partial \lambda_i}{\partial x}. \quad (9.39)$$

Based on the equation for the buckling load factor, given in equation 9.15, the derivative of λ_i with respect to x may be defined as:

$$\frac{\partial \lambda_i}{\partial x} = (\phi_i^t \mathbf{K}_d \phi_i)^{-1} \left\{ \phi_i^t \frac{\partial \mathbf{K}}{\partial x} \phi_i + \lambda_i \phi_i^t \frac{\partial \mathbf{K}_d}{\partial x} \phi_i \right\}. \quad (9.40)$$

Substituting equation 9.40 into 9.39 and collecting terms together yields:

$$\frac{\partial r_i^b}{\partial x} = -\frac{1}{\gamma^b} \frac{1}{\lambda_i^2} (\phi_i^t \mathbf{K}_d \phi_i)^{-1} \left\{ \phi_i^t \frac{\partial \mathbf{K}}{\partial x} \phi_i + \lambda_i \phi_i^t \frac{\partial \mathbf{K}_d}{\partial x} \phi_i \right\}. \quad (9.41)$$

Similar to the sensitivity of the stresses σ_i , *NASTRAN* calculates the sensitivity of the buckling load with respect to the thickness normalized membrane and bending stiffness matrix and the laminate thickness. The sensitivities are then

converted to the sensitivities with respect to laminate membrane and bending stiffness using equation 9.7. Finally, the sensitivity of a buckling response with respect to the control point laminate variables is calculated using equation 4.14.

Examining equation 9.41, the term that depends on the global stiffness matrix, \mathbf{K} , is approximated with respect to the reciprocal membrane and bending stiffness matrices, since this term depends solely on the stiffness of the model. However, the reciprocal approximation of this term is in general not positive definite, which requires the addition of linear approximation to replace the non definite part by convexifying this term [66]. Again from equation 9.41, the term that depends on the differential stiffness \mathbf{K}_d is approximated with respect to the linear membrane and bending stiffness matrices, since this term is dependent on the load redistribution. In addition, the buckling failure index is also approximated in terms of the laminate thickness. The approximate function of the buckling failure index then reads as:

$$\tilde{r}_i^b \simeq \sum_j \left(\Phi_{ij}^m : \mathbf{A}_j^{-1} + \Psi_{ij}^m : \mathbf{A}_j + \Phi_{ij}^b : \mathbf{D}_j^{-1} + \Psi_{ij}^b : \mathbf{D}_j + \alpha_{ij} h_j \right), \quad (9.42)$$

where i refers to the buckling load factor and j refers to the laminate that approximates the buckling response. The sensitivity coefficients Φ_{ij}^m , Φ_{ij}^b , Ψ_{ij}^m , Ψ_{ij}^b , and α_{ij} are extracted from 9.41.

9.4.3. OBJECTIVE FUNCTIONS

MASS

Since the mass depends solely on the laminate thickness, its approximation reduces to:

$$\tilde{r}^m \simeq \sum_j \alpha_j h_j, \quad (9.43)$$

where $\alpha_j = \frac{1}{M_{ref}} \frac{\partial M}{\partial h_j}$, M is the blade mass for the new design, and M_{ref} is the blade mass of the *NREL 5MW* machine.

COST OF ENERGY

The relative *COE* is used as an objective function during the optimization process. The relative Cost Of Energy is defined as:

$$r^c = \frac{COE}{COE_{ref}}, \quad (9.44)$$

where COE_{ref} is the cost of energy of the *NREL 5MW* machine. Since it not evident whether the cost of energy has reciprocal dependencies on the laminate stiffness matrices, a linear approximation is adopted to ensure convexity of the approximate function. The approximation for the objective function then becomes:

$$\tilde{r}^c \simeq \sum_j \left(\Psi_j^m : \mathbf{A}_j + \Psi_j^b : \mathbf{D}_j + \alpha_j h_j \right), \quad (9.45)$$

where Ψ_j^m, Ψ_j^b and α_j are derived from the sensitivities of *COE* with respect to a laminate membrane and bending stiffness matrix together with the laminate thickness.

9.5. SUMMARY

In this chapter, the derivation of the response approximations in-terms of the laminate design variables is presented. The output of this chapter plays a key role in the optimization framework, introduced in chapter 3. Starting with the introduction of a general form of the response approximation, tailored for composite optimization, the different responses used in the optimization study were elucidated. Afterwards, the description of the two methods of sensitivity analysis, used in the current optimization framework, is presented. Finally, detailed description of the response approximations for the aeroelastic and structural responses is given. The response approximations developed in this chapter are summarized in table 9.2.

Table 9.2: Response approximations

Power	$\tilde{r}^p \simeq \sum_j \Psi_j^m : A_j + \Psi_j^b : D_j + \alpha_j h_j$
Tip deflection	$\tilde{r}^\delta \simeq \sum_j \Phi_j^m : A_j^{-1} + \Psi_j^m : A_j + \Phi_j^b : D_j^{-1} + \Psi_j^b : D_j + \alpha_j h_j$
Strength	$\tilde{r}_i^s \simeq \frac{\partial r_i^s}{\partial A_i^{-1}} : A_i^{-1} + s_i^t \Delta N_i$
Buckling	$\tilde{r}_i^b \simeq \sum_j \Phi_{ij}^m : A_j^{-1} + \Psi_{ij}^m : A_j + \Phi_{ij}^b : D_j^{-1} + \Psi_{ij}^b : D_j + \alpha_{ij} h_j$
Mass	$\tilde{r}^m \simeq \sum_j \alpha_j h_j$
Relative <i>COE</i>	$\tilde{r}^c \simeq \sum_j \Psi_j^m : A_j + \Psi_j^b : D_j + \alpha_j h_j$

10

AEROELASTIC OPTIMIZATION OF WIND TURBINE BLADE

The objective of the optimization campaign is to investigate the added benefit of adaptive blades to improve the performance of large scale variable speed stall controlled wind turbines (in the order of megawatts). The term ‘adaptive blade’ refers to twist coupled composite blade that adjusts its aerodynamic characteristics thereby affecting the wind turbine performance [92]. The twist coupling of the adaptive blade is optimized to improve the performance of variable speed stall controlled machines. To this end, an optimization study based on the cost of energy is performed on 5MW stall regulated wind turbine. The cost function is based on the NREL cost model for pitch regulated 5MW wind turbine, that has been modified for stall regulated 5MW machine. A variable stiffness optimization is carried out employing lamination parameters as design variables.

A general model description is presented in section 10.1. The material properties used in current optimization and the finite element model are discussed in section 10.2 and 10.3 respectively, followed by detailed description of the optimization model in section 10.4. The initial stiffness distribution and the corresponding aeroelastic and structural responses are given in section 10.5. A mass minimization is presented in section 10.6, which serves as a baseline design for subsequent optimization cases. Finally, section 10.7 presents the advantage of unbalanced laminates over balanced laminates using several optimization cases, where the COE is used as objective function together with structural and aeroelastic constraints.

10.1. MODEL DESCRIPTION

A baseline blade design for variable speed stall controlled 5MW wind turbine is based on the *NREL 5MW* blade design [72]. However, the *NREL 5MW* machine is a pitch regulated machine, thus the choice of airfoils and twist distribution are modified such that the blade is suitable for use in stall controlled machine. The gross properties of the current machine are given in table 10.1.

Table 10.1: Gross properties for the 5MW baseline wind turbine

Rating	5MW
Rotor orientation, Configuration	Upwind, 3 Blades
Control	Variable Speed, Stall controlled
Rotor, Hub diameter	126 m, 3 m
Hub height	90 m
Cut-in, Rated, Cut-out wind speed	3 m/s, 9 m/s, 25 m/s
Cut-in, Rated rotor speed	6.9 rpm, 10.4 rpm

The chord distribution for the current baseline design is based on the chord distribution of the *NREL 5MW* blade design. The airfoil shapes, at the blade root and inner region of the blade, are taken from the *NREL 5MW* blade design. The airfoils for the outer region of the blade are obtained from an airfoil design study, geared towards airfoil designs with improved stall characteristics at high Reynolds number ($Re = 9 \times 10^6$) [105]. Two airfoils are selected for the outer blade region: 21% thick airfoil (WAP-W-21) and 18% thick airfoil (WAP-W-18). The new 21% thick airfoil is employed between 38% and 69% of the blade span, with a maximum of 96% of the 21% airfoil shape realized at 53% of the blade span. The new 18% thick airfoil is employed between 53% of the blade span till the blade tip, where the blade cross-section consists solely of the 18% thick airfoil starting 70% of the blade span. The polar properties of these two airfoils are shown in figures 10.1a and 10.1b.

The twist distribution for the baseline model is calculated using:

$$\theta = \frac{1}{r/R} \frac{1-a}{\lambda} - \alpha, \quad (10.1)$$

where r/R is the normalized span wise coordinate, while a , α , and λ are respectively, the axial induction factor, angle of attack and tip speed ratio. The twist distribution should be designed for optimum operation below rated wind speed while inducing sufficient stall for high wind speed, specially at the outboard blade region. Consequently, the twist distribution is calculated for a tip speed ratio of $\lambda = 7.55$, $a = 1/3$, and design angle of attack $\alpha = 10$ deg. The design angle of attack is close to the angle of attack for which $\frac{C_l}{C_d}$ is the highest, for maximum power extraction below the rated wind speed. Two spars are modelled at 0.3 and 0.7 chord point. The blade planform is generated using NURBS basis functions of cubic polynomials and 17 control points with which the blade geometry is defined. Table 10.2 contains the planform data

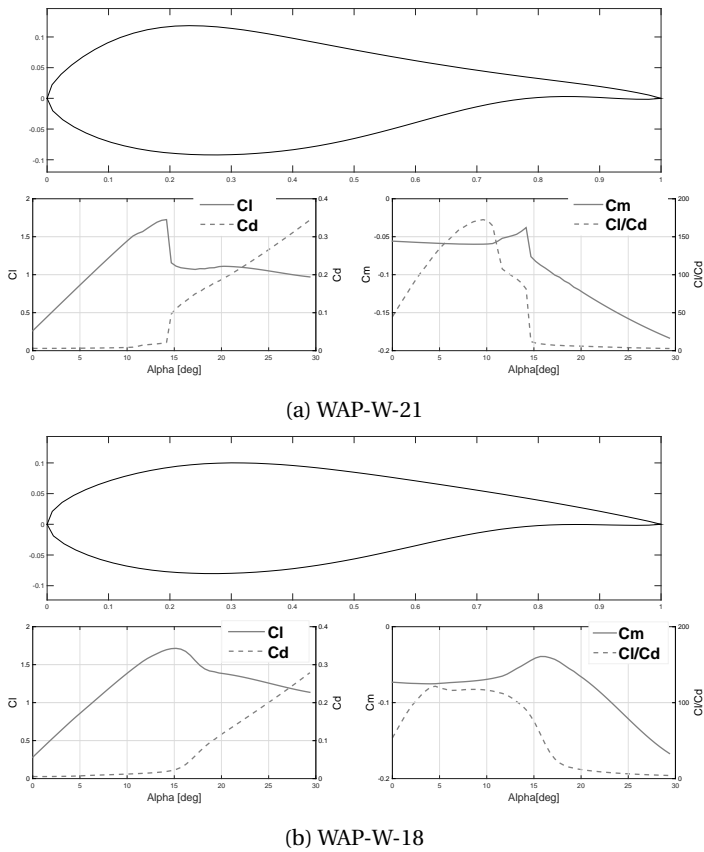


Figure 10.1: Aerodynamic characteristics on the outboard blade region, calculated for $Re = 9 \times 10^6$.

for the current blade design, including among others: twist, chord, and selection of airfoils along the blade span. Furthermore, a 3D representation of the

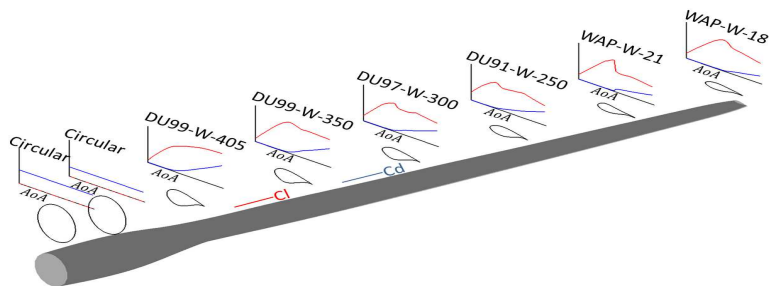


Figure 10.2: Blade shape together with the base airfoils and their aerodynamic characteristics.

Table 10.2: Blade planform properties defined at Control Points (CP)

CP	Twist(deg)	Chord(m)	R(m)	Airfoil
1	8.8	3.5	0.0	Circular
2	8.8	3.8	3.8	Circular
3	8.8	4.2	7.7	Circular
4	8.8	4.6	11.5	DU99-W-405
5	5.6	4.7	15.4	DU99-W-350
6	3.3	4.5	19.2	DU97-W-350
7	1.6	4.2	23.1	DU97-W-300
8	0.2	4.0	26.9	DU97-W-250
9	-0.8	3.7	30.8	WAP-W-21
10	-1.7	3.5	34.6	WAP-W-21
11	-2.4	3.3	38.4	WAP-W-18
12	-3.0	3.0	42.3	WAP-W-18
13	-3.5	2.8	46.1	WAP-W-18
14	-3.9	2.5	50.0	WAP-W-18
15	-4.3	2.3	53.8	WAP-W-18
16	-4.6	2.1	57.7	WAP-W-18
17	-4.9	1.4	61.5	WAP-W-18

turbine blade and the airfoil distribution together with their 2D aerodynamic characteristics is given in figure 10.2.

10.2. MATERIAL PROPERTIES

The spar-caps of the rotor blade are made of laminates, while the remaining structural component of the rotor blade are composed of sandwich laminates. Glass fiber laminates are used for the face-sheets of the sandwich laminates and for the spar-cap laminates. The material properties of the glass fiber laminate, including the strain allowable, are given in table 10.3. The strain allowables in table 10.3 already include a safety factor of 2.977, which is a combination of loads and material safety factor [53].

Table 10.3: Material properties selected from [53].

Component (material)	E_{11}, GPa	E_{22}, GPa	G_{12}, GPa	ν	$\rho, \text{Kg/m}^3$	Allowable		
						$\epsilon_t\%$	$\epsilon_c\%$	$\gamma_{xy}\%$
Face-sheet (Glass)	35	8.33	4.12	0.33	1920	0.95	0.75	0.91
Core (Foam)	0.256	0.256	0.022	0.3	200	-	-	-

The material properties across the blade cross-section are assigned by partitioning the cross-section in three sections along the chord. Three laminates define the material properties of the skin on pressure side and three laminates on the suction side. Furthermore, a single laminate is used to define the material properties of the shear webs. A schematic representation of laminate

assignment per cross-section is shown in figure 10.3.

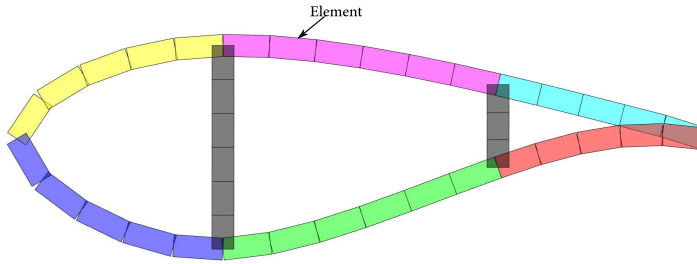


Figure 10.3: Material property assignment over a cross-section, where each colour represents a single laminate.

The initial layup consists of a quasi-isotropic laminate with the layup $[\pm 45, 90, 0]$, in which the 0° is aligned with the blade axis. Finally, table 10.4 shows the ratio of core to face sheet thickness, which is based on the rotor blade design of [115]. The core of the sandwich laminate is made up of a foam material with the properties given in table 10.4.

Table 10.4: Sandwich laminate: ratio of core to face sheet thickness

R(m)	leading edge	trailing edge	shear web
0	2	2	25
1.4	2	2	25
1.5	2	2	25
6.8	21	21	25
9.0	27	27	25
43.1	7	7	25
45.0	7	7	25
61.5	7	7	25

10.3. FINITE ELEMENT MODEL

The finite element model of the blade is generated using the method described in section 4.2, where blade model is composed of quadrilateral shell elements. The blade cross-sections are discretized with 10 elements in chord-wise direction, while an aspect ratio, $ar = 2$, is used to calculate the element size in span-wise direction. This results in 2700 elements to model the whole blade. The large number of elements for the finite element model is motivated by the nature of (shell) buckling mode under compressive stress state. As can be seen from figure 10.4, the buckling of the blade skin is localized to

a small region, resulting in short buckling wavelength. This requires a model with fairly fine discretization to capture the buckling loads with sufficient accuracy.

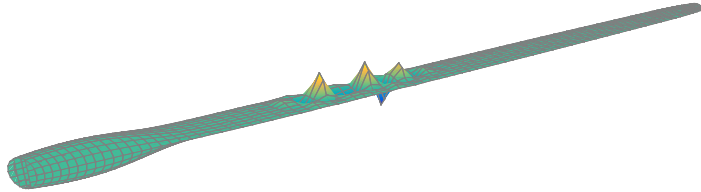


Figure 10.4: Example of buckling mode for current optimization campaign.

10.4. OPTIMIZATION MODEL

The material properties are defined using 7 laminates per cross-section (see section 10.2). Furthermore, the laminate properties are defined using 15 control points along the blade span, which amounts to 105 laminates and 1365 design variables.

The aeroelastic loads are calculated for sampled wind speeds between the cut-in and cut-out wind speed, i.e. $u_{sample} = 5, \dots, 25 \text{ m/s}$, with a sampling interval of 1 m/s . However, the aeroelastic loads calculated at wind speeds above rated wind speed, are used as load cases for the stress and buckling analysis using the finite element solver *NASTRAN*. The aeroelastic loads for lower wind speeds and for certain wind speeds above rated are not considered since they do not affect the structural blade design. Therefore, the aeroelastic loads for wind speeds, $u_{sample} = \{11, 12, 13, 15, 25\} \text{ m/s}$, are the load cases for the structural analysis using *NASTRAN*.

The responses considered in following optimization studies are: stress, buckling, tip deflection, rated power, blade mass, and COE. The finite element solver *NASTRAN* provides stress responses on the upper and lower side of an element. For a finite element model comprised of 2700 elements and five load cases, this amounts to 81000 stress responses. Additionally, 33 buckling loads are considered per load case, amounting to 165 buckling responses. Using the aeroelastic module, both the maximum tip deflection and rated power are analysed. Furthermore, the aeroelastic module calculates the blade mass and cost of energy, which are used as objective functions. The number of responses from the *NASTRAN* analysis and the aeroelastic module are summarized in table 10.5. The failure indices, based on the stress responses, are formulated using the response approximation method described in section 9.4. The strain failure indices, using the stress responses of the FE model, are formulated based on a conservative failure envelope [66]. The strain failure enve-

Table 10.5: Responses and failure indices.

Response types	Number of responses	Number of failure indices/design limits
COE & Blade mass	2	2
Stress responses	81000	1300
Buckling	165	165
Tip deflection & Rated power	2	2

lope is constructed using the strain allowable of glass fiber, listed in table 10.3. The strain failure indices of the whole model and for all load cases amount to 13000. However, due to constraint on computational time, only the highest ten percent of the strain failure indices are included during optimization. Two optimization runs are carried out for each optimization case. The first run lasts only a few iterations and afterwards the elements with the highest ten percent of the strain failure indices are determined. For the second case, a complete optimization run is carried out with the strain constraints calculated for the elements with the highest ten percent failure indices, determined from the last iteration of the first optimization run. This method ensures that the (active) strain failure indices of the final design do not exceed the strain failure envelope, allowing the use of a smaller set of failure indices during optimization to limit computational time. This results in 1300 strain failure responses passed to the optimizer. The failure indices for the buckling loads are calculated using the method describes in section 9.4.2.

The design limits for the tip deflection and rated power together with the normalized values of the COE and blade mass are calculated using the method described in sections 9.4.1 and 9.4.3, where the normalization coefficients are obtained from the machine rating data of the NREL 5MW pitch controlled wind turbine, listed in table 10.6. A list of the failure indices and their amounts used in the current optimization campaign is given in table 10.5.

Furthermore, the major components of the COE are also normalized with the corresponding values of the NREL 5MW pitch controlled machine and are used to illustrate the performance of the blade designs. In addition, the same *OM* and *LRC* (cost components of the COE, described in section 9.2.3) value as for the reference NREL 5MW pitch regulated machine is assumed in the current optimization, resulting in conservative estimation of the COE for all designs.

Table 10.6: Performance of the NREL 5MW pitch regulated machine

COE \$/Kwh	AEP Kwh	ICC \$	Mass Kg	Power _{rated} MW	Torque _{rated} Nm	Thrust _{rated} N	Tip displacement m
0.082	2.4×10^7	1.1×10^7	17.7×10^3	5.3	4.2×10^6	7.1×10^5	6.2

For all optimization cases, both the aeroelastic loads and the data exchange routines are implemented in **MATLAB®**. The computational cost for the current optimization campaign is roughly 2 hours per iteration step, composed of 1.45 hours for generating the responses and sensitivities and 15 min-

utes to carry-out the optimization. The entire optimization takes roughly 1 week, depending on the amount of iteration steps needed to achieve converged runs (usually in the order of 20 to 40 iteration steps). During subsequent optimization, the design space is explored by starting from different initial points in-terms of the initial thickness and stiffness distribution. The results presented in this chapter correspond always with runs having the lowest value for the considered objective function.

10.5. INITIAL DESIGN

The initial thickness distribution for starting design is shown in figure 10.5. In order to present the stiffness distribution of a blade design, a polar plot is used to visualize the in-plane stiffness distribution of the laminates along the blade span by applying the method described in section 2.3.3. The polar plot of the thickness-normalized engineering modulus of elasticity, on the suction side of the blade skin and shear webs, is given in figure 10.6. The x direction of the material coordinate system (0 deg) is indicated by the black line, which for a straight blade is along the beam axis. It is evident from the figure that the major stiffness for the starting design is the same in every direction, suggesting a quasi-isotropic laminates. The same stiffness distribution is also the case for the blade skin on the pressure side. The design load cases and the strain and

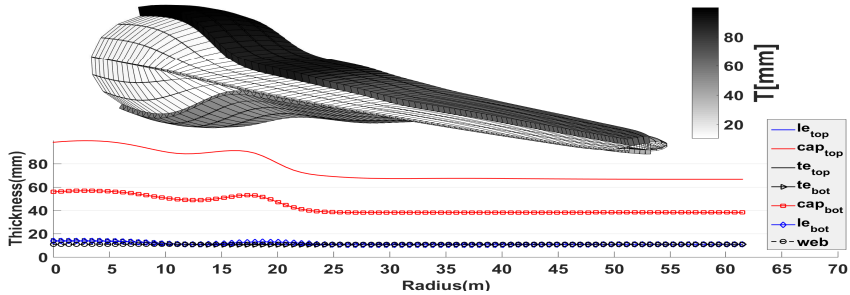


Figure 10.5: Skin thickness distribution for the initial design.

buckling failure indices for the critical wind speed of 15 m/s are given in figure 10.7. From figure 10.7c, element numbers 1 to 900 belong to the blade skin on the suction side, element numbers 901 to 1800 belong to the blade skin on the pressure side, and the remaining element numbers belong to the two shear webs, from blade root to blade tip, respectively. Furthermore, the red data points with the label $strain_{active}$ are the strain failure responses that are passed to the optimizer. The buckling failure indices for the design wind speed of 15 m/s are shown in figure 10.7d. It is evident from figures 10.7c and 10.7d that all the failure indices are well below the failure limit of one, indicating a great potential to reduce the blade mass while complying with structural and aeroelastic constraints.

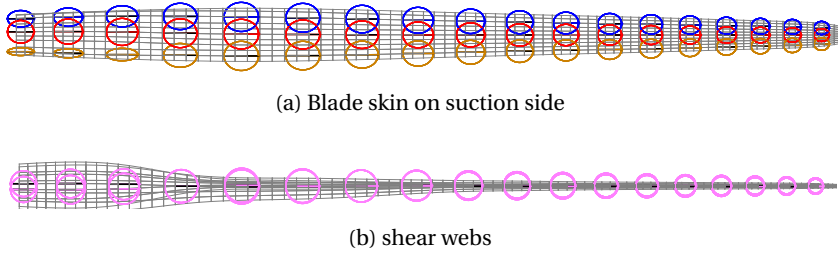


Figure 10.6: Stiffness distribution for the initial design.

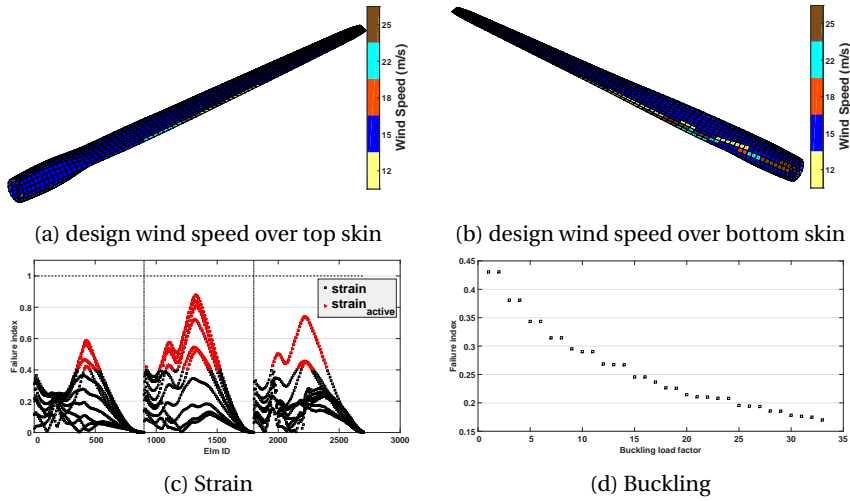


Figure 10.7: Initial design: failure indices and design wind speed/load cases.

10.6. BASELINE DESIGN: MASS MINIMIZATION

The first optimization case is intended as a baseline design, which is then used as starting point in the subsequent optimization studies of twist coupled blades for variable stall controlled wind turbines. The objective of the current optimization is blade mass minimization while complying with strain, buckling, and maximum tip displacement constraints. The evolution of mass minimization is shown in figure 10.8. The optimization starts with an initial blade mass of 41 ton and ends with a mass of 23 ton after 27 iterations. The largest mass reduction occurs within the first thirteen iterations, afterwards, a minimum mass reduction steps are observed till convergence.

The thickness distribution for the final design is given in figure 10.9 providing 3D and 2D representation of the laminate thickness distribution along the blade span. The legends in figure 10.9 represent laminate thickness distribution over the: (*le*) leading edge, (*te*) trailing edge, (*Cap*) spar cap and (*web*)

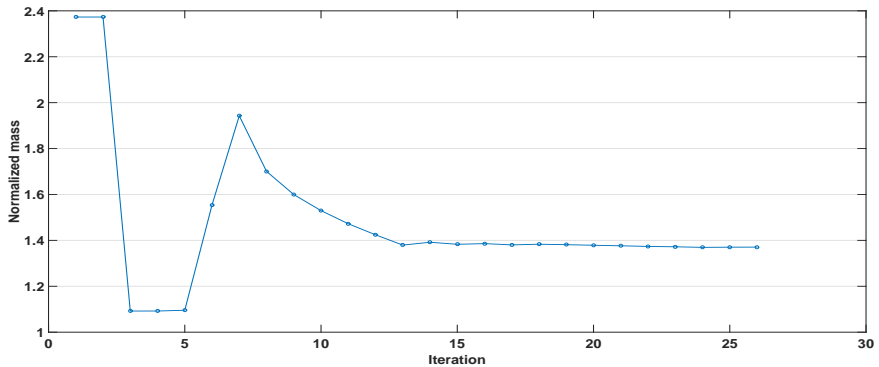


Figure 10.8: Mass evolution using balanced laminates.

shear web. The subscripts *top* and *bot* represent respectively, the blade skin on the suction and pressure side. There is a general thickness reduction for all sections of the turbine blade compared to the initial thickness distribution shown in figure 10.5. Particularly, there is a significant thickness reduction for the spar caps, while the remaining parts of the blade also exhibit moderate thickness reduction. Furthermore, the spar caps on the suction side have the largest laminate thickness, specially between $15m$ and $30m$ of the blade length. This is due to the presence of compression stress on the suction side, resulting in buckling critical regions along the spar caps on the suction side. This is evident in figure 10.10 where the first buckling mode, calculated for the highest aeroelastic load at the wind speed of $15m/s$, is shown. It is evident from the figure that the first buckling mode lies on the suction side, roughly between $10m$ and $40m$ of the blade span and confined within the spar caps. This corresponds with the observed thickness distribution for the spar caps on the suction side. Furthermore, there is also a relative increase of spar caps

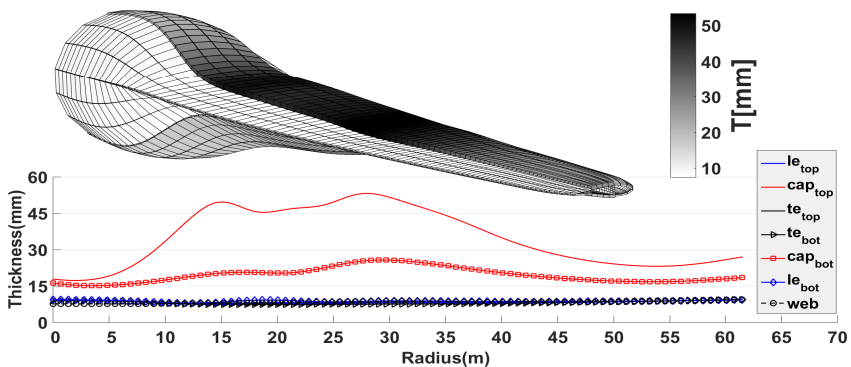


Figure 10.9: Skin thickness distribution for the final design: mass minimization using balanced laminates.

thickness on the pressure side, around the same region as for the spar caps on the suction side. The laminates thickness of the remaining parts (leading edge, trailing edge, and shear webs) is reduced in general, compared to the initial design, resulting in decreased blade mass. The structural failure indices

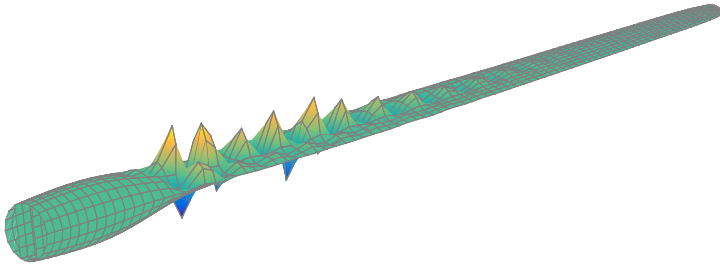


Figure 10.10: final design, 1st buckling mode for aeroelastic load calculated at wind speed = 15 m/s.

of figures 10.7c and 10.7d, for the initial design, indicate a great potential for mass reduction without exceeding the failure limit of one. The design wind speed for the final design is given in figure 10.11a and 10.11a for the blade skin on the suction side and pressure side respectively, which indicates that the wind speed of 15 m/s is the design load case for the structural constraints (strain and buckling). It is evident from figure 10.11d that buckling is the design driver, while the strain failure indices (figure 10.7c) do not reach the failure limit of one, thus are not design drivers. Although the buckling failure is a design driver, it applies only to the blade skin on the suction side; the strain failure indices should be active (reach the failure limit of one) for the blade skin on the pressure side, i.e. for elements between 901 to 1800. This is not the case here because there is an additional constraint on the maximum tip displacement. Figure 10.12 shows the (normalized) maximum tip displacement and power. The maximum tip displacement for the final design reaches the failure limit of one, indicating that stiffness and buckling are the design drivers. The advantage of using composite laminates is their directional dependence of the stiffness properties that allows for tailoring the composite stiffness according to the design specifications. Figure 10.13 shows, for the final design, a polar plot of the thickness normalized engineering modulus. The stiffness distribution is symmetric with respect to the blade axis (denoted by black line in the polar plots), which is an indication that balanced laminates are used during optimization. The major stiffness direction for the spar caps is aligned along the blade axis throughout the blade length, as a consequence of largely stiffness dominated optimization. Due to constrained tip deflection, most of the stiffness distribution are aligned along the blade axis, rather than the quasi-isotropic layout of the initial design. Furthermore, the buckling constraints also play a role on the final stiffness distribution along the spar caps. Therefore, the optimizer aligns the stiffness distribution, of the laminates be-

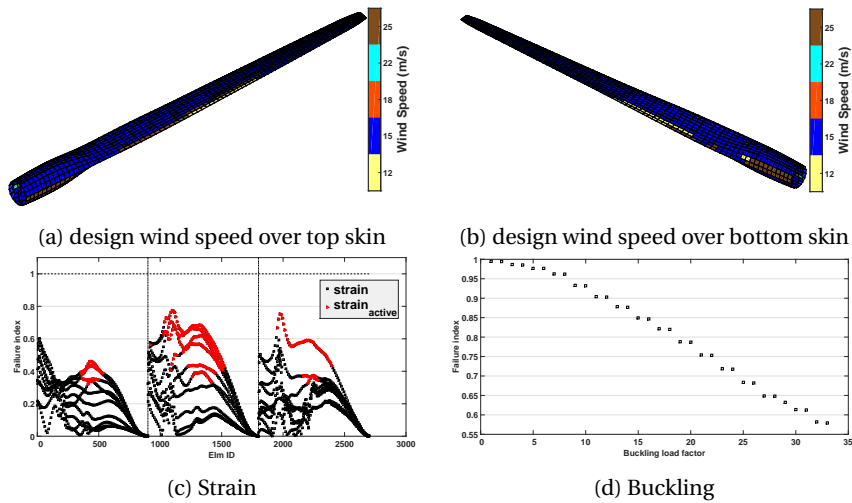


Figure 10.11: Optimized design: design wind speed/load case for mass minimization using balanced laminates together with failure indices for wind speed = 15 m/s.

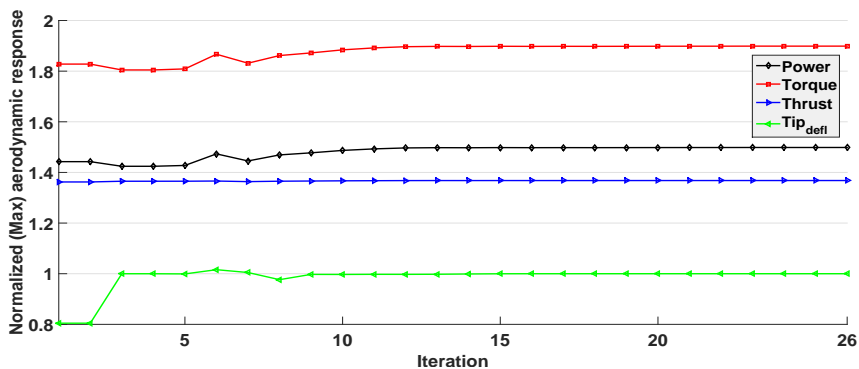


Figure 10.12: Aeroelastic response evolution from mass minimization using balanced laminates.

longing to the spar caps, parallel to the beam axis, preventing buckling failure without excessive increase in laminate thickness. The stiffness distribution of the shear webs did not change from the initial design, remaining a quasi-isotropic layup, since the strain failures of the shear webs, elements starting from 1801 and onwards of figure 10.11c, are not active (don't reach the failure limit of one). Additionally, no buckling of the shear webs is observed for the final design. Furthermore, the shear webs do not contribute, significantly, to the cross-sectional flap-wise bending stiffness of the blade, which affects tip displacement.

The stiffness distribution along the trailing edge, both on suction and pressure side of the skin, remain unchanged from the initial design, specially to-

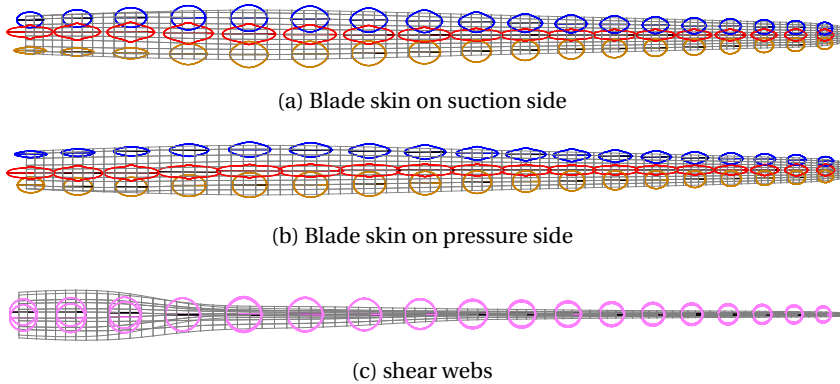


Figure 10.13: Optimized design, stiffness distribution from mass minimization using balanced laminates.

wards the outer-board region of the blade. On the other hand, the major stiffness direction along the leading edge are primarily aligned parallel to the blade axis, providing additional bending stiffness required to comply with the buckling and stiffness constraint, i.e. maximum tip displacement.

10.7. DESIGN STUDIES OF TWIST COUPLED TURBINE BLADE: COE MINIMIZATION

The following sections investigate the benefit of unbalanced laminates over balanced laminates to design adaptive blades with improved performance. The performance of different blade designs is assessed using optimization scheme that minimizes the COE of stall regulated wind turbines while complying with structural and aeroelastic constraints. A complete stiffness variation along the blade span is considered during the optimization. Both balanced and unbalanced composite laminates are investigated during the optimization, while ensuring no structural and aeroelastic failure (strain, buckling, and tip displacement). Furthermore, two operational configurations of the wind turbine are considered, i.e. up-wind and down-wind configuration. The constraint on the maximum tip displacement is removed for a simulation with a down-wind configuration. Finally, a minimization of COE using unbalanced laminates is carried out with an additional constraint on the maximum power, demonstrating the extended capability of twist coupled blades to regulate power on stall controlled wind turbines.

The results are verified using different starting designs for the optimization cases, comprised of different laminate thickness and stiffness distribution. Most of the optimization cases that start from different initial points showed little difference in objective function. Furthermore, the final designs are not all that different from each other.

10.7.1. UP-WIND TURBINE CONFIGURATION: BALANCED LAMINATES

For the first optimization study, balanced laminates are used to minimize the COE of stall regulated 5MW machine, where up-wind turbine configuration is simulated during the optimization process. The optimization starts from the final design of the baseline design (see section 10.6). The optimization run includes both structural and aeroelastic constraints, i.e, strain, buckling and tip displacement constraints. The evolution of COE and its main components is given in figure 10.14, where the reference values of the NREL 5MW pitch regulated machine (given in table 10.6) is used for to normalize the cost components. Only a small reduction for the COE, from 1.1 to 1.09 of the reference COE, is observed after 18 iteration. The blade mass is reduced from 1.45 to 1.39 of the reference blade mass, resulting in a reduction of six percent in blade mass. The ICC is reduced by five percent, mainly due to lower blade mass. However, the AEP is also reduced from the starting design by roughly one percent. The corresponding final skin thickness distribution along the

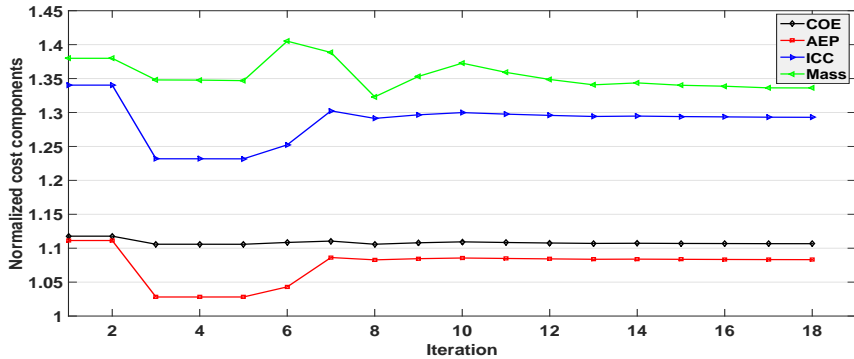


Figure 10.14: Evolution of COE and its components, for the optimization using balanced laminates.

blade span is shown in figure 10.15. The top plot depicts a 3D representation of the thickness distribution while the bottom plot presents a 2D curve of the laminate thickness distribution along the blades span for different blade segments. Compared to the baseline design of figure 10.9, two changes are observed. First, an increased skin thickness of the bottom spar caps is observed, with a maximum of roughly 20mm around 35m of blade span. Second, the laminate thickness along the top and bottom side of the trailing edge skins increases towards the blade tip.

Figures 10.16a and 10.11a show respectively, the design wind speed for the structural elements at the suction and pressure side of the final rotor blade design. According to figures 10.16a and 10.11a, the design wind speed for the structural constraints (strain and buckling) is 15m/s .

Consequently, the strain and buckling failure indices of figures 10.11c and 10.11d are for the design wind speed of 15m/s . Figure 10.16 indicates that

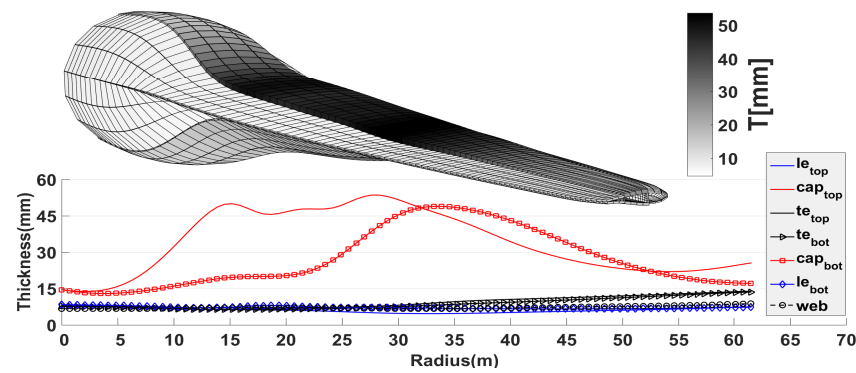


Figure 10.15: Optimized design, skin thickness distribution for COE minimization using balanced laminates.

buckling is still the design driver. The buckling failure indices drive only the design variables on the suction side of the blade since buckling occurs only on the side of the blade with compressive stress, i.e. on the suction side. The

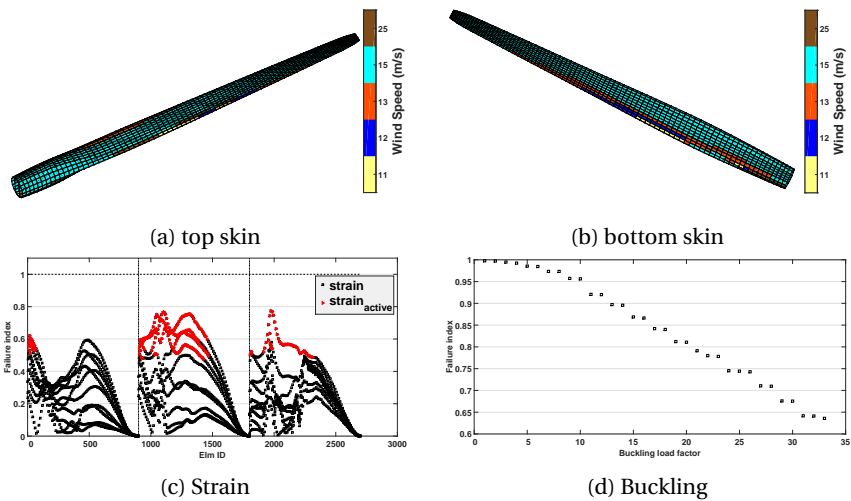


Figure 10.16: Final design from COE minimization using balanced laminates; sizing wind speeds and failure indices for the design wind speed of 15 m/s.

other design driver is the constraint on the tip displacement, as shown in figure 10.17 where several (normalized) aerodynamic responses for all iteration are presented. The reference values for the normalization can be found in table 10.6. The green line represents the normalized tip displacement, which is active after the seventh iteration. Furthermore, a reduction in the maximum power (black line) and maximum torque (red line) of roughly ten percent is observed. The maximum thrust, however, is not reduced significantly com-

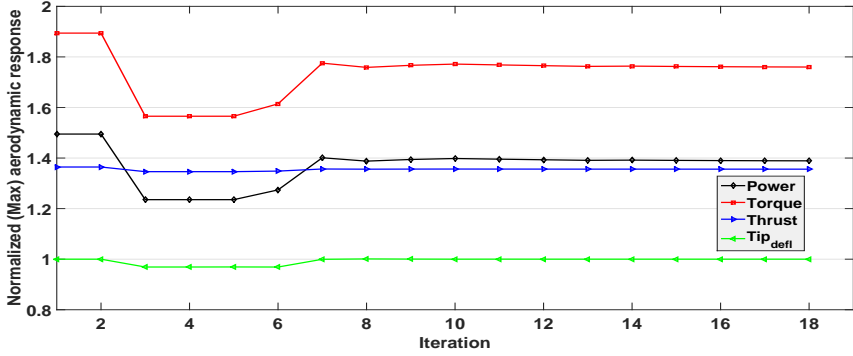


Figure 10.17: Aeroelastic response evolution from COE minimization using balanced laminates.

pared to the baseline design.

The reduction in torque and power is due to a different *induced* twist distribution for the final design compared to the initial design (see figure 10.20). The term *induced* refers to the twist distribution due to the aeroelastic response of the blade, which can be controlled by changing the extension-twist or bend-twist coupling of the blade or the location of the shear center. From the figure, it is observed that the *induced* twist for the initial design (dashed red line) moves slightly towards feather (decreased angle of attack) compared to the structural twist (solid black line), especially towards the outboard region of the blade. For the final design (solid red line), the *induced* twist moves slightly towards stall (increased angle of attack) for the outboard blade region, with a maximum difference of 0.5deg compared to the structural twist. The *induced* twist has a clear influence on the angle of attack (see the top right window of figure 10.20). For the final design, an increased angle of attack for the outboard blade region is observed (solid line), compared to the initial design (dashed line). However, the change in *induced* twist is not due to bend-twist or extension-twist coupling. The middle window of figure 10.18 shows that both the bend-twist and extension-twist couplings are zero for the initial and final design. The legend of the middle plot of figure 10.18 represent: (*ext*) extension-twist coupling, (*bend-flap*) flap-wise bend-twist coupling and (*bend-lag*) lag-wise bend-twist coupling. The different twist coupling coefficients of figure 10.18 are calculated according to,

$$ext = \frac{S_{14}}{\sqrt{S_{11}S_{44}}}, \quad bend_{flap} = \frac{S_{54}}{\sqrt{S_{55}S_{44}}}, \quad \text{and} \quad bend_{lag} = \frac{S_{64}}{\sqrt{S_{66}S_{44}}}, \quad (10.2)$$

where the S_{ij} are the coefficients of a sectional stiffness constant of a beam model. The change in *induced* twist for the final design is due to a shift in the location of the shear center, as shown in the bottom window of figure 10.18. The shear center is a point on a cross-sectional plane, through which the application of a transverse load does not cause twist moment (see figure 10.19). The location of the shear center is calculated from the sectional stiffness con-

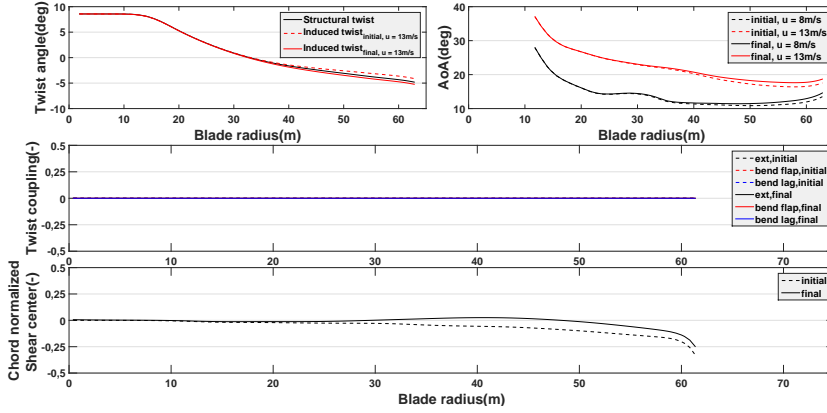


Figure 10.18: Initial and final value for: induced twist, angle of attack, twist coupling, and location of shear center, for COE minimization using balanced laminates.

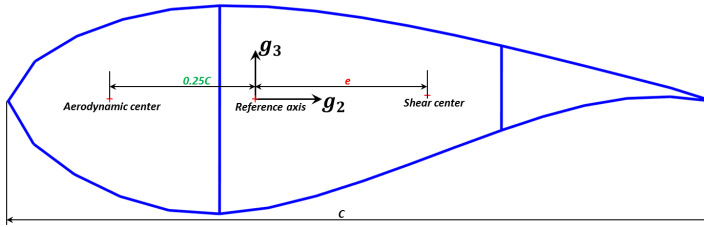


Figure 10.19: Schematic representation of shear center and aerodynamic center on a cross-sectional plane

stants as,

$$e = -\frac{S_{34}}{S_{44}}. \quad (10.3)$$

According to figure 10.19, moving the shear center back towards the trailing edge increases the *induced* twist towards stall, while moving it towards the leading edge shifts the *induced* twist towards feather.

It is observed from the bottom plot of figure 10.18 that for the final design, the location of the shear center has increased (especially towards the outboard blade region) compared to the initial design. The shift of the shear center towards the trailing edge causes the *induced* twist to reduce towards stall (see the top left window of figure 10.18). The location of the shear center is changed by the redistribution of the laminate thickness across the cross-section, as shown in figure 10.15 where the trailing edge laminates have larger thickness compared to the leading edge laminates, shifting the location of the shear center towards the trailing edge. Since balanced laminates can't induce bend-twist or extension-twist coupling, the optimizer shifts the *induced* twist towards stall by moving the location of the shear center towards the trailing edge.

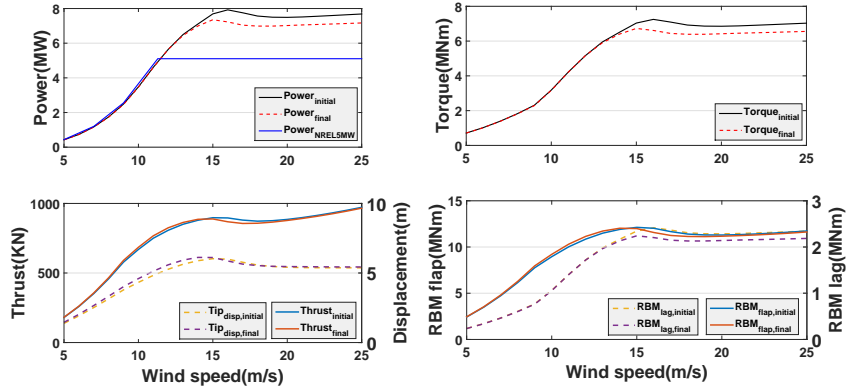


Figure 10.20: Initial and final value for: power, torque, thrust, tip displacement, and root bending moment, for COE minimization using balanced laminates.

Increased angle of attack reduces the maximum power, as shown in figure 10.20. The top left window of figure 10.20 presents the power curves for the initial and final design together with the power curve of the NREL 5MW pitch controlled machine. The same reduction in rated torque is also observed for the final design, see the top right window of figure 10.20. The rated thrust is at the cut-out wind speed, while the maximum tip displacement is around 15 m/s, see the bottom left window of figure 10.20. Finally, the root bending moments (flap and lag) are presented in the bottom right window of figure 10.20.

Finally, the major stiffness direction is visualized in figure 10.21, where a polar plot of the thickness normalized engineering modulus (\hat{E}_{11}) is presented for the blade skin on the suction side, the pressure side and the shear webs. The black line inside the polar plots represents the material x direction, which is aligned with the beam axis. The stiffness distribution of all the laminates is symmetric with respect to the black line, suggesting that balanced laminates are used during the optimization. Most of the laminate stiffness for the in-board blade region, especially towards the blade root, are all aligned along the material direction, providing structural strength (mainly buckling). For the outboard region, the stiffness direction for the leading edge laminates (green curves) is around the angle $\pm 45^\circ$, while for the trailing edge laminates (blue curves), the stiffness direction for the same span-wise location is towards the 90° . A slight shift towards the 90° in stiffness direction of the shear web laminates is also observed, mostly around the mid-span. The stiffness direction of the spar cap laminates (red curves) is aligned with the blade axis for the inner blade region and rotates roughly to $\pm 45^\circ$ close to the blade tip.

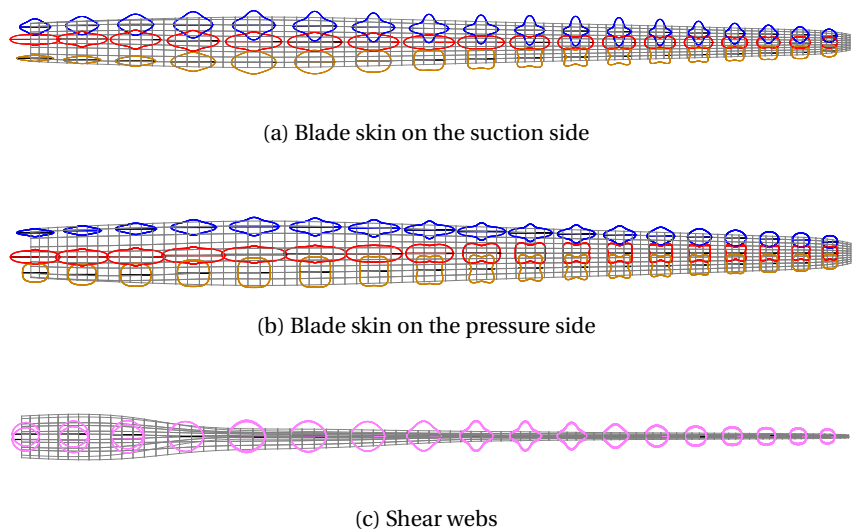


Figure 10.21: Optimized design: stiffness distribution from COE minimization using balanced laminates.

10.7.2. UP-WIND TURBINE CONFIGURATION: UNBALANCED LAMINATES

Unbalanced laminates provide additional coupling among the in-plane and out-of-plane (laminate) degrees of freedom. Furthermore, it allows further steering of the major stiffness direction, while the major stiffness direction for balanced laminates is symmetric with the (chosen) material coordinate system, as explained in the previous section. The use of unbalanced laminates

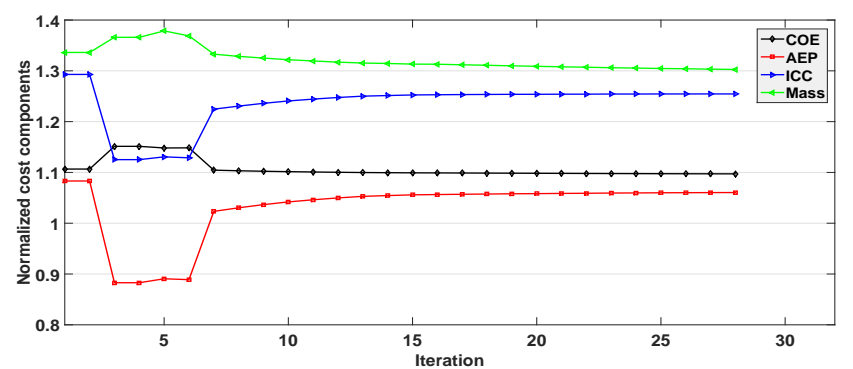


Figure 10.22: Evolution of COE and its components, for the optimization using unbalanced laminates.

increases the number of lamination parameters (design variables) by a factor of two. As discussed in section 2.3.2, the material invariants Γ_2 and Γ_4 contribute, on the laminate level, to the in-plane strain-shear coupling and out-of-plane bend-twist coupling. The starting point of the current optimization case is the final design using balanced laminates (see section 10.7.1). According to figure 10.22, minimizing the COE using unbalanced laminates resulted in a relative reduction of COE of one percent. The blade mass is reduced approximately by three percent, with the ICC also showing the same trend as the blade mass. However, the AEP is also reduced, which is due to the lower rated power of the final design.

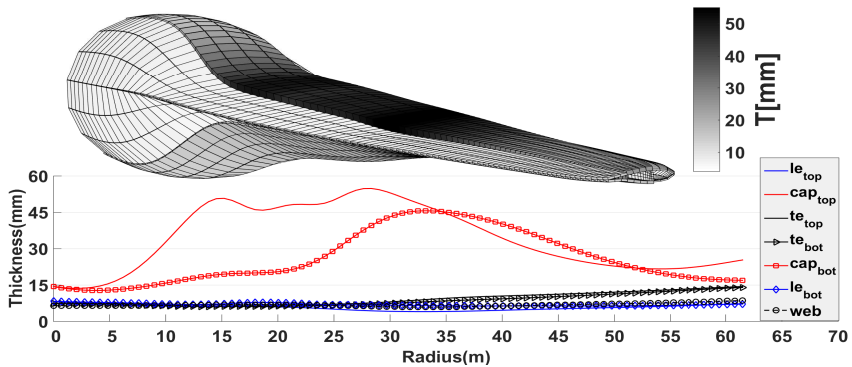


Figure 10.23: Optimized design, skin thickness distribution for COE minimization using unbalanced laminates.

The optimized laminate thickness distributions (both 2D and 3D representation) are given in figure 10.23. Again, it is observed from figure 10.23 that the largest skin thickness is located at the suction side of the wind turbine rotor blade, mainly due to the active buckling constraint. The maximum skin thickness, on the pressure side of the blade, is located towards the middle of the blade, mainly to comply with the stiffness constraint, i.e. maximum tip displacement. Furthermore, for the laminates distributed along the trailing edge, there is a slight skin thickness increase towards the blade tip.

The design wind speeds for the final design are given in figure 10.25a for the blade skin on the suction side and figure 10.25b for the blade skin on the pressure side. Accordingly, the design wind speed for the structural constraints (strain and buckling) is 13 m/s .

Consequently, the strain and buckling failure indices of figures 10.11c and 10.11d respectively are for the design wind speed of 13 m/s . Buckling is still a design driver (see figure 10.25). While the strain failure indices have moved closer to the failure limit of one, strain failure is still not a design driver. Instead, the constraint on maximum tip displacement drives, along with the buckling constraints, the design as can be seen in figure 10.24. Figure 10.24 shows that the tip displacement hits the design limit of one at the seventh iteration. The figure also shows that for the final design, both the rated torque

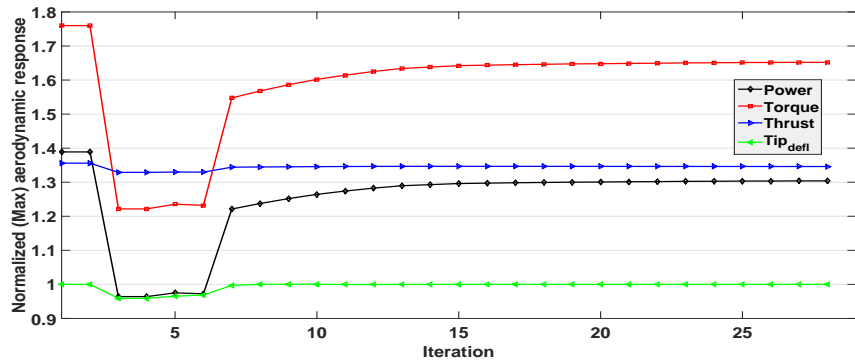


Figure 10.24: Aeroelastic response evolution from COE minimization using unbalanced laminates.

and power are reduced.

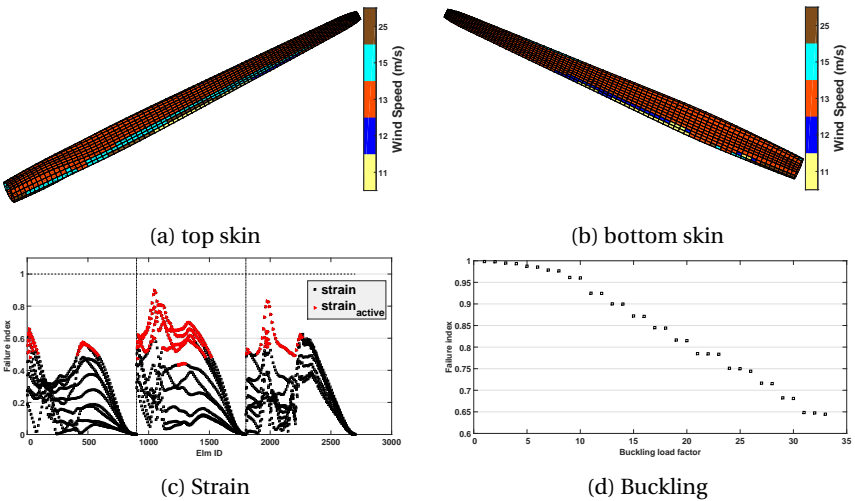


Figure 10.25: Optimized design, sizing wind speed/load case for COE minimization using unbalanced laminates and failure indices for wind speed = 13m/s.

The top left window in figure 10.26 shows the *induced* twist distribution for the initial (dashed red line) and final design (solid red line) of the current optimization, together with the structural twist (black line). From figure 10.26, the *induced* twist for the final design is reduced significantly towards stall, with a maximum difference of 1.5 degree with respect to the structural twist. However, for the inboard blade region between 20% to 35% of blade radius, the *induced* twist of the final design shifts slightly towards feather. The change in *induced* twist is attributed to the twist coupling of the final design, as shown in the middle window of figure 10.26. The dashed lines represent the twist

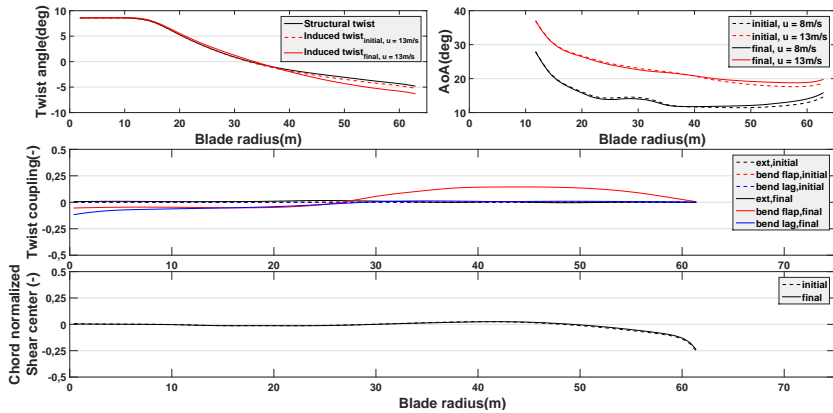


Figure 10.26: Initial and final value for: induced twist, angle of attack, twist coupling, and location of shear center, for COE minimization using unbalanced laminates.

coupling for the initial design (which are all zero), while the solid lines represent the twist coupling for the final design. The legends *ext*, *bend flap*, and *bend lag* represent respectively, the extension-twist coupling, flap-wise bend-twist coupling and lag-wise bend-twist coupling. The flap-wise bend-twist coupling starts with negative coupling coefficient and changes sign roughly at the blade midspan, almost the same location where the *induced* twist changes direction, i.e. changes from twisting towards feather to twisting towards stall. Furthermore, the negative value for flap-wise bend-twist coupling is observed for the inboard blade region, probably causing the observed *induced* twist towards feather, for the inboard blade region. However, there is almost no extension twist coupling both for the initial and final design.

The optimizer did not change the location of the shear center to reduce the *induced* twist, as shown in the bottom window of figure 10.26 where there is no difference in the location of the shear center between the initial and final design. The effect of *induced* twist on the angle of attack is shown in the top right window of figure 10.26, where the angle of attack versus the blade axis is plotted for the initial and final design at different wind speeds. It is evident that the angle of attack of the final design is reduced for the inboard blade region, while the angle of attack increases for the outer blade region. Increased angle of attack results in lower rated power (see figure 10.20). The top left window of figure 10.20 presents the power curves for the initial and final design together with the power curve of the NREL 5MW pitch controlled machine. The same reduction in rated torque is also observed for the final design (see the top right window of figure 10.20). The rated thrust is at the cut-out wind speed, while the maximum tip displacement is around 15 m/s (see the bottom left window of figure 10.20). Finally, the root bending moments (flap-wise and lag-wise) are presented in the bottom right window of the same figure.

The *induced* twist of the final design results in a further decrease of the

rated power, as shown in figure 10.27. Furthermore, figure 10.27 shows additional performance indicators, including torque, thrust, displacement and root bending moments (flap-wise and lag-wise), where the final design shows a general decrease for all the performance indicators.

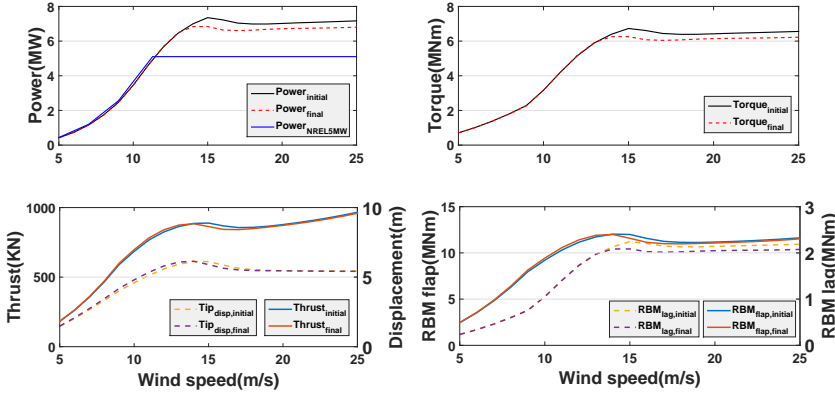


Figure 10.27: Initial and final value for: power, torque, thrust, tip displacement, and root bending moment, for COE minimization using unbalanced laminates.

The major stiffness direction of the optimized unbalanced laminates is shown in figure 10.28. Most of the stiffness direction of the laminates towards the blade tip, both on the suction and pressure side of the blade skin, are rotated in the same direction with respect to the material x direction (black line), inducing (flap-wise) bend-twist coupling. For the inner blade region, the major stiffness direction is still along the beam axis, which is required to comply with the structural constraints, i.e. strain, and buckling constraints. The laminate stiffness distribution for the shear webs is mostly quasi-isotropic, except roughly between 30% to 45% of the blade span, where the major stiffness direction is rotated to 90° with respect to the beam axis.

10.7.3. DOWN-WIND TURBINE CONFIGURATION: UNBALANCED LAMINATES

Another optimization case is carried out where down-wind turbine configuration is adopted during the aeroelastic simulation. This removes the constraint on the tip displacement for the current optimization. For the present optimization, COE minimization is carried out using unbalanced laminates. The current optimization starts from the final design of the COE minimization of an up-wind turbine configuration using unbalanced laminates. Only structural constraints (buckling and strain) are considered during the current optimization. The optimization history of the different components of the COE is shown in figure 10.29, where a converged design is achieved after 11 iterations. The major reduction is for the blade mass, where the mass is reduced more than 17%. However, the ICC is increased by one percent suggesting an

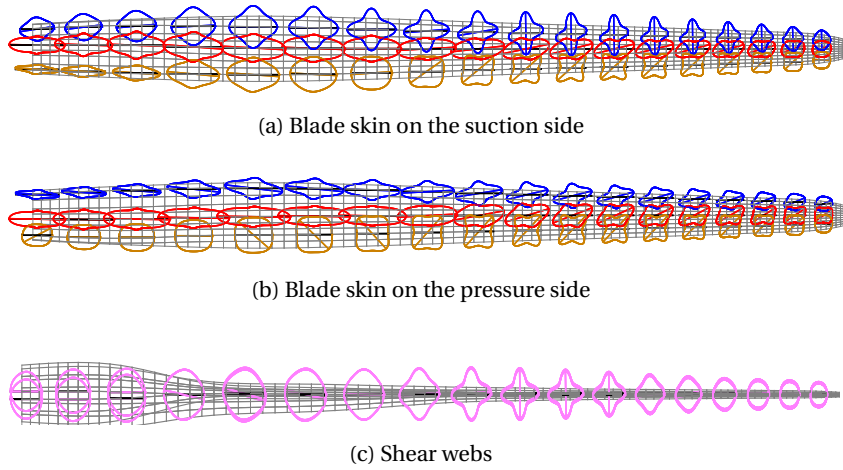


Figure 10.28: Optimized design, stiffness distribution from COE minimization using unbalanced laminates.

increase in power, torque, and thrust. The increase in the rated power is also observed from the increase in the AEP by more than 3%. This leads to the reduction of 2% of the COE compared to the final design using unbalanced laminates for the up-wind turbine configuration.

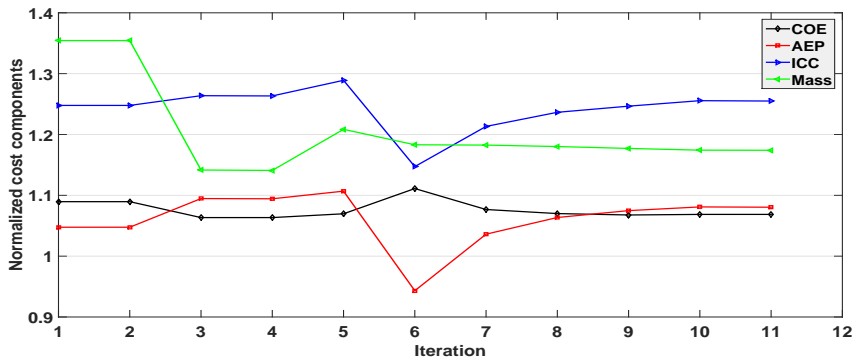


Figure 10.29: Evolution of COE and its components, for the optimization using unbalanced laminates and no constraint on tip deflection.

The corresponding skin thickness distribution is given in figure 10.30, which includes 2D and 3D representation of the skin thickness variation along the blade axis. The largest skin thickness is for the spar caps at the suction side of the blade, having the same thickness distribution as for the starting design, suggesting that buckling constraint is still an active constraint. The skin thickness distribution of the spar caps on the pressure side are different compared

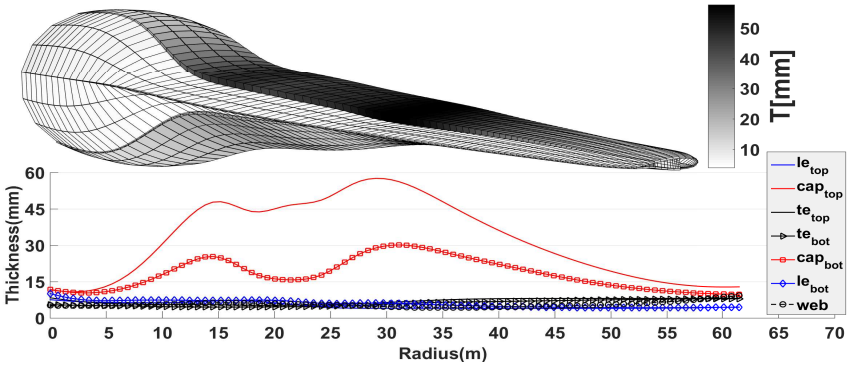


Figure 10.30: Optimized design, skin thickness distribution for COE minimization using unbalanced laminates and down-wind turbine configuration.

to the initial design of the current optimization, showing two local maximums around 15m and 30m of the blade radius.

The design wind speeds for the structural constraints (strain and buckling) are given in figures 10.31a for blade skin on the suction side, and 10.31b for blade skin pressure side, indicating that the design wind speed is 13m/s. The corresponding failure indices, both strain and buckling, are given in figures 10.31c and 10.31d respectively. Figures 10.31c and 10.31d show that the buck-

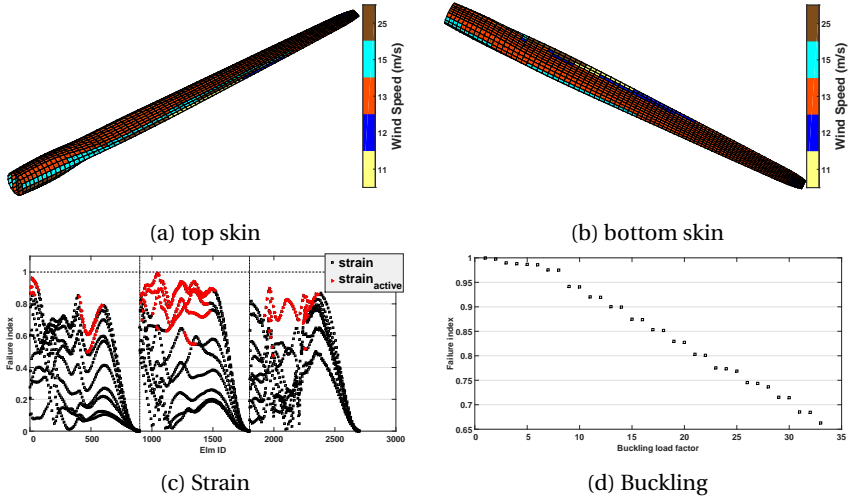


Figure 10.31: Optimized design, sizing wind speed/load case for COE minimization using unbalanced laminates and failure indices for wind speed = 13m/s, no constraint on power or tip deflection.

ling and strain constraints are both design drivers since both types of constraints reach the failure/design limit of one. Furthermore, it is observed from

figure 10.31c that more of the strain failure indices move closer to one, which suggests that the optimizer goes towards fully stressed design, however, without much success due to the structural indeterminate nature of the problem (aeroelastic loads) and the additional buckling constraint.

The history of the normalized aeroelastic responses is shown in figure 10.32, where the tip displacement of the blade is unconstrained, i.e. response values above one. There is a slight increase in the maximum torque and power (4% for torque and 3% for power), while the thrust decreases slightly (0.5%). The increase in torque and power is attributed to the optimized *induced* twist

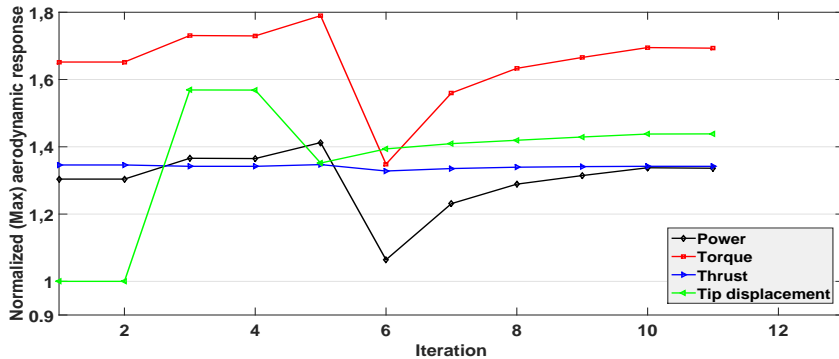


Figure 10.32: Aeroelastic response evolution from COE minimization using unbalanced laminates and no constraint on power or tip displacement.

distribution, as shown in figure 10.33. The top left plot of the figure contains the induced twist distribution for the initial (solid red line) and final (dashed red line) designs together with the *structural* twist (black line). For the final design, the *induced* twist distribution increase further towards feather for the inboard blade region, while slightly decreasing towards stall for the outboard blade region, compared to the initial design. This results in the reduction of the angle of attack (see the top right window of figure 10.33). The new *induced* twist distribution can be attributed to the new twist coupling coefficients (see the middle window of figure 10.33). The final twist coupling coefficients, calculated using equation 10.2, have substantially increased compared to the initial design with the bend-twist coupling having the largest coefficient, mainly due to the additional blade flexibility. Furthermore, the bend-twist coupling changes sign approximately at the mid section of the blade. An increase in lag-twist coupling is observed at the blade root, decreasing to zero at the midspan of the rotor blade. Additionally, a non-zero extension-twist coupling is also observed for the final design. The optimizer did not make use of the shear center location to reduce the *induced* twist towards stall, as shown in the bottom window of figure 10.33 where there is almost no difference in the location of the shear center between the initial and final design.

Figure 10.34 presents the performance indicators, comprised of power, torque, thrust, tip displacement, and root bending moment curves for differ-

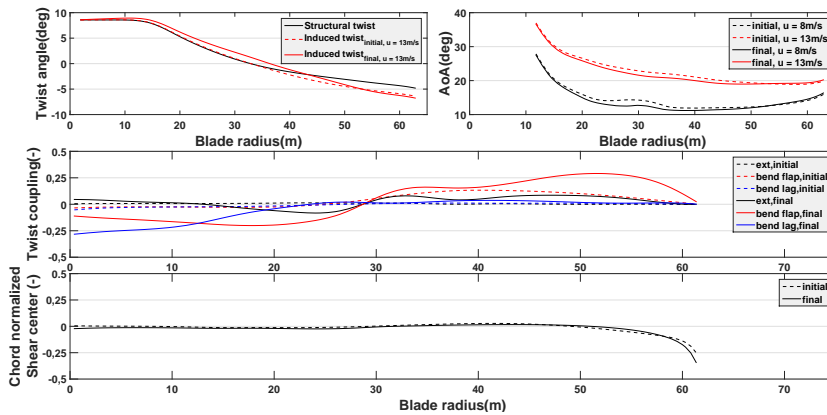


Figure 10.33: Initial and final value for: induced twist, angle of attack, twist coupling, and shear center, for COE minimization using unbalanced laminates, no constraint on power or tip displacement.

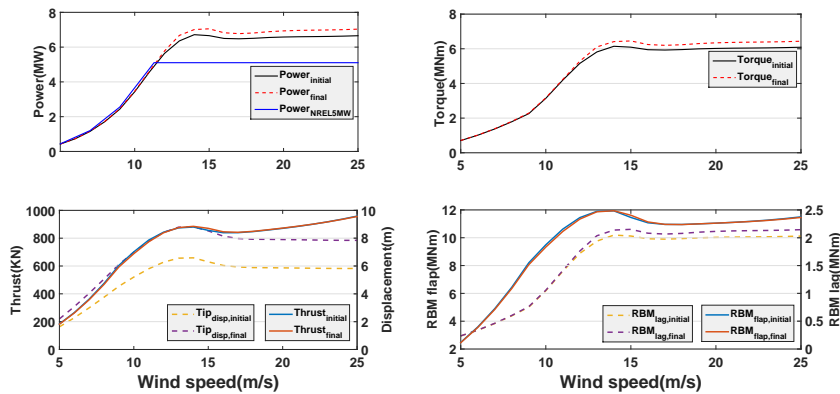


Figure 10.34: Initial and final value for: power, torque, thrust, tip displacement, and root bending moment, for COE minimization using unbalanced laminates, max power constraint.

ent wind speeds and both for the initial and final designs. The top right window shows that the power curve for the final design slightly increases below rated wind speeds and substantially increases above rated wind speed, compared to the initial design. This explains the relative increase of the AEP from figure 10.29. A large increase in tip displacement is observed for the final design (dashed lines in the bottom left window of figure 10.34). However, there is no difference in the thrust curve compared to the initial design (solid lines in the bottom left window of figure 10.34), which is also the case for the flap-wise root bending moment (solid lines in the bottom right window of figure 10.34).

Figure 10.35 shows the span-wise distribution of the major stiffness direction of all the laminates. The lag-wise bend-twist coupling for the inboard

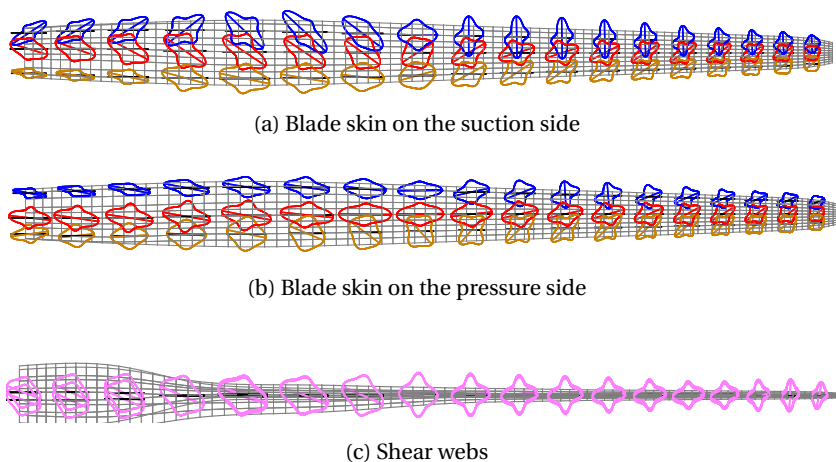


Figure 10.35: Optimized design, stiffness distribution from COE minimization using unbalanced laminates, no constraint on power or tip deflection.

blade region (see the bottom window of figure 10.33) results from the laminate stiffness distribution on the suction side of the blade skin (see figure 10.35a). From figure 10.35a it is observed that close to the blade root, the stiffness direction of the leading edge laminates (blue curve) and trailing edge laminates (brown curve) are symmetric with respect to the material x direction (black line), inducing lag-wise bend-twist coupling. The flap-wise bend-twist coupling is primarily caused by the stiffness distribution of the spar cap laminates, both on the suction and pressure side of the blade skin. Looking at figures 10.35a and 10.35b, the major stiffness direction of the spar cap laminates, on both side of the blade skin, are aligned in the same direction. For the inboard blade region, the major stiffness direction of the spar cap laminates is to the right of the beam axis while for the outboard blade region, it is to the left of the beam axis, which explains the change in the sign of the flap-wise bend-twist coupling coefficient (see the bottom window of figure 10.33). A larger flap-wise bend-twist coupling is achieved towards the outer blade region because of the additional biased stiffness distribution of the trailing edge laminates (brown curves), on both sides of the blade skin. Furthermore, it is observed from figure 10.35 that the stiffness distribution of the shear webs, especially for the inner blade region, contribute to the lag-wise bend-twist coupling.

10.7.4. COE MINIMIZATION WITH CONSTRAINED POWER

Finally, an optimization study is conducted with an additional constraint on maximum power. The constraint on maximum power is set to 110% and 120% of the rated power of the NREL 5MW pitch machine. Besides the constraint on maximum power, structural constraints (strain and buckling) together with the constraint on tip displacement are included in the optimization runs. For

both optimizations, the starting point is the baseline design from section 10.6. Table 10.7 shows the cost components of the final design, where the listed values are normalized with the corresponding value of the NREL 5MW pitch controlled machine, given in table 10.6. From table 10.7, the COE seems to

Table 10.7: Cost components of the final design for different constraint on maximum power. The results are normalized with the corresponding values of the *NREL 5MW* pitch regulated machine.

Constrained Power	COE	AEP	ICC	Blade mass	Load overshoots		
					Power	Torque	Thrust
1.10	1.13	0.97	1.20	1.62	1.10	1.40	1.34
1.20	1.11	1.02	1.24	1.58	1.20	1.52	1.34
Unconstrained	1.09	1.06	1.25	1.30	1.30	1.65	1.35

increase the stringent the constraint on maximum power becomes. The same trend is also observed for the AEP and blade mass, while the ICC decreases for more stringent constraint on maximum power. Furthermore, it is observed that the constraint on maximum power is active for power overshoots less than 1.3 of the rated power of the NREL pitch controlled machine.

The twist coupling of the final designs is shown in figure 10.36, which contains the distribution of the three twist coupling modes (extension, flap-wise bend, and lag-wise bend) along the blade axis. The solid black curves are for the design with a constraint on power equal to 110% of the NREL 5MW pitch controlled machine. The dashed red lines correspond to the design with 120% constraint on maximum power. Finally, the dotted blue lines are for the design with no constraint on maximum power.

It is observed that a significant extension-twist coupling is present for the final designs with a constraint on maximum power. However, the extension-twist coupling for the design with no constraint on power is negligible compared to the other designs. Significant flap-wise bend-twist coupling is achieved for all the design cases, where positive coupling coefficient (throughout the blade span) is obtained only for the design with the most stringent constraint on maximum power. A positive lag-wise bend-twist coupling coefficient is observed only for designs that include a constraint on maximum power, while for the unconstrained design (in-terms of power), the coupling coefficient is mostly negative.

Furthermore, the top right window of figure 10.36 shows the radial variation of the *induced* twist coupling for the different designs. The black line with the label *design* twist refers to the initial twist distribution listed in table 10.2. As expected, the lowest *induced* twist is for the design with power constraint of 110%, having a maximum reduction in twist of 3 deg (with respect to the *design* twist). Furthermore, the design with power constraint of 120%, a maximum difference of 2.5deg in twist is observed.

As a result of lower *induced* twist coupling, a lower power curve is obtained (see figure 10.37). Figure 10.37 contains the power curve of the optimized designs with a different level of constraints on maximum power. Furthermore,

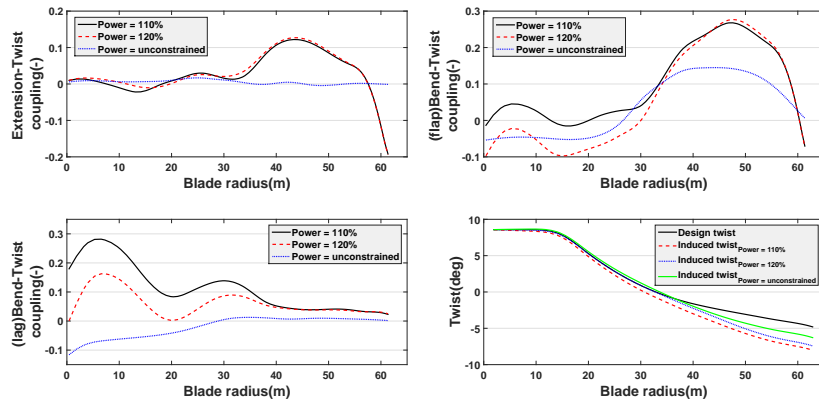


Figure 10.36: Twist coupling and induced twist, for different constrained maximum power.

figure 10.37 also contains the power curve of the NREL 5MW pitch controlled machine. The maximum power tends to decrease for more stringent constraint on power. However, it comes at the cost of reduced power for lower (below rated) wind speeds. This is also observed in lower annual energy production (AEP), as shown in table 10.7.

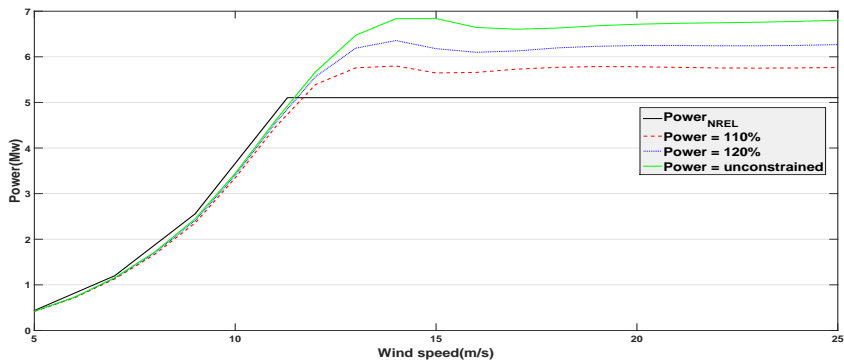


Figure 10.37: Power curve for different constrained maximum power.

Figure 10.38 shows the skin thickness distribution for the two designs with different constraints on maximum power. The maximum skin thickness (for both designs) is for the spar caps on the suction side, suggesting that the buckling constraint is still active. For the blade skins along the trailing edge (on both sides of the rotor blade), the laminate thickness increases suddenly for the outer blade region. A slight increase in the shear web laminate thickness is also observed for both designs. A general increase of the laminate thickness along both sides of the blade skin is observed for the designs that include constraint of maximum power; which is required since the major stiffness di-

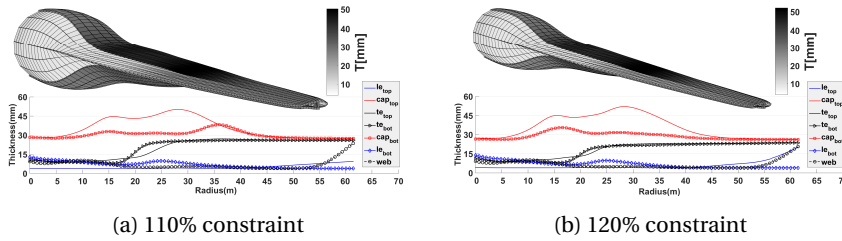


Figure 10.38: Optimized design, skin thickness distribution for COE minimization using balanced laminates, different constraint on maximum power.

rection of most laminates is not aligned along the blade axis (see figure 10.39). Figure 10.39 shows the major stiffness direction of the laminates for both designs having an additional constraint on maximum power. It is observed from the figure that the major stiffness direction of most laminates is at an angle with respect to the beam axis (black line), inducing the twist couplings shown in figure 10.36.

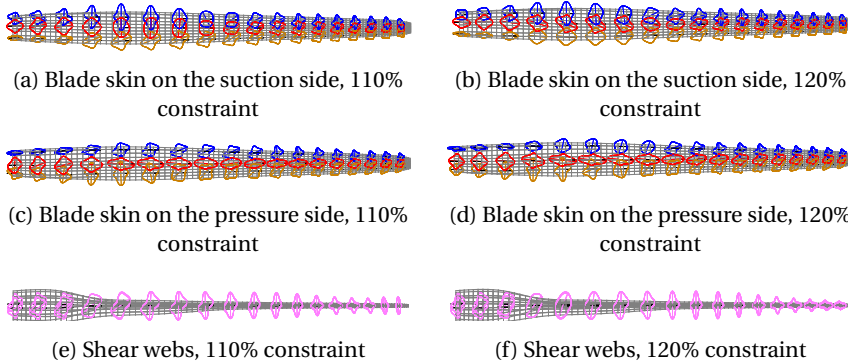


Figure 10.39: Optimized design, stiffness distribution from COE minimization using unbalanced laminates, different constraint on maximum power.

10.8. SUMMARY

This chapter presents several composite stiffness optimization studies of stall controlled wind turbines, that include both structural and aeroelastic constraints during the optimization process.

First, starting from the design of the NREL 5MW pitch controlled machine, an optimization run is carried out to design baseline 5MW stall controlled rotor blade. The objective is mass minimization using balanced laminates as design variables, while satisfying strain, buckling, and maximum tip displacement constraints. Starting from an initial rotor blade mass of 41×10^3 Kg and quasi-isotropic layup for all the laminates, a final design with the blade mass

of 23×10^3 Kg is achieved with the buckling and tip displacement constraints being the design drivers. The major stiffness direction of the spar caps laminates is aligned along the blade axis, which provides the required strength to comply with the structural constraints (stress, buckling and maximum tip displacement) thus resulting in a significant mass reduction of 56% compared to the initial design.

The advantage of unbalanced laminates over balanced laminates is demonstrated by a series of optimization cases, where the cost of energy (COE) is used as an objective function while considering both strain and buckling constraints. The COE for the design with balanced laminates is $1.11COE_{rel}$ compared to $1.09COE_{rel}$ for the design with unbalanced laminates, where $1.00COE_{rel}$ is the cost of energy for the NREL 5MW pitch regulated machine. The maximum power is reduced from 7.4MW (for balanced laminates) to 6.9MW (for unbalanced laminates). The reduction in power is due to a shift of *induced* twist distribution, towards stall, for unbalanced laminates compared to the *induced* twist distribution of balanced laminates. Compared to the *design* twist, a maximum difference in twist angle of $\approx 1.5^\circ$ is achieved for unbalanced laminates while for balanced laminates the difference is less than $\approx 0.5^\circ$. The difference is mainly due to the twist coupling, both extension-twist and bend-twist, which are zero for balanced laminates while for unbalanced laminates a maximum (flap-wise) bend-twist coupling coefficient of 0.14 is achieved. However, the final design with unbalanced laminates showed no significant extension-twist coupling. The reduction of $\approx 0.5^\circ$ in twist angle for balanced laminates is caused by a shift in the location of the shear center towards the trailing edge, caused by a redistribution of the laminate thickness across the cross-section, especially close to the blade tip. The main stiffness direction for the design with balanced laminates is symmetric with respect to the blade axis, while for the unbalanced laminates, the major stiffness direction is rotated to the right (20 to 30°) with respect to the beam axis, providing the aforementioned bend-twist coupling coefficient of 0.14.

Furthermore, both up-wind and down-wind turbine configuration are simulated during the optimization. The constraint on the maximum tip displacement is relaxed for the down-wind configuration. Another optimization case is carried out for the down-wind turbine configuration. The COE is minimized using unbalanced laminates subjected only to strain and buckling constraints. The final design results in COE reduction of $1.07COE_{rel}$, with $1.00COE_{rel}$ referring to the COE of the NREL 5MW pitch regulated machine. Furthermore, the optimized design with down-wind configuration shows an increase in AEP by more than 3% compared to the design for the up-wind configuration. For the down-wind configuration, the increase in power is attributed to the optimized *induced* twist distribution. Compared to the design with up-wind configuration, the *induced* twist distribution increases further towards feather for the inboard blade region while slightly decreasing towards stall for the outboard blade region. The new *induced* twist distribution is at-

tributed to the new twist coupling coefficients, where the final twist coupling coefficients have substantially increased compared to the up-wind design, mainly due to the additional blade flexibility. Furthermore for the down-wind configuration, the bend-twist coupling changes sign approximately at the mid section of the blade, which explains the observed induced twist distribution of the current design. An increase in (lag-wise) bend-twist coupling is observed at the blade root, decreasing to zero at the blade midspan. Additionally, a significant extension-twist coupling is observed for the down-wind configuration. The change in sign for (flap-wise) bend-twist coupling is attributed to the change in major stiffness direction of the laminates, where for the inner blade region, the stiffness direction of most laminates (primarily spar caps) is rotated left with respect to the beam axis, while for the outer blade region the stiffness direction is rotated right with respect to the blade axis.

Finally, an optimization study is carried out with an additional constraint on maximum power. Two optimization cases are carried out to minimize the COE with different level of constraint on the maximum power. The constraint on maximum power is set to 110% and 120% of the rated power of the *NREL 5MW* pitch regulated machine. The results show that the COE and blade mass increase for more stringent constraint on maximum power. On the other hand, the AEP and ICC decrease as the constraint on maximum power become more stringent. It is also observed that the constraint on maximum power is active for power overshoots lower than 130% of the rated power of the *NREL 5MW* pitch controlled machine.

11

CONCLUSIONS AND RECOMMENDATIONS

Recent advances in composite technology allow for controlling the aeroelastic response of wind turbine blades. Particularly, the use of twist coupling for passively regulating the loads and power of wind turbines show a promise to design adaptive blades for stall regulated wind turbines with superior performance. The application of variable stiffness design in combination with an aeroelastically deforming structure, also referred to as aeroelastic tailoring, shows additional promise to effectively exploit the advantage of composite materials to design adaptive blades tailored to the desired specification. The objective of the thesis is restated here as:

Perform an optimization study, based on minimization of the cost of energy (COE), to evaluate the additional benefit of adaptive blades on the performance of large stall regulated wind turbines.

11.1. CONCLUSIONS

The research is divided into two main stages to achieve the objective. For the first stage, an optimization methodology, based on isogeometric formulation, is developed that is tailored towards the design of wind turbine blades. For the second stage, several design studies are carried out for assessing the performance of an adaptive blade to be applied in stall regulated wind turbines. Conclusion of both stages is summarized in sections 11.1.1 and 11.1.2.

11.1.1. STIFFNESS OPTIMIZATION METHODOLOGY FOR WIND TURBINE BLADES

First, the blade geometry including its finite element model is generated based on the Isogeometric analysis (*IGA*) principle. Second, based on the user supplied operational parameters (range of operational wind speeds, turbines rotational speed, etc), the aeroelastic loads are calculated using a *low-fidelity* model. This generates the aeroelastic responses and their sensitivities with respect to the design variables. The (*low-fidelity*) aeroelastic module is a one-dimensional model, based on the *IGA* precept, to predict both the aerodynamic loads and the structural deformations. The *low-fidelity* module is composed of isogeometric based aero-structural model for analysing the static aeroelastic loads on wind turbine rotor blade. First, a computationally efficient formulation is presented to model the cross-sectional properties of thin-walled, multi-cell, and prismatic beams with anisotropic material properties. The formulation is based on the classical laminate theory, making it suitable for use in composite optimisation. Finite element method is then employed to evaluate the sectional stiffness constants of composite blades, which are then implemented in a beam model that is based on an isogeometric formulation of a geometrically exact 3D beam theory. The beam model uses quaternions to parametrize the rotation variable together with the isoparametric interpolation of the rotation parameters, defined at control points. The aerodynamic loads are calculated using a standard BEM theory, with an additional correction to account for a change in the blade shape due to blade deformation. The aerodynamic module is validated against the experimental data of the *MEXICO* rotor, showing a good match between experiment and the present method. Finally, the aeroelastic module is verified using the NREL 61.5m rotor blade as a baseline for comparison, showing a good agreement with the rotor loads calculated from *GH Bladed* and a reasonable agreement with the results from *FAST*. For the *high-fidelity* module, the aeroelastic loads are applied, together with their sensitivity, as design dependent loads onto a finite element model, followed by detailed structural analysis, including the sensitivity of the structural responses, using the finite element solver *NASTRAN*.

The optimization process uses the response approximation formulation of IJsselmuide [66], which is based on a linear and reciprocal approximation of the responses in terms of the design variables, i.e. elements of the membrane and bending stiffness matrix of a laminate together with the laminate thickness. Accordingly in the second step, an approximation model is formulated

using both the responses and their sensitivities, while satisfying the essential properties of convexity, separability, and conservativeness. The response approximations are then passed to the optimizer which iterates on the approximated model till the minimum that satisfies the constraints is found, resulting in new design variables. The new design variables are then passed to the analysis module and the whole process is repeated till the difference between successive optimum values of the objective function is below a given tolerance.

11.1.2. TWIST COUPLED ROTOR BLADE DESIGN FOR STALL REGULATED WIND TURBINES

In the second part of the thesis, several design studies are carried out to demonstrate the functionality of the developed optimization framework. Particularly, the benefit of variable stiffness design in turbine blades for improved performance of large scale stall regulated turbines is investigated with the use of the stiffness optimization process that incorporates both structural and aeroelastic responses.

First, a baseline design for a variable speed stall regulated 5MW wind turbine is created, using the *NREL 5MW* blade design as a starting point. The blade planform is generated using NURBS basis functions of cubic polynomials and 17 control points with which the blade geometry is defined. Among the design changes from the *NREL 5MW* blade design, two airfoils for the outer blade region are selected from an airfoil design study that is geared towards designing airfoils with improved stall characteristics at high Reynolds numbers ($Re = 9 \times 10^6$). The new 21% thick airfoil is employed between 38% and 69% of the blade span, with a maximum of 96% of the 21% airfoil shape realized at 53% of the blade span. The new 18% thick airfoil is employed between 53% of the blade span till the blade tip, where the blade cross-section consists solely of the 18% thick airfoil starting 70% of the blade span.

Considering the new airfoils, a new twist distribution is calculated for optimum variable speed operation below rated wind speed while inducing sufficient stall for high wind speeds, especially at the outboard blade regions. The structural components of the turbine blade are all composed of sandwich laminates, except the spar caps, where glass fiber laminates are used for the face sheets of the sandwich laminates and for the spar cap laminates. Furthermore, two spars are modelled at 0.3 and 0.7 of chord point.

The optimization model consists of 7 laminates per cross-section, defined at 15 control points along the blade span. Per cross-section, 3 laminates are used to define the material properties at the pressure side of the blade and three laminates at the suction side, with the remaining laminate defining the material properties of the shear webs. In total, the optimization model consists of 105 laminates as design variables. The aeroelastic loads, from the *low-fidelity* model, are calculated for sampled wind speeds between the cut-in and cut-out wind speed, while the structural responses, from the *high-fidelity* model, are evaluated for sampled wind speeds above rated wind speed.

Initial optimization case is conducted, where the optimal design serves as

a starting point for subsequent optimization studies. The objective is mass minimization using balanced laminates as design variables, while satisfying strain, buckling, and maximum tip displacement constraints. Starting from an initial rotor blade mass of 41×10^3 Kg and quasi-isotropic layup for all the laminates, a final design with the blade mass of 23×10^3 Kg is achieved with the buckling and tip displacement constraints being the design drivers. The major stiffness direction of the spar caps laminates is aligned along the blade axis, which provides the required strength to comply with the structural constraints (stress, buckling and maximum tip displacement) thus resulting in a significant mass reduction of 56% compared to the initial design. The final design for the stall regulated machine is 31% higher than the blade mass of the *NREL 5MW* pitch regulated machine. The difference in mass is mainly due to the higher load on the variable speed stall regulated machine compared to the pitch regulated machine where for stall regulated machine, there is an overshoot in the aeroelastic loads compared to the pitch regulated machine due to the difference in the control strategy.

COST MODEL

The cost model is based on the *NREL* cost model for pitch controlled wind turbines and modified in [106] to calculate the Cost Of Energy (COE) of stall controlled wind turbines. As part of the COE modification, the change in initial capital cost (ICC) for variable speed stall controlled machines is calculated by linearising the ICC of stall controlled machine around the ICC of the *NREL 5MW* pitch controlled machine in-terms of the load overshoots and blade mass. The load overshoots are comprised of: power, torque and thrust. The load overshoots are defined as the maximum power, torque, or thrust of the new design divided by its rated equivalent of the *NREL 5MW* pitch machine.

It should be noted that the present cost model is only a simplified first order approximation of the COE applied for stall regulated machines, provided that the load overshoots for the new design are not large (≤ 1.5). For larger load overshoots, the linearisation of the ICC in-terms of the load overshoots is not accurate and a more elaborated cost model needs to be formulated. Also nonlinear couplings need to be taken into account such as the coupling between (installed) power and AEP. In addition, the same *OM* and *LRC* value as for the reference *NREL 5MW* pitch machine are assumed in the current optimization, resulting in a conservative estimation of the COE for all designs.

Therefore, the present cost model serves only to provide a first order guess of the direction into which the COE might go during stiffness optimization of stall regulated wind turbine blades. Hence, the cost of energy results from the present optimization study should be treated with care.

BALANCED VS UNBALANCED LAMINATES

The objective of the present optimization is to investigate the benefit of variable stiffness designs to tailor the twist coupling of composite blades to improve the performance of variable speed stall regulated wind turbines. Ac-

cordingly, the advantage of unbalanced laminates over balanced laminates is investigated by minimizing the COE of variable speed stall regulated wind turbines while complying with structural and aeroelastic constraints. A complete stiffness variation along the blade span is considered during the optimization. The objective is to minimize the COE using both balanced and unbalanced composite laminates, while ensuring no structural and aeroelastic failures (strain, buckling and tip displacement). The results are verified using different starting designs for the optimization cases, where the different starting designs are comprised of different thickness and stiffness distribution.

COE minimization subject to buckling, strain and tip displacement constraints showed an advantage of unbalanced laminates over balanced laminates. The COE for the design with balanced laminates is $1.11COE_{rel}$ compared to $1.09COE_{rel}$ for the design with unbalanced laminates, where $1.00COE_{rel}$ is the cost of energy for the *NREL 5MW* pitch regulated machine. The maximum power is reduced from $7.4MW$ (for balanced laminates) to $6.9MW$ (for unbalanced laminates). The reduction in power is due to a shift of *induced* twist distribution, towards stall, for the unbalanced laminates compared to the *induced* twist distribution of balanced laminates. Compared to the *design* twist, a maximum difference in twist angle of $\approx 1.5deg$ is achieved for unbalanced laminates while for balanced laminates the difference is less than $\approx 0.5deg$. The difference is mainly due to the twist coupling, both extension-twist and bend-twist, which are zero for balanced laminates while for unbalanced laminates a maximum (flap-wise) bend-twist coupling coefficient of 0.14 is achieved. However, the final design with unbalanced laminates showed no significant extension-twist coupling. The reduction of $\approx 0.5deg$ in twist angle for balanced laminates is caused by a shift in the location of the shear center towards the trailing edge, caused by a redistribution of the laminate thickness across the cross-section, specially close to the blade tip. However, the design using unbalanced laminates makes almost no use of the location of the shear center to reduce the *induced* twist towards stall. The main stiffness direction for the design with balanced laminates is symmetric with respect to the blade axis, while for the unbalanced laminates, the major stiffness direction is rotated to the right (20 to 30deg) with respect to the beam axis, providing the aforementioned bend-twist coupling coefficient of 0.14.

UP-WIND VS DOWN-WIND CONFIGURATION

Furthermore, two operational configurations of a wind turbine are considered: up-wind and down-wind configuration. The constraint on the maximum tip displacement is relaxed for the down-wind configuration. Another optimization case is carried out for the down-wind turbine configuration. The COE is minimized using unbalanced laminates subjected only to strain and buckling constraints. The final design results in COE reduction of $1.07COE_{rel}$, with $1.00COE_{rel}$ referring to the COE of the *NREL 5MW* pitch regulated machine. Furthermore, the optimized design with down-wind configuration shows an increase in AEP by more than 3% compared to the design for the up-

wind configuration. For the down-wind configuration, the increase in power is attributed to the optimized *induced* twist distribution. Compared to the design with up-wind configuration, the *induced* twist distribution increases further towards feather for the inboard blade region while slightly decreasing towards stall for the outboard blade region. The new *induced* twist distribution is attributed to the new twist coupling coefficients, where the final twist coupling coefficients have substantially increased compared to the up-wind design, mainly due to the additional blade flexibility. Furthermore for the down-wind configuration, the bend-twist coupling changes sign approximately at the mid section of the blade, which explains the observed induced twist distribution of the current design. An increase in (lag-wise) bend-twist coupling is observed at the blade root, decreasing to zero at the blade mid-span. Additionally, a significant extension-twist coupling is observed for the down-wind configuration. The change in sign for (flap-wise) bend-twist coupling is attributed to the change in major stiffness direction of the laminates, where for the inner blade region, the stiffness direction of most laminates (primarily spar caps) is rotated left with respect to the beam axis, while for the outer blade region the stiffness direction is rotated right with respect to the blade axis.

CONSTRAINED POWER

Finally, an optimization study is carried out with additional constraint on maximum power. Two optimization cases are carried out to minimize the COE with different level of constraint on the maximum power. The constraint on maximum power is set to 110% and 120% of the rated power of the *NREL 5MW* pitch regulated machine. The results show that the COE and blade mass increase for more stringent constraint on maximum power. On the other hand, the AEP and ICC decreases as the constraint on maximum power becomes more stringent. Furthermore, the AEP decreases steeper than the ICC as the constraint on maximum power becomes more stringent. This is mainly due to the accumulative effect of the load overshoots on the ICC, dominating the direction in which the COE goes during the optimization. It is also observed that the constraint on maximum power is active for power overshoots lower than 130% of the rated power of the *NREL 5MW* pitch regulated machine. This indicates that a linear approximation of the ICC in-terms of the load overshoots lowers the fidelity of the present cost model, and a higher order approximation of the ICC in-terms of the load overshoots is needed.

11.2. RECOMMENDATIONS

It should be noted that the COE of the present optimization study are all larger than the cost of energy for the *NREL 5MW* pitch regulated machine. This results from the simple cost model used to calculate the COE of stall regulated wind turbines, the accuracy of which depends strongly on the extent of the load overshoots (power, torque and thrust) of the new design compared to the

rated values of the *NREL 5MW* pitch machine. Furthermore, the same *OM* and *LRC* value as for the *NREL 5MW* pitch machine is used in current optimization study. This is a conservative assumptions since there are fewer rotating components for stall controlled machines (no pitch mechanism), which reduces the *OM* and *LRC* of stall controlled machines. Additionally, the rotor blade used in the present optimization study is a retrofit of the rotor blade design for the *NREL 5MW* pitch regulated machine.

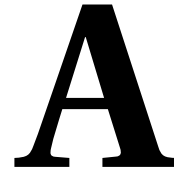
In-order to perform a fair comparison between modern pitch regulated and modern stall regulated machine: first, a new cost model needs to be formulated tailored for calculating the COE of stall regulated wind turbines with large rated power ($\geq 5MW$); second, a holistic design approach needs to be taken to design a new stall controlled wind turbine, where the complete layout of the turbine needs to be adapted for stall regulation. This way, a fair comparison can be performed between pitch and stall controlled machines with similar power rating.

The proposed optimization framework, using variable stiffness laminates, has generated encouraging results when designing adaptive blades while considering structural and aeroelastic constraints. This motivates to address several points to improve the proposed framework, such that the full advantage of composite materials is exploited during the design of adaptive blades and actual realization of the designs in real word application.

The second step after finding an optimum stiffness distribution that meets the objective and satisfies the constraints would be to determine the fiber angles that represent the optimum stiffness distribution. In the second step, point-wise laminate stacking sequence is determined that matches the obtained stiffness distribution while considering manufacturing constraints, such as thickness build up, draping, minimum curvature. Afterwards, the fiber angle distribution is converted into continuous fiber paths, suitable for manufacturing.

The optimization process could be expanded by including shape optimization, in conjunction with stiffness optimization, in a staggered optimization scheme. For the shape optimization part, the blade planform and the blade axis may be used as design variables in addition to the optimum stiffness design (from the stiffness optimization routine) resulting in further optimum design solutions. Currently, the optimization framework presented in chapter 3 is capable of parametrizing a turbine blade in terms of its material and geometric properties, tailored both for material and geometric optimization studies.

Furthermore, the current framework should be expanded to include unsteady aeroelastic responses in the optimization process. Design cases with gust loads; instability analysis, such as conventional flutter and stall flutter; yawed flow condition and tower shadow, could be incorporated to extend the operation envelope of the optimization framework. However, this requires the modelling of the complete wind turbine structure, including the foundation, tower, nacelle, etc., as part of the aeroelastic analysis module.



FINITE ELEMENT ANALYSIS ALTERS

A.1. RESPONSES AND SENSITIVITIES

FILE MANAGEMENT SECTION

ASSIGNOUTPUT4 = ' Resp.op4', unit = 92, unformatted, delete
ASSIGNOUTPUT4 = ' Sens.op4', unit = 94, unformatted, delete
ASSIGNOUTPUT4 = ' dscmcol.op2', unit = 95, unformatted, delete
ASSIGNOUTPUT4 = ' dF.op4', unit = 223, formatted

EXECUTIVE CONTROL STATEMENTS

COMPILESUBDMAP = EXITOPT
ALTER' IF(DSPRINT)DSAPRT'
OUTPUT4R1VALRG,,,// - 1/92///16
OUTPUT4,,,// - 2/92
OUTPUT4DSCM2,,,// - 1/94///16
OUTPUT4,,,// - 2/94
OUTPUT2DSCMCOL,,,// - 1/95/'DSCMCOL'
OUTPUT2,,,// - 9/95/

A.2. ALTER: CORRECT ERROR IN DSCM2

COMPILEPSLGDV
Alter to correct sensitivity from nastran
alter'bcd'r'(7),"
BCDRCASEau/10/'10//s,n,mbcflg//////// - 1

A.3. ALTER: IMPORT SENSITIVITIES

COMPILEPSLGDV

Alter to input load sensitivity (dF) into nastran sensitivity calculation

ALTER495

message/'writedFtoEGKP,blub'

DELETE/EGKP,,,/

INPUTT4/EGKP,,,/1/223/-1/1

altertocorrectsensitivityfromnastran

alter'bcdr'(7),"

BCDRCASEau/0/'/0/'s,n,mbcflg////////-1

BIBLIOGRAPHY

- [1] Anders Ahlström. *Aeroelastic simulation of wind turbine dynamics*. PhD thesis, Department of Mechanics, Royal Institute of Technology Stockholm, 2005.
- [2] Sohail Ahmed and MN Ahmed. Torsional analysis of multi-cell multi-tapered composite beams with cantilever configuration. *Thin-Walled Structures*, 96:75–81, 2015.
- [3] I Akkerman, Y Bazilevs, VM Calo, TJR Hughes, and S Hulshoff. The role of continuity in residual-based variational multiscale modeling of turbulence. *Computational Mechanics*, 41(3):371–378, 2008.
- [4] John Argyris. An excursion into large rotations. *Computer methods in applied mechanics and engineering*, 32(1):85–155, 1982.
- [5] John Argyris and Victor Florin Poterasu. Large rotations revisited application of lie algebra. *Computer methods in applied mechanics and engineering*, 103(1):11–42, 1993.
- [6] Thomas D Ashwill. Sweep-twist adaptive rotor blade: final project report. Technical report, Sandia National Laboratories, 2010.
- [7] F Auricchio, L Beirao da Veiga, J Kiendl, C Lovadina, and A Reali. Locking-free isogeometric collocation methods for spatial timoshenko rods. *Computer Methods in Applied Mechanics and Engineering*, 263:113–126, 2013.
- [8] F Auricchio, L Beirao Da Veiga, C Lovadina, and A Reali. The importance of the exact satisfaction of the incompressibility constraint in nonlinear elasticity: mixed fems versus nurbs-based approximations. *Computer Methods in Applied Mechanics and Engineering*, 199(5):314–323, 2010.
- [9] Klaus Jrgen Bathe and Sa d Bolourchi. Large displacement analysis of three? dimensional beam structures. *International Journal for Numerical Methods in Engineering*, 14(7):961–986, 1979.
- [10] Y Bazilevs, VM Calo, JA Cottrell, TJR Hughes, A Reali, and G Scovazzi. Variational multiscale residual-based turbulence modeling for large eddy simulation of incompressible flows. *Computer Methods in Applied Mechanics and Engineering*, 197(1):173–201, 2007.

- [11] Y Bazilevs and TJR Hughes. Nurbs-based isogeometric analysis for the computation of flows about rotating components. *Computational Mechanics*, 43(1):143–150, 2008.
- [12] V.L. Berdichevsky. Variational-asymptotic method of constructing a theory of shells. *PMM*, 43(4):664–687, 1979.
- [13] P Betsch, A Menzel, and E Stein. On the parametrization of finite rotations in computational mechanics: A classification of concepts with application to smooth shells. *Computer Methods in Applied Mechanics and Engineering*, 155(3):273–305, 1998.
- [14] K Bhaskar and TK Varadan. Benchmark elasticity solution for locally loaded laminated orthotropic cylindrical shells. *AIAA journal*, 32(3):627–632, 1994.
- [15] Mark W Bloomfield, J Enrique Herencia, and Paul M Weaver. Enhanced two-level optimization of anisotropic laminated composite plates with strength and buckling constraints. *Thin-Walled Structures*, 47(11):1161–1167, 2009.
- [16] EA Bossanyi. Gh bladed theory manual. *GH & Partners Ltd*, 2003.
- [17] Carlo L Bottasso and Marco Borri. Integrating finite rotations. *Computer Methods in Applied Mechanics and Engineering*, 164(3):307–331, 1998.
- [18] CL Bottasso, F Campagnolo, A Croce, and C Tibaldi. Optimization-based study of bend–twist coupled rotor blades for passive and integrated passive/active load alleviation. *Wind Energy*, 16(8):1149–1166, 2013.
- [19] GW Bottrell. Passive cyclic pitch control for horizontal axis wind turbines. In *Wind Turbine Dynamics*, volume 1, pages 271–275, 1981.
- [20] Robin Bouclier, Thomas Elguedj, and Alain Combescure. Locking free isogeometric formulations of curved thick beams. *Computer Methods in Applied Mechanics and Engineering*, 245:144–162, 2012.
- [21] Simon-Philippe Breton, Frank N Coton, and Geir Moe. A study on rotational effects and different stall delay models using a prescribed wake vortex scheme and nrel phase vi experiment data. *Wind Energy*, 11(5):459–482, 2008.
- [22] A Buffa, C De Falco, and G Sangalli. Isogeometric analysis: stable elements for the 2d stokes equation. *International Journal for Numerical Methods in Fluids*, 65(11-12):1407–1422, 2011.
- [23] M Capuzzi, A Pirrera, and PM Weaver. A novel adaptive blade concept for large-scale wind turbines. part i: Aeroelastic behaviour. *Energy*, 73:15–24, 2014.

- [24] M Capuzzi, A Pirrera, and PM Weaver. A novel adaptive blade concept for large-scale wind turbines. part ii: Structural design and power performance. *Energy*, 73:25–32, 2014.
- [25] M Capuzzi, A Pirrera, and PM Weaver. Structural design of a novel aeroelastically tailored wind turbine blade. *Thin-Walled Structures*, 95:7–15, 2015.
- [26] Alberto Cardona. *An integrated approach to mechanism analysis*. PhD thesis, Université de Liège, Faculté des Sciences Appliquées, 1991.
- [27] JF Caseiro, RAF Valente, A Reali, J Kiendl, F Auricchio, and RJ Alves De Sousa. On the assumed natural strain method to alleviate locking in solid-shell nurbs-based finite elements. *Computational Mechanics*, 53(6):1341–1353, 2014.
- [28] Ismail Celik and Wei-Ming Zhang. Calculation of numerical uncertainty using richardson extrapolation: application to some simple turbulent flow calculations. *Journal of Fluids Engineering*, 117(3):439–445, 1995.
- [29] Carlos ES Cesnik and Dewey H Hodges. Stiffness constants for initially twisted and curved composite beams. *ASME AEROSP DIV PUBL AD, ASME, NEW YORK, NY(USA), 1992,,* 30:1–8, 1992.
- [30] Carlos ES Cesnik and Dewey H Hodges. Variational-asymptotical analysis of initially curved and twisted composite beams. *Applied Mechanics Reviews*, 46(11S):S211–S220, 1993.
- [31] Carlos ES Cesnik and Dewey H Hodges. Stiffness constants for composite beams including large initial twist and curvature effects. *Applied Mechanics Reviews*, 48(11S):S61–S67, 1995.
- [32] Carlos ES Cesnik and Dewey H Hodges. Vabs: A new concept for composite rotor blade cross-sectional modeling. *Journal of the American Helicopter Society*, 42(1):27–38, 1997.
- [33] Uttam Kumar Chakravarty. On the modeling of composite beam cross-sections. *Composites Part B: Engineering*, 42(4):982–991, 2011.
- [34] MC Cheney and PAM Spierings. Self-regulating composite bearingless wind turbine. *Solar Energy*, 20(3):233–240, 1978.
- [35] Seonho Cho and Seung-Hyun Ha. Isogeometric shape design optimization: exact geometry and enhanced sensitivity. *Structural and Multidisciplinary Optimization*, 38(1):53–70, 2009.
- [36] J Austin Cottrell, Thomas JR Hughes, and Yuri Bazilevs. *Isogeometric analysis: toward integration of CAD and FEA*. John Wiley & Sons, 2009.

- [37] JA Cottrell, TJR Hughes, and A Reali. Studies of refinement and continuity in isogeometric structural analysis. *Computer methods in applied mechanics and engineering*, 196(41):4160–4183, 2007.
- [38] JA Cottrell, A Reali, Y Bazilevs, and TJR Hughes. Isogeometric analysis of structural vibrations. *Computer methods in applied mechanics and engineering*, 195(41):5257–5296, 2006.
- [39] Michael A Crisfield and Gordan Jelenić. Objectivity of strain measures in the geometrically exact three-dimensional beam theory and its finite-element implementation. *Proceedings of the Royal Society of London. Series A: Mathematical, Physical and Engineering Sciences*, 455(1983):1125–1147, 1999.
- [40] Luis A Crivelli and Carlos A Felippa. A three-dimensional non-linear timoshenko beam based on the core-congruential formulation. *International journal for numerical methods in engineering*, 36(21):3647–3673, 1993.
- [41] H Currin. North wind 4kw passive control system design. In *Wind Turbine Dynamics*, 1981.
- [42] L Beirao da Veiga, C Lovadina, and A Reali. Avoiding shear locking for the timoshenko beam problem via isogeometric collocation methods. *Computer Methods in Applied Mechanics and Engineering*, 241:38–51, 2012.
- [43] WC De Goeij, MJL Van Tooren, and Adriaan Beukers. Implementation of bending-torsion coupling in the design of a wind-turbine rotor-blade. *Applied Energy*, 63(3):191–207, 1999.
- [44] Johannes Karl Stefan Dillinger. *Static Aeroelastic Optimization of Composite Wings with Variable Stiffness Laminates*. TU Delft, Delft University of Technology, 2014.
- [45] Alan M Ebner and Joseph J Ucciferro. A theoretical and numerical comparison of elastic nonlinear finite element methods. *Computers & Structures*, 2(5):1043–1061, 1972.
- [46] R Echter, B Oesterle, and M Bischoff. A hierarchic family of isogeometric shell finite elements. *Computer Methods in Applied Mechanics and Engineering*, 254:170–180, 2013.
- [47] Vladimir Fedorov. *Bend-twist coupling effects in wind turbine blades*. PhD thesis, Dissertation, Technical University of Denmark, 2012.
- [48] Etana A Ferede and Mostafa M Abdalla. Cross-sectional modelling of thin-walled composite beams. In *Proceedings of the 55th AIAA/ASME/ASCE/AHS/SC Structures, Structural Dynamics, and Materials Conference*, 2014.

- [49] Lee Jay Fingersh, M Maureen Hand, and Alan S Laxson. Wind turbine design cost and scaling model, 2006.
- [50] Vittorio Giavotto, Marco Borri, Paolo Mantegazza, G Ghiringhelli, V Carmaschi, GC Maffioli, and F Mussi. Anisotropic beam theory and applications. *Computers & Structures*, 16(1):403–413, 1983.
- [51] Ronald N Goldman and Tom Lyche. *Knot insertion and deletion algorithms for B-spline curves and surfaces*, volume 36. SIAM, 1993.
- [52] F Sebastian Grassia. Practical parameterization of rotations using the exponential map. *Journal of graphics tools*, 3(3):29–48, 1998.
- [53] D Todd Griffith and Thomas D Ashwill. The sandia 100-meter all-glass baseline wind turbine blade: Snl100-00. *Sandia National Laboratories, Albuquerque, Report No. SAND2011-3779*, 2011.
- [54] Zafer Gürdal, Raphael T Haftka, and Prabhat Hajela. *Design and optimization of laminated composite materials*. John Wiley & Sons, 1999.
- [55] Raphael T Haftka and Zafer Gürdal. *Elements of structural optimization*, volume 11. Springer Science & Business Media, 2012.
- [56] Martin OL Hansen. *Aerodynamics of wind turbines: rotors, loads and structure*, volume 17. Earthscan, 2000.
- [57] Martin Otto Laver Hansen, Jens Nørkær Sørensen, S Voutsinas, Niels Sørensen, and H Aa Madsen. State of the art in wind turbine aerodynamics and aeroelasticity. *Progress in aerospace sciences*, 42(4):285–330, 2006.
- [58] Khazar Hayat and Sung Kyu Ha. Load mitigation of wind turbine blade by aeroelastic tailoring via unbalanced laminates composites. *Composite Structures*, 128:122–133, 2015.
- [59] Joseph P Hennessey Jr. Some aspects of wind power statistics. *Journal of applied meteorology*, 16(2):119–128, 1977.
- [60] Dewey H Hodges. Nonlinear composite beam theory. *Progress in astronautics and aeronautics*, 213:304, 2006.
- [61] Dewey H Hodges, Ali R Atilgan, Carlos ES Cesnik, and Mark V Fulton. On a simplified strain energy function for geometrically nonlinear behaviour of anisotropic beams. *Composites Engineering*, 2(5):513–526, 1992.
- [62] KH Hotenemser and AHP Swift. Dynamics of an experimental two bladed horizontal axis wind turbine with blade cyclic pitch variation. In *Wind Turbine Dynamics*, volume 1, pages 277–286, 1981.

- [63] Ming-Chen Hsu, Ido Akkerman, and Yuri Bazilevs. High-performance computing of wind turbine aerodynamics using isogeometric analysis. *Computers & Fluids*, 49(1):93–100, 2011.
- [64] Thomas JR Hughes, John A Cottrell, and Yuri Bazilevs. Isogeometric analysis: Cad, finite elements, nurbs, exact geometry and mesh refinement. *Computer methods in applied mechanics and engineering*, 194(39):4135–4195, 2005.
- [65] Thomas JR Hughes, John A Evans, and Alessandro Reali. Finite element and nurbs approximations of eigenvalue, boundary-value, and initial-value problems. *Computer Methods in Applied Mechanics and Engineering*, 272:290–320, 2014.
- [66] Samuel Tsunduka IJsselmuiden. *Optimal design of variable stiffness composite structures using lamination parameters*. TU Delft, Delft University of Technology, 2011.
- [67] IRENA. Renewable energy technologies: cost analysis series (volume 1), 2012.
- [68] Gordan Jelenić and MA Crisfield. Geometrically exact 3d beam theory: implementation of a strain-invariant finite element for statics and dynamics. *Computer Methods in Applied Mechanics and Engineering*, 171(1):141–171, 1999.
- [69] Hung-Sying Jing and Kuan-Goang Tzeng. Elasticity solution for laminated anisotropic cylindrical panels in cylindrical bending. *Composite structures*, 30(3):307–317, 1995.
- [70] Robert M Jones. *Mechanics of composite materials*. Crc Press, 1998.
- [71] Jason M Jonkman and Marshall L Buhl Jr. Fast user's guide. *Golden, CO: National Renewable Energy Laboratory*, 2005.
- [72] Jason Mark Jonkman, Sandy Butterfield, Walter Musial, and George Scott. *Definition of a 5-MW reference wind turbine for offshore system development*. National Renewable Energy Laboratory Golden, CO, 2009.
- [73] NM Karaolis, PJ Mussgrove, and G Jeronimidis. Active and passive aeroelastic power control using asymmetric fibre reinforced laminates for wind turbine blades. In *Proceedings of the 10th British Wind Energy Conference, London*, 1988.
- [74] A Khani, ST IJsselmuiden, MM Abdalla, and Z Gürdal. Design of variable stiffness panels for maximum strength using lamination parameters. *Composites Part B: Engineering*, 42(3):546–552, 2011.

- [75] J Kiendl, F Auricchio, TJR Hughes, and A Reali. Single-variable formulations and isogeometric discretizations for shear deformable beams. *Computer Methods in Applied Mechanics and Engineering*, 284:988–1004, 2015.
- [76] J Kiendl, K-U Bletzinger, J Linhard, and R Wüchner. Isogeometric shell analysis with kirchhoff-love elements. *Computer Methods in Applied Mechanics and Engineering*, 198(49):3902–3914, 2009.
- [77] Nam-Il Kim, Dong Ku Shin, and Moon-Young Kim. Exact solutions for thin-walled open-section composite beams with arbitrary lamination subjected to torsional moment. *Thin-walled structures*, 44(6):638–654, 2006.
- [78] HJT Kooijman. *Bending-torsion coupling of a wind turbine rotor blade*. Netherlands Energy Research Foundation ECN, 1996.
- [79] JB Kosmatka and SB Dong. Saint-venant solutions for prismatic anisotropic beams. *International Journal of Solids and Structures*, 28(7):917–938, 1991.
- [80] JB Kosmatka, HC Lin, and SB Dong. On saint-venant's problem for an inhomogeneous, anisotropic cylinder—part ii: Cross-sectional properties. *Journal of applied mechanics*, 68(3):382–391, 2001.
- [81] Scott Larwood and Mike Zuteck. Swept wind turbine blade aeroelastic modeling for loads and dynamic behavior. *AWEA windpower*, pages 1–17, 2006.
- [82] Sang Jin Lee and Kyoung Sub Park. Vibrations of timoshenko beams with isogeometric approach. *Applied Mathematical Modelling*, 37(22):9174–9190, 2013.
- [83] HC Lin, SB Dong, and JB Kosmatka. On saint-venant's problem for an inhomogeneous, anisotropic cylinder—part iii: End effects. *Journal of applied mechanics*, 68(3):392–398, 2001.
- [84] C Lindenburg and H Snel. Aero-elastic stability analysis tools for large wind turbine rotor blades. In *Proceedings of the 2003 European Wind Energy Conference and Exhibition*, volume 6. European Wind Energy Association Madrid, Spain, 2003.
- [85] Scott Lipton, John A Evans, Yuri Bazilevs, Thomas Elguedj, and Thomas JR Hughes. Robustness of isogeometric structural discretizations under severe mesh distortion. *Computer Methods in Applied Mechanics and Engineering*, 199(5):357–373, 2010.
- [86] Dianzi Liu and Vassili V Toropov. A lamination parameter-based strategy for solving an integer-continuous problem arising in composite optimization. *Computers & Structures*, 128:170–174, 2013.

- [87] Don W Lobitz, Paul S Veers, G Richard Eisler, David J Laino, Paul G Migliore, and Gunjit Bir. *The use of twist-coupled blades to enhance the performance of horizontal axis wind turbines*. Sandia National Laboratories, 2001.
- [88] Don W Lobitz, Paul S Veers, and David J Laino. Performance of twist-coupled blades on variable speed rotors. Technical report, Sandia National Labs., Albuquerque, NM (US); Sandia National Labs., Livermore, CA (US), 1999.
- [89] J Loughlan and M Ata. The constrained torsional characteristics of some carbon fibre composite box-beams. *Thin-walled structures*, 28(3):233–252, 1997.
- [90] Richard H MacNeal. *The NASTRAN theoretical manual*, volume 221. Scientific and Technical Information Office, National Aeronautics and Space Administration, 1970.
- [91] Richard H Macneal and Robert L Harder. A proposed standard set of problems to test finite element accuracy. *Finite elements in Analysis and Design*, 1(1):3–20, 1985.
- [92] Alireza Maheri, Siamak Noroozi, and John Vinney. Application of combined analytical/fea coupled aero-structure simulation in design of wind turbine adaptive blades. *Renewable Energy*, 32(12):2011–2018, 2007.
- [93] Alireza Maheri, Siamak Noroozi, and John Vinney. Decoupled aerodynamic and structural design of wind turbine adaptive blades. *Renewable Energy*, 32(10):1753–1767, 2007.
- [94] James F Manwell, Jon G McGowan, and Anthony L Rogers. *Wind energy explained: theory, design and application*. John Wiley & Sons, 2010.
- [95] Gregory J. Moore. *MSC/NASTRAN Design Sensitivity and Optimization User's Guide*. MSC, April 1994.
- [96] Gregory J. Moore. *MSC/NASTRAN Design Sensitivity and Optimization User's Guide*. MSC, April 1994.
- [97] Eugene C Morgan, Matthew Lackner, Richard M Vogel, and Laurie G Baise. Probability distributions for offshore wind speeds. *Energy Conversion and Management*, 52(1):15–26, 2011.
- [98] PJ Moriarty and AC Hansen. Aerodyn theory manual. *National Renewable Energy Laboratory*, 2005.
- [99] MSC Nastran. Quick reference guide. *MSC. SOFTWARE*, 1, 2004.

- [100] N Nguyen-Thanh, N Valizadeh, MN Nguyen, H Nguyen-Xuan, X Zhuang, P Areias, G Zi, Y Bazilevs, L De Lorenzis, and T Rabczuk. An extended isogeometric thin shell analysis based on kirchhoff-love theory. *Computer Methods in Applied Mechanics and Engineering*, 284:265–291, 2015.
- [101] Cheng-Huat Ong and Stephen W Tsai. *Design, manufacture and testing of a bend-twist D-spar*. Sandia National Laboratories, 1999.
- [102] NJ Pagano. Exact solutions for composite laminates in cylindrical bending. *Journal of composite materials*, 3(3):398–411, 1969.
- [103] NJ Pagano. Exact solutions for rectangular bidirectional composites and sandwich plates. *Journal of composite materials*, 4(1):20–34, 1970.
- [104] Patrik Passon and Martin Kühn. State-of-the-art and development needs of simulation codes for offshore wind turbines. In *Copenhagen Offshore Wind 2005 Conference and Expedition Proceedings*, pages 26–28, 2005.
- [105] R. Pereira, E. Ferede, G.J. van Bussel, and W.A. Timmer. Airfoil optimization paper. *Submitted to Wind Energy Journal*, 2015.
- [106] R. Pereira, G.J. van Bussel, and W.A. Timmer. Planform optimization of active stall controlled hawt rotor. *Submitted to Wind Energy Journal*, 2015.
- [107] WF Phillips, CE Hailey, and GA Gebert. Review of attitude representations used for aircraft kinematics. *Journal of Aircraft*, 38(4):718–737, 2001.
- [108] Les A. Piegl and Wayne Tiller. *The NURBS book*. Springer, 1995.
- [109] Bogdan Popescu and Dewey H Hodges. Asymptotic treatment of the trapeze effect in finite element cross-sectional analysis of composite beams. *International Journal of Non-Linear Mechanics*, 34(4):709–721, 1999.
- [110] Bogdan Popescu and Dewey H Hodges. On asymptotically correct timoshenko-like anisotropic beam theory. *International Journal of Solids and Structures*, 37(3):535–558, 2000.
- [111] Bogdan Popescu, Dewey H Hodges, and Carlos ES Cesnik. Obliqueness effects in asymptotic cross-sectional analysis of composite beams. *Computers & Structures*, 76(4):533–543, 2000.
- [112] Zhanming Qin and Liviu Librescu. On a shear-deformable theory of anisotropic thin-walled beams: further contribution and validations. *Composite Structures*, 56(4):345–358, 2002.

- [113] Alessandro Reali and Hector Gomez. An isogeometric collocation approach for bernoulli–euler beams and kirchhoff plates. *Computer Methods in Applied Mechanics and Engineering*, 284:623–636, 2015.
- [114] JG Ren. Exact solutions for laminated cylindrical shells in cylindrical bending. *Composites Science and Technology*, 29(3):169–187, 1987.
- [115] Brian Ray Resor. Definition of a 5mw/61.5 m wind turbine blade reference model. *Albuquerque, New Mexico, USA, Sandia National Laboratories, SAND2013-2569 2013*, 2013.
- [116] Mark Robinson. *Programming DMAP in MSC.Nastran™ Direct Matrix Abstract Programming*. Mark Robinson, July 2012.
- [117] Ignacio Romero. The interpolation of rotations and its application to finite element models of geometrically exact rods. *Computational mechanics*, 34(2):121–133, 2004.
- [118] J. B. Kosmatka S. B. Dong. On saint-venant’s problem for an inhomogeneous, anisotropic cylinder—part i: Methodology for saint-venant solutions. *Journal of Applied Mechanics-transactions of The Asme - J APPL MECH*, 68(3), 2001.
- [119] JG Schepers, K Boorsma, T Cho, S Gomez-Iradi, P Schaffarczyk, A Jeromin, WZ Shen, T Lutz, K Meister, B Stoevesandt, et al. Final report of iea task 29, mexnext (phase 1): Analysis of mexico wind tunnel measurements. *Wind Energy*, 2013:2012, 2014.
- [120] JG Schepers, JJ Heijdra, D Foussekis, S Øye, R Rawlinson Smith, M Bellessis, K Thomsen, T Larsen, I Kraan, B Visser, et al. *Verification of European wind turbine design codes, VEWTD: final report*. Netherlands Energy Research Foundation ECN, 2002.
- [121] Wen Zhong Shen, Robert Mikkelsen, Jens Nørkær Sørensen, and Christian Bak. Tip loss corrections for wind turbine computations. *Wind Energy*, 8(4):457–475, 2005.
- [122] J. C. Simo and D. D. Fox. On a stress resultant geometrically exact shell model. part i: Formulation and optimal parametrization. *Computer Methods in Applied Mechanics and Engineering*, 72(3):267–304, March 1989.
- [123] JC Simo. A finite strain beam formulation. the three-dimensional dynamic problem. part i. *Computer methods in applied mechanics and engineering*, 49(1):55–70, 1985.
- [124] JC Simo and Loc Vu-Quoc. A three-dimensional finite-strain rod model. part ii: Computational aspects. *Computer methods in applied mechanics and engineering*, 58(1):79–116, 1986.

- [125] Edward C Smith and Inderjit Chopra. Formulation and evaluation of an analytical model for composite box-beams. *J. Am. Helicopter Soc.*, 36(3):23–35, 1991.
- [126] O Song and L Librescu. Free vibration of anisotropic composite thin-walled beams of closed cross-section contour. *Journal of Sound and Vibration*, 167(1):129–147, 1993.
- [127] Stane Srpcič and Miran Saje. Large deformations of thin curved plane beam of constant initial curvature. *International journal of mechanical sciences*, 28(5):275–287, 1986.
- [128] Alan D Stemple and Sung W Lee. A finite element model for composite beams undergoing large deflection with arbitrary cross-sectional warping. *International journal for numerical methods in engineering*, 28(9):2143–2160, 1989.
- [129] Sven-Erik Thor and Patricia Weis-Taylor. Long-term research and development needs for wind energy for the time frame 2000–2020. *Wind Energy*, 5(1):73–75, 2002.
- [130] Loc V Tran, AJM Ferreira, and Hung Nguyen-Xuan. Isogeometric analysis of functionally graded plates using higher-order shear deformation theory. *Composites Part B: Engineering*, 51:368–383, 2013.
- [131] Stephen W Tsai and Nicholas J Pagano. Invariant properties of composite materials. Technical report, DTIC Document, 1968.
- [132] Julien MJF Van Campen, Christos Kassapoglou, and Zafer Gürdal. Generating realistic laminate fiber angle distributions for optimal variable stiffness laminates. *Composites Part B: Engineering*, 43(2):354–360, 2012.
- [133] T Van Engelen. Control design based on aero-hydro-servo-elastic linear models from turbu (ecn). In *Proceeding of the European wind energy conference, Milan, Italy*, 2007.
- [134] Thuc Phuong Vo and Jaehong Lee. Geometrically nonlinear analysis of thin-walled open-section composite beams. *Computers & structures*, 88(5):347–356, 2010.
- [135] Vitali V Volovoi and Dewey H Hodges. Single-and multicelled composite thin-walled beams. *ALAA journal*, 40(5):960–965, 2002.
- [136] Oliver Weeger, Utz Wever, and Bernd Simeon. Isogeometric analysis of nonlinear euler-bernoulli beam vibrations. *Nonlinear Dynamics*, 72(4):813–835, 2013.

- [137] Wenbin Yu. *Variational asymptotic modeling of composite dimensionally reducible structures*. PhD thesis, Georgia Institute of Technology, School of Aerospace Engineering, 2002.
- [138] Wenbin Yu, Dewey H Hodges, Vitali V Volovoi, and Eduardo D Fuchs. A generalized vlasov theory for composite beams. *Thin-Walled Structures*, 43(9):1493–1511, 2005.
- [139] Wenbin Yu, Lin Liao, Dewey H Hodges, and Vitali V Volovoi. Theory of initially twisted, composite, thin-walled beams. *Thin-walled structures*, 43(8):1296–1311, 2005.
- [140] Pinting Zhang and Shuhong Huang. Review of aeroelasticity for wind turbine: Current status, research focus and future perspectives. *Frontiers in Energy*, 5(4):419–434, 2011.
- [141] Dejan Zupan and Miran Saje. The linearized three-dimensional beam theory of naturally curved and twisted beams: The strain vectors formulation. *Computer methods in applied mechanics and engineering*, 195(33):4557–4578, 2006.
- [142] Michael D Zuteck. *Adaptive blade concept assessment: curved planform induced twist investigation*. Citeseer, 2002.

CURRICULUM VITAE

Etana Ferede was born on 23rd of May 1986 in Bishoftu, Ethiopia. Together with his brother, he emigrated to the Netherlands at the age of 12. He followed his High-school education at Coenecoop College, which he completed in 2005. He started his study in Aerospace Engineering at Delft University of Technology on 2006. He obtained his Bachelor of Science in 2009. He continued his Masters education at the same university, specializing in structural design, analysis, and optimization. He obtained his Masters of Science degree with distinction in 2011, where his master thesis focused on aeroelastic tailoring of Airbus A320 wing box. Since October 2011 he started his PhD at TUDelft, department of Wind Energy. His research topic focused on the aeroelastic tailoring of composite wind turbine rotor blades, where the benefits of twist coupled rotor blades in stall controlled wind turbines are investigated. Furthermore, he has been a guest researcher in 2014 at German Aerospace Center (DLR) in Goettingen, Germany.

LIST OF PUBLICATIONS

Journal Papers:

E.A. Ferede, M.M. Abdalla, and G.J.W. van Bussel. *Isogeometric Based Framework for Aeroelastic Wind Turbine Blade Analysis.*, <http://dx.doi.org/10.1002/we.1999>, Wind Energy, 2016.

E.A. Ferede, and M.M. Abdalla. *Cross-Sectional Modelling of Thin-Walled Composite Beams.*, Submitted to Journal of Thin-Walled Structures, 2015.

E.A. Ferede, and M.M. Abdalla. *Isogeometric Formulation of Geometrically Exact 3D Beam Theory.*, to be submitted, 2016

E.A. Ferede, J.K.S. Dilligar, M.M. Abdalla, and G.J.W. van Bussel. *Multidisciplinary Optimization of Composite Rotor Blades: Exploring Twist Coupled Composite Blades in Stall Control.*, to be submitted, 2016.

R. Pereira, E.A. Ferede, G.J.W. van Bussel, and W.A. Timmer. *Design and Optimization of Active Stall Controlled HAWT rotor.*, to be submitted, 2016.

Conference Papers:

E.A. Ferede, J.K.S. Dilligar, and M.M. Abdalla. *Isogeometric Framework for Aeroelastic Wind Turbine Rotor Analysis*, International Forum of Aeroelasticity and Structural Dynamics, St. Petersburg, Russia, 2015.

E.A. Ferede, and M.M. Abdalla. *Cross-Sectional Modelling of Thin-Walled Composite Beams.*, AIAA Sciences and Technology Forum, National Harbor, USA, 2014.

M. Schelbergen, L.O. Bernhammer, E.A. Ferede, and C.J. Simao Ferreira. *Structural optimization of multi-megawatt, offshore vertical axis wind turbine rotors.*, AIAA Sciences and Technology Forum, National Harbor, USA, 2014.

De Breuker, R, Abdalla, MM, Werter, NPM, Vandewaeter, L, Ferede, EA, Dillinger, JKS, and Kruger, W. *An Aeroelastic Multi-Fidelity Approach for Aeroelastic Tailoring.*, Royal Aeronautical Society, Proceedings of the International forum on Aeroelasticity and Structural Dynamics, London, UK, 2013.

E.A. Ferede, M.M. Abdalla, and G.J.W. van Bussel. *NURBS-Based Parametric Modelling of Wind Turbine Blades.*, 9th PhD seminar on Wind Energy in Europe, Visby, Sweden, 2013.